Lightweight gearbox using novel housing architecture and materials

Daniel Amaral

Numéro d'ordre NNT: 2023ECDL0046 Année: 2023

THESE de DOCTORAT DE L'UNIVERSITÉ DE LYON
OPÉRÉE AU SEIN DE L'ÉCOLE CENTRALE DE LYON

ÉCOLE DOCTORALE MEGA

(Mécanique, Énergétique, Génie Civil, Acoustique)

Spécialité : Génie Mécanique

Soutenue le 07/12/2023 par

Daniel R. AMARAL

Lightweight gearbox using novel housing architecture and materials

---

Devant le jury composé de:

Rapporteur:	Stephan RINDERKNECHT	-	Professeur, TU Darmstadt
Rapporteur:	El Mostafa DAYA	-	Professeur, Université de Lorraine
Directeur:	Mohamed ICHCHOU	-	Professeur, LTDS, ECL
Co-Directrice:	Michelle SALVIA	-	Maître de Conférences, LTDS, ECL
Co-Encadrant:	Pascal FOSSAT	-	Chercheur, LTDS, ECL
Présidente:	Cécile LANGLADE	-	Professeur, UTBM
Examinateur:	Przemysław KOŁAKOWSKI	-	PDG/CEO, Adaptronica

Abstract

This PhD thesis is dedicated to the lightening of gearbox housings based on recent developments in various scientific fields, resulting from the joint academic and industrial research. The thesis is structured into five chapters.
The initial chapter presents a thorough literature review, while the subsequent four chapters delve into distinct aspects to enhance the performance of gearbox housings taking into account all the constraints for an optimized design.
Chapters 2 and 4 focus on reducing the weight of gearbox housings by employing optimization techniques in their design and incorporating novel materials. Chapter 2 is devoted to the design of lightweight metallic gearbox housings. Chapter 4 investigates the use of composite materials for manufacturing of gearbox housings. The proposed strategies result in lighter Gearbox Housing (GBH) configurations, leading to improved operational efficiency from an energy saving perspective.
The lightweight design tends to degrade the Noise, Vibration, and Harshness (NVH) signatures. Hence, concurrently, chapters 3 and 5 introduce novel passive Locally Resonant Metamaterial (LRM) solutions tailored to enhance the NVH characteristics of GBHs. Notably, these LRM solutions offer a cost-effective noise control alternative, requiring minimal complexity in the design process and eliminating the need for control systems. An essential advantage of these LRM solutions is their capacity to effectively attenuate noise and vibration within the challenging low-frequency range. Moreover, these passive LRM solutions display an ability to provide broadband attenuation, contributing to a significant reduction in overall noise and vibration levels. The experimental studies presented in chapter 3 validate the benefits of using LRMs to improve the GBH behavior.
The results of this study represent a step forward in the practical implementation of LRM technologies in lightweight GBHs and Electric Vehicle (EV) motor housings. In conclusion, this research bridges the gap between academic innovation and real-world engineering applications, contributing to the development of more efficient and quieter GBHs, thereby improving the overall user experience and promoting sustainable transportation solutions.

Keywords: gearbox housing, lightweight design, NVH control, locally resonant metamaterials, composite design.

Résumé

Cette thèse de doctorat est dédiée à l'allégement de carters de boîtes de vitesses (GBHs) en s'appuyant sur les développements récents dans divers domaines scientifiques, résultant de la recherche conjointe académique et industrielle. La thèse est structurée en cinq chapitres.

Le premier chapitre présente une revue bibliographique approfondie, tandis que les quatre chapitres suivants sont consacrés aux différentes techniques pour améliorer les performances des carters de boîte de vitesses avec une prise en compte des contraintes de conception.

Les chapitres 2 et 4 se concentrent sur la réduction de la masse des carters de boîte de vitesses en utilisant des techniques d'optimisation pour leur conception et en incorporant de nouveaux matériaux. Le chapitre 2 porte sur la conception des carters de boîtes de vitesses métalliques légers. Le chapitre 4 étudie l'utilisation des matériaux composites pour la fabrication des carters de boîtes de vitesses. Les stratégies proposées aboutissent à des configurations de carter de boîte de vitesse (GBH) plus légères, ce qui améliore l'efficacité opérationnelle du point de vue d'économie énergétique.

La réduction de masse des carters a tendance à dégrader le confort acoustique et vibratoire (NVH). Par conséquent, les chapitres 3 et 5 introduisent de nouvelles solutions NVH passives avec métamatériaux à résonance locale (LRM) conçues pour améliorer des caractéristiques NVH des GBHs. Notamment, ces solutions LRM offrent une alternative avantageuse pour le contrôle du bruit. Elles nécessitent une conception relativement simple tout en supprimant l'utilisation de systèmes de contrôle. Un avantage essentiel de ces solutions LRM est leur capacité à atténuer efficacement le bruit et les vibrations dans la gamme des basses fréquences. De plus, les solutions LRM affichent une capacité à fournir une atténuation en large bande, contribuant à une réduction significative des niveaux globaux de bruit et de vibration. Les études expérimentales présentés aussi au chapitre 3 valident les avantages de l'application LRM dans le GBH.

Les résultats généraux de cette étude représentent une avancée dans la mise en œuvre pratique des technologies LRM pour la réalisation de GBHs et de carters de moteur de véhicules électriques plus légères. En conclusion, cette recherche connecte l'innovation académique et les applications d'ingénierie, contribuant au développement de GBHs plus légères, efficaces et silencieux, améliorant ainsi le confort de l'utilisateur tout en promouvant des solutions de transport plus écoresponsables.

Mots-clés: carter de boîte de vitesses, conception de structure allégée, contrôle acoustique et vibratoire, métamatériaux à résonance locale, conception composite.

Acknowledgments

The author acknowledges the support from the European Commission's Horizon 2020 program. The LIVE-I (Lightening and Innovating transmission for improving Vehicle Environmental Impacts) is a European Industrial Doctorate (EID) under the Marie Skłodowska-Curie Actions (MSCA) with the grant agreement number 860243.

There couldn't be two more ideal locations for conducting a Marie Skłodowska-Curie program than a PhD research project bridging France and Poland, particularly Warsaw—the city where the renowned scientist was born.

Within the LIVE-I Innovative Training Network (ITN), I had the privilege of collaborating with a remarkable group of professors, researchers, and colleagues whose dedication and passion have been truly inspiring. Among them, I developed an exceptional connection with my colleagues, who were always available to engage in interesting discussions. I am optimistic that the strong bonds forged during this enriching experience will pave the way for fruitful collaborations in the future.

I want to take this opportunity to express my gratitude to the academic supervisory team: Prof. Mohamed Ichchou, Prof. Michelle Salvia, Dr. Pascal Fossat at École Centrale de Lyon, and the industrial supervisor, Dr. Przemysław Kołakowski. Their remarkable expertise and dedication as researchers have been an enlightening beacon throughout my PhD journey. I am profoundly thankful for their guidance, trust, and patience, which have played a pivotal role in shaping my academic and professional growth.

I extend my heartfelt gratitude to my colleagues at École Centrale de Lyon, who have become cherished friends and brought energy to our days, sharing memorable moments together in the E6 and TMM.

I am very grateful to the incredibly supportive people I found in Adaptronica. A special thanks to Arek, Janek, Marek, Damian, Darek, Krzysztof, Łukasz and Mr. Motylewski. They made my stay in Poland a pleasant experience and taught me a lot about vibration control and experimental work in the field. They made an incredible contribution to my professional development. Thanks to Mr. Wodek for his exceptional skills in manufacturing the gearbox housing mock-up for the experiments. Dziękuję bardzo wszystkim!

I wish to express my gratitude to the esteemed members of the jury, Prof. El Mostafa DAYA from Université de Lorraine, Prof. Stephan RINDERKNECHT from TU Darmstadt, and Prof. Cécile LANGLADE from Université de Technologie de Belfort-Montbéliard, for their roles as reviewers and examiners of this work. I want to thank them for their dedication, effort, and commitment of time.

Quero expressar a minha gratidão a todos os professores que contribuíram para a minha formação. Um agradecimento especial aos Professores Paulo Tavares de Castro, José Luis Esteves e António Torres Marques, que contribuíram muito para o meu desenvolvimento académico e profissional.

Agradeço aos meus amigos de longa data pelo constante estímulo, bem como pelas opiniões e sugestões sempre genuínas.

Dedico um afetuoso e enorme obrigado à minha mãe, Sara, ao meu pai, Fernando, ao meu irmão, Diogo, e a todos os membros da minha família, assim como à Daniela, pelo seu apoio leal e encorajamento constante que me permitiram chegar até aqui. Sem eles, esta conquista não teria sido possível.

Contents

List of Acronyms

Introduction

Research Framework and Motivation

Contemporary society is confronted with a multitude of environmental problems, one of which stems from transportation and mobility. Therefore, the pursuit of environmentally friendly transport and mobility solutions is a vital subject. One approach to achieving this goal is by reducing the weight of vehicles.

The reduction of the weight of vehicles has several advantages both in the manufacturing and operation stages. During manufacturing, it is possible to decrease the component transportation and assembly costs since smaller cranes and transport machines can be used. Moreover, fewer raw materials are needed to manufacture equivalent components. In the operation stage of the vehicles, the reduction of the mass of the vehicles represents a reduction of greenhouse gases emission (and other harmful gases/particles), in the case of internal combustion engine (ICE) vehicles, and the increase of the range for electric vehicles (EVs) and hybrid electric vehicles (HEVs) in the electric propulsion mode. Additionally, the mass reduction can improve the vehicle's maneuverability.

The present work is part of the LIVE-I Project, which is a European Industrial Doctorate (EID) program. The acronym stands for Lightening and Innovating Transmission for Improving Vehicle Environmental Impacts, and it has received funding from the European Union's Horizon 2020 research and innovation programme through Marie-Curie grant agreement No 860243. The project's main aim is to achieve a breakthrough in the design of lightweight gear transmissions. The technical objective is to demonstrate a significant weight reduction of gearboxes using state-of-the-art modeling tools together with advanced materials. The LIVE-I project is constituted by nine different PhD projects. This PhD project, in specific, is devoted to the lightening of gearbox housings through the development of new housing architectures following new paradigms in the design using metamaterials. This project is characterized by its multidisciplinary approach, incorporating subjects from various engineering fields, including mechanics, structural design, metamaterials, machine design and vibroacoustics. As an industrial PhD, the project places special emphasis on the practical engineering applications.

The vehicle weight reduction is achieved by the lightweight of its constitutive components. On the other hand, the vehicle components must fulfill their specific requirements, which are frequently dependent on the component mass. Hence, there is a trade-off between weight and performance. In order to overcome this trade-off, innovative solutions are needed to manufacture lightweight, capable and effective components. It is also essential to consider the environmental impact of introducing new materials and manufacturing processes required to reduce weight, following the vehicles' end-of-life directives [119]. As mentioned, each vehicle component has

specific requirements that must be met. In this work, the focus is on the Gearbox Housing (GBH). A review is conducted on historic gearbox developments as well as current conventional gearbox solutions to better understand the challenges in designing a lightweight gearbox housing that accomplishes all requirements.

In engineering applications, lightweight design of components often leads to noise and vibration issues. A lightweight gearbox is no exception in this regard. In order to develop sustainable and marketable solutions, it is essential to consider not only technical application demands but also customer needs, expectations, and desires. NVH are key indicators of driver comfort, and therefore, lightweight solutions must be developed in conjunction with innovation in the area of NVH.

The LIVE-I consortium consists of academic and industrial partners, including Magna, a major worldwide supplier of automotive gearboxes. Figure 1 illustrates a state-of-the-art automotive gearbox from Magna.

Figure 1: Example of 7-Speed DCT Gearbox from Magna

The teeth meshing process is the primary source of vibration in gearboxes. This vibration is transmitted to the housing through the bearing support contact areas, and consequently, the vibration of the housing generates noise in the nearby environment. The structural response of the components on the described path can attenuate or amplify these vibrations. While other projects inside LIVE-I consortium focus on studying the behavior of gears, shafts, and bearings in the gearbox, this work aims to reduce the mass of the gearbox housing and improve its vibroacoustic behavior. In other words, the work focus is on the last part of the described vibroacoustic path of the gearbox.

The abovementioned circumstances and background provide the context for the development of this work. The following section will provide a detailed description of the project objectives and the contributions of this work.

Objectives and Thesis Outline

The main objective of this project is to improve the design of gearbox housings in order to make them lighter and effective in all their requirements. This involves

conducting an extensive examination of current research, with a focus on addressing unexplored challenges. The project proposes the use of innovative housing architectures and metamaterials to develop lightweight and capable gearbox housings. By pushing the boundaries of conventional designs, this work aims to establish new paradigms that will redefine the industry's perspective of gearbox housing possibilities.

The mass reduction of the housing can be achieved in two ways, one through the improvement of its geometry and another through the change of its constitutive materials. In the recent literature, early studies have been conducted on the application of composite materials, such as carbon and glass fiber composites, on gearbox housings [150, 151, 59, 58]. Although the results suggest that composite gearbox housings can provide a structurally viable alternative to metallic solutions, the literature does not define processes or guidelines for the design of optimized lightweight gearbox housings. Therefore, further investigation is needed in this area to develop more effective solutions.

In the literature, topology optimizations of GBHs have been explored to reduce the component mass while maximizing its structural stiffness [112, 158, 78]. However, the realized topology optimization investigations do not further assess how the mass reduction and geometric modifications influence housing vibration and noise radiation. Including these assessments in the housing mass reduction study is of the utmost importance to allow the industrial adoption of lightweight gearbox housings. This research aims to enhance understanding by expanding the scope of analysis to include vibration characteristics and noise radiation, thereby providing a comprehensive assessment of the subject.

The manuscript commences with a review of gearbox functions, encompassing their general principles. Subsequently, it focuses on the specific context of automotive gearboxes. Notably, it then places particular emphasis on the requirements of gearbox housings, exploring their traditional geometry, their conventional materials and the manufacturing processes involved.

The manuscript proceeds with a literature review that examines the use of composite materials in gearbox housings. This entails summarizing various aspects such as composite matrices, reinforcing materials, reinforcement arrangements, failure criteria assessments, and manufacturing processes. Additionally, it encompasses a review of the first attempts to incorporate composite materials into gearbox housing design, followed by an analysis of the most recent documented applications of composites in this domain. The section concludes with an overview of techniques employed for composite design optimization.

The subsequent section provides important insights into NVH assessments and its metrics. It delves into the current noise-related challenges and regulations, presents a summary of structure vibroacoustic interaction concepts, describes the conventional vibroacoustic control methods, and offers examples of design processes for vibroacoustic enhancement.

Particular attention is given to vibroacoustic metamaterials and the modeling of locally resonant metamaterials, exploring their potential for application in gearbox

housings. Additionally, the manuscript evaluates the suitability of recent metamaterial solutions for gearbox housing applications. Given the rapidly evolving nature of this field, a detailed and up-to-date review of existing work is essential to avoid duplication and to remain updated with the latest practices.

The work contributions are divided into two parts:

- The second chapter is devoted to the improvement of metallic housings through the improvement of their geometry. An initial analytical approach is implemented to achieve mass reduction in a simple plate while preserving its stiffness by incorporating ribs into thinner panels. Following this, a more general approach using topology optimization methods for component geometry improvement is described, along with a brief discussion of modal optimization and conventional noise control methods. Subsequently, noise radiation assessments are performed and the results before and after topology optimization are compared. The third chapter explores the application of metamaterials for NVH control in metallic GBHs, improving their NVH signature. The results were obtained through numerical simulations and validated through experimental works.

- The fourth chapter focuses on exploring alternative materials for gearbox housing construction. A comprehensive discussion of the different possibilities is presented, including an assessment of their viability as potential solutions. A particular focus is given to the design of composite GBH solutions. Different design approaches are described and implemented in this section. The process commences with the utilization of the ABD composite matrix to define the composite stacking. Subsequently, a stacking and layer orientation optimization process is presented and implemented, allowing for further enhancement of the composite design. The failure criteria and safety evaluations are also reported during the composite design studies. The NVH impact of the material change in the gearbox housing is assessed by evaluating the sound power radiated from the optimized composite solution and comparing it with the aluminum counterpart. The fifth chapter reports the investigation of metamaterial solutions to enhance the NVH of the composite gearbox housing designs. The last chapter also showcases solutions suited for industrial integration.

Chapter 1

Literature Review

This chapter provides a review of gearbox functions and their fundamental principles, followed by an exploration of housing-specific requirements and trends in automotive gearboxes. Traditional designs, materials, and manufacturing methods of gearbox housings are investigated. The focus then shifts to composite materials and design. The text proceeds by reviewing early efforts to incorporate composites in GBH design and analyzing recent applications. The chapter discusses NVH assessments and metrics, exploring structure vibroacoustic interaction concepts, noise-related challenges, and regulations. Traditional vibroacoustic control methods are outlined, supplemented with design process examples for enhancing vibroacoustics. The chapter addresses the topic of metamaterials, particularly locally resonant metamaterials. Recent experiments involving LRMs in engineering applications are summarized, along with exploration of modeling and optimization possibilities.

1.1 Gearbox and its Housing

1.1.1 Gearbox Function

A gearbox is a mechanical system consisting of an arrangement of gears within a housing. Similarly to other gear systems, the function of the gearbox is to alter torque and speed between a driving device and a load. Typically, gearboxes increase torque while reducing rotating speed whilst transferring energy from one device to another.

Gearboxes may have several sizes and shapes, depending on their intended use and the specific requirements of the application. However, generally, the gears are typically mounted on shafts, which are supported by bearings to allow for rotation. These bearings are in turn attached to the GBH, which provides mechanical support for the gearbox components. The GBH is also responsible for containing the lubricant and dissipating heat generated by the gearbox, among other functions.

Gearboxes are used in wind turbines, machine tools, industrial equipment, conveyors, ship, automotive and aerospace applications. According to their application, additional requirements may arise. In machine tools, the main objective is controlling the machining speed regardless of the speed of the driving device. For instance, in turning operations on lathe machines, the machining speed (also known as cutting speed) is a function of the diameter of the part to be machined. For this reason, a

gearbox must be used to provide a correct machining speed in the operations. As a rule, in machine tools applications, the gear ratio is altered by shifting the gears when the machine is stopped.

In automotive applications, gearboxes main function is to amplify the output torque, while reducing the output rotational speed, according to the set gear ratio. In contrast to machine tools, the gear ratio shifting should be done without stopping the motor. The presence of clutches allows the shifting with a running motor. Clutches are also needed because in vehicles with Internal Combustion Engine (ICE), since the engine cannot develop torque with no engine speed. Additionally, for the vehicle's initial motion, the first gear couple on the gearbox needs to have a high rotational speed reduction, increasing the torque available on the wheels. A gearbox that includes multiple gear ratios is an essential component of an efficient motor system, as it allows for optimal power usage and reduced fuel consumption and emissions. The highest gear is often configured as overdrive, signifying an augmentation in rotational speed from the engine to the wheels. In certain gearboxes, the top gear adopts a "direct-drive" configuration, with a rotational speed ratio of 1:1 and thereby sidestepping frictional losses in the gear meshing processes. Additionally, the gearbox should be able to facilitate both forward and reverse driving.

1.1.2 Automotive Gearbox Context

The majority of the primordial automobiles used a belt-drive as a single-speed transmission. The first introduction of a gear transmission in a vehicle was made in 1894 by the French motor vehicle manufacturer *Panhard et Levassor*, the manual transmission consisted of a sliding-gear three-speed transmission. The mechanism was non-synchronous, in other words, the gear teeth must be aligned in order for the respective gears to mesh [67]. As a result of the lack of synchronizers in early manual transmission systems, drivers often experienced grinding or crunching sounds during gear shifts. These transmission systems became known as "crash boxes" due to this characteristic. The synchromesh transmission was invented in 1918 by Earl Avery Thompson [164] and the earliest synchromesh transmissions were produced in the late 1920s. However, only in the 1950s the synchromesh transmissions in vehicles were mass adopted, and in the beginning the majority of the implementations were just for specific gear ratio shifts [67].

Automakers, and more specifically vehicle gearbox manufacturers, suit the number of gearbox speeds attending customer needs, in a compromise between efficiency, shifting needs and cost. Having more gearbox speeds enable the first gear speed to have a high gear ratio, leading to higher starting acceleration, while the top gears can have a lower gear ratio to achieve better fuel economy at high speeds. The employment of more gear ratios permits the use of smaller, more economical engines to power vehicles and can improve the efficiency of existing engines. Over the decades, the number of gear ratios on vehicle gearbox transmission increased from three or four forward speeds to five or six.

There are two common types of gear sets used in gearboxes. The first is the

fixed axis gear set, where each gear ratio is represented by a gear pair comprising a fixed gear and a speed gear. The second is the planetary gear set, also known as an epicyclic gear train, where the gear system consists of three main components: a sun gear, planet gears, and a ring gear. The sun gear is located at the center and is typically the input shaft that receives rotating power from an external source. The planet gears, also known as pinions, are smaller gears that mesh with both the sun gear and the ring gear. These gears are typically mounted on a carrier, which is connected to the output shaft. The ring gear is the outermost gear and meshes with the planet gears. The gear ratios are achieved by selecting the appropriate planetary gear sets to couple.

The fluid clutch, initially developed for marine applications in 1905, served as the basis for the invention of the first Automatic Transmission (AT) by the steam engineer Alfred Munro [131]. However, the early design used air as the power carrier fluid, resulting in low system efficiency. In the next decade, General Motors developed the first AT using hydraulic fluid. In 1940, General Motors started the commercialization of vehicles with AT [67]. After World War II, there was a significant increase in the adoption of vehicles equipped with automatic transmissions. The main reason for this adoption was the simplicity offered by automatic transmissions, which made driving easier and more comfortable for the masses. Over the years, automatic transmissions have evolved alongside improvements in control electronics [74].

Regarding the gearbox speed selection mechanism, the gearboxes are categorized into three groups:

- Manual transmissions, where the gear ratio selection is performed by the vehicle driver using a gear lever (also known as gear stick) and the clutch actuator.

- Automatic transmissions, for which the speed shifts are not made manually by the vehicle driver, but instead by a control system. The driver only needs to select the desired driving mode (e.g. "Drive", "Reverse", "Park"). Automatic transmissions are subdivided into different typologies: Hydraulic AT, Continuously Variable Transmission (CVT), Automated Manual Transmission (AMT) and Dual-Clutch Transmission (DCT). The latter two typologies are architecturally similar to a conventional manual transmission, however their actuation is automatic.

- Semi-automatic transmissions, where similarly to a manual transmission the driver's control and input are still required to shift gear ratios, however the actuation of the clutch system is fully automated.

DCT is a gearbox concept that is becoming mainstream across manufacturers. An example of this type of gearbox is shown in the Figure 1. A DCT is a type of gearbox that utilizes two separate clutches, one for the even-numbered gears and the other for the odd-numbered gears. This allows for seamless and rapid gear changes,

as the next gear is pre-selected and engaged by the opposite clutch while the current gear is still engaged. Dual-clutch gearboxes are popular in high-performance sports cars, as they provide fast, smooth gear changes that allow the engine to maintain optimal power output. They are also becoming more common in mainstream vehicles as manufacturers strive to improve efficiency and reduce emissions.

1.1.3 Gearbox Housing Requirements

The housing of an automotive gearbox has both inner and outer connections. Externally, the gearbox is typically mounted in the main vehicle structure (chassis) using bolted connections. Regarding the internal components, the gears are assembled onto shafts, which are then connected to bearings that are supported on the gearbox housing. Additionally, the housing is subject to several secondary connections, such as exterior connections to auxiliary components like actuators and electric units. The reliability of these connections play a vital role in ensuring the proper functioning of the gearbox and the vehicle as a whole.

In addition to the general requirements of a gearbox, the gearbox housing has specific requirements that must be taken into account. These requirements include:

- Provide mechanical support for the primary rotating gearbox components through the bearings mount.
- Support the selector mechanisms, actuators, cooling systems and eventual pumps.
- Ensure correct gear meshing by respecting the assembly tolerances of the rotating components.
- Cope with system loading generated by the transmitted torque.
- Provide mechanical protection of the gearbox inner components.
- Contain the lubricant inside the gearbox and guarantee the correct lubricant flow.
- Dissipate the inner generated heat.
- Have a geometry that allows the assembly of all the gearbox components.
- Allow the assembly of the gearbox into the entire vehicle system.
- Provide good NVH characteristics.

As mentioned in the last point, the gearboxes must provide good NVH characteristics, meaning that when designing them, their vibration and noise emissions should be minimized. In a gearbox, gear meshing generates noise that can be classified into two types: gear whine and gear rattle. Gear whine is caused by the vibration due to the presence of Transmission Error (TE) in the meshing and the varying mesh

stiffness. Related with the mismatches in the gear tooth profiles. Gear rattle is an impact-induced noise caused by the unloaded gear pairs of the gearbox. The backlash required for lubrication purposes is a key influence factor for this noise.

The stiffness requirements of the housing are directly linked to the mechanical loads that the housing must withstand at the bearings' connections. The mechanical loading at the bearing supports is a critical factor that depends on the geometries, characteristics, and assembly configurations of the rotating components. This loading is influenced by a variety of factors, such as the transmission ratio, the angle of inclination of the gear teeth (in the case of helical gears), the transmitted power, the input speed, and the distance between axes [158]. The bearing support plays a crucial role in transferring loads from the shafts to the housing structure in both radial and axial directions. The housing must be designed to withstand these loads without deformation or failure.

1.1.4 Gearbox Housing Geometry and Manufacturing

Automotive gearbox housings are geometrically complex structures that depend heavily on the arrangement of internal components, external connections, and attached auxiliary components. They typically have numerous openings, connections, patterns, and thickness changes over their surfaces.

In the literature there are various design guidelines for gearbox housings [18, 122, 79, 158], which provide design rules to determine sidewall thicknesses, the thickness and width of the bearing flanges, the thicknesses of the supporting ribs, the bolt diameters in the connections. However, it's important to note that these guidelines only provide estimates of the geometric parameters and clearly do not guarantee an optimized design.

In order to fulfill the static structural requirements, the housing is often reinforced with ribs. The addition of ribs may also be aimed at controlling the radiated noise by the housing structure. While structures are typically stiffened to decrease the vibrating power, this stiffening can increase the radiation efficiency, meaning that the radiated power may not always be reduced. Le Moyne et al. [105] studied the acoustic influence of the ribs in gearbox housings, and its modeling alternatives. Additionally, they inferred that when using Boundary Element Methods (BEM) in acoustic simulations, the ribs should be modelled with elements of a maximum size of one eighth of the rib thickness, in order to achieve accurate acoustic results.

Following guidelines and analytical dimensioning, it is possible to design gearbox housings that can withstand the expected loads during operation. However, to achieve a lightweight design for the GBH, an optimized geometry is crucial. Topology optimization methods can be used for this purpose, allowing for multi-objective optimization of the housing geometry. Topology optimization is a mathematical technique that optimizes the distribution of materials within a defined design space while respecting specified constraints. In the automotive domain, several examples of topology applications can be found [91, 41, 127]. In the literature, some works can be found on the topic of structural optimization of GBHs [158, 78, 112]. However,

they do not investigate the NVH issues resulting from the mass reduction of the gearbox housing.

Currently, industrial production of gearbox housings is made by casting processes. Sand casting is used for the production of gearbox housing prototypes during the development process due to its flexibility and cost-effectiveness. The mass industrial production of gearbox housings is usually carried out through die casting, a manufacturing process that involves injecting molten metal under high pressure into a mold cavity. This process allows for the creation of complex geometries with accuracy and repeatability. Die casting is an efficient process, as it allows for the production of large numbers of identical parts with consistent quality in a short time. The housing wall thickness must be as uniform as possible to avoid issues such as hot tears, shrinkage cavities, or incomplete mold cavity filling. Moreover, depending on the material properties and casting process used, there is a minimum thickness requirement for the housing walls. In the design, it is also important to ensure that thickness transitions are smooth to reduce residual stresses in the casting. These considerations must be taken into account if the manufacturing process remains the same. Several studies, including [42], [129], [145], and [158], emphasize the significance of such constraints.

The conventional materials used for manufacturing automotive gearbox housings are typically cast metal alloys, including but not limited to iron, aluminium, and magnesium alloys. In the field of racing competition engineering, former aluminium casting technologies were unable to provide extremely thin sections. As a result, magnesium alloys became a popular choice for gearbox housings due to its high strength-to-weight ratio. Magnesium alloys are generally 30% lighter than aluminium alloys [95, 96]. Depending on the designs, mass reductions of around 20% can be achieved, despite the need for thicker cross-sections due to the lower stiffness of the magnesium alloys. Additionally, magnesium has better shock absorption properties comparing to aluminium, enhancing the durability of the component. On the other hand, magnesium alloys are more expensive and more susceptible to corrosion.

Nevertheless, with the development of new aluminium casting techniques, aluminium housings started to be preferred in the Formula One industry. Likewise, titanium alloys have also been considered for gearbox housing manufacturing due to their high strength-to-weight ratio and resistance to corrosion and wear [28]. Despite the increasing use of composite materials in Formula One, titanium alloys are still widely used in transmissions. One major drawback of using titanium is the need for a significant investment in machining tools.

1.2 Composite Gearbox Housing Solutions

A composite material is a material that is constituted of a combination of two or more heterogeneous materials. The first composite structures used in vehicles were combinations of steel and wood in the chassis [5]. At that time, the primary reasons

for using these composite structures were their availability, cost-effectiveness, and the ease with which they could be manufactured. Improving vehicle performance was not yet a primary goal.

Nowadays, composite materials typically refer to materials that incorporate reinforcing materials, such as strong fibers, which may be either continuous or non-continuous, within a matrix material [66]. The fibers serve to reinforce the matrix, resulting in a material with superior strength and durability compared to the matrix material alone. The use of composite materials has become increasingly popular in a wide range of industries due to their unique properties and versatility.

1.2.1 Matrices and Reinforcing Materials

Composite materials are widely used in many industries, including aerospace, automotive, marine, and sports equipment, due to their unique combination of properties such as high strength, low weight, and resistance to corrosion and fatigue. One of the most commonly used fibers in composite materials is glass fiber, which is produced in large quantities and can be found in a variety of applications, from boat hulls to wind turbine blades. There are several types of glass fiber with different properties. Within the automotive sector, E-glass fiber is the most widely used.

Carbon and aramid fibers are more expensive than glass fibers but are often used in high-performance applications. Aramid fibers, due to its chemically inert surface, have a weaker interface connection with the matrix. While this can be a limitation regarding the composite's overall strength and load-bearing capacity, it is a suitable property for impact bearing. Carbon fibers, in particular, have excellent mechanical properties, including high strength, low weight, and high stiffness. They are commonly used in aerospace applications, such as aircraft structures and rocket components.

A diverse range of carbon fibers is available, typically categorized into groups based on their distinctive properties and performance characteristics. These classifications include High Modulus Carbon Fibers (high stiffness), High-Strength Carbon Fibers (high tensile strength), and Intermediate Modulus Carbon Fibers (balance between stiffness and strength).

Apart from the commonly used fibers, there are other types of fibers that can be used in composite materials, such as silicon carbide and boron fibers. Silicon carbide fibers have excellent thermal and chemical stability, making them suitable for high-temperature applications, while boron fibers have high strength and stiffness, making them useful in aerospace and defense applications.

Regarding the matrix material, it plays a critical role in the performance of composite materials. The matrix material surrounds the fibers and transfers load between them, helping to distribute stress evenly throughout the material. Polymeric matrices are the most commonly used matrix materials in composite materials, as they offer good adhesion to fibers and can be easily molded into complex shapes.

Polymeric matrices can be Thermoplastic (TP) polymers (such as polypropylenes, polyamides, and polyetheretherketones) or Thermoset (TS) resins (including

unsaturated polyesters, phenolics, polyurethanes, and epoxies) [66]. TP polymers are processed via heating and cooling processes without undergoing chemical reactions. TPs soften when heated and harden when cooled. Hence, the TPs are manipulated in their soften phase, arranging the matrix material.

In contrast, TS resins undergo a distinct manufacturing process involving chemical reactions. Curing agents are blended with the TS resin, and upon exposure to heat, these agents trigger cross-linking reactions (cure process), ultimately giving rise to the composite material. Once cured, TS composites cannot be melted or reshaped without degrading their properties [66].

Mineral matrices, such as silicon carbide and carbon, offer high temperature and wear resistance, but they are more brittle and can be challenging to process. Metallic matrices, such as aluminium alloys and titanium alloys, can offer high strength and stiffness, but they are heavier than polymeric matrices and usually more expensive.

Mechanical properties, such as stiffness, strength, and toughness, of composite materials depend on the properties of both the fibers and matrix materials. Researchers have developed various analytical and experimental techniques to study and optimize these properties, including micromechanical models, finite element analysis, and mechanical testing [66].

1.2.2 Reinforcement Arrangements

Reinforcement arrangements in composite materials refer to the ways in which the reinforcing material is arranged within the composite structure. The most widely used composite reinforcement arrangements are briefly explained in the following subsections. Special attention is dedicated to the composite laminate architecture due to its extensive utilization in engineering applications. The optimization of composite laminates plays a crucial role in facilitating the lightweight design of components.

1.2.2.1 Random Reinforcement

In random reinforcement, the reinforcing fibers or particles are randomly distributed throughout the composite. Commonly, short fibers are employed in this arrangement. This can create a material with isotropic properties, meaning that it has similar properties in all directions.

Random reinforcement can be made using a variety of fiber materials, such as carbon, glass, or aramid, as well as particle materials, such as silica or aluminium. The fibers or particles are typically embedded in a host material to create a filled material.

The manufacturing processes for filled materials are typically less costly than for unidirectional or woven composites. However, one of the main disadvantages of random reinforcement is that the strength and stiffness of the material may not be as high as in unidirectional or woven composites. Additionally, the distribution of the fibers or particles may not be uniform, which can lead to variations in properties

within the material [66, 5, 55].

1.2.2.2 Unidirectional Reinforcement

Unidirectional (UD) reinforcement is a type of reinforcement arrangement commonly used in composite materials. In UD reinforcement, all the reinforcing fibers or filaments are oriented in the same direction. This creates a material with high strength and stiffness along the direction of the fibers, but relatively low strength and stiffness in other directions.

UD reinforcement can be achieved using a variety of materials, such as carbon fibers, glass fibers, or aramid fibers. The fibers are typically embedded in a matrix material, such as epoxy or resin, to create a composite material.

UD reinforcement is often used in applications where high strength and stiffness are needed in a specific direction. For example, it is commonly used in the aerospace industry to create structural components for aircraft, such as wings and fuselages. In these applications, the UD fibers are typically arranged in a specific orientation to provide the necessary strength and stiffness properties for the component.

However, UD reinforcement can also have some limitations. Because the material is only strong in one direction, it may not be suitable for applications where loads will be applied in multiple directions. Additionally, the manufacturing process for UD composites can be complex and time-consuming, which can make them more expensive than other types of reinforcement arrangements [66, 5, 55].

1.2.2.3 Woven Reinforcement - Fabric

Woven reinforcement is another common type of reinforcement arrangement used in composite materials. In woven reinforcement, the reinforcing fibers are woven together in a specific pattern to create a fabric. The most common pattern used in woven reinforcement is plain weave, in which the fibers are woven over and under each other in an alternating pattern, an example is shown in the Figure 1.1 [66]. Fabrics can be found in rolls in dry form or impregnated with resin.

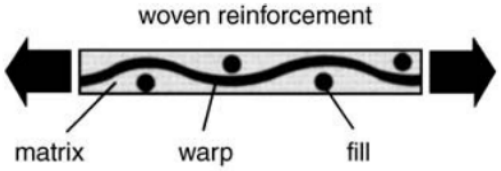

Figure 1.1: Cross-section of woven reinforcement layer with crossed fibers [66].

Woven reinforcement has some advantages over unidirectional reinforcement, thanks to the woven fiber pattern. This arrangement allows the resulting material to exhibit strength and stiffness in more than one direction. Additionally, woven reinforcement is relatively straightforward to manufacture and can be produced in large quantities.

One of the main disadvantages of woven reinforcement is that the woven pattern can result in some loss of strength and stiffness compared to unidirectional reinforcement due to fiber crimping. Additionally, the properties of the material can be influenced by the specific weave pattern used, which can make it more difficult to optimize the material for specific applications.

Overall, woven reinforcement is a versatile and commonly used reinforcement arrangement in composite materials. It is suitable for a wide range of applications and can provide a good balance of strength, stiffness, and cost [66, 5, 55].

1.2.2.4 Composite Laminate

Composite laminate is a type of composite material that is formed by the superposition of many layers (or plies), fabrics or mats. The individual layers are stacked and bonded together to create a single, integrated material with specific properties. The layers of a composite laminate can be arranged depending on the specific properties needed for the application. Composite laminates are commonly used in aerospace, automotive, and construction applications, where high strength and stiffness are needed in lightweight materials. They are also used in sporting goods, such as golf clubs and tennis rackets.

Balanced laminates have an equal number of layers of reinforcement on both sides of the middle plane of the laminate. For every layer in one direction on one side of the midplane, there is an identical layer oriented in the opposite direction on the other side of the midplane. Another critical aspect of composite laminate design is the arrangement of the layers. This arrangement can be symmetric or asymmetric. Symmetric laminates have identical arrangements of layers on both sides of the midplane, while asymmetric laminates have different arrangements on each side. Symmetric laminates are commonly used to prevent thermal residual stresses and deformations during cooling [66]. Additionally, symmetric laminates distribute applied loads evenly, reducing the generation of shear stresses within the laminate. In contrast, asymmetric laminates can induce the formation of shear stresses, increasing the risk of delamination and interlaminar shear failure.

A quasi-isotropic laminate is a type of composite material structure composed of multiple layers arranged in such a way that the resulting material exhibits nearly equal mechanical properties in all directions within its plane. In other words, it is designed to have approximately isotropic behavior within its plane, meaning that it possesses similar strength and stiffness characteristics in multiple directions. To achieve quasi-isotropic behavior, the individual layers in the laminate are oriented at different angles relative to each other. Common angles used in quasi-isotropic laminates include 0 degrees, 45 degrees, and 90 degrees, among others. By strategically arranging these layers at different angles, the composite material can achieve a balance of strength and stiffness properties.

The properties of a composite laminate are determined by a number of factors, including the materials used in the reinforcement and matrix, the orientation and arrangement of the layers, and the thickness of the laminate. By varying these factors,

composite laminates can be designed to meet specific performance requirements of applications. Several criteria should be considered when designing composite laminates to ensure that the final product meets the required mechanical properties and performance characteristics. Some of the major criteria include:

- Load requirements: The load requirements of the application will determine the strength, stiffness, and durability requirements of the composite laminate. The designer must consider the magnitude, direction, and frequency of the loads that the composite laminate will be subjected to.
- Material selection: The selection of the appropriate reinforcement and matrix materials will depend on the load requirements and other factors, such as environmental exposure, temperature, and cost. The designer must choose materials that are compatible, offer appropriate mechanical properties, and can be processed efficiently.
- Laminate configuration: The configuration of the laminate, including the number and orientation of the layers, can significantly impact the mechanical properties of the composite. The designer must choose an appropriate layup that optimizes strength, stiffness, and weight while also considering the manufacturability and cost. The overall mass of the component should be minimized in the optimization if the objective is to achieve a lightweight component. Additional constraints should be taken into account, for example, no more than four plies with the same orientation should be placed consecutively [66].
- Manufacturing process: The manufacturing process used to produce the composite laminate will affect the quality, repeatability, and cost of the final product. The designer must consider the chosen manufacturing method and its capabilities, as well as the design for manufacturability of the composite laminate.
- Cost considerations: The cost of materials, manufacturing, and assembly must be considered when designing composite laminates. The designer must balance the performance requirements with the cost of the final product to ensure that it is economically viable.

The conception process for components made of composite materials is inherently more complex than that for conventional isotropic materials. While the conventional process involves selecting an existing material and designing the component accordingly, composites require a more integrated approach where the material itself is designed based on the functional requirements. When designing a component made of composites, the designer has the flexibility to choose the specific reinforcement, matrix, and manufacturing process that best suit the desired performance criteria. This selection process is critical as it directly influences the mechanical properties, strength, and durability of the final composite material.

One key advantage of composites is the ability to optimize the mechanical behavior along specific directions through careful fiber orientation. By precisely aligning the reinforcing fibers in the composite, the designer can tailor the material's stiffness, strength, and other properties to meet the specific demands of the application. This enables the creation of components with exceptional performance characteristics, allowing for lightweight and efficient designs.

It is important to note that unlike classical metallic materials, composite materials generally exhibit elastic behavior until failure. They lack the ability to yield through localized plastic deformation. This behavior necessitates a different design approach, where factors such as load distribution, stress concentrations, and failure mechanisms specific to composites must be considered during the conception process.

The CLPT is a widely used in the analysis and design of laminated composite plates [66, 5, 55]. The CLPT is based on the principle of virtual work and the theory of elasticity. Strain-displacement relations provide an association between plate strains and displacements in the x, y, and z directions. The stress-strain relations are based in Hooke's law, which presumes linear elastic behavior for each layer. While the compatibility equations assure displacement compatibility between adjacent layers, the equilibrium equations guarantee the balance of forces within the plate. The study and design of laminated structures are made possible by the identification of displacements, strains, and stresses within the composite plate through the solution of these equations. The CLPT offers a condensed method for forecasting the behavior of composite laminates.

The ABD matrix, also known as the laminate stiffness matrix, is derived from the CLPT and provides a convenient way to characterize the mechanical behavior of the laminate [61]. The components of the ABD matrix are determined by the material properties of the individual plies, their orientations, and the laminate stacking sequence. It relates the applied loads and moments to the resulting strains and curvatures in a laminated composite.

For the calculation of the stiffness matrix, $[C]$, for each orthotropic lamina within a laminate, the Equation 1.1 is employed, where E_1 is the Young's modulus in the longitudinal direction, E_2 is the Young's modulus in the transversal direction, υ_{12} is the Poisson's ratio in the longitudinal direction, υ_{21} is the Poisson's ratio in the transversal direction and G_{12} is the in-plane shear modulus [132].

$$[\mathrm{C}] = \begin{bmatrix} \dfrac{E_1}{1-\upsilon_{12}\upsilon_{21}} & \dfrac{E_2\upsilon_{12}}{1-\upsilon_{12}\upsilon_{21}} & 0 \\ \dfrac{E_1\upsilon_{21}}{1-\upsilon_{12}\upsilon_{21}} & \dfrac{E_2}{1-\upsilon_{12}\upsilon_{21}} & 0 \\ 0 & 0 & G_{12} \end{bmatrix} \tag{1.1}$$

When analyzing a laminate with thickness h comprising n orthotropic layers subjected to a complex loading that includes both forces and moments (refer to

Figure 1.2), it is essential to establish a reference frame. The origin of the through-thickness axis (z) is positioned at the geometric midplane of the laminate. The plies within the laminate are numbered consecutively, commencing from the top face. The z coordinates corresponding to the upper and lower boundaries of the k^{th} ply are respectively represented as h_{k-1} and h_k.

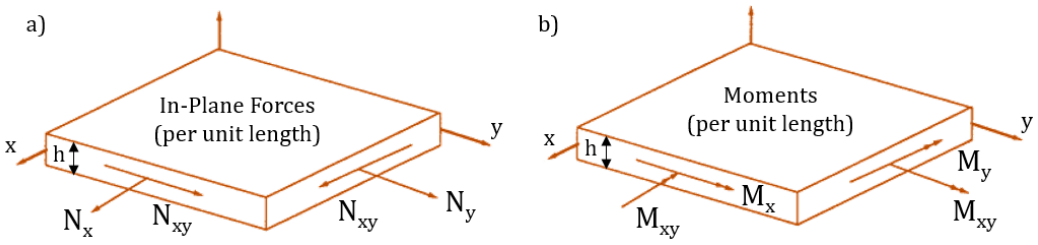

Figure 1.2: Composite laminate with thickness h subjected to a complex loading (forces and moments), adapted from [132].

The lamina stiffness matrix [C] is expressed in the lamina principal directions (ply coordinate system). Hence for calculation of the laminate stiffness matrix, it is essential to transform each lamina stiffness matrix to the global laminate coordinate system. This transformation is done by a coordinate transformation matrix. The lamina stiffness matrix expressed in the global laminate coordinate system is denoted by $[\overline{\mathrm{C}}]$.

The equations governing the relation between mechanical loading in the laminate and the resulting strains and curvatures are expressed in Equation 1.2. The matrices $[A]_{\mathrm{k}}$, $[B]_{\mathrm{k}}$ and $[D]_{\mathrm{k}}$ featured in the Equation 1.2 are outlined in the Equations 1.3, 1.4 and 1.5, respectively. The compact representation of the ABD matrix is shown in the Equation 1.6.

$$\begin{aligned}
\begin{bmatrix} \mathrm{N}_x \\ \mathrm{N}_\mathrm{y} \\ \mathrm{N}_\mathrm{xy} \end{bmatrix} &= \sum_{\mathrm{k}=0}^{\mathrm{n}} \left\{ [A]_\mathrm{k} \begin{bmatrix} \varepsilon_\mathrm{x}^0 \\ \varepsilon_\mathrm{y}^0 \\ \gamma_\mathrm{xy}^0 \end{bmatrix} + [B]_\mathrm{k} \begin{bmatrix} \kappa_\mathrm{x}^0 \\ \kappa_\mathrm{y}^0 \\ \kappa_\mathrm{xy}^0 \end{bmatrix} \right\} \\
\begin{bmatrix} \mathrm{M}_\mathrm{x} \\ \mathrm{M}_\mathrm{y} \\ \mathrm{M}_\mathrm{xy} \end{bmatrix} &= \sum_{\mathrm{k}=0}^{\mathrm{n}} \left\{ [B]_\mathrm{k} \begin{bmatrix} \varepsilon_\mathrm{x}^0 \\ \varepsilon_\mathrm{y}^0 \\ \gamma_\mathrm{xy}^0 \end{bmatrix} + [D]_\mathrm{k} \begin{bmatrix} \kappa_\mathrm{x}^0 \\ \kappa_\mathrm{y}^0 \\ \kappa_\mathrm{xc}^0 \end{bmatrix} \right\}
\end{aligned} \tag{1.2}$$

$$[A]_\mathrm{k} = \left[\overline{\mathrm{C}}\right]_\mathrm{k} \cdot (\mathrm{h_k} - \mathrm{h_{k-1}}) \tag{1.3}$$

$$[B]_\mathrm{k} = \left[\overline{\mathrm{C}}\right]_\mathrm{k} \cdot \frac{1}{2} \cdot \left(\mathrm{h_k^2} - \mathrm{h_{k-1}^2}\right) \tag{1.4}$$

$$[D]_\mathrm{k} = \left[\overline{\mathrm{C}}\right]_\mathrm{k} \cdot \frac{1}{3} \cdot \left(\mathrm{h_k^3} - \mathrm{h_{k-1}^3}\right) \tag{1.5}$$

The $[A]$ submatrix, defined in Equation 1.7, relates the applied forces (N_x, N_y, N_{xy}) to the resulting strains (ε_x, ε_y, γ_{xy}) in the laminate. It represents the extensional stiffness matrix and captures the in-plane properties of the laminate.

The $[B]$ submatrix, defined in Equation 1.8, relates the applied forces (M_x, M_y, M_{xy}) to the resulting curvatures (κ_x, κ_y, κ_{xy}) and the applied forces (N_x, N_y, N_{xy}) to the resulting curvatures (κ_x, κ_y, κ_{xy}) in the laminate. It represents the bending-extensional stiffness matrix and captures the coupling effects between the bending and extensional behavior of the laminate. For symmetric laminates and isotropic materials the components of the B submatrix equal 0.

The $[D]$ submatrix, defined in Equation 1.9, relates the applied moments (M_x, M_y, M_{xy}) to the resulting curvatures (κ_x, κ_y, κ_{xy}) in the laminate. It represents the bending stiffness matrix and captures the out-of-plane behavior of the laminate.

$$\begin{bmatrix} N \\ M \end{bmatrix} = \begin{bmatrix} A & B \\ B & D \end{bmatrix} \begin{bmatrix} \varepsilon \\ \kappa \end{bmatrix} \tag{1.6}$$

$$[A] = \sum_{\mathrm{k}=0}^{\mathrm{n}} \left[\overline{\mathrm{C}}\right]_{\mathrm{k}} \cdot (\mathrm{h_k} - \mathrm{h_{k-1}}) \tag{1.7}$$

$$[B] = \sum_{\mathrm{k}=0}^{\mathrm{n}} \left[\overline{\mathrm{C}}\right]_{\mathrm{k}} \cdot \frac{1}{2} \cdot \left(\mathrm{h_k^2} - \mathrm{h_{k-1}^2}\right) \tag{1.8}$$

$$[D] = \sum_{\mathrm{k}=0}^{\mathrm{n}} \left[\overline{\mathrm{C}}\right]_{\mathrm{k}} \cdot \frac{1}{3} \cdot \left(\mathrm{h_k^3} - \mathrm{h_{k-1}^3}\right) \tag{1.9}$$

The ABD matrix is a valuable tool in laminate design and analysis, it allows engineers to predict the response of laminated composite structures. By manipulating the ABD matrix, one can optimize the laminate configuration, material selection, and stacking sequence to meet the desired performance requirements. It is important to note that the ABD matrix assumes linear elasticity and does not account for failure modes such as delamination or fiber breakage. In cases where non-linear behavior or failure analysis is required, more advanced techniques and failure criteria, should be employed.

Overall, designing components made of composite material requires a comprehensive understanding of the material's behavior, an optimized selection of reinforcement and matrix materials, consideration of fiber orientation, and the application of specialized manufacturing techniques. By embracing the unique properties and potential of composites, designers can unlock innovative solutions that surpass the limitations of conventional isotropic materials.

1.2.2.5 Sandwich Structure

A sandwich structure can be considered a particular case of a composite laminate. A sandwich structure results from the assembly of two thin face sheets or skins

on a lighter core that is used to keep the two skins separated. The face sheets are typically made of high-strength materials such as carbon fiber composites or aluminium, while the core material can be a lightweight material/configuration like foam, honeycomb, or balsa wood.

The assembly of the face sheets to the core in sandwich structures is typically accomplished using bonding adhesives. In the case of thermoset prepregs, the bonding can also be done during the curing process. In some exceptional cases, welding may be employed, as in the case of metallic sandwich assemblies. The quality of the bond is crucial for ensuring the performance and longevity of the structure. The key advantages of sandwich structures include their lightweight nature and high flexural rigidity, which make them desirable for various applications. While sandwich structures are often praised for their excellent thermal insulation properties, this characteristic can pose challenges in specific applications. For example, in housing applications where heat generated by the gearbox needs to be dissipated, the high thermal insulation of the structure can impede heat dissipation and potentially lead to overheating issues.

Sandwich structures with honeycomb core tend to have relatively low acoustic isolation properties. Hence, this factor should be considered when selecting sandwich structures for applications where noise control is important. Additionally, the fire resistance of sandwich structures can be a concern, depending on the type of core material used. Some core materials may have lower fire resistance properties, which could potentially compromise the overall fire safety of the structure [66].

In summary, while sandwich structures offer benefits such as lightweight construction and high flexural rigidity, certain considerations must be taken into account. The thermal insulation properties, although advantageous in some scenarios, can pose challenges in applications requiring heat dissipation. Acoustic isolation may be limited, and the fire resistance characteristics can vary depending on the core material chosen. Careful evaluation of these factors is necessary to ensure that sandwich structures are appropriately applied and meet the specific requirements of the intended application.

1.2.3 Composite Failure Criteria and Safety

Failure criteria play a pivotal role in assessing the structural integrity and reliability of composite materials. These criteria are instrumental in predicting and analyzing various failure modes, including matrix cracking, fiber breakage, delamination, and overall material failure. Over the years, several failure criteria have been developed, each offering its own distinct approach along with specific advantages and disadvantages.

The simplest failure criteria for composites are the Maximum Stress and Maximum Strain criteria. These criteria involve comparing the maximum stress or strain experienced by the composite material with its corresponding strength or strain limits. While these criteria offer a straightforward approach, they fail to consider the effect of multiaxial stress states and the intricate stress-strain behavior of compos-

ites. As a result, their accuracy may be limited, particularly for advanced composite materials.

The Tsai-Hill criterion improves upon the Maximum Stress criterion by accounting for the multiaxial stress state in composite materials. It incorporates both normal and shear stresses by utilizing a quadratic failure surface in stress space. By comparing the quadratic form of the stresses with a critical value derived from material testing, the Tsai-Hill criterion predicts failure. Widely employed for predicting composite laminate failure, this criterion provides valuable insights into the failure behavior of composites.

The Tsai-Wu criterion represents another widely used failure criterion for composite materials. It encompasses both the tensile and compressive strength limits, as well as the shear strength limits of the material. Using an elliptical failure surface in stress space, this criterion evaluates the combined stress state in comparison to a critical value. This approach offers a reliable estimation of the failure envelope under various loading conditions, thereby enhancing the analysis of composite material failure.

The Tsai-Wu failure criterion for plane stress is expressed as an equality stated in the Equation 1.10, with the parameters defined in the Equation 1.11 and where σ_1 and σ_2 are the normal stresses in the material's principal directions and τ_{12} is the shear stress in the material's principal directions. In the parameters stated in the Equation 1.11, X_t is the longitudinal tensile strength, Y_t is the transverse tensile strength, X_c is the longitudinal compressive strength, Y_c is the transverse compressive strength and S is the shear strength. When the sum of the terms of the left part of Equation 1.10 reaches the value of 1, the Tsai-Wu failure criterion predicts the failure of the composite.

$$F_1\sigma_1 + F_2\sigma_2 + F_3\tau_{12} + F_4\sigma_1^2 + F_5\sigma_2^2 + F_6\tau_{12}^2 + F_7\sigma_1\sigma_2 = 1 \tag{1.10}$$

$$\begin{aligned} F_1 = \frac{1}{X_t} + \frac{1}{X_c}; F_2 = \frac{1}{Y_t} + \frac{1}{Y_c}; F_3 = 0; \\ F_4 = -\frac{1}{X_t X_c}; F_5 = -\frac{1}{Y_t Y_c}; F_6 = \frac{1}{S^2}; \\ F_7 = \frac{1}{Y_t}[1 - (F_1 + F_2)Y_t - (F_4 + F_5)(Y_t)^2] \end{aligned} \tag{1.11}$$

In addition to the aforementioned criteria, there are other approaches such as the Hashin, Puck, and LaRC03 criteria, which offer a more detailed analysis of failure modes in composites. These criteria take into account fiber and matrix failure, as well as their interactions. However, they require extensive material characterization data obtained from experimental tests that induce these specific failure modes.

1.2.4 Manufacturing Processes and Recycling

The semi-processed constituents employed in the production of composites encompass prepregs and dry fibers. Prepreg is a condensed form of "pre-impregnated"

fibers, wherein reinforcement fibers are impregnated with a resin matrix prior to their manufacturing. Conversely, dry fibers are unprocessed reinforcement fibers that necessitate resin infusion throughout the composite manufacturing procedure.

Numerous manufacturing processes are employed in the production of composite material components. These methods include Compression Molding, Pultrusion, Filament Winding, Injection Molding, Automated Fiber Placement (AFP), and Automated Tape Laying (ATL). Additionally, specific composite manufacturing processes tailored to the type of resin used for the composite matrix. For thermoset matrices, methods like Hand Lay-Up, Vacuum Bagging, Resin Transfer Molding (RTM) and Vacuum Assisted Resin Infusion (VARI) are commonly utilized [66, 55, 149].

Hand Lay-Up is a manual process used for simple shapes and low-volume production. Vacuum Bagging uses a vacuum bag to remove air and compact the laminate, and is used for moderately complex shapes and small to medium production volumes. RTM involves injecting liquid resin into a closed mold containing dry reinforcement materials and is suitable for producing medium to large complex components with good surface finish and dimensional accuracy. Compression molding is used for producing flat or moderately curved components in high volumes. Filament winding is used for manufacturing cylindrical or tubular components such as pipes, pressure vessels, and rocket casings [66, 55, 149].

AFP and ATL processes use computer-controlled machines to lay down continuous fiber tapes or tows onto a mold surface and are used for producing complex-shaped components with high fiber volume fraction and tailored properties. Injection molding is widely used for manufacturing thermoplastic composite components, allowing for high production rates of complex, yet small, geometries [66, 55, 149].

The widespread adoption of composite materials has historically been limited due to various challenges. These challenges include high material costs, inadequate design tools, concerns over repairability and recyclability, as well as slow and inefficient production processes. However, the automotive industry now has access to new composite manufacturing technologies that address these issues, making composite materials a more viable option.

Audi has developed a process called Ultra-RTM, which bears similarities to pressure-controlled RTM [149]. This innovative process involves a fully automated flexible fiber lay-up, a 2D to 3D preforming process that utilizes binder activation, and the press-molding of the finished preform. In Ultra-RTM, the resin injection is fast-curing, resulting in the production of high-quality finished products. As part of their advancements in Fiber-Reinforced Polymer (FRP) manufacturing, Audi has also established a production line specifically for manufacturing the Carbon Fiber Reinforced Polymer (CFRP) rear wall of the Audi A8.

Among the various composite manufacturing technologies employed in the automotive industry, compression molding is the most widely utilized. The fundamental process involves converting prepregs into the desired product using matched metal molds. Prepreg Compression Molding (PCM) is highly effective in creating high-quality finished products with excellent dimensional accuracy and surface

finish, making it a preferred method for manufacturing various automotive components. Typically, the cycle time for most compression molding operations ranges from 1 to 3 minutes. PCM offers several advantages, including fast cycle times, cost-effectiveness, and the ability to produce complex structural components. However, the high initial capital cost for expensive molds, presses, and material preparation units can present a barrier to adoption [149].

In thermoset matrix prepreg technology, the formation of voids is a significant concern, particularly during the impregnation stage (intra-laminar voids) and the laying-up stage (inter-laminar voids). These voids can result from entrapped moisture or volatiles generated during the curing process, adversely affecting the final product's mechanical properties. To mitigate void formation, several factors must be considered, including the rheological evaluation of resins, control over moisture and impregnation levels in prepregs, and optimization of processing conditions to allow for sufficient time to remove trapped void content [149]. By carefully monitoring and controlling these factors, manufacturers can produce prepreg components with minimal void content, ensuring high-quality end products.

The eventual shift from metallic material to FRPs in the manufacturing of GBHs can pose challenges in their recyclability. Generally, the recycling of metallic materials is simpler compared to FRPs. Recycling FRPs is challenging and, in some cases, currently impossible with existing technologies. End-life material processing is a crucial factor should be considered when choosing the material to construct the GBH, as it impacts the environmental sustainability and long-term viability of the manufacturing. For these reasons, it is important to assess the current state of composite recycling, including the advancements made, and the challenges faced [82, 197, 141].

The contemporaneous ways of recycling are mechanical, thermal, and chemical [82]. Mechanical recycling involves the physical breakdown of composites into smaller particles, which can be used as fillers or reinforcement in other products. Techniques like shredding, grinding, and milling are used to break down composites into smaller components. This method has gained popularity due to its relative simplicity and cost-effectiveness. However, mechanical recycling is often limited to low-quality applications, such as construction materials, as it degrades the mechanical properties of the original composite.

Composite materials that incorporate thermoplastic matrices are commonly recycled through a multi-step process. Initially, the end-of-life composite is shredded/cut into smaller pieces. Subsequently, these fragments undergo a transformation involving heating and the application of pressure to manufacture new parts. This recycling method results in new composite parts that are reinforced with short, discontinuous fibers. Consequently, these recycled components exhibit inferior mechanical properties compared to the original composite components.

For thermoset-based composites, thermal recycling involves the use of high temperatures to break down composite materials. One method is pyrolysis, which involves heating composites in an oxygen-free environment to produce gas and liquid byproducts that can be used as fuels or chemical feedstocks. Another technique,

known as incineration, involves burning composites to generate energy [82]. Thermal recycling can be an efficient way to recover energy from composite waste, but it does not address the issue of material reuse or preservation of valuable constituents.

Composites with thermoset matrix can follow chemical recycling processes, which aim to break down composite materials into their constituent polymers or fibers through chemical reactions. Solvent-based methods, such as dissolution and depolymerization, are employed to separate the different components [82]. Chemical recycling offers the potential to recover high-quality materials from composites, enabling them to be reused in similar or even higher-value applications. However, this method is still in the early stages of development and faces challenges in terms of scalability and cost-effectiveness.

There are three main issues associated with composite recycling: the complexity of composites, the lack of standardized processes and the economic viability [82, 197]. Composite materials are made of different material intertwined, making separation and recovery difficult. Additionally, composites may contain additives, coatings, or adhesives that further complicate the recycling process.

The lack of standardized recycling processes for composites poses a significant challenge. Unlike plastics or metals, which have well-established recycling infrastructures, composite recycling is still a fragmented field with diverse methodologies. The absence of universally accepted guidelines and standards makes it difficult to scale up recycling efforts and integrate composite waste management into existing recycling systems.

The economic viability of composite recycling remains a concern. The high cost of recycling technologies and the limited market demand for recycled composites pose obstacles to widespread adoption. As a result, recycling composites can often be more expensive than producing new materials, discouraging investment in recycling infrastructure.

To address these challenges, progresses were made through extensive research documented in recent literature. This research encompasses not only the recycling stage [82, 141] but also the development and manufacturing processes, including notable advancements like the creation of biodegradable thermosets and thermoplastic matrices [197]. These technological breakthroughs have the potential to greatly minimize the environmental footprint associated with composite materials, making their utilization more widespread and sustainable.

1.2.5 Composite Gearbox Housings: Early Developments and Automotive Racing Applications

The first application of composite materials in a gearbox housing is difficult to pinpoint. Nonetheless, one of the pioneering applications of composite materials in gearbox housing was seen in the aerospace domain, specifically in the Advanced Rotorcraft Transmission (ART) program, a collaborative effort between the US Army and NASA. As part of this program, a graphite fiber composite with a polybismalimide matrix (50% fiber content) was employed in the helicopter GBH [88]. Com-

parative analysis against contemporary state-of-the-art designs revealed substantial benefits, including significant reductions in weight and noise emissions. It should be noted, however, that concurrent advancements were made in the gearbox itself during this period, making it challenging to isolate the precise impact of introducing the composite material on the performance of the GBH.

In order to explore the state of the art in the composite materials in automotive applications, a review in the automotive racing competition domain is important. During the early years of Formula One racing competitions, chassis were predominantly constructed by tubular aluminium frames covered by aluminium panels. In the early 1960s the first composite chassis was built by Cooper Car Company. This innovative structure featured an aluminium outer skin, an aluminium honeycomb core, and an inner skin made of Glass Fiber Reinforced Polymer (GFRP). The structure components were bonded by phenolic film adhesive. Although this composite chassis car did not participate in Formula One competitions, it served as the role model for Formula 1 chassis design for the following two decades [150].

In 1981, the McLaren team revolutionized Formula One competitions by introducing the first carbon fiber composite monocoque. This monocoque was constructed by layering UD carbon fiber prepreg tape over a mandrel with the desired shape. The mandrel, made of aluminium alloy, was later removed to allow for the composite to cure in an autoclave. This advancement became the standard for Formula One chassis and offered not only an exceptional stiffness-to-weight ratio but also remarkable energy absorption properties, thus enhancing safety in the sport [150, 113, 48].

Composite construction was also applied to the gearbox housings, namely the introduction of CFRPs in the housing. The first investigation on the topic was performed by Ferrari in 1994, followed by the Arrows team in 1998 [150]. The first implementations of this concept were made in 2003 and 2004, by Renault and Honda Racing Formula One teams, respectively. Renault used a casing with a titanium lower section and a CFRP upper section in its R23 car. Honda Racing Formula One team built a lightweight composite gearbox housing also in conjunction with metal alloys, see Figure 1.3 [150].

The primary advantage of composites lies in their favorable stiffness-to-weight ratio, allowing them to provide mechanical support for gearbox components and handle system loading with reduced mass. On the other hand, CFRPs are not as proficient as metals in handling point loads [66]. Consequently, special attention must be given to the design of the bearing connections and other couplings to effectively distribute concentrated loads across the composite material. Often, metallic inserts are incorporated in these areas to reinforce the structure. Moreover, the coefficient of thermal expansion of CFRPs is generally lower, hence the increase on the operating temperature may induce high stresses between the joints with metallic materials.

In the Formula One racing industry, nowadays, achieving an overall weight reduction of the vehicle is no longer the primary design objective due to the existence of minimum weight regulations that can be easily met using current technology. How-

Figure 1.3: Honda Racing Formula One Composite Gearbox Housing [150].

ever, meticulous control over mass distribution remains crucial, as it significantly influences the car's handling characteristics.

In the racing industry, the predominant method of composite manufacturing remains part hand layup followed by a curing process in autoclaves. However, there is a growing emergence of new manufacturing processes that are being developed and implemented. An example of this is trackside 3D printing, which was introduced by McLaren to Formula One in 2017. This innovative approach enables teams to make small, last-minute modifications to the front or rear wings and various areas of bodywork. Currently, 3D printing is extensively utilized both trackside and in factory settings for manufacturing and prototyping purposes.

In the Formula One competition world, there is a continuous exploration of new 3D printing solutions that offer enhanced capabilities. In the realm of TP composites, technologies such as Fused Deposition Modeling (FDM) and PolyJet with microscopic layer resolution are being leveraged to achieve intricate and precise 3D-printed components [138]. These advancements in 3D printing enable teams to create complex geometries and optimize performance through customized designs.

Another notable example of new manufacturing technology is Fiber Patch Placement (FPP), which facilitates the automated production of intricate composite parts [60, 198]. While FPP is currently predominantly employed in the aerospace sector, it holds potential for further application and adoption in the automotive industry. FPP technology can be used with TS (cure after placement) and TP matrices.

The primary emphasis of the racing industry is on optimizing performance, where extensive structural optimizations are conducted through a combination of simulations and experiments. These efforts aim to push the boundaries of performance and enhance the overall competitiveness of the vehicles. While considerations such as durability, serviceability, and cost are still relevant, they are typically secondary factors in the pursuit of maximum performance. Conversely, in the broader automotive industry, cost considerations play a crucial role. Automotive components need to be marketable and economically viable, necessitating careful consideration

of production and development costs. While performance remains important, it is often balanced with cost-effectiveness to meet market demands and ensure mass production feasibility. Achieving the right balance between performance and cost is essential for success in the automotive industry.

1.2.6 Recent applications of composite on the gearbox housing

In recent publications, some efforts for using composite materials on the GBH may be found. In 2017, Schneider et al. [151] developed and tested a composite gearbox housing for a small electric vehicle gearbox. The research consisted in the substitution of an existing aluminium housing by a composite material formed by carbon fiber-reinforced organo sheets (carbon fibers embedded within a thermoplastic matrix) and UD carbon fiber composite tapes (embedded thermoplastic matrix) for structural reinforcement.

They started by performing a standard topology optimization, not considering the composite material to be used. This process resulted in a housing design concept that indicated areas where more or less material was required. The housing concept served as a guide for positioning the composite material and optimizing the layers of the organo sheets to achieve the required stiffness. The design process was performed manually, relying on interpretation and processing of the results. Topology optimization techniques were used as a baseline to determine where reinforcements should be localized in order to minimize the mass of the composite component.

After the initial design process, it was observed that the displacements of the housing were excessive. To address this, crossed UD composite tapes were introduced to reinforce the housing. Additionally, aluminium inserts were incorporated to transmit loads from the bearings to the composite housing, as the composite material alone does not provide the necessary hardness for bearing seats. To prevent corrosion, a glass fiber reinforced composite was introduced between the metallic inserts and the carbon fiber composite.

The manufacturing processes for the composite housing included compression molding, water jet cutting, and finally injection molding of short glass fiber reinforced thermoplastic. In the initial phase, the organo sheets and reinforcing UD tapes were heated and reformed through a pressing process to create the desired preform. The preform was then cut to size using water jet cutting. In the subsequent phase, the preform was heated again and molded with an injection molding tool to achieve the final structural geometry, including ribs and other functional surfaces. Preheating was crucial to ensure an optimal connection between the organo sheet and the glass fiber reinforced thermoplastic.

The developed prototype is shown in the Figure 1.4 demonstrated the feasibility of using composite materials in GBHs. However, it should be noted that the design process relied on manual techniques, and further assessments such as fatigue, thermal, and NVH studies were not conducted in this research [151].

In 2018, Šedivý et al. conducted a study [153] aimed at improving the design of an upper gearbox housing. The objective was to develop a hybrid metal-composite

Figure 1.4: Composite gearbox housing by Schneider et al. [151].

housing that would possess equivalent stiffness but with a lower mass compared to the original gearbox made from duralumin. The researchers employed wet lay-up technology using carbon-epoxy fabrics to manufacture the composite parts of the gearbox. However, during the initial attempt, it was observed that all the bearings exhibited lower radial stiffness.

In order to address the lower stiffness issue, special commercial reinforcement strips were introduced into the design. These strips played a crucial role in achieving the required radial stiffness for the housing. As a result of this modification, a significant mass reduction of 24.9% was achieved, while simultaneously increasing the radial stiffness in the vicinity of the bearings [153]. However, this study only focused on the evaluation of radial stiffnesses in the bearing regions, while there are many other requirements to be fulfilled to achieve a functional gearbox housing.

In 2019, a series of studies were undertaken to investigate the vibroacoustic implications of replacing the material in a gearbox housing [58, 59]. The original housing, depicted in Figure 1.5a, was composed of steel. The research aimed to assess the effects of adopting composite solutions as alternatives. Throughout the studies, the geometric model of the gearbox housing remained unchanged. The test involved the utilization of different composite materials.

The first composite configuration was a GFRP composed by 24 layers of plain weave fabric combined with an unsaturated polyester resin matrix, see Figure 1.5b. The second composite configuration consisted of another GFRP reinforced with chopped strand mat layers, maintaning an unsaturated polyester resin matrix, see Figure 1.5c. The GFRP housings were manufactured by hand lay-up method with vacuum assistance [159]. The third composite configuration consisted of a CFRP manufactured with carbon twill weave fabric prepregs (epoxy resin), see Figure 1.5d. The manufacturing process for the CFRP housing, as illustrated in Figure 1.5d, is described in an article by Jucha et al. [80]. The original housing geometry was maintained, and only the material of the upper part of the gearbox housing was altered. The weight reduction achieved by employing these three composite configurations exceeded 60% in comparison with the steel original upper housing.

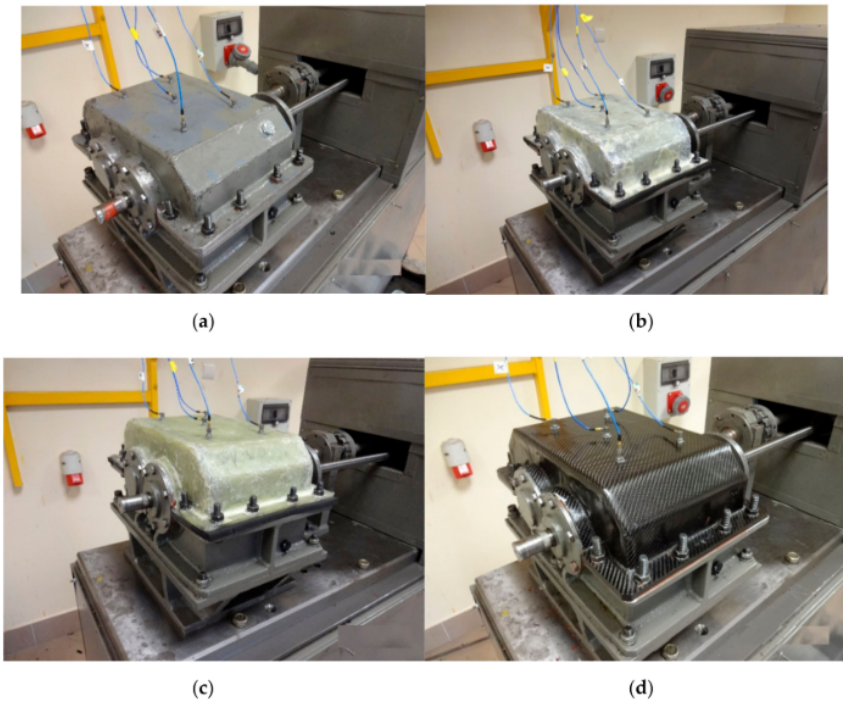

Figure 1.5: Housing configurations mounted on the test stand alongside with measuring transducers: (a) Steel housing, (b) GFRP - plain weave fabric, (c) GFRP - chopped strand mat, (d) CFRP housing [58].

The housing configurations were excited by a meshing gear pair inside the gearbox, the gear rotation was made by a power circulating test stand. The results showed that for the studied composite housings, the vibration and noise emission peaks are located in the lower ranges, lower than 1 kHz. For higher band ranges, composite housings have a significantly lower noise and vibration response level than the steel housing. Composite elements exhibit lower vibration levels compared to their steel counterparts in the frequency range above 1 kHz. The authors attribute this superior performance to the damping increase [58]. When operating at frequencies above 4 kHz, the GFRP housing constructed with chopped strand mats exhibits notable improvements in noise and vibration reduction compared to the original steel housing. Specifically, it achieves a noise attenuation effect of 15 dB and a vibration reduction of 27 dB.

These works [58, 59] provided a first step forward in the NVH evaluation of composite gearbox housings. However, there was no design study, neither optimization of the design. The authors simply aimed to resemble the geometries of the composite housings to the original steel housing geometry. As a result, there is considerable potential for further optimization and improvement in the design of the gearbox housing. Additionally, in the case of the carbon fiber housing, optimization of stacking, prepregs' orientation and thicknesses could be done to reach even lighter components.

Overall, in addition to the advantages associated with their lower mass, the findings from these studies [58, 59] strongly suggest that composite gearbox housings present a viable alternative to metallic solutions, particularly in terms of vibroacoustic performance.

According to recent market reports, the global composite materials market in the automotive sector was valued at approximately USD 9.4 billion in 2020 [149]. This figure is expected to rise to roughly USD 19.4 billion by 2027, with a compound annual growth rate of 10.9% [149]. This suggests a growing trend towards the adoption of FRPs in the automotive industry, owing to their exceptional mechanical properties and lightweight characteristics. The integration of FRPs in automobile design can help reduce vehicle weight, ultimately leading to improved performance and fuel efficiency.

1.2.7 Composite Design Optimization

Extensive research has focused on optimizing composite components, yielding a wide range of approaches. In this field, the utilization of design tools, particularly numerical optimizations, empowers engineers to swiftly and economically attain desired outcomes. These tools expedite the analysis of alternative designs, eliminating the cumbersome manual iterative evaluations that were previously necessary. Consequently, engineers and designers can efficiently explore various options and obtain optimal results in a fraction of the time and effort.

Toropov et al. [166] introduced a genetic algorithm-based process for optimizing composite components. In their approach, the component model is divided into

patches, and the thickness of each prepreg direction within each patch is optimized. The optimization process takes into consideration Critical Load Cases, which are essential for capturing the structural performance requirements.

The process incorporates various manufacturing constraints to ensure the feasibility of the optimized designs. For example, it limits the maximum number of successive plies in any given direction, such as allowing a maximum of four consecutive ply layers with the same orientation. Additionally, it enforces a minimum proportion requirement for each possible ply angle within every composite laminate, ensuring that each contains at least 10% of each ply angle. Moreover, it imposes a thickness ratio constraint between adjacent composite patches to prevent abrupt changes across laminate boundaries. For instance, a thickness ratio of 2:1 could be enforced between connected patches [166].

While the described process successfully optimizes the thicknesses of the prepregs, it does not optimize the directions of the prepregs. Therefore, there is room for further optimization by considering the orientations of the prepregs in addition to their thicknesses. This enhancement would allow for a more comprehensive optimization of composite components, considering both material distribution and orientation to achieve superior performance.

Zhou et al. [201] proposed a three-phase design optimization process for composite components. In which, prepreg orientations are pre-selected, in the application example the authors considered $0°$, $+45°/-45°$, and $90°$ plies. The objective of the first phase is to achieve optimal material distribution in terms of thicknesses of each prepreg direction. To ensure manufacturing feasibility, the authors incorporated some manufacturing constraints. These constraints included a maximum thickness limit for each fiber orientation, ensuring balanced $+45°/-45°$ plies, setting lower and upper limits for the total laminate thickness, and specifying a minimum percentage requirement for each available fiber orientation.

In the second phase, the authors performed design fine-tuning through ply-bundle sizing optimization. They introduced discrete unit ply thickness increments as design variables. Detailed behavior constraints, including considerations for ply failure, were taken into account. The manufacturing constraints from the first phase, such as orientation percentage, were carried over into this design phase. The authors mentioned that typically some manual editing and post-processing is needed during the process. The third phase involved the detailed design, specifically ply stacking sequence optimization, while maintaining the constraints defined in the previous phases [201].

It is important to note that this optimization process [201] focused solely on optimizing individual component parts, without considering optimization across different areas of a component simultaneously. Additionally, the process only considered predefined prepreg directions ($0°$, $+45°/-45°$, and $90°$ plies), without optimizing the directions themselves like in the work of Toropov et al. [166]. By incorporating the optimization of prepreg directions, further mass reduction could be achieved. This enhancement would lead to improved overall performance and weight reduction in composite components.

Zhou et al. [202] presented a new method for simultaneously optimizing the overall topology, component partitioning, and unidirectional (or curvilinear) material orientation for each component. Contrarily to the previous composite material optimizations, it does not assume a prescribed set of discrete orientations. Output structures are made of components with unidirectional or curvilinear orientations. Their method generates output structures composed of components with unidirectional (or curvilinear) orientations. To represent fractional membership to each component, the authors introduced a vector field variable analogous to the component field variable used in multi-material topology optimization. They developed a hypercube-to-simplex projection and penalization scheme to effectively solve general multi-component topology optimization problems. However, this method is limited to 2D application cases and if discrete fiber directions are considered it leads to fiber discontinuities in connections, creating much weaker spots in the manufactured component.

Di Boon et al. [47] explored the applications of machine learning methods in the design process of FRP composite components. Advanced manufacturing techniques, such as AFP and Additive Manufacturing (AM), enable the fabrication of these components with customized material and structural configurations. However, to fully utilize this customizability, improvements are needed in the design process. The researchers identified machine learning as a potential solution capable of handling the complexity of the design problem.

In their review [47], they discussed the applications of machine learning methods in various aspects of structural component design. These include studies on microstructure-based material design, the use of machine learning models in stress analysis, and topology optimization of FRP composites. Furthermore, the researchers proposed a design automation framework aiming to provide a comprehensive and efficient approach for the design and optimization of FRP composite components. On the other hand, the authors also underlined the high complexity, associated with building the required models and the inputs' acquisition, can be a challenge to the implementation of the proposed frameworks.

The optimization of composite components has been a subject of research and development, with different approaches proposed over time. Overall, further advancements are needed to achieve comprehensive optimization of composite components, considering both material distribution and fiber reinforcement orientation, while addressing challenges related to complexity and implementation.

1.3 Noise, Vibration and Harshness

In the automotive domain, (NVH) are important considerations in the design and development of gearbox housings. NVH refers to the undesirable noise, vibrations, and harshness levels experienced by people inside and around a vehicle. In the context of gearbox housings, NVH plays a crucial role in ensuring optimal performance, durability, and user comfort. Even though noise and vibration are properties that can

be measured, in absolute and objective procedures, harshness is a more subjective concept. Harshness refers to the perception of uncomfortable or jarring sensations by a person due to vibrations or noise.

The main source of vibration in a gearbox is the process of gear meshing. As mentioned in the Section 1.1.3, the emitted noise by a gearbox has two main origins, one is the rattle noise and the other is whine noise. Rattle noise is provenience mainly from the impact of the gear teeth caused by backlash and torque fluctuation, resulting in a broadband noise. Whine noise is generated by the TE, which occurs due to inaccuracies and deviations which induce imperfect gear meshing and therefore originate a vibration excitation for the system.

These vibrations are then transmitted to the housing through the contact areas of the bearing support. As a result, the housing vibrations generate noise in the surrounding environment. The vibrations can be either dampened or amplified by the structural response of the components along this path, encompassing gears, shafts, and bearings. Even though the main source of vibration in a gearbox is the process of gear meshing, there are other common vibration sources, for example problems in the bearings or additional wear and damage in the rotating components.

The behavior of gears, shafts, and bearings within the gearbox is the subject of separate studies conducted within the LIVE-I project. In this particular work, the primary focus is directed towards enhancing the vibroacoustic performance of the gearbox housing. Essentially, this work concentrates on the final segment of the gearbox's vibroacoustic path. Hence, this section provides important vibroacoustic concepts needed to analyze the gearbox housing and reviews the existing NVH issues.

1.3.1 Current Noise Issues and Regulations

Noise pollution constitutes an environmental risk to human health. It is defined as unwanted or harmful outdoor sound, and the road traffic is the greatest contributor to its generation [54, 72].

Noise is an undesirable outcome of transportation and industrial activities, posing as a widespread pollutant that directly affects the health and well-being of exposed humans and wildlife. In order to address this issue, the environmental noise directives 2002/49/EC and 2007/46/EC, along with EU regulation 540/2014, define various noise indicators to be utilized in noise mapping and action planning. These indicators provide a physical scale for characterizing environmental noise, establishing a correlation with its detrimental effects.

The commonly used EU indicator, L_{den}, represents the average noise level experienced by citizens throughout the day, evening, and night over the course of a year. Within the transportation sector, road traffic noise stands out as the most significant source of noise pollution. Estimates suggest that over 125 million people are affected by noise levels from road traffic, exceeding 55 dB L_{den}, with more than 37 million individuals exposed to even higher noise levels, surpassing 65 dB L_{den} [54, 53]. While rail traffic noise impacts 8 million people with noise levels exceeding 55 dB L_{den}, aircraft noise affects around 3 million people above the same threshold

[54, 53]. These statistics highlight the pressing need for effective noise reduction strategies within the road transportation to safeguard public health and quality of life.

The World Health Organization [181] reported a wide range of negative health effects in humans subject to noise levels at night above 40 dB. Their definition of health embraces not only the absence of disease, but also the state of complete physical, mental and social well-being. According to that, the environmental noise annoyance is one of the major environmental health hazards. Health problems like stress reactions, sleep disorders, hearing loss, hypertension and cardiovascular diseases are deeply associated with the exposure to prolonged or high noise levels [181]. They also mention its association with sleep disturbance and mental health problems.

In Western Europe, more than 1 million premature deaths are linked to road traffic noise pollution [54]. They also mention the high economic damage related with the loss of productivity of workers whose health and well-being are affected by noise, the additional burden on health care systems and the depreciation of real-estate value.

The objective of the environmental noise directives and regulations is to establish a common basis in the European Union for developing measures to reduce noise emitted by several source areas, such as road and rail vehicles, aircraft, industrial equipment and mobile machinery. It is important to reduce environmental noise, particularly when it induces harmful effects on human health [54, 53]. Hall et al. highlighted that low frequency noise is particularly sensitive to the human ear and that it is a difficult frequency range to address in noise attenuation by traditional noise control means [72].

The growing demands for mobility increase noise pollution in our communities, which has evident adverse consequences. Population growth and denser urbanization are further increasing the problem of noise. Even though tackling this problem is not a straightforward task, it is of utmost importance to work on it. Innovation and the application of recent noise control technologies may have a significant contribution, undertaking this problem.

1.3.2 Sound Metrics and Assessment

Sound is generated by the vibration of objects, which creates disturbances in the surrounding medium, for example in the surrounding air. These sound energy propagate as waves, and their intensity or energy level determines the loudness of the sound. The three-dimensional acoustic wave equation in a homogeneous, inviscid, isotropic, compressible fluid is stated in the Equation 1.12, where c is the speed of sound in the fluid [57]. The amplitude of the sound wave corresponds to the maximum displacement of air particles caused by the vibration. Higher amplitudes produce louder sounds, while lower amplitudes result in softer sounds.

$$\frac{\partial^2 p}{\partial x^2} + \frac{\partial^2 p}{\partial y^2} + \frac{\partial^2 p}{\partial z^2} = \frac{1}{c^2}\frac{\partial^2 p}{\partial t^2} \tag{1.12}$$

For NVH evaluations, the focus is on sound that can be perceived. The absolute thresholds of hearing (ATH) are the minimum sound levels of a pure tone which an average human ear is able to perceive [50]. In the case of the sound pressure (p), which is a sound field quantity, the threshold is set at $p_0 = 20\mu Pa$, becoming the reference for the calculation of the sound pressure level, as seen in Table 1.1, which corresponds to the 0 dB in sound pressure level. The human ear can detect a minimum pressure fluctuation in the order of 10^{-9} of the atmospheric pressure [50]. The logarithmic decibel scale is widely used in the field of acoustics, in order to cope with the wide pressure and power ranges. The human ear is not equally sensitive to sounds of all frequencies. In order to account for this, a weighting system known as the A-weighting scale (dBA) is often used to approximate the subjective loudness perception of humans.

Sound intensity (I) is a sound energy quantity. The sound pressure and the particle velocity are used to compute the sound intensity, see Equation 1.13, where $\Re$ is the real part of the complex value and the asterisk represents the conjugate complex value [63]. The reference for the sound intensity level is set at a sound intensity of $10^{-12} W/m^2$, as seen in Table 1.1.

$$\vec{I} = \frac{1}{2}\Re(p\vec{v}^*) \tag{1.13}$$

Sound power is the rate at which sound energy is emitted, reflected, transmitted or received, per unit time. Sound power is measured as the total sound power emitted by a source in all directions in watts. Sound power measurements are often specified in the noise regulations of many products. Sound power, being independent of the evaluation location, serves as a superior and more objective criterion for measuring gearbox noise emission. The radiated sound power is calculated by the integral of the sound intensity in the normal direction across the circumscribing surface, according to the Equation 1.14. Any surface, including the surface of the radiating object, can serve as the circumscribing surface.

$$P = \int_S \vec{I} \cdot \vec{n}\, dS \tag{1.14}$$

The sound power through a surface is then defined as the product of the sound pressure and the velocity, at a point on the surface in the direction normal to the surface, integrated over the surface in question. The sound power radiated, over the frequency domain, can be obtained by integrating the far-field intensity over a hemispherical surface centered on the panel/structure [57], as written in the Equation 1.15.

$$P(\omega) = \int_S I(\theta, \phi, \omega)\, dS = \int_0^{\pi/2} \int_0^{2\pi} I(\theta, \phi, \omega) r^2 sin(\theta)\, d\theta\, d\phi \tag{1.15}$$

Sound power levels are also independent of distance to the source and are also indicated in decibels, by the following formula:

$$L_w = 10 \cdot log\left(\frac{P}{P_0}\right) \tag{1.16}$$

where the reference power $P_0 = 10^{-12}W$.

Measurement	Unit	dB Scale Reference
Sound Pressure (p)	Pa	20^{-6}
Sound Intensity (I)	W/m^2	10^{-12}
Sound Power (P)	W	10^{-12}

Table 1.1: Noise and Vibration Assessments.

In order to normalize the sound power results, it is possible to divide the sound power radiated results by the power injected into the structure or component. The power injected is calculated according to the integral over the area of load application stated in Equation 1.17, where $\boldsymbol{f}$ and $\boldsymbol{v}$ denote the applied force and velocity complex amplitudes in the loading area, respectively, and ^{H} is the complex transpose conjugate operator [178]. The ratio of the sound power radiated to the power injected in the structure is given by the Equation 1.18.

$$P_{injeted}(\omega) = \frac{1}{2}\int_A \Re e\{\boldsymbol{v}(\omega)\boldsymbol{f}(\omega)^H\}\, dA \tag{1.17}$$

$$PowerRatio(\omega) = \frac{P_{radiated}(\omega)}{P_{injeted\,total}(\omega)} \tag{1.18}$$

The loudness of sound refers to the perceived intensity or amplitude of a sound wave. It is a subjective perception that depends on the physical characteristics of the sound wave and the sensitivity of the human ear. It's important to note that the loudness perception can vary from person to person, and factors such as age, hearing ability, and individual sensitivity can influence how loud a sound appears [64].

1.3.3 Structure Vibroacoustic Interaction

For structures in which the thickness dimension is much less than those defining the extent of the surface, the sound emission originated from vibration occurs mainly from the direction normal to the surface. The surface in contact with the surrounding fluid, provides a mechanism for displacing and compressing the fluid, in the case of the gearbox housing, the surrounding air. Consequently, those vibrating structures will radiate or transmit sound [57].

Waves exhibit physical properties that can be described using specific parameters. The spatial period of a simple harmonic wave is described by its wavelength

λ. The wavenumber, k, represents phase change per unit distance, and it is given by the Equation 1.19, where ω is the frequency and c_{ph} is the 'phase velocity' of the wave. For two- and three-dimensional wavefields, these quantities for each principal direction are grouped in a wave vector $\mathbf{k}$.

$$k = \frac{\omega}{c_{ph}} = \frac{2\pi}{\lambda} \tag{1.19}$$

The relationship between k and ω is termed the dispersion relation. It is not only a property of the wave, but also dependent from the type of wave-supporting medium. Normally, this relation is plotted in dispersion curves. The group speed c_g represents the speed at which energy is transported by a wave. The phase and group speeds are equal for non-dispersive waves [57].

In order to analyze the interaction between a structure and a fluid, it is essential to establish the relationship between the vibration of the structure and the pressure gradient in the surrounding fluid. Assuming a surface in the x-y plane, the normal vibration velocity at a point on a surface determines the value at that point of the pressure gradient in the direction normal to the surface [57], see Equation 1.20. In the context of sound radiation analysis, this equality serves as a consistent fluid boundary condition.

$$\left(\frac{\partial p}{\partial z}\right)_{z=z0} = -i\omega\rho_0(v)_{z=z0} \tag{1.20}$$

The vibrational fields of complex structures at audio frequencies exhibit intricate behavior due to their strong dependence on several factors such as frequency, structural characteristics, material properties, and operating conditions [57]. This inherent complexity is also evident in the majority of industrial GBHs. The evaluation of audio-frequency vibrational fields in complex structures is typically performed within finite frequency bands, such as octave bands, or in discrete frequencies.

Vibroacoustic problems primarily arise from resonances, which occur when the excitation frequency coincides with the natural frequency of a structure. At resonance, the response of a system is theoretically unbounded. However, most physical systems exhibit dissipation of energy, mitigating the accumulation of energy within the structure. This dissipation is typically achieved through damping, which can take various forms, such as material damping or interface damping (joints and bolted connections). Damping involves the conversion of mechanical vibration energy into other forms, commonly heat [40]. Damping is an effective means to reduce vibration levels, particularly in attenuating resonance peaks. Alongside with the damping coefficient (c), the damping in a system is also often described by the damping ratio ($\xi = c/c_c$), where (c_c) is the critical damping ($c_c = 2\sqrt{km}$). When $\xi < 1$ the system is underdamped, when $\xi = 1$ the system is critically damped and when $\xi > 1$ the system is overdamped. In order to represent the structural damping in analytical or numerical studies, the literature states that it is reasonably to assign a complex elastic modulus to the material: $E^* = E'(1 + i\eta)$, where η is termed the 'loss factor' [57], which for instance for metallic materials it generally assumes values near

1/1000.

A usual measure in the frequency domain studies is the Frequency Response Function (FRF), defined as a measure of the complex amplitude of the linear vibrational or acoustic response at one position normalized by the complex amplitude of the external source of excitation, as a function of excitation frequency [57]. The FRF is dependent on the excitation and measurement positions and can be obtained for diverse quantities, such as acceleration, displacement, pressure or power.

A frequently employed measure of surface vibration is the space-average value of the time-average squared vibration velocity, commonly known as "mean square velocity". The utilization of this quantification allows the estimate of the sound emitted by the vibrating structure, since they are physically related, without the need of the modeling and simulation of the acoustic domain. The mean square velocity [57], in the time domain, is defined in the Equation 1.21.

$$\langle \bar{v_n^2} \rangle = \frac{1}{S} \int_S \left[\frac{1}{T} \int_0^T v_n^2(x,z)\, dt \right] dS \tag{1.21}$$

In numerical finite element method (FEM) simulations in the frequency domain, assuming that the structure of volume Ω vibrates with a displacement field $\hat{u}$ and a velocity field $\hat{v} = i\omega\hat{u}$. Equation 1.22 [6] is employed to determine the mean square velocity of the structure in direction i. In this equation, $\{\hat{u}\}$ denotes the nodal displacement vector, $[L_i]$ represents the localization matrix for the degrees of freedom in direction i, and $[C_{uu}^{(1)}]$ denotes the volume-coupling matrix specified by Equation 1.23.

$$\langle V_i^2 \rangle(\omega) = \frac{1}{2\Omega} \int_\Omega |\hat{\nu}|^2\, dV = \frac{1}{2\Omega} (\langle \hat{\nu}^* \rangle [L_i]^T [C_{uu}^{(1)}][L_i]\{\hat{\nu}\}) = \frac{\omega^2}{2\Omega} (\langle \hat{u}^* \rangle [L_i]^T [C_{uu}^{(1)}][L_i]\{\hat{u}\}) \tag{1.22}$$

$$[C_{uu}^{(1)}] = \int_\Omega [N^S]^T [N^S]\, dV \tag{1.23}$$

The evaluation of surface vibration serves as the key parameter for estimating sound emission from a vibrating structure, taking into account a specified radiation efficiency value, or determining the radiation efficiency based on the values of the radiated sound power. Therefore, the mean square velocity in direction i can also be defined on a surface S, see Equation 1.24 [6]. The volume-coupling matrix $[C_{uu}^{(2)}]$ is now given by the Equation 1.25.

$$\langle V_i^2 \rangle(\omega) = \frac{1}{2S} \int_S |\hat{\nu}|^2\, dS = \frac{1}{2S} (\langle \hat{\nu}^* \rangle [L_i]^T [C_{uu}^{(1)}][L_i]\{\hat{\nu}\}) = \frac{\omega^2}{2S} (\langle \hat{u}^* \rangle [L_i]^T [C_{uu}^{(1)}][L_i]\{\hat{u}\}) \tag{1.24}$$

$$[C_{uu}^{(2)}] = \int_S [N^S]^T [N^S]\, dS \tag{1.25}$$

The $[N^S]$ is the matrix of surface nodal shape functions used to interpolate displacement u on surface S. It is also possible to define the mean square normal velocity of surface S, see Equation 1.26 [6].

$$\langle V_n^2 \rangle(\omega) = \frac{1}{2S} \int_S |\hat{\nu} \cdot n|^2 \, dS = \frac{\omega^2}{2S} (\langle \hat{u}^* \rangle [C_{uu}^{(3)}] \{\hat{u}\}) \tag{1.26}$$

$$[C_{uu}^{(3)}] = \int_S [N^S]^T \langle n \rangle \{n\} [N^S] \, dS \tag{1.27}$$

The sound emission from a vibrating complexly shaped structure is not linear dependent from the mean square velocity of the structure [16, 123]. For example, within the area of vibroacoustic metamaterials application, Claeys et al. [36] and Jung et al. [81] found major mismatches between the mean square velocity of the structure and the acoustic radiation from the structure, due to the increase of the radiation efficiency in certain frequency ranges, in which vibration concentrations generate piston-like radiation of acoustic waves. The radiation efficiency (σ) from a vibrating surface is given by the Equation 1.28 [16], where P_{rad} is the radiated sound power, S is the surface area, ρ_0 is the fluid density, c_0 is the speed of sound in the fluid, and V_n^2 is the mean square velocity.

$$\sigma(\omega) = \frac{P_{rad}(\omega)}{\rho_0 c_0 S \langle V_n^2(\omega) \rangle} \tag{1.28}$$

1.3.4 Conventional Vibroacoustic Control Methods

The NVH characteristics of a component are firstly determined by its design, as well as its structural and dynamic properties. Therefore, design modifications to the component will change its NVH characteristics. Stiffeners are largely used to increase the components' global stiffness [71, 161]. Two vibroacoustic consequences occur with the introduction of stiffeners in a structure: a decrease in vibration levels and an increase in radiation efficiency [123]. Depending on which effect dominates, sound radiation can increase or decrease. The radiation efficiency increases due to near-field vibration components next to the stiffeners, which radiate sound more efficiently [16].

Generally, adding mass to a component is a way of reducing vibration and noise emissions. However, the mass increment far from the excitation point is ineffective in decreasing vibration levels or sound radiation [16]. Moreover, it goes against the objective of the lightweight design concept. Another common practice to reduce noise radiation from components is the application of acoustic treatment material layers with high sound absorption coefficients. These materials are designed to vibrate and dissipate sound energy as heat, thereby reducing the amount of noise that is radiated from the component. In order to maximize the absorption of sound waves, it is essential to apply the absorptive material with a thickness of one-quarter wavelength on the surface of the vibrating structure. Sound waves induce variations

in pressure and particle velocity. At one-quarter wavelength distance from the radiating surface, there is low pressure and high fluid particle velocity, making it the most effective region for sound absorption. It is important to note that a thick layer of acoustic treatment material is needed to attenuate low frequencies, making this method inefficient [57]. Another method is through the introduction of reflective partitions into the transmission path, which induce a high change of acoustic impedance, a method that is commonly used in ICE vehicle exhaust expansion chambers. These two methods are also used in synergy, for example in automobile dash panel structures [57].

Finally, active control methods can be employed to enhance NVH properties. However, these methods increase substantially the complexity and cost of the system and should be considered only if other passive measures have proven ineffective [16].

1.3.5 Design for Vibroacoustic Enhancement

In the interest of having virtuous vibroacoustic properties in a GBH, a primordial condition is the disagreement between periodic load components with a given frequency and the eigenmodes of the structure. This can be achieved by carefully designing the GBH to prevent the overlap of eigenmodes with the peaks in the excitation response across the frequency spectrum.

Dai et al. [41] conducted a shell shape optimization study on a side cover of a 6-speed transaxle system with the objective of minimizing the maximum surface velocity. The authors specifically focused on this single value as their optimization target, as they acknowledged that selecting radiated sound power as an objective function was not feasible due to the limitations of current commercial solvers [41].

Graf et al. [71] presented a noteworthy design enhancement for a clutch cover, aimed at improving its NVH characteristics. The researchers utilized a simulation model based on measured excitation to analyze and optimize the design. Figure 1.6 illustrates the application of rib reinforcement on the clutch cover, which resulted in significant improvements.

The improved design demonstrated superior vibroacoustic behavior, as depicted in Figure 1.7. This observation underscores the importance of early design studies, as they enable the identification of potential enhancements. The study also included a thorough comparison between experimental and numerically simulated results, revealing a good correlation between the two. This indicates that simulation techniques can successfully yield improved designs, even without manufacturing physical prototypes.

Son et al. [161] conducted an investigation into rib designs aimed at enhancing the local stiffness of gearbox housings for agricultural electric vehicles. The local stiffness modification enables the shift of natural frequencies of the housing, allowing the disagreement between the excitation and the eigenmodes of the structure. The researchers performed a parametric study, exploring various geometric parameters of the ribs. By altering the length and height of the ribs, they calculated the corresponding mass addition and the increase in stiffness.

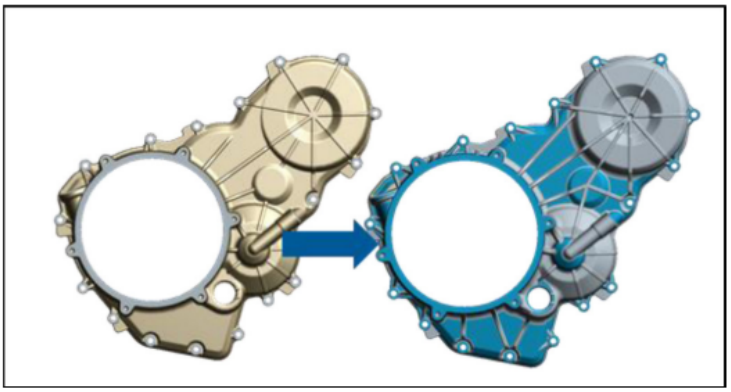

Figure 1.6: Clutch cover design improvement - baseline cover (left) and improved design cover (right) [71].

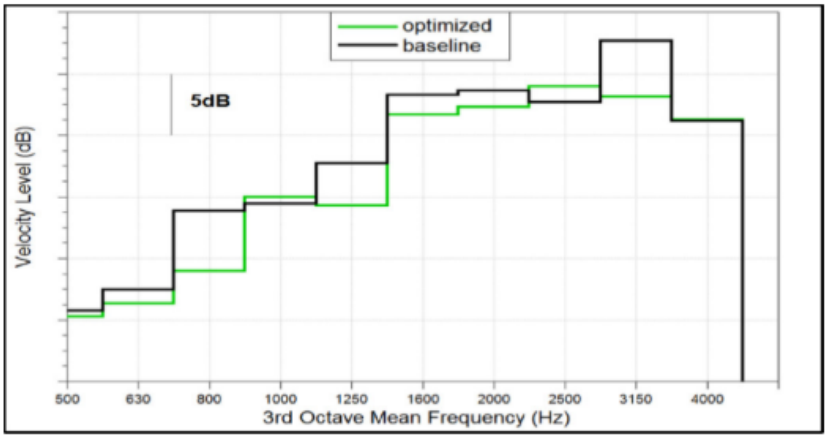

Figure 1.7: Comparison of the total surface velocity levels of the cover between the baseline and optimized design [71].

Since the introduction of rib reinforcements modify the resonance characteristics of the housing, a method for comparing housing stiffness at different frequencies was required [161]. To address this, the authors employed a stiffness line over frequency approach, enabling normalized results of stiffness across the frequency spectrum. Figure 1.8 illustrates the parameters considered in the rib design. To compare the results of the parametric study, the researchers utilized a ratio of the stiffness increase rate to the mass of the rib. This metric was defined as the efficiency (%/g) [161]. Through the comprehensive parametric study, the researchers were able to identify the optimal combination of design parameters that yielded the highest efficiency in terms of stiffness increase.

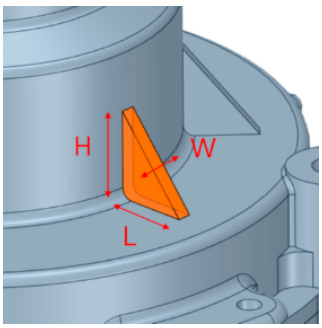

Figure 1.8: Parameters of the rib design [161].

The research conducted by Son et al. provides insights into improving the local stiffness of gearbox housings through rib designs. By systematically varying the rib geometry and evaluating stiffness enhancements, the study enables the determination of the most efficient design parameters for achieving desired stiffness improvements. The efficiency metric introduced by the authors facilitates quantitative comparisons and allows for design decisions. Overall, as demonstrated in the research, these ribbed designs enable not only an increase in stiffness but also the NVH enhancement of housing structures.

1.4 Metamaterials and Vibroacoustic Metamaterials

In nature, we can find different materials and even cellular solids, such as cork, wood, coral, sponge, and honeycomb [163]. Conversely, metamaterials are man-made structures that are designed to have unique physical properties that cannot be found in conventional materials [43]. The prefix "meta" comes from the Greek word, $\mu\varepsilon\tau\acute{\alpha}$, which means "beyond". Metamaterial's unique properties derive from their designed microstructures. The study and development of metamaterials started in the electromagnetic domain and then was extended to the mechanical domain and, more specifically, to the field of vibroacoustics [120]. The physics of the metamaterials can be highly counter-intuitive, inducing a burst of new research [128, 35, 10].

Metamaterials are a novel class of complex engineered materials, and generally

they take the form of Unit Cell (UC) assemblies of non-homogeneous material composition and/or topology. The topic generated enthusiasm in the scientific community since they can be designed to exhibit unconventional electromagnetic, acoustic or mechanical properties. Depending on the physics field, metamaterial characteristics are vast and diverse. The electromagnetic metamaterials' distinct characteristics are, for example, negative refraction, waveguiding characteristics or cloaking [46, 152, 33, 118, 154]. In the literature, mechanical metamaterials are categorized in subgroups, for example: Pentamode metamaterials (or meta-fluid) which are able to deform without changing their volume; Auxetic metamaterials (dilational materials), which are characterized by the increase in transverse dimension when an axial tensile load is applied to it, or in other words, materials with a negative Poisson's ratio; Metamaterials with negative stiffness; or even metamaterials with bi-stable UCs. In the bibliography, a vast range of mechanical metamaterials are lattice materials, which are open-cell cellular materials composed of a large number of architected structural elements, such as slender beams or rods [163, 43, 11, 196, 17, 7]. In order to control elastic and acoustic waves, vibroacoustic metamaterials are nowadays applied in several fields. Harmful consequences of seismic waves on man-made structures can be prevented through the use of seismic metamaterials [2, 92, 23]. Along with the study of new metamaterials, new applications for them can be sought and mastered. The recent developments in computational methods may, as well, allow synergies between topology and material composition to reach unprecedented properties for engineering applications [163].

The most outstanding functionality of metamaterials in vibroacoustics the capability of enabling strong attenuation of vibration and noise in specific frequency ranges. These frequency ranges are called band gaps (BGs) or stop bands (SBs), and in a nutshell, they are the ranges of frequencies where free wave propagation is not allowed. BG behavior was first investigated in the quantum mechanics' field, more specifically in the band-discretized movement of electrons in crystal lattices [180, 160]. The concept was transposed to electromagnetic waves [190, 75, 191], and after to elastic and acoustic wave propagation field by Sigalas and Economou [157], where they tested lattice configurations of spherical inclusions in other mediums for evaluation of BGs.

There are two types of vibroacoustic metamaterials: Phononic Crystals and Locally Resonant Metamaterials. A Phononic Crystal (PC) relies on interference-based attenuation and require periodic arrangement, while a LRM generate vibration attenuation through sub-wavelength resonant inclusions or additions.

1.4.1 Phononic Crystals

The denomination of PC was initiated by Kushwaha et al. [99] in 1993. The concept of phononic crystals in vibroacoustics is an analogy to the other photonic crystals in electromagnetics. The prefix "phonon" derives from the Greek word "phōnē", which means sound. Photons are quantized light waves, analogously phonons can be thought of as quantized sound waves [68].

A study published in the Journal Nature in 1995 presented experimental sound attenuation results through a 2D periodic sculpture constituted by several steel cylinders [126]. The mentioned structure is a PC, once the attenuation of the propagation of acoustic waves is due to the periodicity of the arrangement near the Bragg interference frequency region. Based on this first study, two years later, Kushwaha [98] performed computations for two-dimensional periodic arrays of rigid stainless steel cylinders in the air. Goffaux et al. [69] investigated experimentally the sound attenuation reached in the BGs for finite thickness PC samples and realized a comparison with the mass law. Additional studies were carried out in this area, studying the lattice layout effects on the sound attenuation [146, 25].

Phononic Crystals are not restricted to solid inclusions on fluid mediums. PCs can consist of solid inclusions on solid mediums. In [172], Vasseur et al. confirmed the existence of absolute acoustic BGs in two-dimensional periodic composite media, through acoustic wave transmission experiments in binary solid/solid composite media composed of arrays of duralumin cylindrical inclusions embedded in an epoxy resin matrix. By the definition PCs are periodic structures made of different materials designed to control the propagation of mechanical waves [124]. PCs may be one-dimensional, such as a periodic structure made of alternate homogeneous solid layers with distinct material properties [20, 21, 125]; two-dimensional, for example a lattice of vacuum cylinders in a solid background [103] or a pattern of solid cylinders in the air [126]; or three-dimensional, like the inclusion of solid spheres in another solid background material [157, 143]. Examples of one-dimensional, two-dimensional and three-dimensional PCs are illustrated in the Figure 1.9.

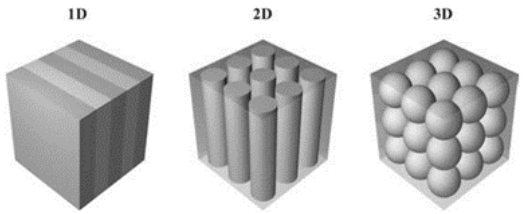

Figure 1.9: Examples of one-dimensional, two-dimensional and three-dimensional PCs [124].

Delpero et al. [45] demonstrated novel techniques for enhancing Sound Transmission Loss (STL) across partitions using PCs. They created a three-dimensional phononic crystal with a UC designed to achieve a BG in the mid-range of the acoustic frequency spectrum. The PC was investigated experimentally and compared with conventional sandwich panels with foam cores. The performance of the phononic crystal core was remarkable in terms of amplitude reduction in the transmissibility and width of the attenuation band. However, the investigated PC core revealed a poorer static performance than the honeycomb structures and foams, traditional core options for sandwich panels. Following this work, Delpero et al. [44] introduced inertial amplification and longitudinal-torsional coupling mechanisms in the

PC core to widen the BG. In 2018, Van Damme et al. [171] presented a PC consisting of a sandwich plate with inner stiffeners organized in checkerboard patterns. The inner filled spaces have a considerably higher bending stiffness than the void parts, resulting in wave scattering. In 2020, Kirchhof et al. [87] explored tuning of microscale PCs via applied mechanical pressure. The pressure applied shifted the PC's BGs to higher frequencies.

In PCs, similarly to the photonic crystals, the BGs are originated from the high impedance contrast between the periodic inclusions and the hosting medium. Bragg scattering, a phenomenon of destructive interference between incoming and scattered waves, happens for wavelengths corresponding to the characteristic periodicity length scale, leading to wave propagation attenuation through the complex medium for these frequency ranges. As expected, in order to create BGs at low frequencies, the characteristic periodicity length of the PC must be high. This fact implies the need for huge and bulky structures.

1.4.2 Locally Resonant Metamaterials

At the begging of the millennium, a new solution to control vibration and noise was introduced, the LRMs. The establishment of BGs at low frequencies with PCs implies that the characteristic periodicity length of the PC must be high, enforcing the creation of large structures. This reality can be an obstacle in a lightweight design. On the contrary, the BGs of LRMs are not created by the structure's periodicity, but by the sub-sized resonators' dynamic behavior, which create a Fano-type interference of their reverberated waves on the primary waves [70]. LRMs' UC size and the spacing between the UCs are not required to be of the same order of the wavelength to target. This fact allows the LRMs to prevail over PCs in engineering applications to attenuate low-frequency vibration. Often LRMs are referred by different nomenclature such as sonic crystals [62, 29, 51], locally resonant sonic materials [117, 156], acoustic metamaterials [46, 100], elastic metamaterials [139, 134] or even locally resonant phononic crystals [137].

The concept of using negative material properties to manipulate electromagnetic waves was first introduced by Veselago in 1968 in the field of electromagnetics [174]. However, since naturally occurring materials do not exhibit negative material properties, it wasn't until the turn of the millennium that a more practical study on the subject was conducted by Pendry et al. in 1999 [140]. Their study demonstrated that microstructures made of nonmagnetic conducting sheets could exhibit effective magnetic permeability, which can be adjusted to values not achievable in naturally occurring materials. Unlike the previous approach relying on Bragg interference, this new approach utilized resonances of the microstructure for wave manipulation at a specific frequency [140]. This concept was later applied to the field of vibroacoustics by Liu et al. [117] and Sheng et al. [156]. They achieved a higher STL compared to the conventional mass-density law of sound transmission by constructing an LRM consisting of small metallic spherical inclusions coated by a thin uniform layer of silicone rubber in an epoxy matrix. The LR system is depicted in

Figure 1.10. The system induced BGs associated with the inner resonances of the arrangement. Negative effective mass density for the elastic wave propagation was achieved in these frequencies regions [156, 120]. This pioneering approach opened the path to the modern research of metamaterials in the field of vibroacoustics. The concept were expanded in other works [70, 155, 93] to different material combinations and geometry. Krushynska et al. [93] investigated the influence of geometric and material parameters, filling fraction and inclusion shape on the width of the BG. Some works also focused on the description of negative effective mass density by analytical models [116, 155].

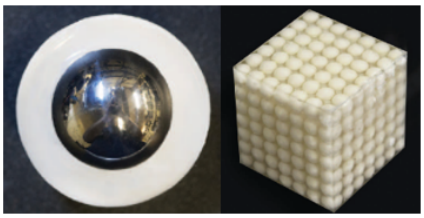

Figure 1.10: Metamaterial sample with resonance-induced negative effective mass effect. Cross-section view of the UC consisting of a small metallic sphere coated by a layer of silicone rubber (left) and assembly of several UCs bonded in an epoxy matrix (right) [120].

Li et al. [107] studied and demonstrated theoretically the concept of double-negative acoustic mediums, which simultaneously have negative effective bulk modulus and effective negative density. Calius et al. [26] and Wester et al. [179] performed additional experiments on this topic. Sample panels with inner small resonating elements were experimentally tested in impedance tubes. The two obtained minimum values for the STL correspond to the two natural frequencies of the partition-resonators systems. The first mode involves the joint movement of the partition and resonator masses, and the second mode involves the out-of-phase movement of the two masses in opposite directions. As theoretically expected, the transmission loss peak occurred at the anti-resonance, where the two modal contributions to the motion of the partition roughly cancel. The influence of the composite properties, such as the filling fraction and the inclusions' radius, in the BGs was assessed for periodic square arrays of lead discs [185]. Still regarding LRMs with spherical inclusions, Comi et al. [38] conducted numerical studies and demonstrated that hexagonal lattices were more effective in wave filtering than traditional square lattices in two dimensions. Specifically, the dispersion spectrum for the hexagonal lattice exhibited a significantly larger BG than that of the square lattice. The authors also evaluated various combinations of materials for the inclusions, fillers, and external frame.

Vibroacoustic LRMs take diverse shapes and can be based on different resonating mechanisms. They can be LRMs with resonating inclusions, as previously mentioned; they can be membrane-type LRMs; they take the form of beams or plates

with micro-resonators attached; there are even acoustic C-shaped LRMs. For example, Hu et al. [76] presented an acoustic C-shape LRM based on Helmholtz resonance. Comparisons were made between this LRM and an arrangement of rigid cylinders for the creation of acoustic lens, concluding the proposed acoustic C-shape LRM exhibit higher acoustic wave focusing characteristics.

A great number of LRMs mentioned in the literature consist of beams and plates with attached micro-resonators, where the micro-resonators can assume many different forms. Wang et al. [176] investigated the propagation of longitudinal elastic waves in slender beams with harmonic oscillators periodically attached. Similarly, Liu et al. [114] examined the flexural wave propagation in beams with periodic geometric changes, assessing the effects of periodicity on the frequency band structure. In another study on LRM beams, Xiao et al. [189] investigated flexural wave propagation and vibration transmission in LR beams consisting of a periodic array of vibration absorbers attached to a uniform beam. Additionally, they presented a design for LRM beams using periodic arrays of beam-like resonators attached to a thin homogeneous beam [187]. Claeys et al. [37] compared the attenuation achieved for interference BG and resonance BG in Euler-Bernoulli beams and in plates. They explored the importance of the spacing between tuned resonators to define their resonance frequency, as a mean to obtain global vibration attenuation. The authors demonstrated that the spacing between resonators should be smaller than half of the infinite plate propagation wavelength to achieve relevant vibration attenuation. Moreover, they provided evidence that mass addition is ineffective in creating BGs, as a large amount of mass is needed to obtain a complete BG. Claeys et al. [37] also demonstrated that the increase in damping in LRMs decreases the value of maximal attenuation but widens up the attenuation band.

Regarding LRM plates, Wu et al. analyzed the dispersion relation of Lamb waves in plates with periodic circular stubs in the surface [183]. Through numerical and experimental studies, they noticed complete BG forms as the stub height reaches about three times the plate thickness. In 2011, Oudich et al. [137] studied an LRM composed of a periodic arrangement of silicone rubber stubs deposited on a thin aluminium plate. Also, through numerical and experimental studies, they discovered a complete BG for the out-of-plane Lamb wave modes propagating in various samples fabricated with different stub heights. The authors also refer to the simplicity of manufacturing the proposed structures. In the following year, by the addition of tungsten masses on top of the silicone rubber stubs, Badreddine Assouar et al. [9] achieved a widening and a shift of the toward lower frequencies of the complete BG. The BG transition to lower frequencies is due to the tungsten cap on the stubs acting as a highly concentrated mass that shifts the eigenmodes of the stubs towards lower frequencies.

Xiao at al. [188] investigated analytically and numerically the flexural wave propagation and vibration transmission in an LR thin plate with a 2D periodic array of attached spring–mass resonators. In 2014, Claeys et al. [36] continued investigating the topic and provided guidelines for BG design in this type of LRM. They also focused on reducing the acoustic radiation from a structurally excited

plate using small mass-spring resonators. It was also concluded that a BG applied at or above the coincidence frequency of the plate reduces the total zone of efficient acoustic radiation. In that year, Xiao et al. [186] proposed a design of LRM consisting of a periodic array of beam-like resonators with their center attached to a thin homogeneous plate, obtaining a complete BG for flexural plate waves, see Figure 1.11. The BGs of this LRM can be tuned by changing the thickness and length of beam-like resonators. Additionally, they remarked that the proposed structures can be fabricated using a single metallic material, which can facilitate its manufacturing and furthermore increase the metamaterial's durability in harsh environments. Hall et al. [72] introduced the idea of multi-layer LRM structures for acoustic barriers. Li et al. [109] studied the effective dynamic properties of these metamaterials. In the work of Li et al. [108], an LRM combined in double-panel structures with poroelastic cores was presented to improve acoustic insulation.

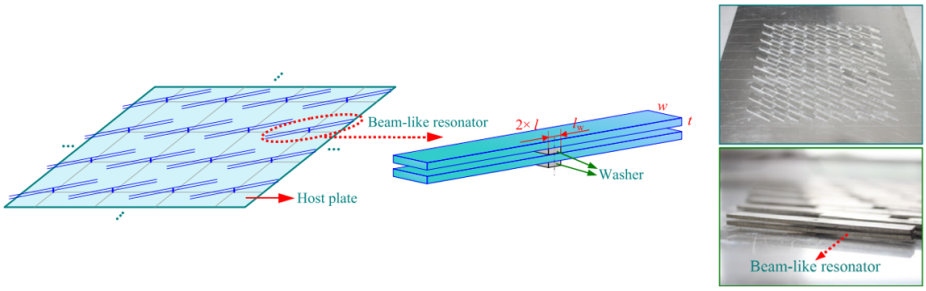

Figure 1.11: Plate with a periodic array of metallic beam-like resonators [186].

As a remark, another system analogous to LRM discussed in the literature is the Multiple Tuned Mass Damper (MTMD) system. For example, in a study by Li et al. [106], MTMD arrangements were examined as a means of reducing unwanted vibrations caused by ground acceleration. These arrangements consisted of several tuned mass dampers (TMDs) with a uniform distribution of natural frequencies, and the researchers investigated various combinations of stiffness, mass, damping coefficient, and damping ratio in each MTMD system. The structures were modeled as single-degree-of-freedom systems. Bachy et al. highlighted the main difference between MTMD systems and LRMs [8]. They mention that an LRM can be considered an MTMD configuration on a smaller scale. The main difference between the two concepts is the number and size of the resonant structures. LRMs are constituted by a higher number of smaller resonant structures, which allow the reduction of mass of each resonant structure and reduce the space required for its application. According to Bachy et al. [8], multiple studies on vibration energy absorption indicate that multi-structures with distributed vibration absorbers, such as MTMD configurations and LRMs, are more effective at attenuating frequency broadband than traditional Tuned Mass Damper (TMD) configurations.

In the literature, there are also some realizations of membrane-type acoustic

metamaterials [194, 193], combinations of membranes with the Helmholtz resonators [97] and introduction of membranes in honeycomb sandwich structures [111]. Yang et al. presented a membrane-type acoustic metamaterial to reach nearly total reflection at the frequencies in between two eigenmodes [194]. The researchers continued investigating this type of metamaterial, demonstrating a broadband sound shield comprising simple stacking of membrane-type metamaterials operative over different frequency regimes [193]. Zhang et al. [199] provided an analytical approach for fast calculating STL of the membrane-type acoustic metamaterials. The researchers found the first STL valley and the STL peak are heavily influenced by the mass attached to the membrane, whereas the membrane properties have a greater impact on the second STL valley. Langfeldt et al. [101] investigated the STL through membranes with arbitrarily shaped masses. The same authors proposed a new analytical model for predicting oblique incidence STL of baffled panels with multi-celled membrane metamaterial [102].

Kumar et al. [97] describe a metastructure that utilizes double negative material properties to absorb low-frequency noise emissions from aircraft. The metastructure developed by Kumar et al. [97] comprised of hexagonal cells arranged in a periodic array, with interconnecting necks that acted as Helmholtz resonators. Thin elastic membranes were mounted on both ends of the cells, enabling the achievement of negative mass density through in-phase membrane movement. Meanwhile, the combined effect of out-of-phase acceleration of the membranes and Helmholtz resonator resulted in a negative bulk modulus. Li et al. [111] published an article proposing a lightweight multi-layer honeycomb membrane-type acoustic metamaterial. As seen in Figure 1.12, the introduction of the membranes on the honeycomb cell enhanced the STL. While the peaks and dips of the structure remain largely unaffected, the researchers noted that increasing the membrane thickness can enhance the overall STL of the metastructure.

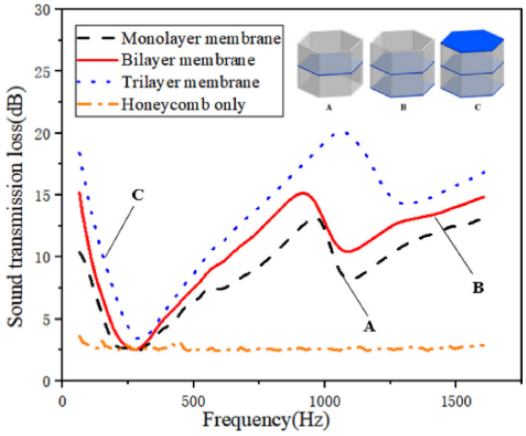

Figure 1.12: STL experimental results for honeycomb structures with membranes [111].

Regarding the numerical simulation of LRMs, Krushynska et al. [94] cautioned that the accuracy of predictions based on 2D simulations of 3D LRMs depends significantly on the shape of the resonators in the LRM. In order to achieve accurate predictions for certain designs through numerical simulations, it is necessary to use 3D finite element method representations. Meanwhile, Van Belle et al. [169] have conducted a study on LRM and PC plates, in infinite and finite configurations. They concluded that the presence of structural modes in the finite case can affect the prediction accuracy of the STL performances.

1.4.3 Current Experiments on LRM Engineering Applications

Few works focus on translating the LRM academic developments to practical applications. When it comes to engineering applications, there are additional criteria that must be met. It is crucial to identify LRMs that can meet other functional requirements, including structural integrity, shielding from contaminated environments, and providing adequate thermal conductivity. Claeys et al. [34] suggested a design of sandwich panels with resonators added into the internal cavities, see Figure 1.13. Multiple configurations of resonator distributions were considered and their corresponding BGs were examined. To numerically simulate the LRM demonstrator, Claeys et al. decoupled the structural model and the acoustic model, enabling the structural mesh to be very refined while the acoustic model had a coarser mesh.

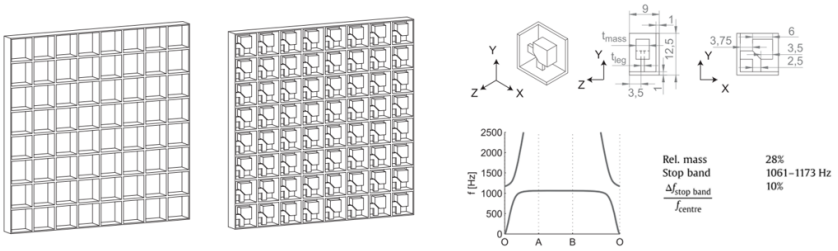

Figure 1.13: Sandwich structure with and without resonators on the inner side (left). Resonator geometry and UC dispersion curve with BG (right) [34].

Melo et al. [128] and Claeys et al. [35] analyzed a square cross-section Polyvinyl chloride (PVC) duct that contained resonant structures arranged in different configurations, including those with two kinds of tuned resonators, each resonating at different frequencies. Figure 1.14 depicts the resonators and the duct with resonators. The aim of the research was to investigate the production of BGs in the frequency range where the resonant structures were tuned, as shown in Figure 1.15. The researchers used two different UC modeling approaches: the direct approach for 1D UC analysis, which considers the effects of the duct's geometry, and the inverse approach for 2D UC analysis. The results of the studies showed that the resonant structures did indeed produce BGs in the frequency range where they were tuned. The experimental results confirmed these findings. Furthermore, the re-

search revealed that increased damping led to a less pronounced peak attenuation but widened the range of the BG.

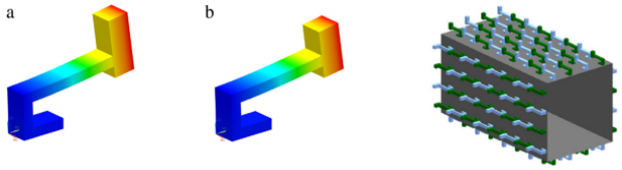

Figure 1.14: First modes of the clamped resonant structures (512.58 Hz for resonator type A and 577.41 Hz for resonator type B (left). PVC duct with two types of resonant structures attached (right) [35].

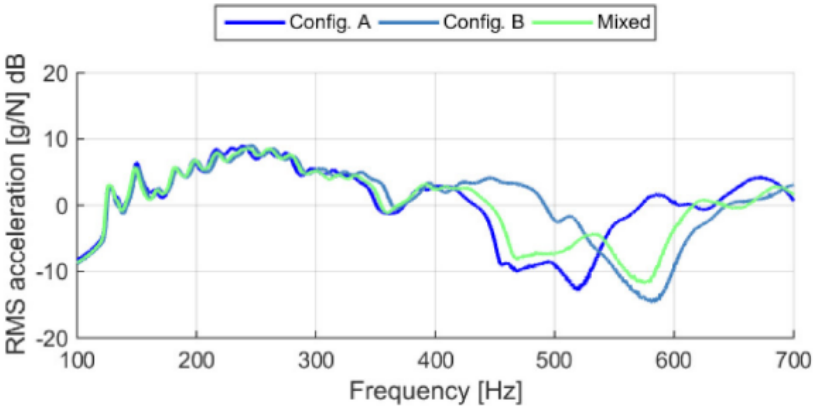

Figure 1.15: FRF of the RMS acceleration for configurations with type A resonators, with type B resonators and mixed (half of each type of resonator) [128].

Sangiuliano et al. [148] introduced an application case of LRMs to reduce the vibration of a simple plate structure subjected to a frequency-dependent force, as depicted in Figure 1.16. The objective of the created metastructure was to prevent the amplification of vibration levels by the structural modes. Small resonators made of polymethylmethacrylate (PMMA) with a steel mass attached were bonded to the plate structure. Yu et al. [195] proposed a resonant structure that could be incorporated into plates to reduce noise and vibration in industrial applications. The resonant structure was made of Acrylonitrile Butadiene Styrene (ABS) for the spring part and steel for the mass part, and was manufactured using injection molding with the metal part already in place. This ensured permanent attachment between the plastic and steel components, providing a solution for the manufacturability of Locally Resonant (LR) structures in mass production. The authors verified that the metamaterial structure exhibited higher vibration reduction in the target frequency band compared to other conventional NVH solutions.

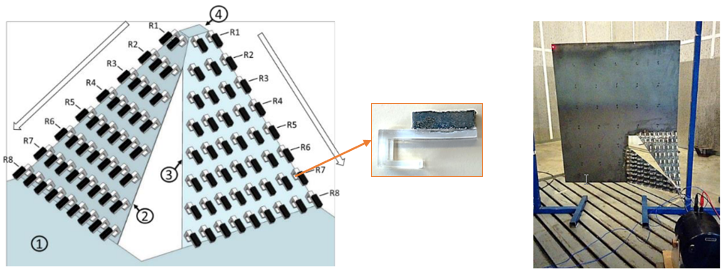

Figure 1.16: LRM Application tested in the work of Sangiuliano et al. [148].

The first application of LRMs to industrial automotive structures was reported by Jung et al. [81]. The authors attached small tuned resonators to an automobile dash panel structure and measured its acoustic and vibration responses, see Figure 1.17. The resonators were attached to the host part using a permanent magnet, enabling the application into more complex surfaces without any structural changes. The authors examined the vibration response and the acoustic response. However, they observed some discrepancies between the numerical and experimental results, which were attributed to the lack of periodicity in the experimental setup assumed in the numerical analysis and the coupling of flexural and in-plane waves on the curved surface of the dash panel, weakening the effect of the local resonators. Broadband reductions in surface velocity were observed. Comparing the vibration and the acoustic response, it was concluded that there was an increase in the radiation efficiency, caused by vibration concentration in some areas, leading to piston-like radiation of acoustic waves. This increase in radiation efficiency was previously discussed by Claeys et al. [36] for the case of an LRM flat plate, where the introduction of resonators in the plate increased the radiation efficiency in frequencies just above the BG due to a coincidence effect of the acoustic wave. To mitigate this issue, the authors suggested introducing a material with high damping in the vibration concentration area. Despite these challenges, the measurement results demonstrate a significant reduction in vibration and noise radiation from the dash panel structure in the defined BGs [81].

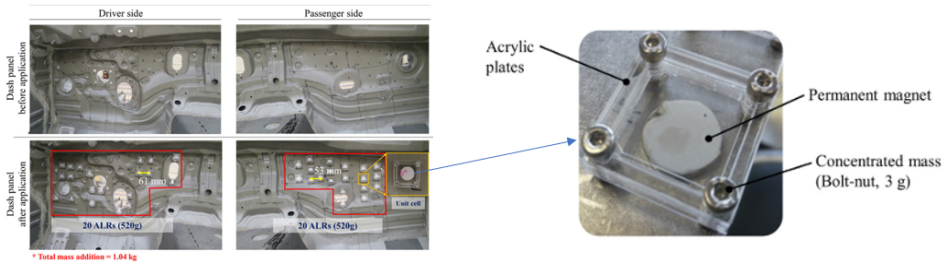

Figure 1.17: Automobile dash panel structure with small tuned resonators [81].

Droz et al. [49] conducted a study on the effects of tunable resonators on the STL of an aircraft sidewall panel under diffuse acoustic field excitation, as shown in Figure 1.18. The tunable resonators used in the study were 3D-printed cantilever beams with interchangeable tip-end magnets. The study considered different spatial arrangements of the resonators, including multi-resonant configurations and the combination with other sound-absorbing treatments. Chang et al. [30] presented a study on improving automobile acoustic insulation pads using LRMs. They incorporated a metamaterial layer into the insulation pad to enhance its performance in reducing sound transmission, while also reducing the thickness of the isolation and absorption layers to decrease the pad's weight. The effectiveness of the LRM-enhanced insulation pad was tested on a vehicle firewall, as shown in Figure 1.19. In the same year, Sangiuliano et al. [147] applied LRMs to the rear shock towers of a vehicle, as depicted in Figure 1.20. The metamaterial configuration showed similar or better performance in reducing NVH compared to the currently used Tuned Vibration Absorber (TVA) configuration. Moreover, it reduced the added mass of the NVH solution by 48%, making it a more lightweight option.

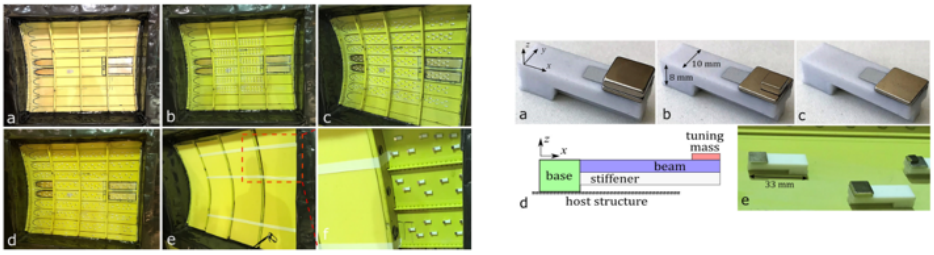

Figure 1.18: Curved panel with small-scale resonators distributions (left); Pictures and schematic of the small-scale resonators (right) [49].

Figure 1.19: Considered small-scale resonators in [30] (left); Sound insulation pad with metamaterial layer (right) [30].

1.4.4 LRM Modeling and Optimization

In the preceding section, two types of vibroacoustic metamaterials were discussed: PCs and LRMs. PCs rely on the interference of waves to create BGs and require

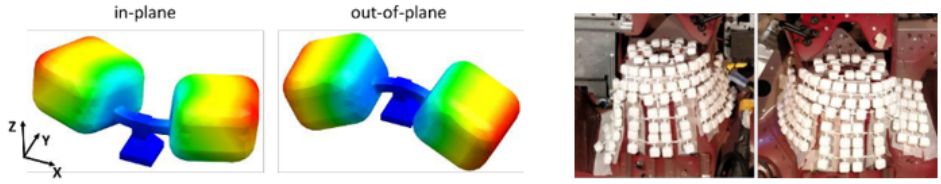

Figure 1.20: Considered small-scale resonators in [147] (left); Metamaterial applied on the rear shock tower (right) [147].

periodic arrangements. On the other hand, LRMs utilize sub-wavelength resonant inclusions or additions to generate BGs. LRMs are particularly suitable for engineering applications, especially in the low-frequency range where the wavelengths are higher. Unlike PCs, LRMs do not depend on periodicity, and their resonating structures are smaller than the wavelengths to target. Additionally, the resonating structures of LRMs can be tuned to specific frequency zones, enabling effective reduction of vibrations and noise emission within those frequencies. Considering these advantages, a particular emphasis will be given to the physics and modeling of LRMs in order to develop methods for reducing noise emissions from GBHs while maintaining a lightweight and compact design. This research is essential for complying with noise regulations and providing optimal acoustic comfort for the individuals inside and outside the vehicle.

In order to optimize the BGs of metamaterial structures, several approaches have been proposed in the literature, including those by Yang et al. [192], Chen et al. [31], Kook et al. [90], Wormser et al. [182], and Han et al. [73]. Van Belle et al. [170] developed a fast design optimization process for 3D UC metamaterials to attenuate bending waves. Their metamaterial UC design creates a BG for bending waves by utilizing the first out-of-plane bending mode of the micro-resonator. To expedite the process, they used a reduced-order UC modeling for predicting the size and frequency location of the BGs. They observed that the optimization tends to maximize the allowed mass ratio (defined in the design constraints) since an increase in the mass of the micro-resonators increases the BG size [37, 170]. Furthermore, the optimization process tends to minimize the base dimensions (length and height) of the micro-resonators. Pires et al. [142] conducted a study on the impact of micro-resonator footprint size on their performance. According to their results, utilizing smaller footprints lead to wider BGs. Thus, it is recommended to employ micro-resonators with the smallest possible footprint, as long as a reliable connection to the host structure is maintained.

Elias and Matsagar [52] published a review on the developments in vibration control of structures using passive resonating systems, where it can be noticed that the research in the optimization of the multi-resonator distributions and its characteristics was not in a mature state. In 2018, Kim et al. [86] progressed in the optimization of multiple linear TMDs in one dimension, defining a method to set the

different dynamic characteristics of each TMD. Some other methodologies for the optimization of MTMDs can be found in the recent literature, for example Vellar et al. [173] defined a method for optimization of MTMDs' design parameters and their best positions over the buildings subjected to earthquakes.

Americano da Costa et al. [4] proposed a process to optimize the design of spatially distributed TMDs to minimize system responses while considering upper bounds for damping ratios. They concluded that the TMDs parameters and distribution highly depend on the considered damping ratios. Their process starts with defining a single TMD design and sequentially moves to a set of TMDs organized in series and finally moves to a group of spatially distributed TMDs with different characteristics. Despite recent progress, studies on optimizing multi-resonator systems have highlighted the high sensitivity of these optimizations to various factors, such as input parameters and uncertainties in material damping. Additionally, the objective function used in optimization must be tailored to the specific application objective. As shown in the works of Zouari et al. [203], the change of the mechanical parameters for the resonator varies the limits of the BGs. Also, due to variability in AM, detuned resonators can change the attenuation performance, affecting the BGs in real applications [13, 56]. Bachy et al. [8] state that traditional lumped mass models still need to be enhanced in order to consider the real topology of the elements in metastructures. They also highlight the effects of uncertainties in quantifying damping performances of resonating structures in different environmental conditions, aging of materials and assembly conditions. The reviewed literature indicates that optimizing the design of metamaterials is a complex process, especially in real-world applications, where variability and uncertainties pose challenges for a priori optimization processes.

Chapter 2

Lightweight Metallic Gearbox Housing Design

This chapter focuses on the design of lightweight metallic GBHs. The chapter explores the derivation of analytical expressions to determine optimal rib dimensions for reinforcing plate structures, facilitating the creation of lightweight panels. The investigation advances into the realm of topology optimization, presenting a comprehensive methodology for enhancing component geometry. Modal optimization and conventional noise control techniques are also discussed in the context of this study. The chapter culminates with an evaluation of sound power radiation, with a comparative analysis of results obtained both pre and post the application of topology optimization.

Contents

2.1 Analytical Design of Lightweight Ribbed Panels

2.1.1 Introduction

A ribbed panel can be considered as a plate reinforced with a beam-grid. The implementation of beam reinforcement in a plate offers an opportunity to create a structure that possesses equivalent flexural stiffness to a conventional plate geometry while significantly reducing its overall volume. Assuming the same material density, the reduction in volume leads to a corresponding decrease in mass.

This section aims to illustrate this concept by providing a deductive analysis that enables the achievement of lower material volume while preserving the desired flexural stiffness. This deduction is present in the section 2.1.2. The approach involves replacing a regular plate with a constant thickness with a beam-grid architecture. The design approach leverages the intrinsic beams' resistance against bending forces. Through the arrangement of these reinforcing beams, a reinforced plate structure can be designed to match its flexural stiffness to the one of a traditional plate with a higher thickness.

One of the notable advantages of using beam-grid reinforced architecture in components and structures is its significant reduction in volume. Consequently, this reduction in volume results in a decrease in mass while maintaining the desired flexural stiffness. In order to demonstrate the effectiveness of this approach, a numerical analysis is presented in the section 2.1.3. These results provide quantitative evidence of the reduced volume achieved by employing the beam-grid architecture while attaining the desired flexural performance. The presented data solidifies the viability and practicality of this design strategy for developing lightweight yet structurally capable structures.

2.1.2 Formulation

For the beam grid to match the flexural stiffness of an isotropic plate, the beams within the grid need to be appropriately sized and spaced. The dimensions of the beams, their material properties and the grid spacing must be carefully chosen to ensure that the equilibrium equation for the beam grid matches the equilibrium equation for the isotropic plate. In this subsection, the design of the required beam grid to substitute a conventional plate panel will be carried out using analytical methods, as mentioned in the introduction of this section. Assuming a square plate of side dimension L and thickness h_{plate}, the volume of the plate can be determined by the Equation 2.1.

$$V_{plate} = L^2 h_{plate} \tag{2.1}$$

For the purpose of substituting the plate by a beam grid with the same structural static stiffness, beams of squared cross-section were considered, thereby $b = h$, where b and h are the beam cross-section dimensions. The beam-grid is illustrated in the Figure 2.1. The spacing between each consecutive beam is given by l. The dimensions of the beam grid and the number of beams in the grid in each direction (N_{beams}) will be correlated by the Equation 2.2. The number of beams, N_{beams}, must be a positive integer. Rearranging the Equation 2.2 it is possible to calculate the spacing between beams, see Equation 2.3. The volume of the beam grid can be obtained by the calculation of the volume of a plate with a thickness equal to b and then subtracting the voids in the beam grid, this calculation is given by the Equation 2.4.

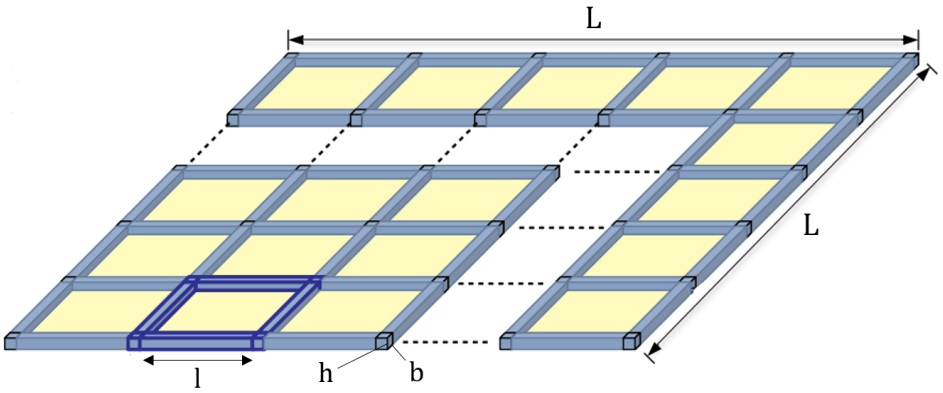

Figure 2.1: Beam-grid illustration, adapted from [19].

$$L = N_{beams} b + (N_{beams} - 1) l \tag{2.2}$$

$$l = \frac{L - N_{beams} b}{N_{beams} - 1} \tag{2.3}$$

$$V_{beam-grid} = L^2 b - (N_{beams} - 1)^2 l b \tag{2.4}$$

The equilibrium equation for an isotropic plate can be derived based on the theory of elasticity. The equation describes the equilibrium of bending moments and shearing forces within the plate. For a two-dimensional isotropic plate subjected to small deflections, the equilibrium equation is given by the Equation 2.5. The value D represents the flexural rigidity of the plate and for an isotropic plate is calculated by the Equation 2.6, where E is the Young's modulus of the plate material, υ is the Poisson's ratio and h_{plate} is the thickness of the plate. The equilibrium equation relates the fourth-order derivatives of the deflection (w) with respect to the plate's

Cartesian coordinates (x and y) to the bending and shearing forces acting on the plate. On the other hand, for a beam grid the equilibrium equation is given by the Equation 2.7, where I is the moment of inertia of the beams' cross-section, l is the spacing between the beams, G is the shear modulus of the beams' material, J is the torsional constant of the beams.

$$D\frac{\partial^4 w}{\partial x^4} + 2D\frac{\partial^4 w}{\partial x^2 \partial y^2} + D\frac{\partial^4 w}{\partial y^4} = 0 \tag{2.5}$$

$$D = \frac{Eh_{plate}^3}{12(1-\upsilon^2)} \tag{2.6}$$

$$\frac{EI}{l}\frac{\partial^4 w}{\partial x^4} + \frac{2GJ}{l}\frac{\partial^4 w}{\partial x^2 \partial y^2} + \frac{EI}{l}\frac{\partial^4 w}{\partial y^4} = 0 \tag{2.7}$$

In order to achieve the same structural static stiffness, two conditions must be satisfied. The first condition relates to the equality in the principal directions (x and y), as shown in Equation 2.8. By substituting the moment of inertia of a square section and incorporating the expression for the flexural rigidity of the plate, Equation 2.8 leads to Equation 2.9. Rearranging and isolating the value of the cross-section side, the Equation 2.10 is obtained. To achieve the same structural static stiffness, the cross-section side must assume a value equal or higher than the one obtained in the Equation 2.10.

$$\frac{EI}{l} = D \tag{2.8}$$

$$\frac{Eb^4}{12l} = \frac{Eh_{plate}^3}{12(1-\upsilon^2)} \tag{2.9}$$

$$b = \sqrt[4]{\frac{h_{plate}^3}{(1-\upsilon^2)}l} \tag{2.10}$$

The second condition pertains to the torsional stiffness. To ensure equivalent torsional stiffness, the equality stated in Equation 2.11 must be satisfied. The torsional constant for square section beams is defined by Equation 2.12. By substituting this expression and incorporating the flexural rigidity of the plate, Equation 2.13 is derived. Equation 2.14 highlights the minimum value of the cross-section side obtained from the second condition.

$$\frac{2GJ}{l} = 2D \tag{2.11}$$

$$J = 2.25(\frac{b}{2})^4 \tag{2.12}$$

$$\frac{2.25G}{l}\left(\frac{b}{2}\right)^4 = \frac{Eh_{plate}^3}{12(1-\upsilon^2)} \tag{2.13}$$

$$b = \sqrt[4]{\frac{16Eh_{plate}^3}{27G(1-\upsilon^2)}}l \tag{2.14}$$

The minimum cross-section side (b) that reproduces at least the same stiffness can be determined by selecting the highest value obtained from Equation (2.10) and Equation (2.14). These equations establish the relationship between the beams' cross-section side, the material properties, and the spacing between the beams. By choosing the maximum value from these equations, we ensure that the resulting cross-section meets or exceeds the required stiffness criteria.

2.1.3 Numerical Application

The relations established in the previous subsection provide valuable insights into various aspects of the beam-grid configuration. Specifically, these relationships allow us to determine the minimum required thickness of the square section sides for the beams and calculate the total volume of the beam grid based on the number of reinforcement beams in each direction.

For the purpose of numerical application and analysis, a domain size of $1m^2$ was considered for both configurations, with an initial thickness of 6 mm for the simple plate. The material properties were set to those of structural steel, as outlined in Table 2.1. Different numbers of reinforcement beams in each direction were considered, calculating the corresponding minimum beam thicknesses and the total volume of the beam grid. The results of these calculations are presented in Table 2.2.

The numerical results derived from the application of the analytical expressions demonstrate that as the number of reinforcement beams increases, the total volume of the beam grid also increases, despite the decrease in minimum beam thickness. This indicates that in order to achieve a lower volume (and consequently lower mass), one should opt for a lower number of reinforcement beams with higher thickness. However, it is important to note that this approach results in a less homogeneous structure. While the structure remains theoretically equivalent in terms of stiffness, it exhibits discontinuous and separate reinforcements. Thus, there exists a trade-off between reducing volume and maintaining structural homogeneity.

In order to have a better perception of the variation of the required beam thicknesses and the total volume according to the number of reinforcement beams considered, a calculation of more results was performed, and the results were plotted. Figure 2.2 illustrates the relationship between the required thickness of the square section sides (b) and the number of reinforcement beams. Similarly, Figure 2.3 depicts the spacing between adjacent beams (l) as a function of the number of reinforcement beams. Finally, Figure 2.4 provides an overview of the total beam-grid volume in relation to the number of reinforcement beams in each direction. These visualizations further enhance the comprehension of the design considerations and trade-offs involved in optimizing the beam-grid configuration.

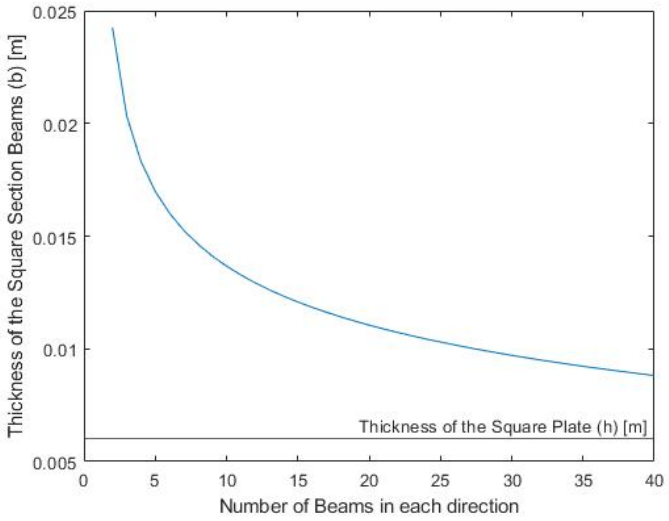

Figure 2.2: Minimum required thickness of the sides of the square section of the beams (b_{min}) in function of the number of reinforcement beams in each direction.

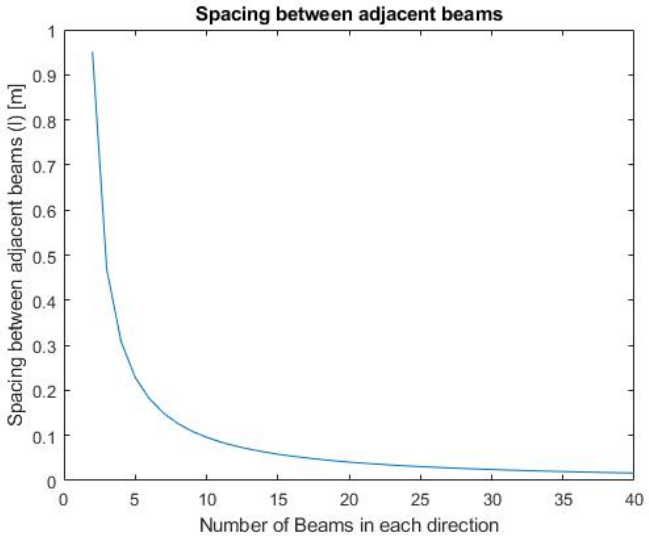

Figure 2.3: Spacing between adjacent beams (l) in function of the number of reinforcement beams in each direction.

Property	Value	Unit
E	200	GPa
G	77	GPa
υ	0.3	
ρ	7850	kg/m^3

Table 2.1: Material Properties of the Steel [39].

N_{beams}	$b_{min}[m]$	Total beam-grid volume $[m^3]$
5	0.0170	0.0028
10	0.0137	0.0035
20	0.0111	0.0043
30	0.0097	0.0048
40	0.0088	0.0051
Max	0.006	0.0060

Table 2.2: Values of the minimum required thickness of the sides of the square section of the beams (b_{min}) and total beam-grid volume for different number of reinforcement beams in each direction (N_{beams}).

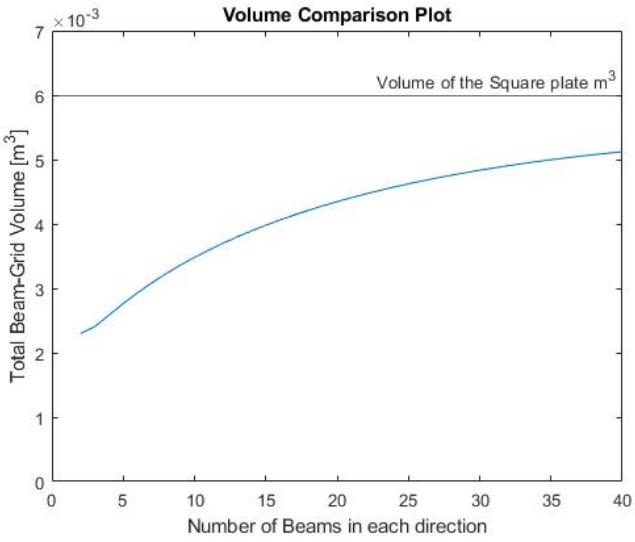

Figure 2.4: Total Beam-Grid Volume in function of the number of reinforcement beams in each direction.

2.1.4 Discussion and Considerations

In summary, this section introduces a deductive approach to designing ribbed panels, which offers the potential to reduce volume and mass while maintaining the same flexural stiffness as a traditional plate design. For gearbox housing designers seeking to replace constant-thickness housing parts, this analytical approach can serve as a baseline for dimensioning ribbed panels. Depending on the application goals, the number of reinforcement beams can be optimized according to the stated trade-off between mass and homogeneity. Subsequently, the optimal reinforcement beams' dimensions can be estimated by applying of the established analytical relations. This straightforward analytical study contributes to the advancement of structural design methodologies, particularly in the pursuit of lightweight and efficient engineering solutions.

As a final remark, as mentioned in the section 1.3.4, the introduction of stiffeners has a significant impact on the flexural wave dispersion characteristics and radiation efficiency of structures. The presence of stiffeners imposes constraints on normal displacement, rotation, and twist, leading to partial reflection of incident bending waves and resulting in multiple scattering effects that influence the behavior of bending wave propagation. Consequently, the mode shapes exhibit complex forms, and the distribution of natural frequencies is substantially changed. At higher frequencies, where the bending wavelength is significantly smaller than the spacing between beam reinforcements, two scenarios arise depending on the relative stiffness of the stiffeners compared to the plate bending stiffness. If the stiffeners have considerably high bending and torsional stiffness relative to the plate bending stiffness, the individual inter-stiffener panels can be discretized and treated as smaller bounded plates. However, if the stiffeners do not possess significantly high bending and torsional stiffness compared to the plate bending stiffness, the boundary conditions of the smaller panels are determined by the dynamic properties of the surrounding stiffeners and the rest of the structure. Consequently, the boundary conditions become frequency-dependent [135, 57].

2.2 Gearbox Housing Global Design Optimization

2.2.1 Introduction

As discussed in the section 1.1.4, empirical methods exist for determining thicknesses, heights, and other parameters during the design of gearbox housings. These methods ensure that the housing can withstand the loads transmitted at the bearing supports. However, while these empirical methods result in a design that meets the structural requirements, they do not optimize the housing design in terms of material utilization or maximizing its global stiffness.

On the section 2.1, it was demonstrated that for panel structures, optimization can be achieved through analytical deductions. Nevertheless, for more complex geometries, optimal design cannot be obtained so straightforwardly. The core principle

of lightweight design is to reduce mass while preserving the benefits and strengths of the design. To address this challenge, topology optimization methods can be employed, enabling multi-objective optimization of the housing geometry.

While some works in the literature focus on the structural optimization of gearbox housings [158, 78, 112], they disregard the investigation of the other implications of mass reduction in the housing design. For example the implications in the NVH signature of the housing. Therefore, it is essential to explore and integrate NVH considerations into the optimization process to achieve a lightweight design that not only reduces mass but also mitigates potential noise and vibration issues. This research aim to address this gap and develop methodologies that encompass both structural optimization and NVH analysis for gearbox housing designs.

2.2.2 Topology Optimization Formulation

Topology optimization is a mathematical method that optimizes the material distribution within a specified design space. The first step involves defining the available volume where material can be placed or utilizing the original geometry of the object as the initial design [158]. The goal of topology optimization is to determine the optimal arrangement of material within the specified volume. When the objective is to maximize the stiffness of the structure, the compliance of the structure needs to be minimized. This implies minimizing the total strain energy within the structure, as shown in Equation 2.15. The equations used in topology optimization can vary depending on the specific method employed [83, 104]. However, a common approach is the density-based topology optimization method, which uses a density variable, denoted as ρ_{var}, to represent the relative amount of material within each finite element.

The density variables ρ_{var} are constrained to values between 0 and 1, where 0 signifies the absence of material (void) and 1 represents a fully solid material, as indicated by Equation 2.16. During the optimization process, the algorithm iteratively adjusts the values of ρ_{var} within the design space to discover the optimal distribution of material that meets the defined objectives. Equation 2.17 establishes the volume constraint equation, which is instrumental in ensuring that the overall volume of the structure does not exceed a specified limit V_c.

Equation 2.18 states the equilibrium equation, where $\mathbf{K}(\boldsymbol{\rho})$ is the global stiffness matrix of the structure, $\mathbf{u}$ is the displacement vector, while $\mathbf{f}$ denoted the vector with the applied nodal forces. The set of finite element indices is denoted as $\mathbb{N}_e$, and v_i corresponds to the volume of the cell i. It is important to note that the finite elements correspond to the design cells within the structure. The design variables vector is represented as $\boldsymbol{\rho}$. The volume of the structure V is computed in each iteration using Equation 2.17, and it is constrained by the volume limit V_c. Additionally, the design variables $\boldsymbol{\rho}$ are limited by a minimum, ρ_{var_min}, to prevent singularities in the stiffness matrix and ensure numerical stability during the optimization process. These constraints help maintain the integrity of the solution and avoid unrealistic or unfeasible designs.

$$min : c(\boldsymbol{\rho}) = \mathbf{f}^T \mathbf{u} \tag{2.15}$$

$$0 \leq \rho_{var\_min} \leq \rho_{var\_i} \leq 1 \quad \forall i \in \mathbb{N}_e \tag{2.16}$$

$$V = \sum_{i \in \mathbb{N}} \rho_{var\_i} \cdot v_i \leq V_c \tag{2.17}$$

$$\mathbf{K}(\boldsymbol{\rho})\mathbf{u} = \mathbf{f} \tag{2.18}$$

The global stiffness matrix of the structure, $\mathbf{K}(\boldsymbol{\rho})$, is updated iteratively using the finite element assembly operator. This process is governed by Equations 2.19 and 2.20, which involve the design variables vector. By updating the global stiffness matrix in each iteration based on the design variables, the topology optimization method can adaptively refine the structural stiffness to achieve an optimal configuration. This iterative process enables the exploration of various material arrangements and their impact on the overall stiffness of the housing structure.

$$\mathbf{K}(\boldsymbol{\rho}) = \sum_{i \in \mathbb{N}} \mathbf{K}_i(\rho_i) \tag{2.19}$$

$$\mathbf{K}_i = \rho_{var\_i}^p \mathbf{K}_{0,i} \tag{2.20}$$

In the final solution, it is desirable for the design variables to approach values close to 1 or 0. To achieve this, a penalization parameter p is considered to diminish the undesirable presence of intermediate values [175]. As a rule, p assume at least the value of 3 [104]. This approach, known as Solid Isotropic Material with Penalization (SIMP). Even though this is the most widely used in the literature for topology optimization, there are several other topology optimization techniques and algorithms [14].

The optimization volume domain, illustrated in Figure 2.5, is intricately shaped and constrained by diverse factors. Internal volume restrictions stem from the presence of gearbox inner components (depicted in grey), while external limitations are contingent on the surrounding environment. Consequently, the optimization volume lies within the boundaries defined by these constraints, as highlighted by the green region in Figure 2.5. External connections, such as fixation to the system or actuators, are denoted by the number 1, while internal component connections, such as bearing support interfaces or other gearbox inner connections, are indicated by the number 2.

The volume domain can adopt different shapes, varying in complexity. Regardless of the specific shape, the optimization process remains consistent. The methodology and principles used to optimize the material distribution within the volume domain remain the same, irrespective of the complexity or geometry of the region. This flexibility in the shape and complexity of the volume domain enables

the application of topology optimization to a wide range of design problems, accommodating different structural requirements and design constraints. The key lies in effectively defining and representing the volume domain, considering all the relevant boundaries and connections, to ensure an accurate optimization process.

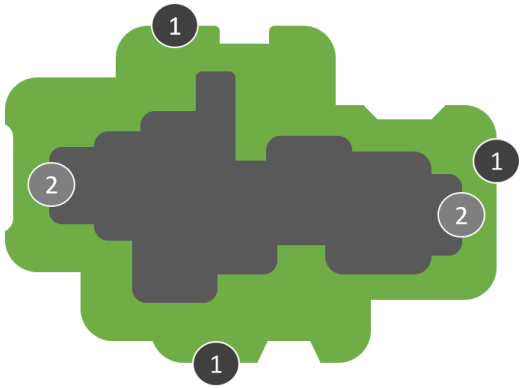

Figure 2.5: Cross-section example of the volume domain available for the optimization of the gearbox housing design.

To perform topology optimization, it is necessary to establish the design material properties, which are known for conventional metallic materials. Additionally, specifying the relevant external load cases within the optimization model is essential. In the case of the gearbox housing, these load cases can be obtained by global gearbox simulations or by experimental data. These parameters significantly influence the optimization process, ultimately shaping its behavior and the resulting output.

In order to ensure compatibility with other components and meet functional requirements, it is essential to keep the connection geometries of the GBH outside the optimization loop. This includes interfaces such as bearing and actuator interfaces, as well as support structures. By excluding these connection geometries from the optimization process, their shape and position remain fixed, guaranteeing their compatibility and functionality. For example, in the case of a simple geometry, similar to the one considered in the works of Figlus et al. [58, 59], specific geometries that should be excluded from the optimization loop are the bearing interface and the connection interface of the down housing part. The regions highlighted in blue in Figure 2.6 need to be preserved in their original shape and position to fulfill their function.

In addition to the considerations mentioned earlier, other conditions and constraints may be incorporated into the topology optimization process. These additional conditions serve to respect the gearbox requirements, not only functional but also the ones regarding material safety. For instance, maximum allowed displacements in certain areas of the structure can be defined as constraints. This ensures that critical regions, such as those depicted in Figure 2.7, do not exceed specified displacement limits. Additionally, a von Mises stress condition may be imposed

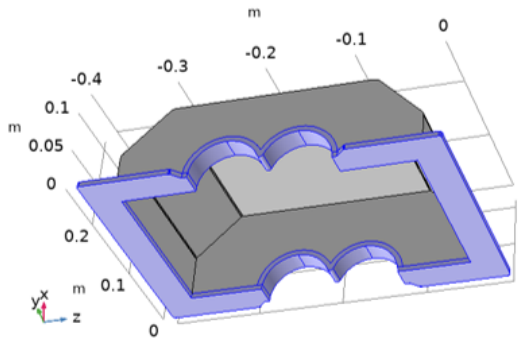

Figure 2.6: Volume outside the optimization loop (in blue).

to limit the maximum stress in any area of the geometry. This condition ensures that the optimized design maintains stress levels below the material's yield stress, safeguarding against structural failure.

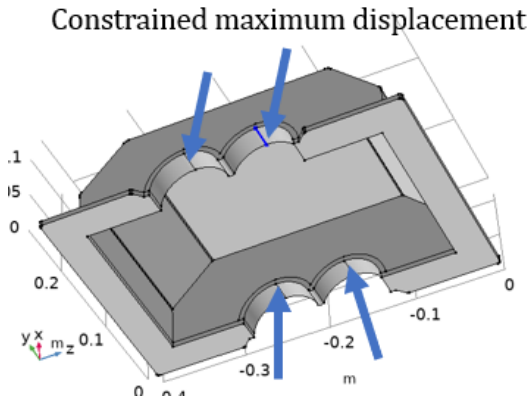

Figure 2.7: Constraint on the maximum displacement at the bearing supports.

After completing the topology optimization process, and through the definition of a minimum material stiffness contribution, the optimized structural skeleton of the housing is obtained. It identifies the areas where material can be removed to achieve component mass reduction while ensuring that the remaining material provides sufficient stiffness to meet the establish criteria.

Figure 2.8 illustrates an example of the optimized geometry for a simple case, where different colors represent different stiffness contributions. The areas highlighted in red indicate regions with a high stiffness contribution, meaning they play a significant role in the overall structural integrity. On the other hand, the blue areas represent regions with a lower stiffness contribution compared to the red areas but still have a higher stiffness contribution than the areas that were removed.

The colors between red and blue represent intermediate stiffness contributions, ranging from the maximum contribution in the red areas to the defined minimum

threshold contribution. The removed areas fall below the defined minimum material stiffness contribution threshold. For housing geometries with higher geometric complexity, surface smoothing algorithms can be applied to refine the obtained geometry. These algorithms help in achieving a smoother and reducing abrupt transitions.

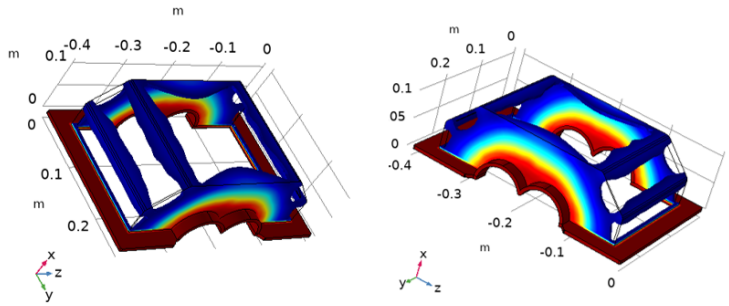

Figure 2.8: Steel structural skeleton of the housing after optimization.

As mentioned in the section 1.1.3, the gearbox housing serves multiple functions beyond structural integrity. It must effectively contain and maintain lubricant within the operating area of the gears, as well as protect the internal components from environmental factors like moisture and dust. Therefore, it is crucial to treat any voids and openings that may arise in the gearbox housing after the optimization process.

One approach to addressing this issue is by closing the gaps in the 3D model of the optimized gearbox housing. This can be achieved by adding material with a minimum wall thickness, as illustrated in Figure 2.12. The specific minimum wall thickness can be determined based on manufacturing requirements, such as those applicable to casting processes [158]. By incorporating this minimum wall thickness, the gaps and openings in the optimized design can be effectively closed, ensuring that the housing meets the necessary sealing and protection requirements.

Alternatively, some commercial optimization software packages offer the option to set constraints that preserve a closed geometry throughout the optimization process. The choice between modifying the optimized design to close any voids and openings or utilizing closed environment optimization depends on the specific requirements and constraints of the design project. Both approaches are valid, and the decision should be made based on factors such as design complexity, manufacturing considerations, and available software capabilities.

2.2.3 Gearbox Housing Topology Optimization

The loads experienced by the bearing support in the gearbox housing are not solely determined by the gearbox inner rotating components, but also by the housing itself. Hence, to accurately determine the loads at the bearing interface, an iterative process is necessary. This involves updating the housing design in each iteration, as shown in the diagram in Figure 2.9. The initial design space can take any shape, and

with each iteration, a new housing design is obtained. This design can be updated in the global gearbox simulation in a reduced way, through a Component Mode Synthesis (CMS). These global gearbox simulations are normally done in gearbox dedicated software programs, which are widely used by other researchers in the LIVE-I project. After this update, more accurate bearings' loads can be obtained, which then can be inputted in the topology optimization process.

The topology optimization implementations for demonstration were conducted in COMSOL Multiphysics (version 5.6). The starting housing design was similar to the one presented by Figlus et al. [58, 59]. Representative load cases (LCs) were applied in different directions. The load magnitude was 1 kN, which is a typical order of magnitude of the loading in the gearbox bearings. A total of 12 critical LCs were applied on the bearings' support interfaces. Given that the objective of the demonstration is to showcase the topology optimization process and in the absence of more precise data, the same weighting factor was assigned to all LCs during the optimization. However, in a real industrial application where estimated bearing loads are available, they shall be used to start the structural optimization.

The properties of the considered steel material are the following: Young's modulus of 200e9 $[Pa]$, Poisson's ratio of 0.3 and Density of 7850 $[kg/m^3]$, as outlined in Table 2.1. For the optimization solving, the considered optimization method was the Method of Moving Asymptotes (MMA). The aim defined for mass reduction was 30%. And the objective function for minimization was the normalized strain energy in the structure, that way the global stiffness is maximized. As mentioned before, analogously to the external and internal boundary conditions, the connection geometries of the GBH should be kept outside the optimization loop, e.g. bearing and actuators interfaces, supports. For the simple geometry case example, the geometries to keep out of the optimization loop are the bearing interface and the down housing part connection interface, seen in blue in the Figure 2.6.

Topology optimizations were performed according to the method described in subsection 2.2.2. Different isotropic materials were used to assess the influence of material properties on the topology optimization results. In order to have a comparison with a material with substantially different properties, a PMMA was chosen. The properties of the considered PMMA are sated in the Table 2.3.

Property	Symbol	Value
Young's Modulus	E	3.2 GPa
Poisson's Ratio	υ	0.35
Isotropic Loss Factor	η	5 %
Density	ρ	1190 kg/m^3
Glass Transition Temperature	T_g	100°C

Table 2.3: Material Properties of the PMMA [39, 5]

Following the optimizations, the housing's structural skeletons were obtained,

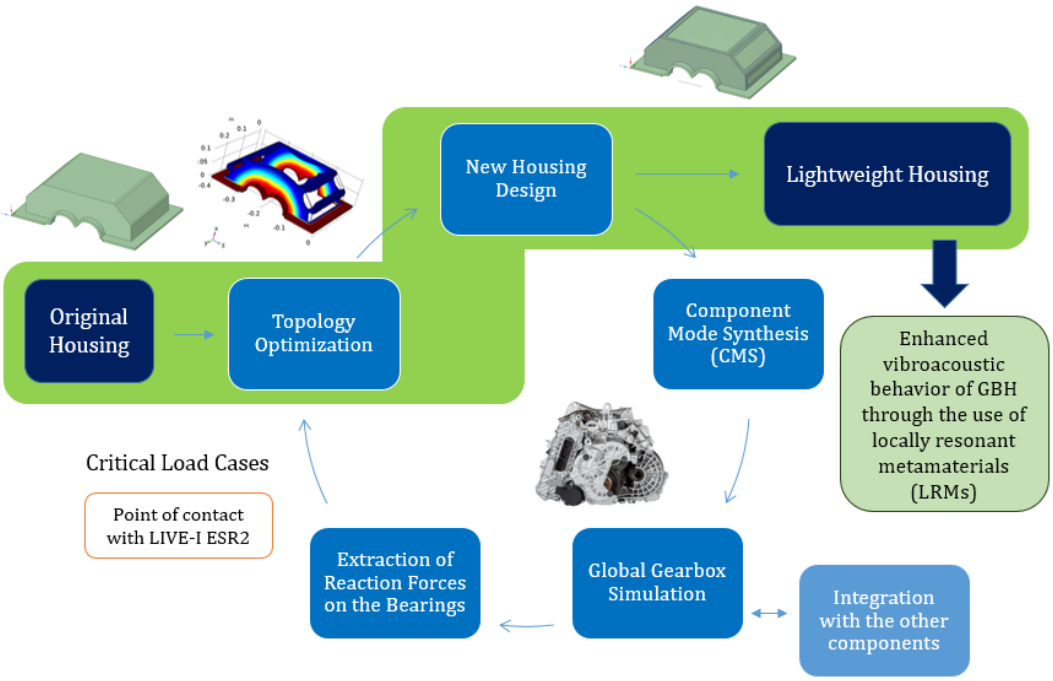

Figure 2.9: Iterative Topology Optimization Process.

and the regions where material could be removed were defined. The optimization outputs for the steel case and the PMMA case can be observed in Figure 2.8 and Figure 2.10, respectively. It is evident that the two topology optimization results exhibit significant differences. This observation aligns with the understanding that the geometry output of topology optimization is highly dependent on the chosen material for the component.

The distinct material properties of steel and PMMA lead to variations in the optimized designs, as the optimization process seeks to minimize structural weight while considering the material's characteristics. Therefore, the choice of material has a substantial impact on the resulting geometry obtained through topology optimization.

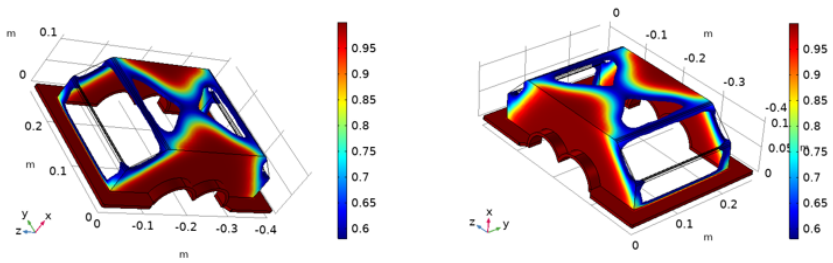

Figure 2.10: Structural skeleton of the housing after optimization using PMMA.

To further explore the impact of additional constraints on the optimization output, other constraints were introduced during the optimization process. One such constraint was the maximum allowed displacement in all the bearing support interfaces, which was set at 2 mm (as shown in Figure 2.7). It is worth noting that the maximum allowed displacement can be customized to any desired value, and it is also possible to define relative displacements in the geometry design.

Another constraint focused on the maximum value of the von Mises stress throughout the entire geometry. The stress limit should be defined according to the material yield stress and established safety factors. For the application case, the stress limit was set to 200 MPa. By incorporating these additional restrictions into the optimization process, we obtained optimized geometries with distinct characteristics. Figure 2.11 illustrates the optimized geometry considering these constraints, and it clearly demonstrates the differences compared to the design shown in Figure 2.8, which represents the optimization without the additional constraints.

The inclusion of these constraints in the optimization process significantly influences the final output of the optimized geometry. These constraints play a crucial role in shaping the design by ensuring that certain performance criteria, such as maximum displacement and stress levels, are not exceeded.

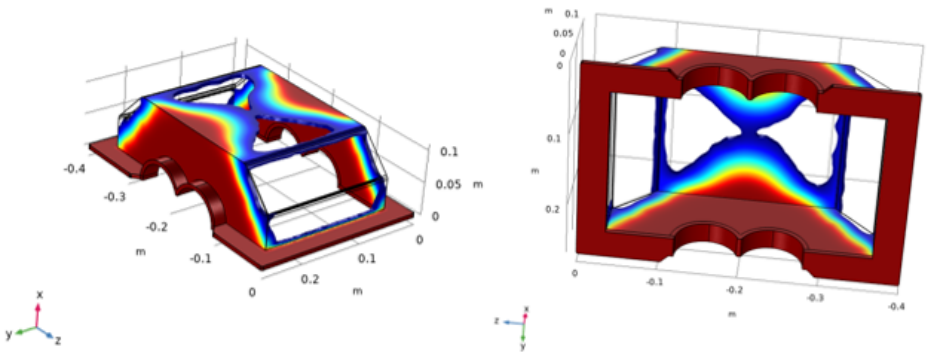

Figure 2.11: Steel structural skeleton of the housing after optimization with additional displacement and stress constraints.

As described in the subsection 2.2.2, in order to respect all the gearbox housing design, the housing geometry must be closed. Considering, for example, the first optimization output on the steel housing, see Figure 2.8, suitable measures can be taken to close the voids in the gearbox housing after optimization. This process results in the optimized geometry presented in Figure 2.12. The minimum wall thickness considered was 2 mm. Hence, generally there was a reduction of thickness in some parts of the housing. The thickness of the top plate and the side plates was reduced from 6 mm to 2 mm, generating a lightweight version of the GBH. The mass of the lightweight GBH is 6.81 kg compared to the 8.92 kg of the original steel GBH, which is a 24% relative mass reduction. If we consider the inclusion of bearings parts, the total mass of the original GBH is 10.98 kg, while the total mass

of lightweight GBH is 8.87 kg, which represents a 20% relative mass reduction.

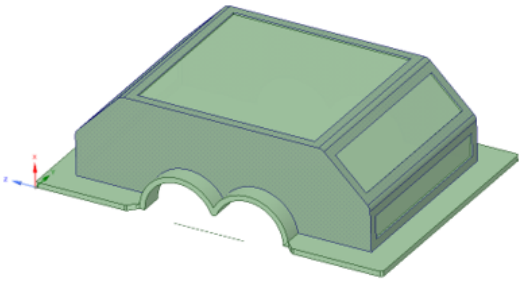

Figure 2.12: Lightweight version of the considered steel gearbox housing.

2.2.4 Lightweight Design Consequences in the housing NVH

It is important to consider that the material removal and thickness reduction in certain areas of the housing can have an impact on the natural frequencies and the global NVH signature of the housing [158]. There are two main approaches to address the NVH concerns in the housing design. One approach is to introduce an additional objective function that considers the location of natural frequencies in the frequency spectrum. This can be done if the excitation peaks' frequencies are known in advance. In order to achieve this, specific weighting factors need to be assigned to each objective function to balance the structural optimization and the desired NVH performance.

Another approach is to iteratively optimize the housing design while taking into account the NVH factors. This iterative process allows for the refinement of the design to strike a balance between structural optimization and the maintenance of the desired NVH performance. By iteratively considering both aspects, it is possible to achieve a design that meets the structural requirements while also addressing the NVH concerns of the gearbox housing.

Modal analysis following mass distribution optimization provides a convenient mean to evaluate the modifications in the eigenmodes of the structure. Building upon the previous example of the structurally optimized GBH part shown in Figure 2.12 and the original housing design, modal analyses were conducted. From the analyses it was possible to notice that the reduction of mass induces a considerable shift of the first eigenmode to lower frequency, from 882 Hz to 426 Hz. This eigenmode corresponds to the local eigenmode of the GBH top plate.

The GBH design must prevent its eigenmodes from aligning with the critical peaks in excitation. This precaution is crucial to forestall resonance complications and uphold the structural integrity of the system. When the excitation response across the frequency spectrum is known, conducting parametric optimizations becomes feasible, allowing for strategic adjustments to relocate the eigenmodes away from critical peaks of excitation. The parameters that can be adjusted in these op-

timizations are typically the geometric dimensions of the GBH. Modal optimization is a method to achieve the desired shift of eigenmodes over the frequency spectrum. It involves combining eigenfrequency studies with an optimization process. To conduct modal optimization successfully, the target eigenfrequencies need to be defined, along with the parameters that can be varied within specified upper and lower bounds. By leveraging this approach, it is possible to manipulate the GBH's eigenmodes and ensure they are separated from the excitation peaks, thereby improving the overall performance and stability of the system.

A modal parametric optimization with a parametrization of the thickness of the top plate was performed to illustrate the mentioned approach. Considering a hypothetical scenario where the aim is to shift the first eigenfrequency of the lightweight GBH (Figure 2.12) from its original value of 426Hz to 460Hz by modifying the thickness of the top part of the housing. For this case, the objective function (F) to minimize is stated in the Equation 2.21, where $f_{eigenfrequency}$ is the resultant first eigenfrequency in each iteration and $f_{desired}$ is the frequency where one wants to shift the first eigenfrequency to. The housing top part thickness was parameterized, with its lower and upper bounds set at 0.5 mm and 6 mm, respectively. The Nelder–Mead method was utilized to minimize the objective function iteratively. After conducting the optimization study, the optimal thickness to achieve the desired first eigenfrequency was obtained, as depicted in Figure 2.13.

$$F = (f_{desired} - f_{eigenfrequency})^2 \tag{2.21}$$

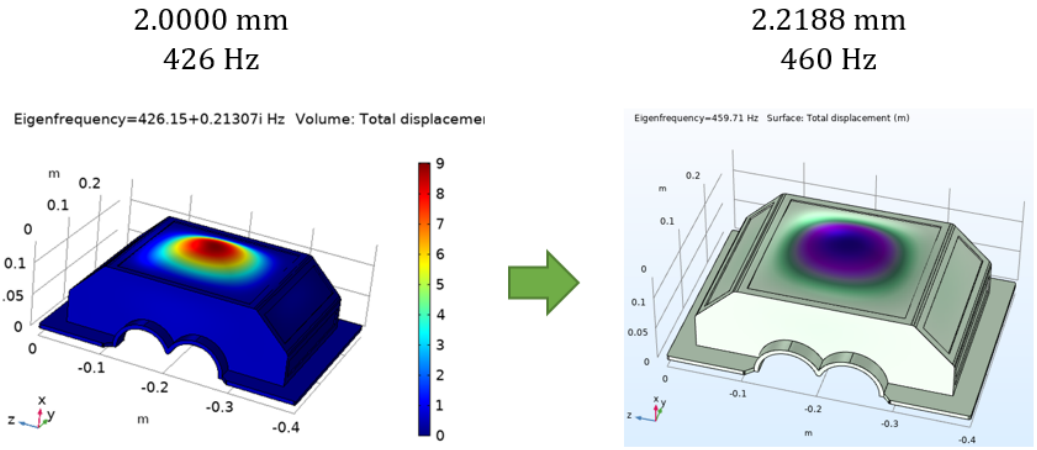

Figure 2.13: Shift in the first eigenfrequency after modal optimization.

As highlighted in the section 1.3.4, the use of coatings can be effective in attenuating noise emissions in gearbox housings, particularly for high-frequency noise. However, it is important to note that these viscoelastic coatings are considered as a solution of last resort by gearbox and EV motor manufacturers.

In contrast, as discussed in the section 1.3.5, the rib design approach is a more common method for vibroacoustic enhancement in gearbox housings. By considering the excitations and natural frequencies of the housing, specific rib reinforcement designs can be implemented. These designs aim to shift the natural frequency of the housing away from the excitation peaks of the gearbox assembly, thereby reducing noise radiation. This approach provides a proactive means of addressing NVH concerns in gearbox housings.

The above-mentioned methods are the traditional NVH enhancement techniques during the design phase. On the other hand, as widely discussed in the section 1.4, recent developments in the area of metamaterials, and in particular LRMs, can lead to the development of innovative passive solutions for NVH control in gearbox housings. In the context of gearbox housings, LRMs can be strategically integrated into the design to achieve specific NVH control objectives. By tailoring the properties of the LRM structures, such as their size, shape, and arrangement, it is possible to manipulate the propagation of vibration waves within the housing and its noise emission. The Chapters 3 and 5 of this thesis investigate these novel concepts.

The following section will concentrate on evaluating the sound radiation from the housing in two scenarios. The first without any geometric modifications, and the second after the application of topology optimization. By comparing these two cases, it is possible to assess the impact of the design optimization process on the acoustic response of the housing.

2.3 Sound Power Radiated Assessments of Gearbox Housings

In order to assess the impact of the mass reduction and the geometry changes in the NVH signature of the considered housing, this section describes a vibroacoustic study on the housing noise emission. For the first noise radiation comparison, the two GBH versions are considered, the original GBH (see Figure 2.6) and the lightweight version of the GBH (as seen in the Figure 2.12).

In order to numerically evaluate the sound radiation from structures, structural-acoustic models are needed. They are mathematical representations or simulations that combine both the structural and acoustic aspects of a system. It involves the integration of structural dynamics and acoustic wave propagation to analyze the interaction between the mechanical vibrations of a structure and the sound waves generated or transmitted by it.

2.3.1 Structural-Acoustic Model and Formulation

In a structural-acoustic model, the structural component describes the mechanical behavior of the structure, including its geometry, material properties, and boundary conditions. It considers the dynamic response of the structure to external forces or

excitations. The acoustic component accounts for the sound waves generated by the structural vibrations and their propagation through the surrounding medium, in the case of the gearbox housing it is air. It takes into account the acoustic properties of the medium, including its density, speed of sound, and absorption characteristics. Fluid-structure interaction equations allow the coupling of the structural and acoustic components, which enable the analysis of how vibrations in a structure contribute to the generation, transmission, and radiation of sound.

The sound power radiated, over the frequency domain, is obtained by integrating the far-field intensity over a hemispherical surface centered on the structure [57], as written in Equation 1.15. Sound Power Levels are indicated in decibels, by the following formula stated in Equation 1.16, where the reference power $P_0 = 10^{-12}W$.

As outlined in the section 1.1.3, the mechanical loading experienced by the bearing connections in the GBH is dependent on multiple factors, such as the geometries, characteristics, and assembly configurations of the rotating components. These factors encompass the transmission ratio, the inclination angle of the gear teeth, the transmitted power, the input speed, and the distance between axes. Within the bearing support, loads are transferred from the shafts to the housing structure, exerting forces in both radial and axial directions. To simulate the loading conditions, a characteristic loading pattern was applied to the bearing connections in the GBH, as shown in Figure 2.14. To determine the loading on the bearings, a simple gearbox with helical gears was used as a reference. The distribution of loading for each of the four bearing connection regions is illustrated in Figure 2.15.

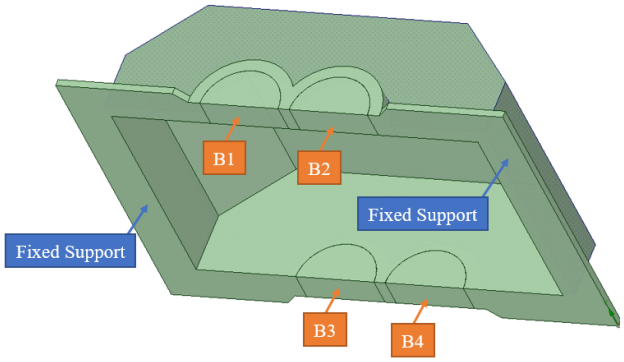

Figure 2.14: Location of the excitation for each bearing: Bearing 1 (B1), Bearing 2 (B2), Bearing 3 (B3), Bearing 4 (B4); and the Fixed Support Boundary Conditions.

The numerical simulations were performed in the commercial software COMSOL Multiphysics (version 5.6). The model was solved in the frequency domain using the solid mechanics and pressure acoustics modules, with an acoustic-structure boundary within COMSOL Multiphysics. As outlined in Table 2.1, the properties of the considered steel material are the following: Density of 7850 $[kg/m^3]$, Young's modulus of 200e9 $[Pa]$, Poisson's ratio of 0.3 and isotropic structural loss factor of 0.1%. The structural-acoustic model is described in the Figure 2.16. A hemispherical acoustic air domain of 0.4 m radius was set around the GBH. The considered air

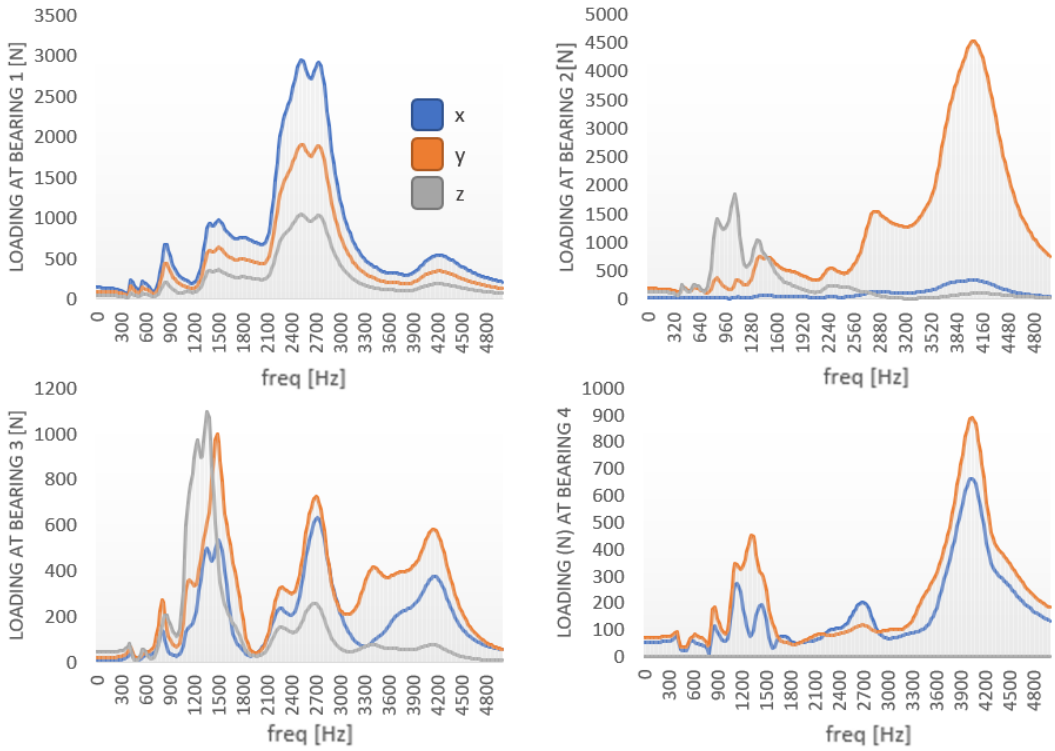

Figure 2.15: Loading for each of the four bearings in x (side), y (upwards) and z (axial) directions.

material properties depend on the ambient pressure p_A and temperature T. The speed of sound c and the density ρ are defined through the ideal gas law (assuming adiabatic behavior), according to Equation 2.22 where R stands for universal gas constant ($R = 8.3144621[J/(molK)]$), γ stands for the ratio of specific heats ($\gamma = 1.4$) and the M_n is the molar mass $M_n = 0.02897[kg/mol]$. The considered ambient pressure and temperature were 1 atm and 20°C (293.15 [K]), respectively.

$$c^2 = \gamma \frac{R}{M_n} T \qquad \rho = \frac{M_n p_A}{RT} \tag{2.22}$$

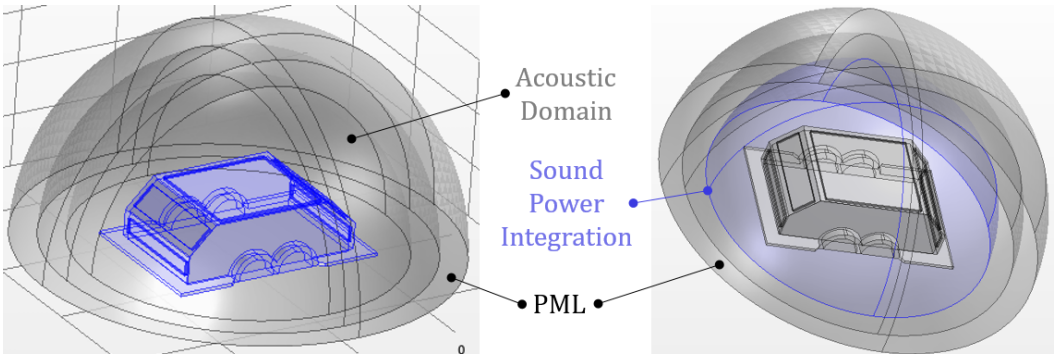

Figure 2.16: Description of the structural-acoustic models' setup.

A Perfectly Matched Layer (PML) was set between the radius of 0.35 m and 0.4 m to represent the open environment, as seen in Figure 2.16. In acoustics, the PML is a widely used technique for absorbing outgoing waves at the boundaries of a computational domain, simulating an infinite domain [15]. The PML equations are typically derived from the governing equations of the acoustic wave propagation problem and involve introducing additional terms to the equations to create an absorbing layer. The PML equations for acoustics are derived of the linearized equations of motion and the conservation of mass for compressible fluids [115].

Figure 2.17 provides a global mesh visualization of structural-acoustic model and detailed view in the PML mesh. The global maximum element size was set as the speed of sound divided by five times the highest frequency to be modelled. The PML mesh has 4 elements through its thickness, as can be seen in the Figure 2.17. The structural-acoustic model for the original GBH was constituted by 810509 elements, with an average and minimum quality of 67% and 18%, respectively. The lightweight GBH model comprised 852208 elements, with an average and minimum quality of 65% and 14%, respectively.

The sound power radiated was integrated at a radius of 0.3 m, according to the Equation 1.15. The structural loading of the model was based on the bearing loading depicted in Figure 2.15, and it was applied to the designated geometry areas illustrated in Figure 2.14. A fixed support was considered in the connecting interface to the other half of the GBH, as shown in Figure 2.14. The computational analysis was carried out on a high-performance server equipped with two E5-2680

v2 processors operating at 2.80GHz, with 380 Gb of RAM memory. Each model required a total computation time of 112 hours to complete the simulations.

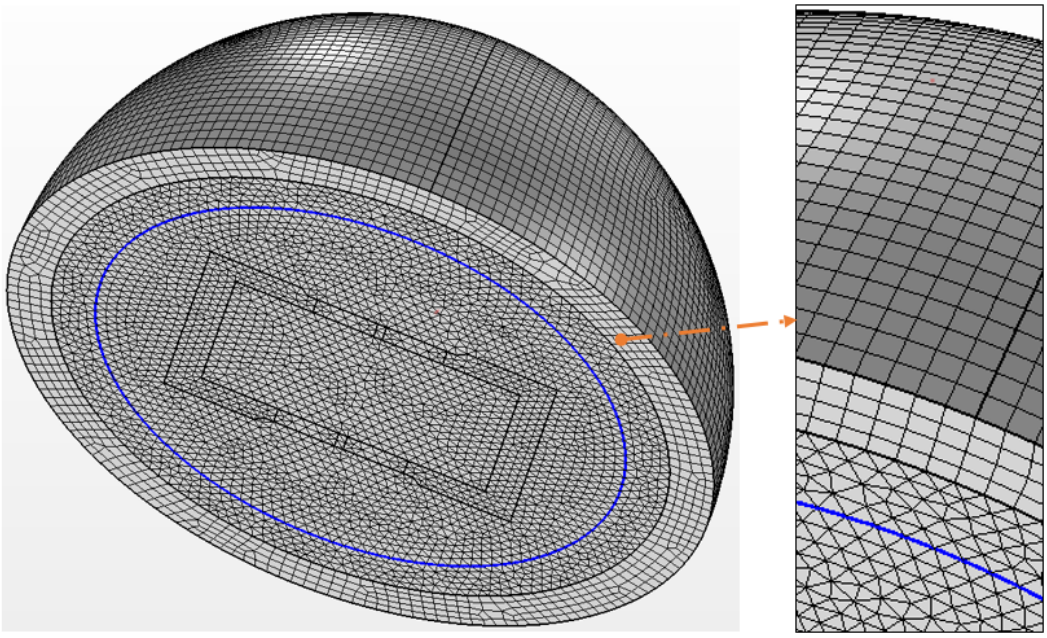

Figure 2.17: Structural-acoustic model global mesh (left) and detail of the mesh in the PML (right).

2.3.2 Results and GBHs Sound Radiation Comparison

The sound power radiated integration results were computed in both structural-acoustic models, described in the previous section. The comparison of the sound power radiated from the original GBH and the lightweight GBH is shown in Figure 2.18. As evident from the figure, reducing the mass of the GBH leads to a shift in the frequency location of the sound power radiation peaks. Additionally, the deformation shapes of the housing indicate that the peaks in sound power generally correspond to the eigenmodes of the structure, with many of them aligning with the local eigenmodes of the top plate. Notably, a significant observation is the emergence of a peak at 425 Hz when the mass of the GBH is reduced, indicating a shift in the first local eigenmode of the top plate.

In order to ensure an equitable comparison, the sound power radiated results were normalized by dividing them by the power injected into the structure. The total power injected is calculated by the summation of the power injected in each bearing, see Equation 2.23. The power injected for each bearing was determined through integration over the area of load application, as expressed in Equation 1.17. Figure 2.19 illustrates the ratio of the sound power radiated to the power injected in the structure, as given by Equation 1.18, for both the original GBH and the lightweight GBH.

The observed trend in the nominal results of the radiated sound power is consistent with the findings in the normalized results. Comparing the results indicates that reducing the mass of the structure not only causes a shift in the eigenmodes but also introduces new eigenmodes within the analyzed spectrum. This is clearly demonstrated by the increased number of peaks observed in the radiated sound power results of the lightweight version of the housing, in contrast to the original housing. This outcome is in line with expectations, as the reduction in thickness in certain areas of the housing geometry induces the presence of additional local modes in these regions characterized by lower thickness.

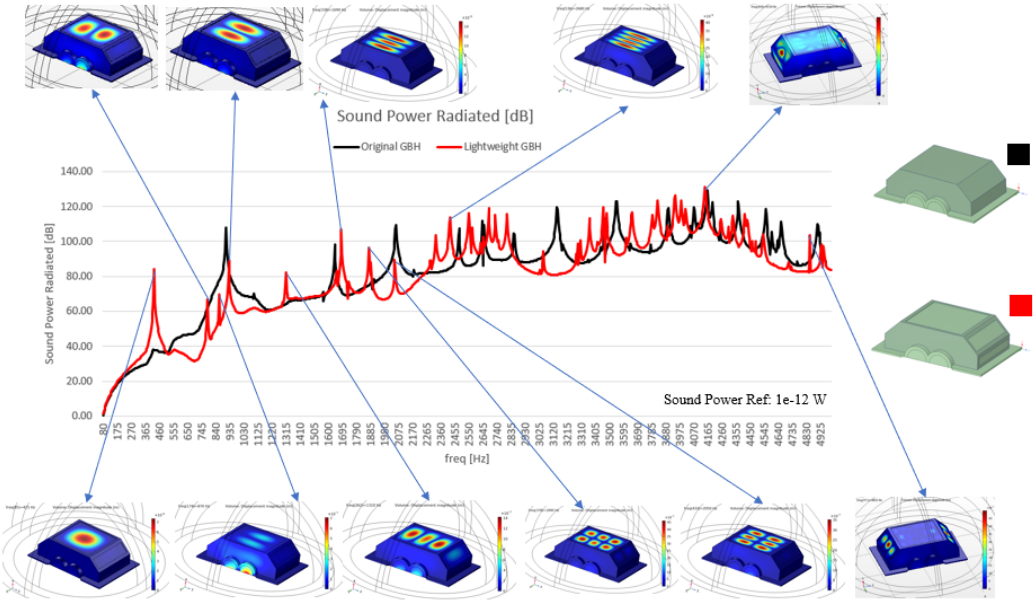

Figure 2.18: Sound power radiated comparison between the original GBH (black) and the lightweight version of the GBH (red), complemented with a number of housing deformation shapes.

$$P_{injected\,total}(\omega) = P_{injected\,B1}(\omega) + P_{injected\,B2}(\omega) + P_{injected\,B3}(\omega) + P_{injected\,B4}(\omega) \tag{2.23}$$

The goal of this research is to create innovative and lightweight designs for gearbox housings that exhibit desirable NVH characteristics. The advancements in the field of metamaterials have opened up potential opportunities to leverage the NVH characteristics of GBHs through the application of metamaterial concepts. Metamaterials offer the ability to manipulate sound waves, vibration, and other forms of energy, providing researchers and engineers with new tools to control and mitigate NVH issues.

The upcoming chapter of this research will focus on exploring and investigating simple and cost-effective solutions based on LRMs for application in GBHs. LRMs involve the integration of specific resonant elements or structures within a material or

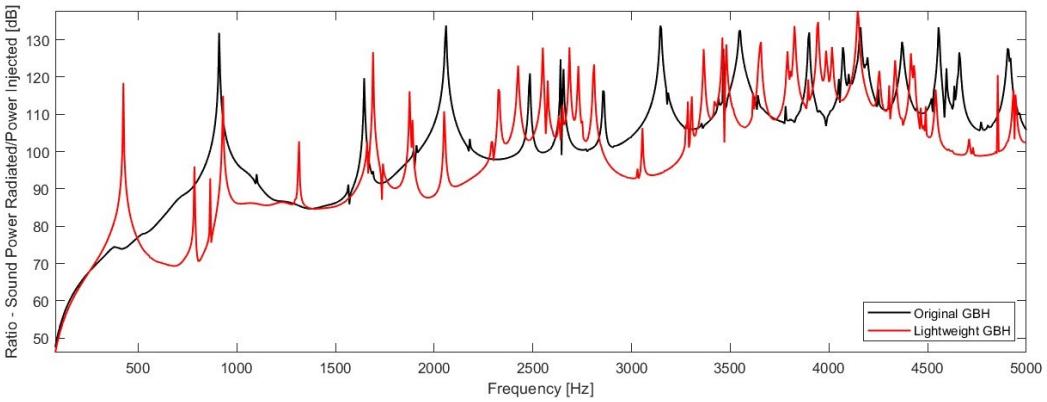

Figure 2.19: Ratio between the sound power radiated and the power injected in the structure of the original GBH (black) and the lightweight GBH (red).

architecture to modify its dynamic response and acoustic properties. The placement of these resonant elements allows the creation of zones of vibration attenuation, thereby reducing the noise emission from GBHs.

The use of LRMs in GBHs holds several advantages in comparison with other conventional methods. Firstly, they offer the potential for significant weight reduction, which is highly desirable in industries where lightweight design is essential for improved fuel efficiency, performance, and environmental sustainability. Additionally, LRMs can target specific frequency ranges and modes of vibration, allowing for tailored NVH control in GBHs. Furthermore, LRMs can be implemented using cost-effective manufacturing techniques, making them suitable for practical and scalable applications in the industry.

By exploring and evaluating various LRM solutions, this research aims to contribute to the development of innovative GBH designs that effectively address NVH challenges. The findings and insights gained from this investigation will provide valuable knowledge for engineering designers working in the field of gearbox technology, helping them to create more efficient, quieter, and comfortable vehicles.

Chapter 3

Metamaterials for NVH Control in Lightweight Metallic GBHs

This chapter investigates the utilization of metamaterials, particularly locally resonant metamaterials, for enhancing NVH characteristics of metallic GBHs. It encompasses preliminary analyses, numerical simulations, and experimental validations. The preliminary research highlights that high-damping resonators exhibit broader attenuation responses, and solid modeling enhances the accuracy of LRM behavior prediction. Numerical simulations confirm that integrating LRMs within GBHs substantially reduces noise emissions across the frequency spectrum. Experimental results corroborate this effectiveness, showcasing significant attenuation throughout the entire spectrum. Moreover, LRM implementations offer minimal mass increase, facilitating lightweight NVH-improved GBH designs. The concluding three sections of this chapter are based on the article "Lightweight gearbox housing with enhanced vibro-acoustic behavior through the use of locally resonant metamaterials" [3], published in Applied Acoustics journal.

Contents

3.1 Metamaterial Solutions for Application on GBHs

As stated in section 1.4.3, some automotive metamaterial solutions can be found in the recent literature, although to our knowledge, there is no application of these concepts to GBHs neither to EV motor housings. It is worth noting that modern EV motor housings and GBHs both enclose geared systems and share similar structures and functionalities. In fact, currently, they are often manufactured by the same companies. Therefore, solutions developed for GBHs can also be adapted and applied to EV motor housings.

Industrial manufacturers have tight deadlines to bring new products to market, which can make optimizing the design of metamaterials challenging. The reviewed literature suggests that the process of optimizing metamaterial designs is complex, particularly in real-world applications where design complexity and uncertainties present significant challenges. Consequently, the pursuit of optimal design solutions becomes excessively time-consuming and impractical to implement within industrial processes.

Another important point raised by the manufacturers is the housing manufacturing cost. Production costs are a relevant factor in the industry, for that reason it is important to consider cost implications when developing solutions for automotive components. Any proposed solutions should aim to minimize additional costs and ensure that they are economically viable for manufacturers to implement.

As a result, it may be worthwhile to explore whether even fast design LRM solutions can provide benefits in application in GBHs by improving their NVH behavior and enabling lightweight design. While they may not provide the maximum possible benefit, even suboptimal solutions could still offer significant improvements and be more practical for industrial implementation within the given time and cost constraints.

Ultimately, the potential of LRMs in the vibroacoustic field has been demonstrated in numerous academic studies. However, there has been a limited exploration of their practical implementation for engineering solutions. Currently, gearboxes predominantly rely on conventional methods to meet NVH targets. Nevertheless, by capitalizing on recent advancements in the field of metamaterials, there is an opportunity to develop innovative solutions that can enhance gearbox design and performance.

The following section describes the formulation to be used in the study of the LRM solutions to be applied in the GBHs.

3.2 Dispersion Relations and BG Evaluation in LRMs

Although LR structures can be applied in non-periodic ways, the majority of the literature focuses on simplifying the analysis of LRMs by assuming an infinite periodic distribution of LR structures [77, 93, 117]. This approach allows for a comprehensive representation of the LRM using a UC and Floquet-Bloch boundary conditions.

Figure 3.1 illustrates a schematic representation of a two-dimensional periodic structure.

For the LRM preliminary design studies, the LRM will be a studied as an infinite periodic arrangement.The periodic structure consists of a repetitive pattern of the UC in two directions, being $\mathbf{d}_x$ and $\mathbf{d}_y$ the basis vectors of the UC. Given that the structure is periodic, any point P in the structure can be expressed with respect to a corresponding point U in the unit cell, translated n_x cells along $\mathbf{d}_x$ and n_x times along $\mathbf{d}_y$, see Equation 3.1 [37].

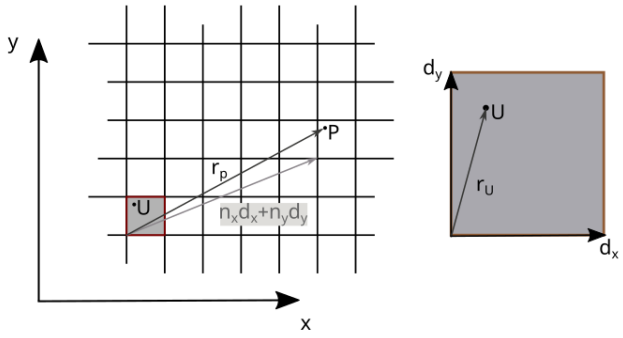

Figure 3.1: Schematic presentation of an infinite periodic structure (left). A unit cell of the structure (right).

$$\mathbf{r}_P = \mathbf{r}_U + n_x\mathbf{d}_x + n_y\mathbf{d}_y \tag{3.1}$$

According to Bloch's theorem, the behavior of a two-dimensional periodic system can be described by the response of a reference unit cell. The amplitude and phase variation of a wave propagating through an infinite periodic structure can be characterized by an exponential term, as shown in Equation 3.2 [22, 37], where the '$\cdot$' denotes a scalar product.

$$u(\mathbf{r}_P, \omega) = u_{ref}(\mathbf{r}_U, \omega)e^{\mathbf{k}\cdot(n_x\mathbf{d}_x + n_y\mathbf{d}_y)} \tag{3.2}$$

The wave vector $\mathbf{k} = (k_x, k_y)$ defines the amplitude and phase change. In infinite periodic structures, the propagation vector $\boldsymbol{\mu}$, defined in Equation 3.3, expresses the complex phase shifts when in motion within a cell in the $\mathbf{d}_x$ and $\mathbf{d}_y$-directions.

$$\boldsymbol{\mu} = (\mu_x, \mu_y) = (\mathbf{k}\cdot\mathbf{d}_x, \mathbf{k}\cdot\mathbf{d}_y) = \mathbf{k}\cdot\mathbf{d} \tag{3.3}$$

Employing this notation to rewrite the Bloch theorem, Equation 3.4 is reached, where $\mathbf{n}$ is a vector indicating the amount of cells moved in each direction in relation to the reference UC.

$$u(\mathbf{r}_P, \omega) = u_{ref}(\mathbf{r}_U, \omega)e^{\boldsymbol{\mu}\cdot\mathbf{n}} \tag{3.4}$$

Utilizing the theory of infinite periodic structures enables the investigation of wave propagation in LRMs without relying on computationally intensive finite-structure vibroacoustic numerical models [77, 37]. The unique vibroacoustic characteristics of LRMs are evaluated based on the presence of BGs in the dispersion curves. These dispersion curves depict the relationship between frequency and wavenumbers, providing valuable insights into the behavior of LRMs.

For rectangular lattices, the periodic zone in the wave domain, called a Brillouin zone, can be circumscribed in $[-\pi, \pi]$ in both principal directions. Employing the UC symmetries, the area to study can be further reduced in the Irreducible Brillouin Zone (IBZ). The IBZ depends on the shape and symmetries of the UC [89]. There is a common practice of assessing the abovementioned BGs in the LRM dispersion curves, by the calculation of the dispersion curves exclusively on the IBZ boundaries, also known Irreducible Brillouin Contour (IBC) [22, 77, 81].

Various methods can be employed to calculate dispersion curves for infinite periodic structures of LRMs and represent their constitutive UCs. These methods include lumped parameter modeling, plane wave expansion (PWE) method, multiple scattering (MS) method, finite difference (FD) methods, and finite element (FE) methods. These methods serve different purposes and are chosen based on the specific problem and its characteristics. Lumped parameter modeling simplifies systems into discrete elements, PWE and MS methods are specialized for periodic and scattering problems. FD and FE methods are numerical techniques for solving PDEs and are widely used in various engineering and scientific disciplines, with FE offering more flexibility in handling complex geometries and material properties. The FE approach is particularly versatile in analyzing wave propagation within complex structures, making it most suitable for modeling UCs with complex topologies and geometries [27]. Consequently, the FE approach has gained popularity in recent works focusing on LRM applications, as indicated by the literature review in the section 1.4.3.

Given the objective of investigating LRMs in a real-world application, it is essential to comprehensively analyze the LRM UCs to capture their realistic behavior. Therefore, the FE-based UC modeling method is considered the most suitable approach for accurately representing the UCs of LRMs. Furthermore, considering the abovementioned infinite formulation, the analyses of the LRMs will involve the discretization of the UC using the FE method and applying Bloch-Floquet boundary conditions on the UC boundaries to obtain a dispersion Eigenvalue Problem (EVP). This strategy allows for the determination of dispersion curves and the characterization of wave propagation in LRM structures.

Generally, there are two modeling approaches to get the dispersion curves. One is the inverse or $\boldsymbol{\omega(\mu)}$ approach in which the real propagation constants $\boldsymbol{\mu}$ are defined and the dispersion EVP is solved to frequencies $\boldsymbol{\omega}$. And the other is the direct or $\boldsymbol{\mu(\omega)}$ approach which imposes the real frequencies $\boldsymbol{\omega}$ and solves the dispersion EVP to propagation constants $\boldsymbol{\mu}$ [77]. The $\boldsymbol{\mu(\omega)}$ approach is well-suited for analyzing one-dimensional periodic structures. However, when dealing with two-dimensional periodic structures, the inverse approach, $\boldsymbol{\omega(\mu)}$, is more commonly used [77].

3.3 Investigation of LRM Modeling and Resonator Damping Effects on Vibration Responses

The preliminary investigation of LRM involved evaluating different modeling techniques and assessing the influence of damping on the vibroacoustic responses. This research aimed to gain insights into the effectiveness and behavior of LRM in reducing vibrations and improving acoustic characteristics.

In the section 3.3.1 the impact of LRM damping on the vibroacoustic responses was investigated. Different damping values were applied to the micro-resonators, and the resulting changes in vibration attenuation and sound power radiation were analyzed. This analysis provided insights into the role of damping in optimizing the performance of LRM solutions and achieving desired vibroacoustic characteristics.

In the section 3.3.2, the focus was on exploring various modeling approaches to accurately represent the LRM system, including the use of shell-plate modeling with point forces to simulate the micro-resonators and full FEM solid modeling for a more detailed representation. Comparisons were made between these modeling techniques to understand their advantages and limitations in capturing the dynamic behavior of the micro-resonators and the overall system.

3.3.1 Micro-resonators Damping Impact on Vibration Response

The investigation was initiated by the modeling of three plate models: a baseline plate, a plate with micro-resonators, and a plate with point masses representing the equivalent masses of the micro-resonators. The dimensions of the plate and the characteristics of the micro-resonators were adopted from the research conducted by Qin et al. [144], and all relevant modeling details can be found in the Table 3.1.

The plate models were implemented using COMSOL 5.6 software. Vibration and acoustic analyses were subsequently performed on each model, and the obtained results were compared against the baseline plate and the plate with point masses. In the plate model incorporating micro-resonators, each individual micro-resonator was represented by a point load, following the expression provided in Equation 3.5. In the Equation, f is the frequency variable, $displacement_{connection-point}$ is the evaluated plate-shell displacement in the resonator point, η is the damping of the resonator, $m_{resonator}$ is the mass of the resonator and $k_{resonator}$ is the stiffness of the resonator.

Two types of micro-resonators were considered, type 1 micro-resonators tuned for 200 Hz ($m_1 = 0.020kg$ and $k_1 = 3.2 \cdot 10^4 N//m$) and type 2 micro-resonators tuned for 300 Hz ($m_2 = 0.014kg$ and $k_2 = 5.0 \cdot 10^4 N//m$). The two types of micro-resonators were assembled in intercalated rows, starting with a type 1 micro-resonators row. The evaluations of the plate models were performed within a frequency spectrum up to 500 Hz.

Symbol	Description	Value
m_{R1}	Mass of the resonator $R1$	0.020 kg
k_{R1}	Spring stiffness of the resonator $R1$	3.2×10^4 N/m
m_{R2}	Mass of the resonator $R2$	0.014 kg
k_{R2}	Spring stiffness of the resonator $R2$	5×10^4 N/m
a_L	Lattice constant	0.05 m
h_p	Thickness of the base plate	0.003 m
a	Length of the finite base plate	0.8 m
b	Width of the finite base plate	0.5 m
F_0	Amplitude of excitation force	1 N
(x_0, y_0)	Force position on the finite base plate	(0.1 m, 0.1 m)

Table 3.1: Micro-resonators properties, plate dimensions and study details [144].

$$F_{resonator} = \frac{(2\pi f)^2 \cdot m_{resonator} \cdot displacement_{connection-point}}{\left(\frac{(2\pi f) \cdot m_{resonator}}{(1+i \cdot \eta) k_{resonator}} - 1\right)} \tag{3.5}$$

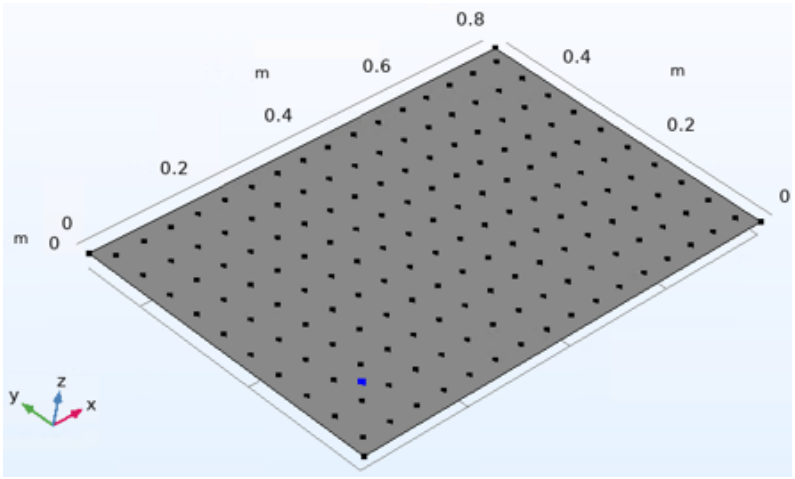

Figure 3.2: Plate with point forces representing the micro-resonators (black points) and a point load excitation (blue point), modelled in COMSOL 5.6.

Considering that the introduction of micro-resonators in the plate results in an increase in mass, it is essential to assess the impact of this additional mass on the vibroacoustic behavior of the plate. The increased mass and different mass distribution alter the plate's eigenmodes and shift them across the frequency spectrum. To investigate this effect, a comparison of vibration responses was conducted between the original plate and the plate with point masses representing the mass of the micro-resonators. The results of this comparison are depicted in Figure 3.3. As expected, the introduction of the additional mass causes the response peaks to shift.

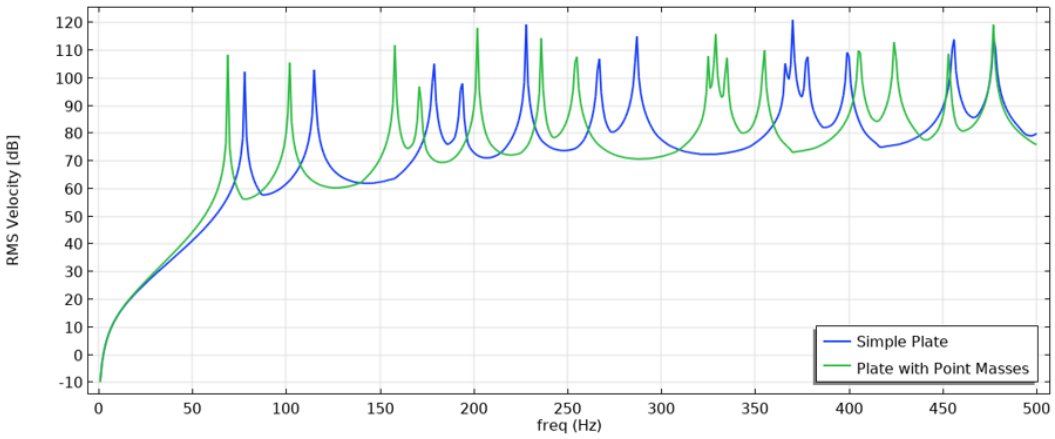

Figure 3.3: Comparison of RMS velocity results between the original plate and the plate with point masses (same mass as the micro-resonators).

The Figure 3.4 depicts the comparison of vibration responses between the plate with point masses (equivalent to the micro-resonators' mass) and the plate with two groups of micro-resonators. Notably, two significant attenuations were observed at the frequencies where the micro-resonators were specifically tuned, namely at 200 Hz and 300 Hz. Furthermore, it is evident that the vibration response is affected beyond the micro-resonators' resonance frequencies.

The changes in the vibration response below 125 Hz are minimal, primarily resulting in slight amplitude variations in the RMS velocity peaks of the plate. However, as the frequency surpasses this threshold, the alterations in the vibration response become more pronounced and evident in the plot. It is important to note that these changes are not solely attributed to the added mass, as the comparison is made with a plate having the same mass distribution, but rather arise due to the dynamic influence of the resonating mechanisms induced by the presence of the micro-resonators.

The Figure 3.5 illustrates the RMS velocity results obtained from the plate with two groups of micro-resonators, where different damping values were applied to the micro-resonators. The graph demonstrates that increasing the damping of the micro-resonators leads to a broader attenuation across the frequency spectrum, while the magnitude of the attenuation peaks is reduced. It is important to note that the increase in damping significantly attenuates all the RMS velocity peaks within the considered spectrum, except the two peaks below 100 Hz, which exhibit only a slight reduction. This behavior is related to the system's increased global damping.

Figure 3.6 presents a comparison of RMS velocity results between the original plate and the plate with two groups of micro-resonators featuring different damping values. The figure provides clear evidence that incorporating micro-resonators with damping in the plate leads to a substantial and wide-ranging attenuation of vibration

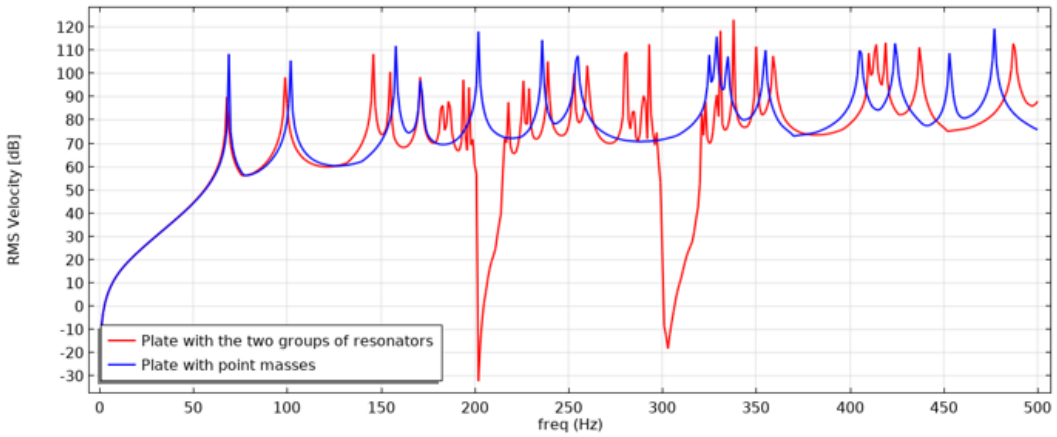

Figure 3.4: Comparison of RMS velocity results between the plate with point masses (same mass as the micro-resonators) and the plate with two groups of micro-resonators.

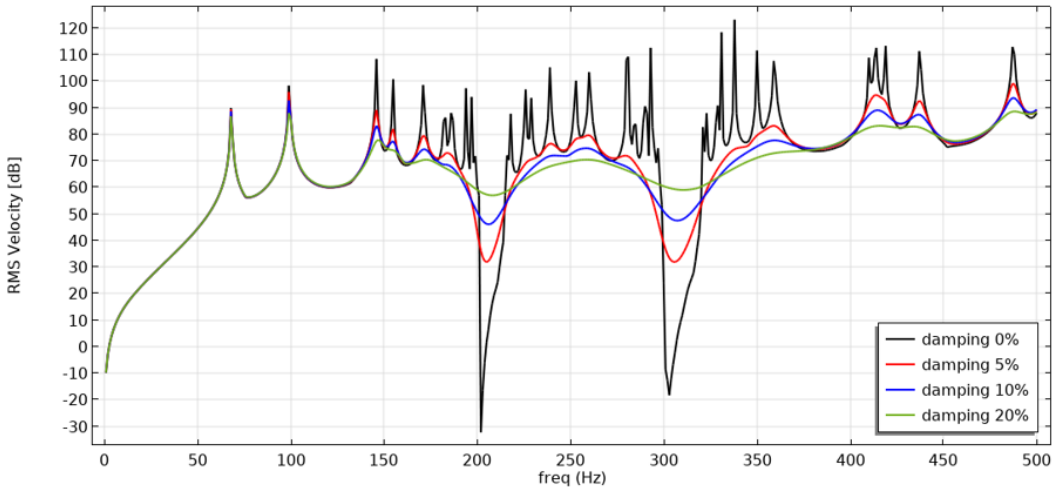

Figure 3.5: Comparison of RMS velocity results between the plate with two groups of micro-resonators with different values of damping of the micro-resonators.

across the entire frequency spectrum being considered.

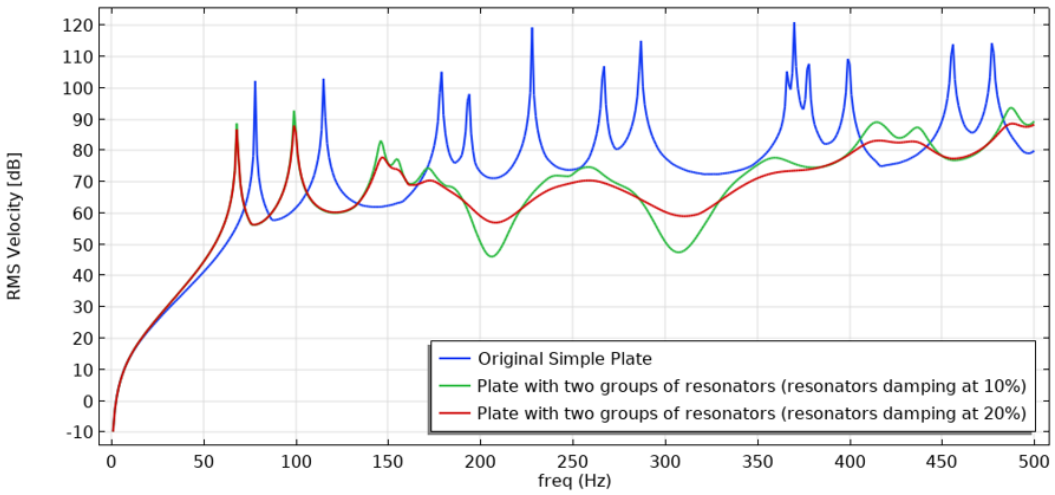

Figure 3.6: Comparison of RMS velocity results between the original plate and the plate with two groups of micro-resonators with different values of damping of the micro-resonators.

In order to evaluate the noise emission associated with the vibration responses, structural-acoustic models were developed. Three models were created: one for the baseline plate, another for the plate with micro-resonators without damping, and a third model for the plate with micro-resonators having a damping of 10%. For all models, the sound power radiated was evaluated by integrating it over a hemisphere using Equation 1.15. Similar approach to the one described in the section 2.3.1.

The comparison of results between the original plate and the plate with two groups of micro-resonators is presented in Figure 3.7 for the case of micro-resonators without damping. It is evident that the presence of resonators without damping introduces numerous additional peaks in the radiated sound power across the considered frequency spectrum. This behavior is attributed to the dynamic characteristics of the micro-resonators, as observed in the previous Figure 3.4 for the evaluation of RMS velocity. Additionally, Figure 3.7 reveals two dips in the sound emission response at the frequencies where the micro-resonators are tuned. However, it is important to note that the introduction of micro-resonators without damping does not lead to a reduction in noise emission levels across the entire frequency spectrum.

In Figure 3.8, the results for the case of micro-resonators with 10% damping are depicted. It can be concluded that an increase in damping is beneficial for achieving a broad attenuation of the sound power radiated. This underscores the importance of damping in the micro-resonators within an LRM solution to effectively reduce vibration levels across a significant frequency range.

In this preliminary investigation, the impact of micro-resonators' damping on the vibration responses was explored. Multiple models were created, each assigned different damping values for the micro-resonators, in order to observe the corre-

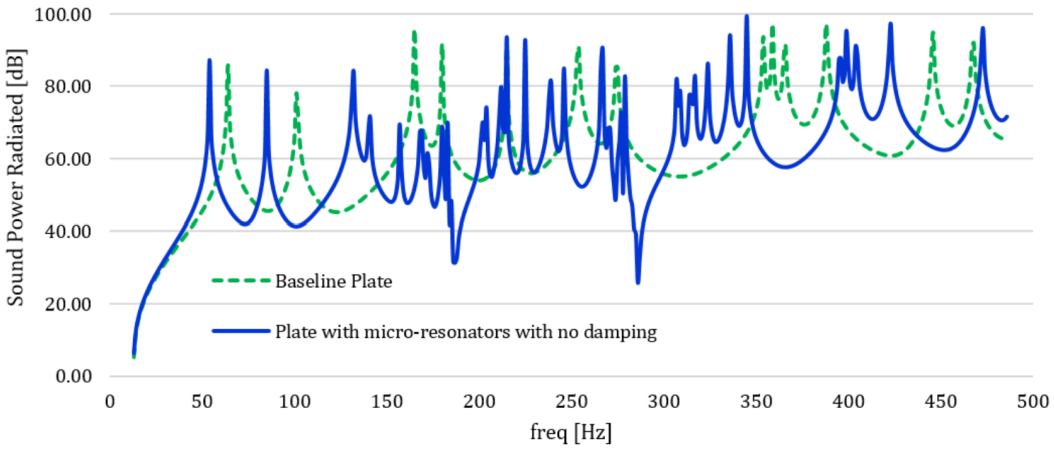

Figure 3.7: Comparison of sound power radiated results between the original plate (dashed green) and the plate with two groups of micro-resonators with no damping on the micro-resonators (blue).

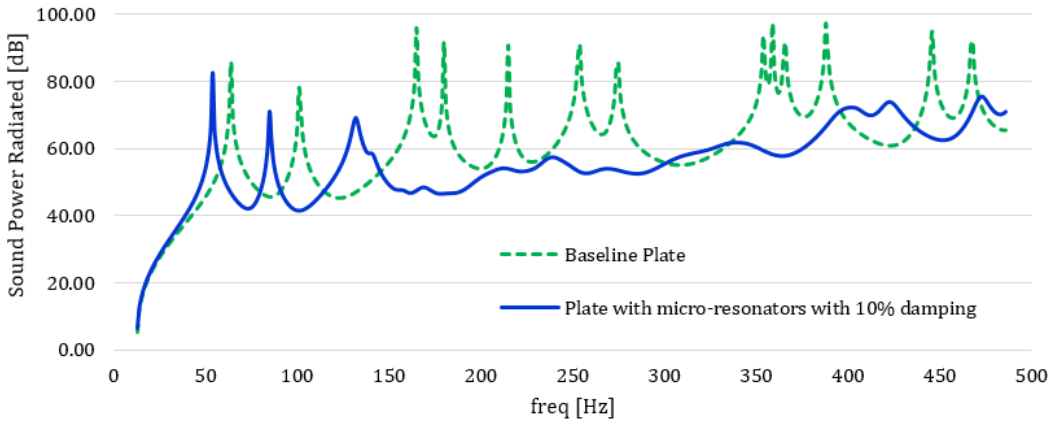

Figure 3.8: Comparison of sound power radiated results between the original plate (dashed green) and the plate with two groups of micro-resonators with 10% damping on the micro-resonators (blue).

sponding impact on vibration attenuation across the frequency spectrum. Increasing the damping resulted in broader attenuation and reduced magnitude of the peaks, indicating the importance of damping in improving the vibroacoustic behavior of the plate.

Furthermore, the noise emission associated with the vibration responses was investigated. Structural-acoustic models were developed to assess the sound power radiated by the plates. Comparative analyses were performed between the original plate and the plate integrated with micro-resonators, considering scenarios with and without damping. The results indicated that the introduction of micro-resonators, without any damping, resulted in attenuation within the frequency regions where the micro-resonators were tuned. However, it also caused additional sound power radiation peaks across the frequency spectrum. On the other hand, when damping was incorporated in the micro-resonators, notable benefits were observed. The inclusion of damping facilitated broadband attenuation of the sound power radiated, contributing to a more favorable acoustic performance. These findings emphasize the importance of considering the damping characteristics to effectively manage noise emission and improve the overall acoustic behavior of the system.

Finally, it is acknowledged that there is a need to further explore the modeling techniques for LRM solutions. These first studies used a shell-plate modeling approach with point forces representing the micro-resonators. This approach was chosen for its simplicity and computational efficiency. However, there are alternative methods that can be explored to refine the modeling and better capture the behavior of LRM solutions.

3.3.2 Comparison between different of micro-resonators modeling alternatives

In this section, a comparative analysis was conducted between two types of modeling approaches: shell-plate modeling with point forces representing the micro-resonators, and full FEM solid modeling of the plate and micro-resonators. The aim is to gain insights into the advantages and limitations of each modeling approach, facilitating informed decisions regarding the most appropriate modeling technique for the research of LRM solutions in gearbox housings.

A solid LRM UC was developed to perform the comparison, as illustrated in Figure 3.9. The UC comprised two micro-resonators, each designed to resonate at a specific frequency. One micro-resonator had its first eigenmode (bending mode) tuned for 200 Hz, while the other was tuned for 300 Hz. The micro-resonators were constructed using PMMA for the spring part and steel for the mass part in the tip of the micro-resonant structures.

In the 3D solid modeling approach, the masses of the micro-resonators were kept consistent with those used in the shell-plate modeling with point forces. This ensured that the overall mass distribution of the micro-resonators was maintained across both modeling techniques. In terms of the design of the spring components of the micro-resonators, specific considerations were made to achieve the desired

stiffness required for tuning the resonant frequencies. This was achieved by adjusting the length of the beam section in the micro-resonators. Through the modification of the dimensions of the spring parts, the desired resonance frequencies were attained.

The plate with micro-resonators was modelled by the periodic repetition of the UC illustrated in Figure 3.9. The plate with the micro-resonators modeled with solid FEM is seen in the Figure 3.10. The UC was repeated 9 times in x-direction and 10 times in y-direction. This model allowed to represent a solid FEM LRM plate for the vibration response comparison with the previous plate with point forces model.

In order to provide a more comprehensive analysis and to better capture the differences in the vibration response, a wider frequency spectrum up to 3000 Hz was considered. Figure 3.11 presents the RMS velocity plots of the plate with two groups of micro-resonators, considering both the shell-plate modeling with point forces and the 3D solid FEM modeling. In both approaches, no damping was considered for the micro-resonators.

The resonant attenuations associated with the first bending mode of the micro-resonators were accurately captured by both modeling techniques. As depicted in Figure 3.11, these resonant attenuations were observed in the frequency ranges of 200-230 Hz and 295-322 Hz. However, notable differences were observed in the higher frequency response. The response peaks were predicted differently, with lower vibration levels in the solid FEM modeling.

Additionally, the 3D solid FEM model successfully captured additional attenuations corresponding to the other eigenmodes of the micro-resonators. These attenuations were observed in the frequency ranges of 343-357 Hz (type 1 micro-resonator's 2nd eigenmode), 508-529 Hz (type 2 micro-resonator's 2nd eigenmode), 1260-1282 Hz (type 1 micro-resonator's 4th eigenmode), 1990-2050 Hz (type 2 micro-resonator's 4th eigenmode), and 2657-2722 Hz (type 1 micro-resonator's 5th eigenmode). The mode shapes for the first five eigenmodes for both micro-resonators are depicted in the Figure 3.12.

By introducing 10% damping to the micro-resonators, the differences in the vibration response across the spectrum became even more pronounced, as shown in Figure 3.13. Once again, the resonant attenuations associated with the first bending mode of the micro-resonators were accurately captured by both modeling approaches. However, the 3D solid FEM modeling successfully captured the broadband attenuation, while the shell-plate modeling with point forces did not capture this behavior.

It is important to note that these additional attenuations are dependent on the geometry of the micro-resonators and, in conjunction with the damping, are responsible for the broadband attenuation observed over the wider frequency spectrum. The results highlight the importance of accurately modeling the micro-resonators and their corresponding eigenmodes in order to effectively capture the broadband attenuation of vibrations. The solid modeling technique allows for a more detailed representation of the LRM physical structure, capturing its behavior more accurately.

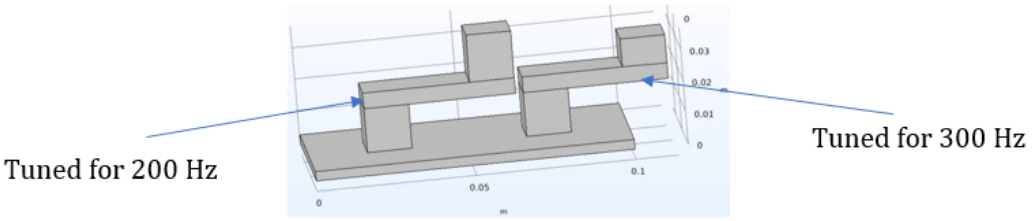

Figure 3.9: LRM UC with two micro-resonators, one tuned for 200 Hz and the other tuned for 300 Hz.

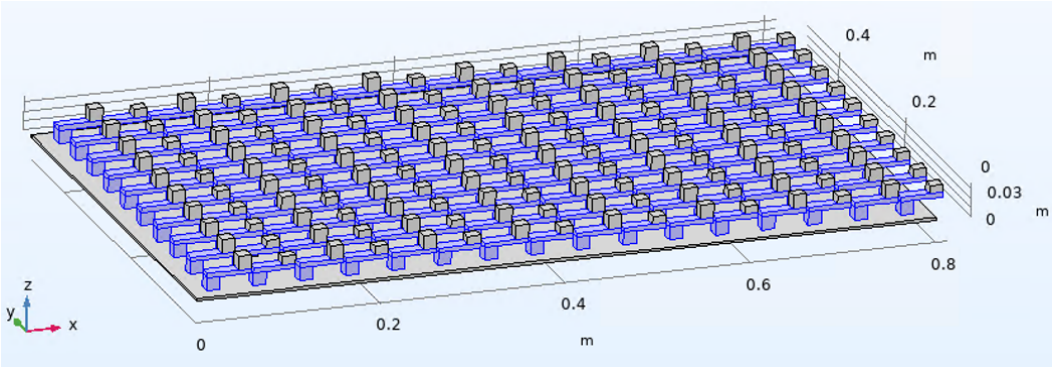

Figure 3.10: Plate with two groups of micro-resonators, one tuned for 200 Hz and the other tuned for 300 Hz.

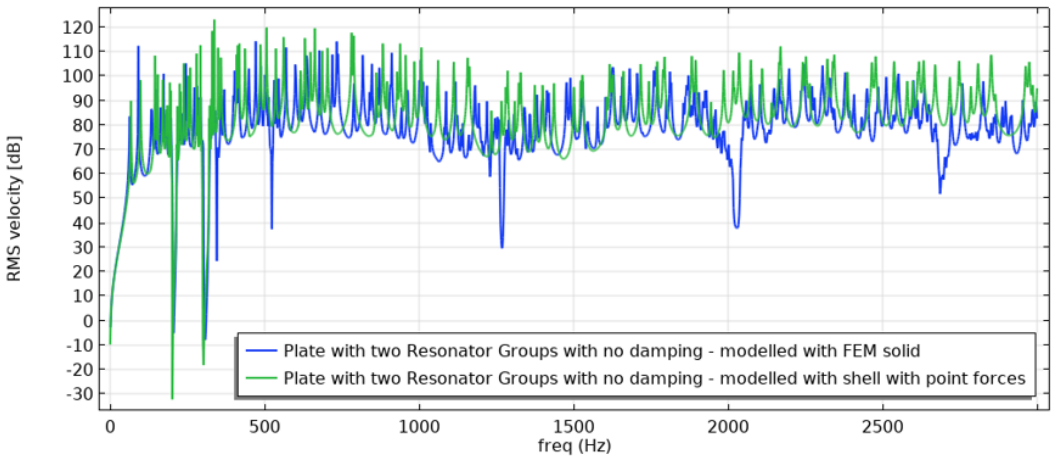

Figure 3.11: Comparison between the RMS velocity of the plate with two groups of micro-resonators considering the two modeling approaches, micro-resonators with no damping.

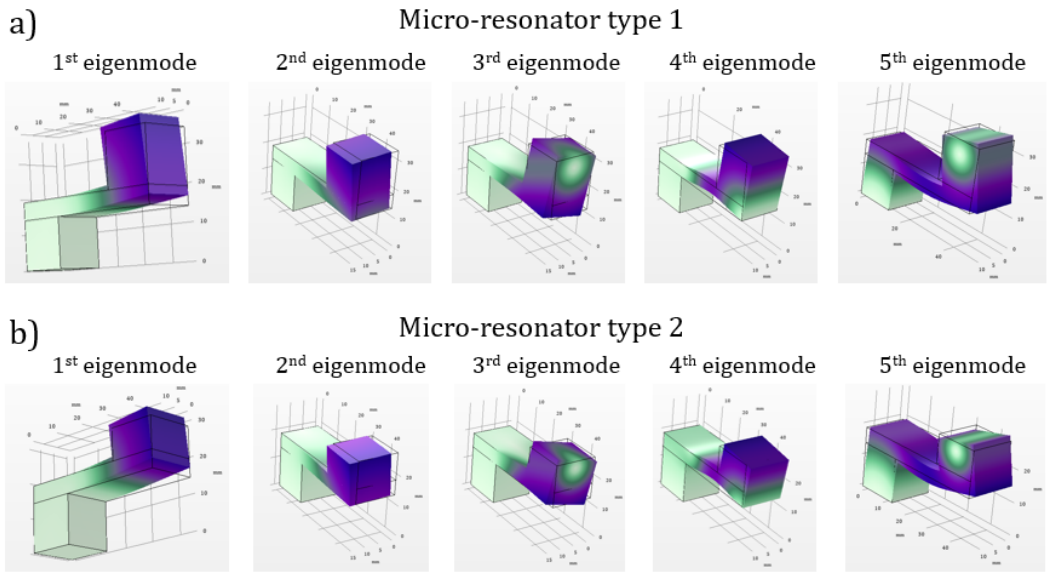

Figure 3.12: a) Mode shapes for the first five eigenmodes for micro-resonator type 1; b) Mode shapes for the first five eigenmodes for micro-resonator type 2.

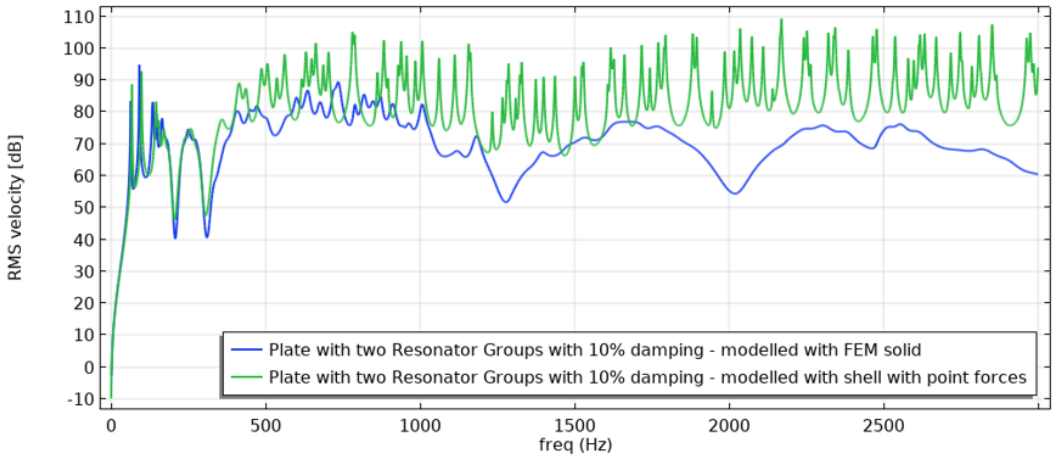

Figure 3.13: Comparison between the RMS velocity of the plate with two groups of micro-resonators considering the two modeling approaches, micro-resonators with 10% damping.

3.4 GBH Locally Resonant Metamaterial Solutions

3.4.1 First GBH Locally Resonant Metamaterial Solution

As emphasized in the literature review, it is challenging to attenuate low-frequency peaks using traditional noise and vibration reduction techniques [65]. This is the case of the noise emission peak observed at 425 Hz for the lightweight version of the housing, see Figures 2.18 and 2.19. One promising approach to address this challenge is by introducing vibroacoustic LRMs. Thus, this section investigates simple and cost-effective LRM solutions that can enhance the NVH characteristics of GBHs.

The initial step of the study was to determine the appropriate location for applying the LRM solution. As demonstrated in Figure 2.18, the sound power radiated peaks in the lower frequency region are caused by the vibration of the top plate of the lightweight GBH. Therefore, in this study, an LRM solution was applied to the top plate to reduce the vibration at these frequencies. Similarly, in more complex industrial GBHs, it is crucial to apply the LRM solutions in positions where the vibration levels are high at these low frequencies, typically corresponding to areas with lower stiffness.

Due to the simple geometry of the considered GBH, it is possible to clearly identify the mode shape of the corresponding peak at 425 Hz, which corresponds to the first local eigenmode of the top plate. So in this specific case, it would be possible to optimize the LRM mass distribution over the top plate (for example, mass concentration in the plate center). However, in an industrial GBH, optimizing the LRM mass distribution would not be a simple task, as highlighted in the literature review. For that reason, a constant mass distribution LRM solution was employed in this study to showcase that simple and fast design solutions are possible to be introduced in the GBHs, without spending excruciating time in the design phase and without reaching highly complex LR distributions, which would entail high costs. Even though it is known a priori that the LRM solution might be suboptimal.

As seen in the LR metamaterial literature review, the LRM solution is expected to provide not only the useful attenuation in the low-frequency region where they are tuned to, but also a considerable broadband attenuation. The broadband attenuation is originated from the structural damping associated with the LRM [187, 168, 37, 65].

For the first LRM solution to be applied in the lightweight GBH, a UC size of 20 mm x 20 mm was considered. Given that the top plate dimensions are 204 x 190 mm, it is possible to fit 90 UCs in a rectangular pattern. The bibliography contains several distinct types of micro-resonator designs with various geometries and resonant mechanisms [136, 35, 203, 148, 195, 49, 30, 147]. In this case, a simple micro-resonator geometry was considered, based on the same resonant mechanism of the micro-resonators presented in [35, 148, 195, 49, 30], see Figure 3.14. The micro-resonator consists of an acrylic part and a steel mass on the top. The up-and-down vertical movement of the micro-resonators mass will dynamically absorb

the vibrational energy of the host structure, damping the bending waves on the structure.

The material characteristics of the acrylic polymer (PMMA) examined within this study are detailed in the Table 2.3. The material properties of the steel are stated in the Table 2.1. Even for a micro-resonator with a simple geometry, there are several design variables to be controlled [136, 110, 203]. For this micro-resonator design, several dimensional parameters must be defined, such as its width, the length/thickness of the flexible part and the dimensions of the mass part.

The proposed resonating UC has two main advantages. First, it is prone to application on the outside of the GBH without requiring a structural redesign, making it a viable solution for dealing with specific NVH problems encountered even during the final stages of industrial design. The second advantage relates to its easy frequency tuning. The frequency tuning of a micro-resonator is performed using the relation between the natural frequency and parameters of a vibration system. The micro-resonator spring part affects mainly the stiffness (k), and the concentrated mass part affects the mass (m). The following methods can be used to decrease the stiffness of the micro-resonator: decrease the thickness of the micro-resonator spring part; increase the length of the micro-resonator spring part; change the shape of the micro-resonator spring part, for example, by the inclusion of slits in the micro-resonator spring part. Opposite methods can be used to increase the stiffness of the micro-resonator. The mass of the micro-resonator can be adjusted simply by changing the concentrated mass (changing the mass dimensions or changing the material). Using these relations, it is possible to tune the frequency band where the vibration is highly attenuated.

Jung et al. [81] and Claeys et al. [34] stated additional properties that an LRM should have in practical engineering applications, for example, its manufacturability, its compatibility, and its sub-wavelength scale characteristics. Regarding manufacturability, the proposed micro-resonator spring part can be manufactured by AM, and the mass part of the micro-resonator can be bonded to the spring part by adhesive bonding. The micro-resonator design can also be easily adapted for mass production, as shown in 2019 by Yu et al. [195]. The resonator was designed by changing its dimensions within the design limits, taking into consideration the following objectives:

1. Tuning the first eigenfrequency (bending mode) of the micro-resonator to the desired hard-to-tackle low frequency;

2. Maximize the ratio of the modal mass of the micro-resonator's first eigenmode by the total mass of the micro-resonator;

3. Minimize the nonessential mass addition, since lightweight design is the goal, the total mass added by the micro-resonator should be minimized (e.g., minimize the mass of the bending beam part of the micro-resonator).

Aiming for the previously stated objectives, and defining the tuning eigenfrequency of 425 Hz, a micro-resonator width of 16 mm was defined, the PMMA

(acrylic) base was defined as a square cross-section of 4×4 mm, the PMMA beam was defined with a thickness of 1 mm and a length of 14.547 mm, and finally the steel mass was defined as a square cross-section of 4×4 mm.

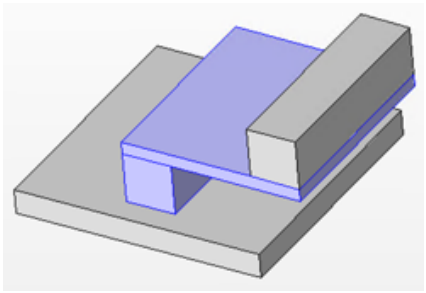

Figure 3.14: UC with micro-resonator: PMMA part (blue) and steel part (grey).

According to the reasons mentioned in the section 3.2, an inverse approach was followed to calculate the dispersion curves. The wave vector components, k_x and k_y, were spanned to obtain the corresponding eigenfrequencies. To perform this analysis, the IBC was established based on the diagram shown on the Figure 3.15 (b).

In order to cover the entire IBC, an auxiliary variable k was introduced, which varied from 0 to 4. The variation of k allowed for the systematic exploration of different regions within the IBC. Specifically, for k values ranging from 0 to 1, the wave vector $\mathbf{k} = (k_x, k_y)$ spanned from $(0, 0)$ to $(\pi/al, 0)$, where al represents the side length of the constitutive UC. Similarly, for k values ranging from 1 to 2, the wave vector $\mathbf{k} = (k_x, k_y)$ spanned from $(\pi/al, 0)$ to $(\pi/al, \pi/al)$. The ranges of $\mathbf{k}$ for k values from 2 to 3 and from 3 to 4 followed the patterns $(\pi/al, \pi/al)$ to $(0, \pi/al)$ and $(0, \pi/al)$ to $(0, 0)$ respectively.

By systematically varying the wave vector components within the IBC, the dispersion curves were obtained, providing insights into the relationship between the eigenfrequencies and the wave vectors for the considered LRM arrangement. In Figure 3.15 (b), the dispersion curves for the LRM UC are presented, while Figure 3.15 (a) displays the dispersion curves for a simple plate case with identical dimensions, serving as a basis for comparison.

Both graphs exhibit bending and shear wave propagation curves. The presence of the micro-resonator in the UC introduces discontinuities in the bending wave propagation. A complete BG is found between 425 Hz and 474 Hz, which is created by the up-and-down movement of the micro-resonator mass, which dampens the vibration of the structure and dissipates the vibrational energy. This behavior is crucial, as the BG acts as a vibration barrier for specific frequency ranges, preventing the transmission of unwanted vibrations and noise through the structure.

Figure 3.16 displays the lightweight gearbox housing incorporating the LRM solution, with a zoomed-in view highlighting the placement of the micro-resonators within the LRM assembly. This particular LRM configuration is referred to as LRM1.

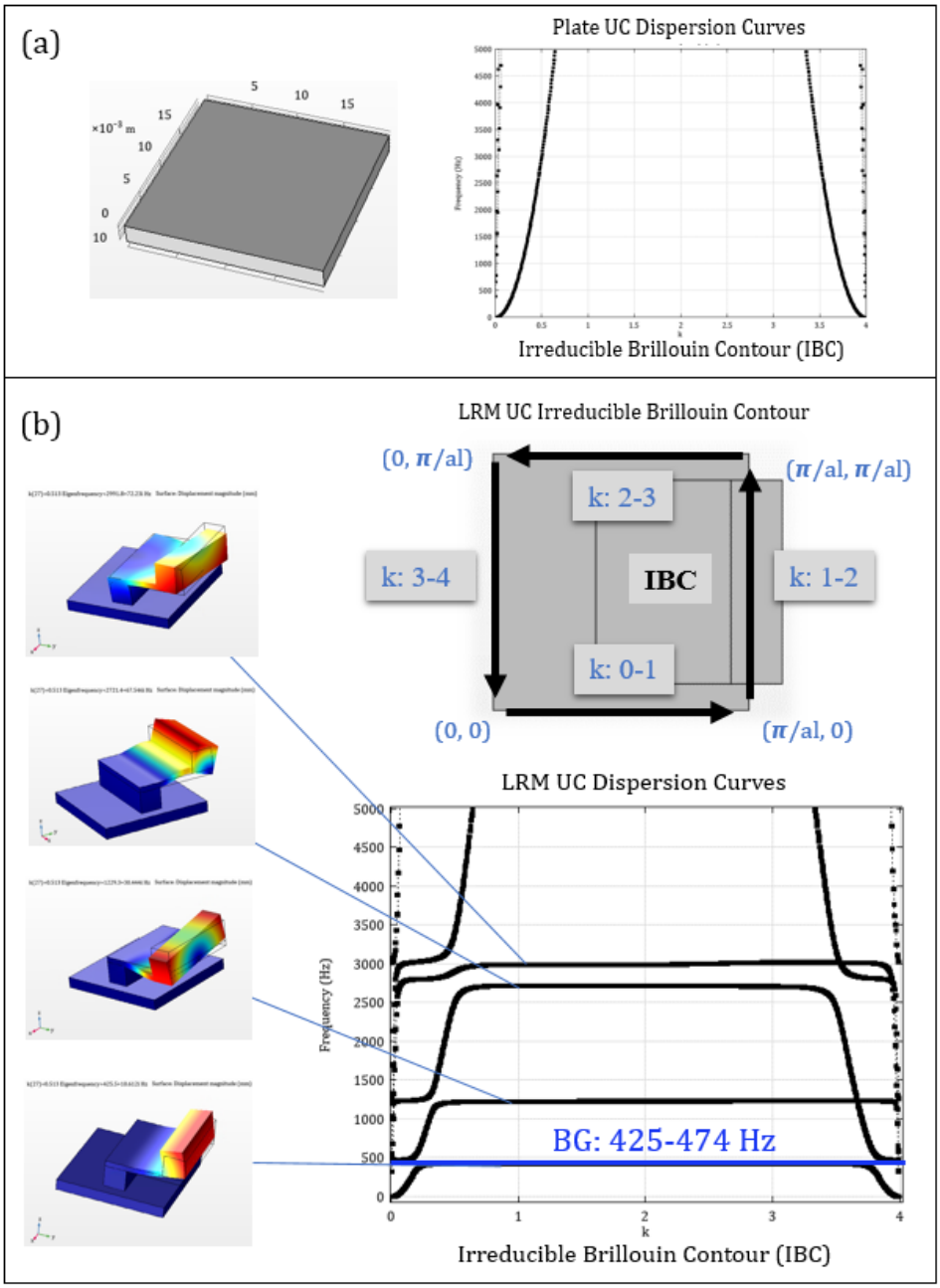

Figure 3.15: (a) Dispersion curves for a simple plate with the dimensions of the UC; (b) Dispersion curves for the LRM UC including the IBC definition and illustrations of the UC eigenmodes.

To quantify the mass addition resulting from the LRM implementation, it is important to consider the masses of the original GBH and the lightweight GBH. The original GBH has a mass of 10.98 kg (including the bearings part), while the lightweight GBH weighs 8.87 kg (including the bearings part), resulting in a reduction of 2.10 kg (equivalent to a 20% reduction).

In the LRM1 solution, the added mass contributed by all the micro-resonators is only 0.232 kg, representing a mere 2.6% increase relative to the mass of the lightweight GBH. It is noteworthy that the introduction of LRM in this configuration results in a minimal mass addition compared to the previously achieved mass reduction. Despite the slight increase in mass due to the LRM implementation, the total mass of the lightweight GBH still exhibits a significant reduction of over 17% compared to the original GBH mass. The LRM technology offers a promising approach since its application can maintain the lightweight design.

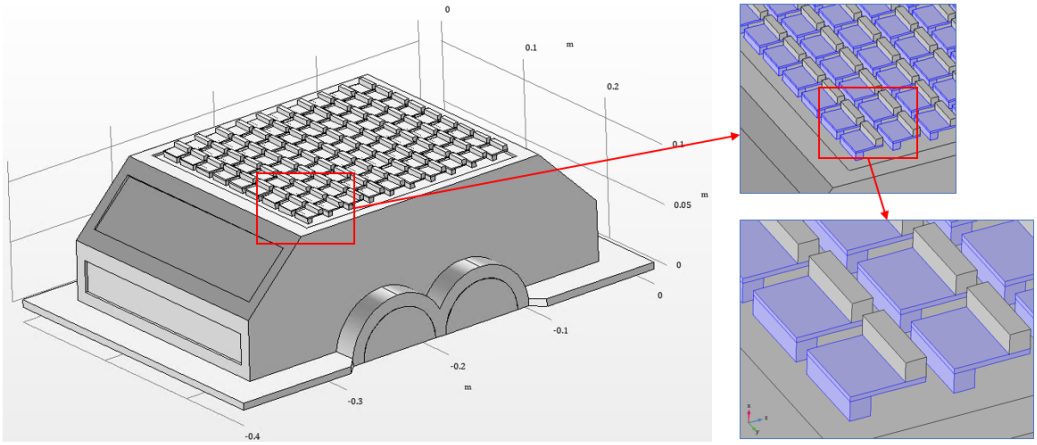

Figure 3.16: Lightweight GBH with LRM1 solution applied in the top of the GBH.

Numerical simulations were conducted to compute the sound power radiated by the lightweight gearbox housing with the LRM1 solution applied under the same loading conditions described in Figure 2.15. The setup for these simulations remained consistent with the description provided in the section 2.3. The structural-acoustic model employed for the analysis of the lightweight GBH with the LRM1 solution consisted of a total of 982855 elements. The elements exhibited an average quality of 64% and a minimum quality of 15%, indicating the suitability of the mesh used in the model.

In the model, the acoustic-structure boundary connection was extended to encompass all the micro-resonators, as illustrated in Figure 3.17. This comprehensive approach allows for the consideration of noise emission resulting from the vibration of the micro-resonators themselves during the simulation. While simplified LRM studies in the literature often overlook this aspect, incorporating it into the model leads to more realistic and accurate results.

The comparison of results among the original GBH, the lightweight version of

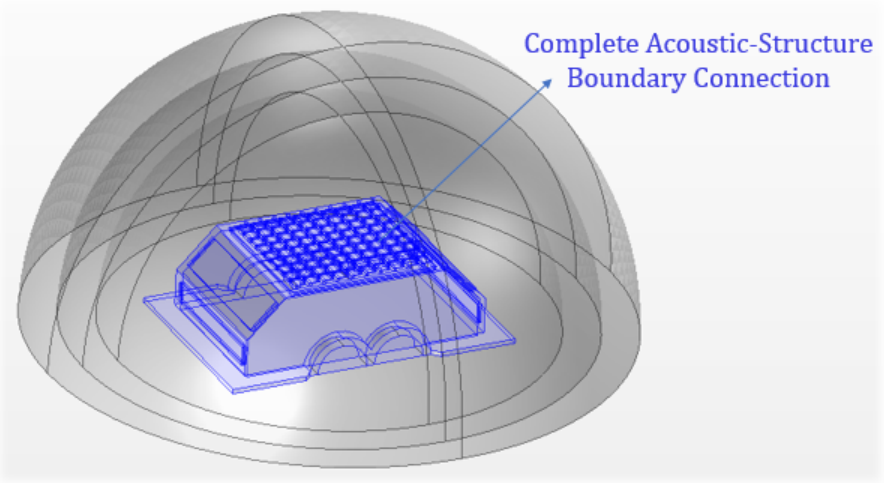

Figure 3.17: Structural-acoustic model used for analysis of the lightweight GBH with the LRM1 solution.

the GBH, and the lightweight GBH with the LRM1 solution applied is presented in Figure 3.18. The results confirm the attenuation of the predicted BG between 425 Hz and 474 Hz.

The introduction of the LRM1 solution in the housing leads to a reduction in the sound power radiated peak at 425 Hz, exhibiting a behavior similar to that of a TMD. The presence of the micro-resonators effectively decreases the original peak at 425 Hz and introduces two additional smaller peaks in close proximity, one at 330 Hz and another at 575 Hz. Furthermore, as previously discussed, the LRM1 solution provides broadband attenuation of the sound power radiated across the analyzed spectrum. A significant reduction of the sound radiation peaks is noticeable in Figure 3.18.

These results demonstrate the effectiveness of the LRM1 solution in attenuating the sound power radiated by the lightweight GBH. By introducing the LRM1 solution, the housing exhibits improved acoustic performance, reducing specific peaks and providing overall noise reduction across a wide frequency range.

In order to ensure an objective comparison, the sound power radiated results were normalized by dividing them by the power injected into the structure. The ratio of the sound power radiated to the power injected in the structure was calculated using Equation 1.18 for the three configurations. The total power injected was calculated by the summation of the power injected in each bearing, according to the Equation 2.23. The power injected for each bearing was determined through integration over the area of load application, as expressed in Equation 1.17.

The comparison of the ratio of the sound power radiated to the power injected in the structure, including the lightweight GBH with the LRM1 solution applied, is depicted in Figure 3.19. The normalized results exhibit the same trends as the nominal results for the sound power radiated. This indicates that the LRM1 solution

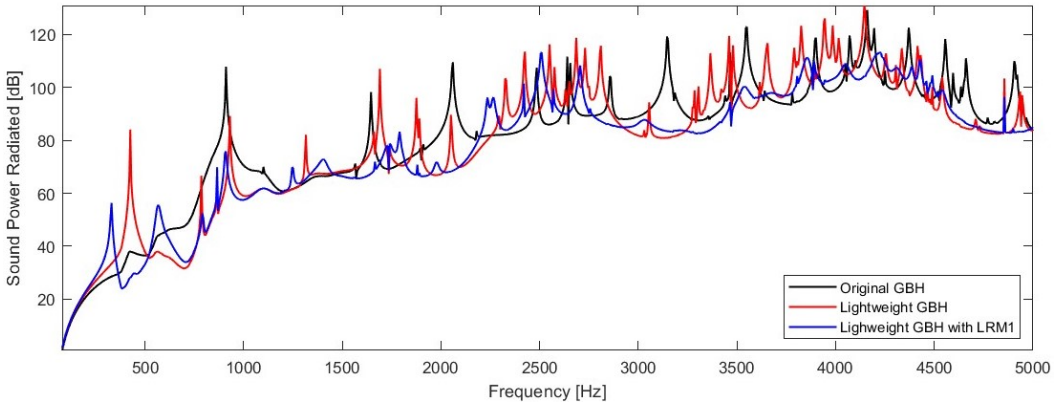

Figure 3.18: Sound power radiated comparison between the original GBH (black), the lightweight version of the GBH (red) and the lightweight GBH with the LRM1 solution applied (blue).

effectively reduces the sound power radiated relative to the injected power. These findings underscore the potential of the LRM1 solution in achieving noise reduction in practical GBH applications.

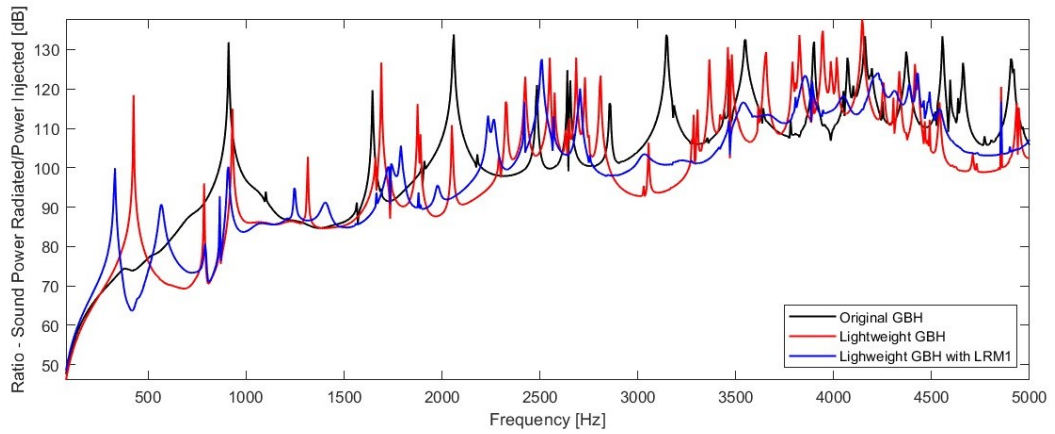

Figure 3.19: Ratio between the sound power radiated and the power injected in the structure of the original GBH (black), the lightweight GBH (red) and the lightweight GBH with the LRM1 solution applied (blue).

3.4.2 Second GBH Locally Resonant Metamaterial Solution

A second LRM solution was developed, consisting of an LRM with two groups of intercalated micro-resonators. This solution was designated LRM2. One group comprises micro-resonators similar to the previously described ones, as shown in Figure 3.14. The second group consists of micro-resonators with similar architecture but different dimensions, such that their first eigenfrequency (bending mode) is

tuned to another frequency. For this case, a frequency of 870 Hz was selected to create an additional BG coinciding with the region of the other peaks at lower frequencies.

The dimensional changes implemented were as follows: the length of the PMMA beam was adjusted to 12 mm, and the cross-section of the steel mass was modified to 3 (length) × 2.6953 (height) mm. Using the same dispersion curve analysis method described earlier in the section 3.2, a BG was achieved between 870 Hz and 925 Hz. The two groups of micro-resonators were assembled in intercalated lines, as illustrated in Figure 3.20. The total mass added by the two groups of micro-resonators was 0.185 kg, corresponding to a 2.1% increase relative to the mass of the lightweight GBH. The incorporation of the second group of micro-resonators demonstrates the flexibility and versatility of the LRM concept in customizing the solution to target multiple frequency ranges simultaneously, leading to further enhanced noise reduction capabilities.

Numerical simulations were conducted to compute the sound power radiated by the lightweight GBH with the second LRM solution applied, under the same loading conditions, as seen in Figure 2.15, and using the setup described in the section 2.3. The structural-acoustic model for the lightweight GBH with the LRM2 solution consisted of 975,256 elements, with an average quality of 64% and a minimum quality of 8%. The results can be seen in Figure 3.21. Comparing both LRM solutions, the LRM solution with two types of micro-resonators combined shows a higher attenuation of the sound power radiated in the frequency region where the new group of micro-resonators was tuned for, attenuating the peaks in the vicinity. Complementing this remark, the peak at 930 Hz present in the sound power radiated for the first LRM solution is attenuated, as shown in Figure 3.22 that attenuating is due to the movement of the masses of the micro-resonators in the second group. The amplitude of the secondary peak after the first BG, around 500 Hz, was also decreased with the LRM2 solution.

At higher frequencies, both LRM solutions exhibit a comparable trend of attenuation. Nonetheless, there are slight differences in their attenuation characteristics in specific frequency ranges. The solution with a single group of micro-resonators shows slightly higher attenuation in certain frequency ranges, while the solution with two groups of micro-resonators exhibits marginally higher attenuation in other frequency regions.

To assess the effectiveness of the LRM solutions, the ratio of the sound power radiated to the power injected in the structure was again calculated using Equation 1.18 for all the configurations. The total power injected was calculated by the summation of the power injected in each bearing, according to the Equation 2.23. The power injected for each bearing was determined through integration over the area of load application, as expressed in Equation 1.17. The normalized ratios are depicted in Figure 3.23 for the original GBH, the lightweight GBH, the lightweight GBH with the LRM1 solution applied, and the lightweight GBH with the LRM2 solution applied. The normalized results show similar trends to the nominal results for the sound power radiated, indicating that the LRM solutions effectively reduce

Frequency Band [Hz]	LRM1	LRM2
50-5000	85,22%	82,38%
50-1000	89,00%	98,30%

Table 3.2: Relative reduction in the normalized sound power radiated for LRM1 and LRM2.

sound power radiated relative to the injected power.

To compare the effectiveness of the LRM solutions, Table 3.2 provides the relative reduction in normalized sound power radiated for LRM1 and LRM2 in two frequency bands. One is the full spectrum considered (50-5000 Hz) and the other is the lower frequency spectrum (50-1000 Hz). It is evident that the solution with two groups of micro-resonators provides higher noise attenuation in the lower frequency band. On the other hand, the solution with a single group of micro-resonators exhibits higher relative noise attenuation over the entire considered spectrum (50-5000 Hz).

These findings emphasize that the choice of LRM solution design approach can lead to improved attenuation results in specific frequency regions. The choice between solutions depends on the specific frequency range of interest and the desired noise reduction objectives for the GBH application. Nevertheless, it is crucial to note that both LRM solutions demonstrate substantial and comparable attenuation, achieving reductions of over 80% throughout the entire spectrum.

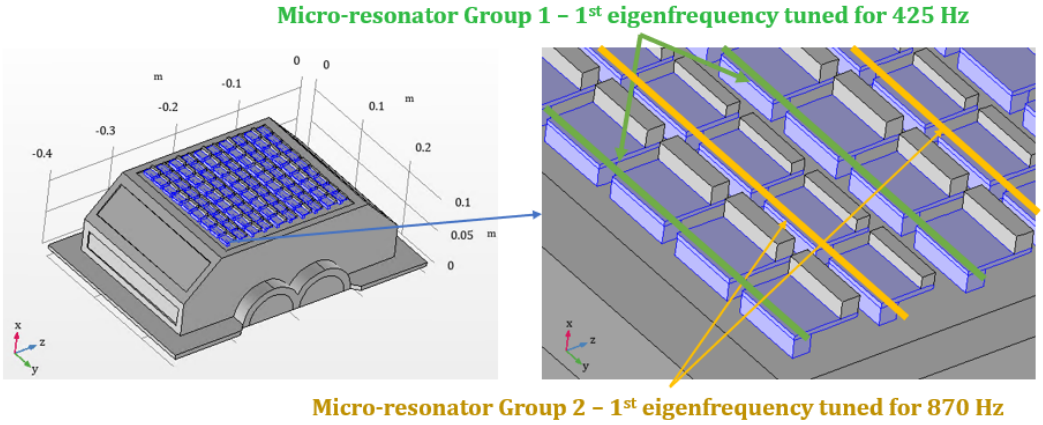

Figure 3.20: Lightweight GBH with LRM solution with 2 groups of micro-resonators applied in the top of the GBH (LRM2).

3.5 Experimental Validation

3.5.1 Experimental Details and Method

The experimental validation of the LRM solution concept for attenuating low-frequency peaks and achieving broadband vibration attenuation was conducted us-

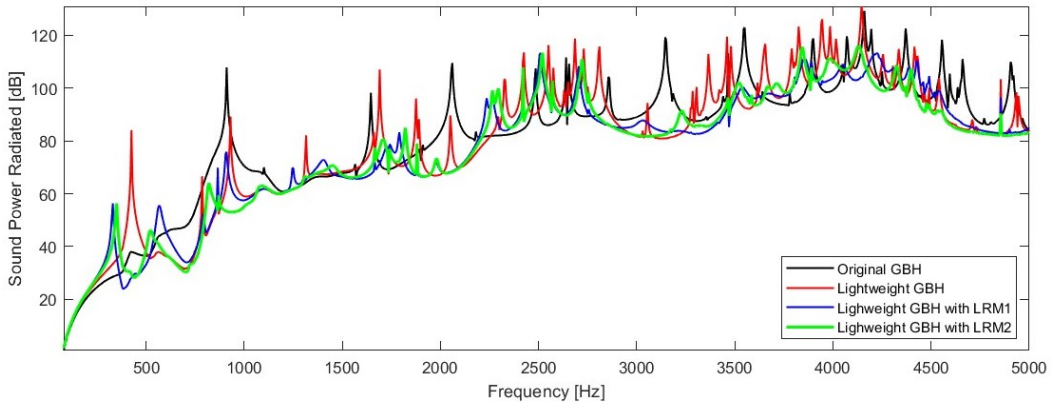

Figure 3.21: Sound power radiated comparison between the original GBH (black), the lightweight GBH (red), the lightweight GBH with the LRM1 solution applied (blue) and the lightweight GBH with the LRM2 solution (green).

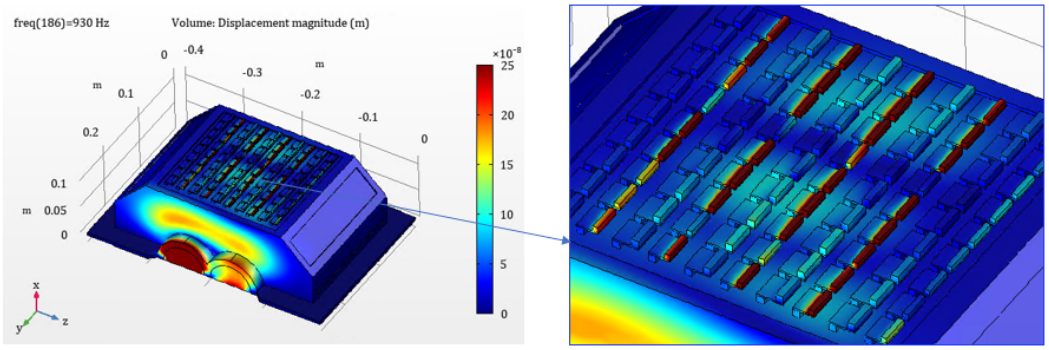

Figure 3.22: Displacement of the lightweight GBH with the LRM2 solution at 930 Hz.

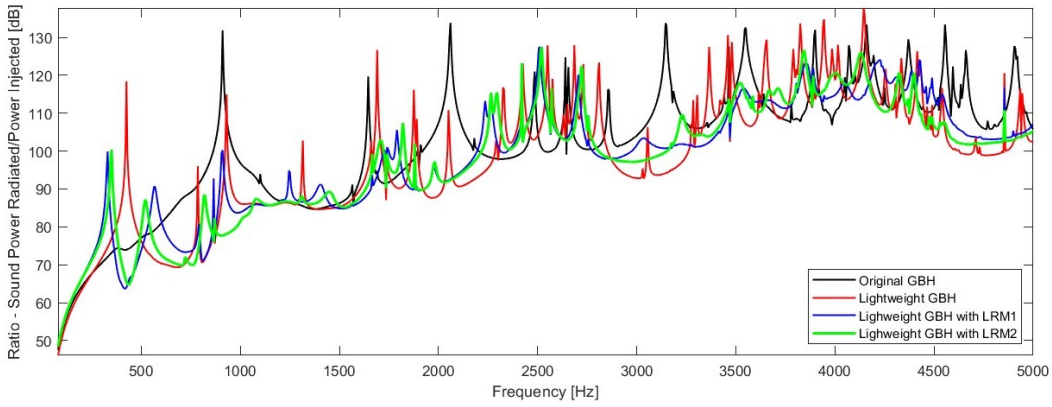

Figure 3.23: Ratio between the sound power radiated and the power injected in the structure of the original GBH (black), the lightweight GBH (red), the lightweight GBH with the LRM1 solution applied (blue) and the lightweight GBH with the LRM2 solution applied (green).

ing an aluminium alloy (AA7075) housing. The material properties of the aluminium alloy (AA7075) are presented in the Table 3.3. The housing, seen in Figure 3.24, was specifically manufactured for this purpose, and detailed geometric information can be found in the appendix B. The design of the manufactured housing incorporates an M4 bolted connection between the top plate and the main structure. This design feature enables easy interchangeability between the baseline configuration and different LRM solution configurations within the GBH. This interchangeability allows for convenient testing and comparison of the performance of LRM solutions in the GBH architecture.

Property	Value	Unit
E	70	GPa
G	24	GPa
υ	0.33	
ρ	2700	kg/m^3

Table 3.3: Material Properties of the Aluminium Alloy (AA7075) [39].

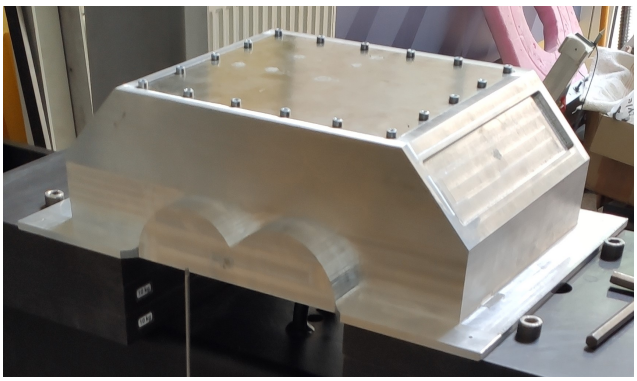

Figure 3.24: Manufactured aluminium alloy (AA7075) housing.

The experimental setup, as depicted in Figure 3.25, was designed to validate the LRM solution concept. The mock-up GBH was connected to the experimental stand using a bolted connection consisting of 14 M6 bolts tightened to a torque of 5.4 Nm. The input force in the mock-up GBH was generated by an electrodynamic shaker Robotron 11076 connected to a 3 mm diameter stinger, measuring 400 mm in length. The input force was applied at the center of the bearing's region and was measured using a PCB Piezotronics ICP dynamic force sensor positioned between the stinger and the housing.

The top plate of the GBH was fastened to the top flange using 18 M4 bolts tightened to a torque of 1.6 Nm. This ensured a secure connection between the top plate and the GBH structure. To measure acceleration, seven positions on the GBH,

as shown in Figure 3.26, were instrumented with accelerometers. The measurement setup included one triaxial accelerometer sensor (I-TEDS model-66A12) and six uniaxial accelerometer sensors (type 4508-B-002). These sensors were connected to two acquisition units (Bruel & Kjaer Type 3050-A-060) linked to an Ethernet switch (Cisco SG300-10MP Managed Switch). The signal time recording was made using Bruel & Kjaer Pulse Recording software, using a 6.4kHz frequency range. Subsequent signal processing and post-processing tasks were performed using the Bruel & Kjaer Pulse Reflex software and MATLAB. This experimental setup enabled the acquisition and analysis of relevant data to evaluate the effectiveness of the LRM solutions in attenuating vibration in the housing.

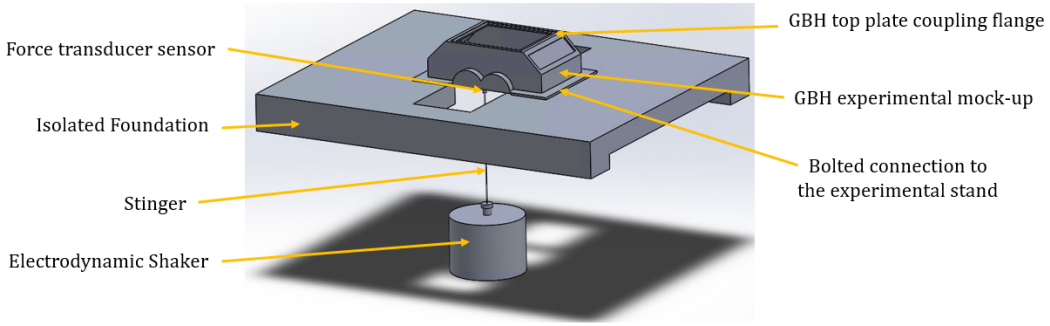

Figure 3.25: 3D illustration of the experimental setup.

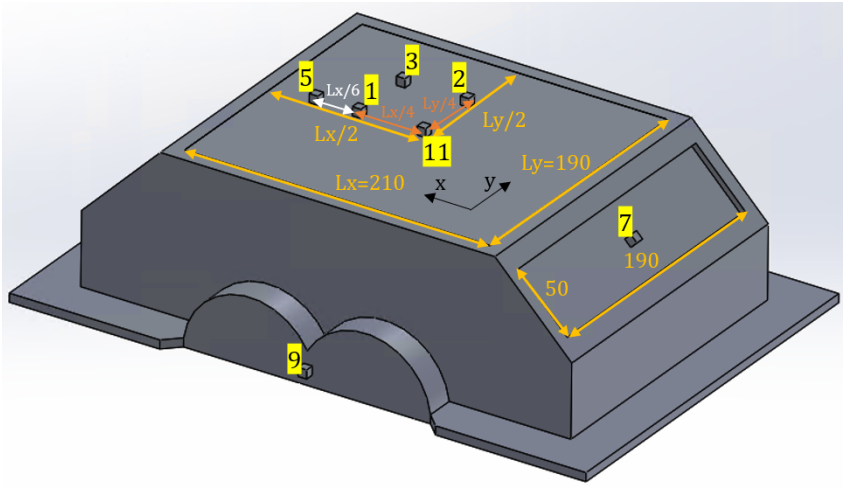

Figure 3.26: Accelerometer sensors positions on the GBH (dimensions in mm).

For experimental validation of the LRM solution concept, the original 2mm aluminium top plate of the manufactured housing was replaced with an LRM plate. The LRM plate was constructed using an aluminium plate with 72 micro-resonators made of ABS and steel. ABS was used for the spring part of the resonator, instead of the PMMA, due to its FDM manufacturing feasibility. These micro-resonators were

arranged in a rectangular pattern with a unit cell size of 20x20 mm, as depicted in Figure 3.27. To ensure the effectiveness of the LRM solution, the micro-resonators were specifically tuned to match the first eigenfrequency of the original top plate. Through experimental modal analysis of the housing, it was determined that the first eigenfrequency of the top plate was 393 Hz. Accordingly, the micro-resonators were tuned numerically to this frequency before the manufacturing process. The micro-resonator width of 16 mm was maintained, the ABS base was defined as a square cross-section of 4×4 mm, the ABS beam was defined with a thickness of 1 mm and a length of 13.973 mm, and the steel mass was maintained as a square cross-section of 4×4 mm.

The ABS part of the micro-resonators was manufactured by AM using a FDM 3D printing machine from Stratasys. The ABS material properties are stated in the Table 3.4. The steel masses were created by cutting a steel rod with square cross-section of 4×4 mm. Both the steel mass connection in each micro-resonator and the connection of each micro-resonator to the aluminium plate were made using accelerometer bonding wax.

Property	Symbol	Value
Young's Modulus	E	2 GPa
Poisson's Ratio	υ	0.4
Density	ρ	1050 kg/m^3
Glass Transition Temperature	T_g	105.2°C

Table 3.4: ABS Material Properties [162]

The micro-resonator tuning of the first eigenmode (bending mode) was verified experimentally. The electrodynamic shaker Robotron 11076 was used for creating a sine sweep excitation over the frequency range of interest. The experimental verification was made by attaching the ABS-Steel micro-resonator to the dynamic force sensor on top of the electrodynamic shaker, and the micro-resonator vibration response was measured with a Laser Doppler Vibrometer (LDV), see Figure 3.28. Through these experimental measurements, it was confirmed that the manufactured micro-resonators were tuned to the desired frequency, ensuring that they were capable of exhibiting resonant behavior at the intended frequency.

Figure 3.29 shows the aluminium GBH mock-up with LRM solution applied, mounted in the test platform. Since the LRM solution was applied on the outside part of the housing, in the top plate, there is no available space for the placement of the accelerometers. Hence, the accelerometers were placed, according to the placement described in the Figure 3.26, in the inner part of the housing as shown in the Figure 3.30.

Figure 3.27: Close-up view of the LRM Plate (aluminium plate with 72 ABS-Steel micro-resonators) next to a 10 cent euro coin (for scale perception).

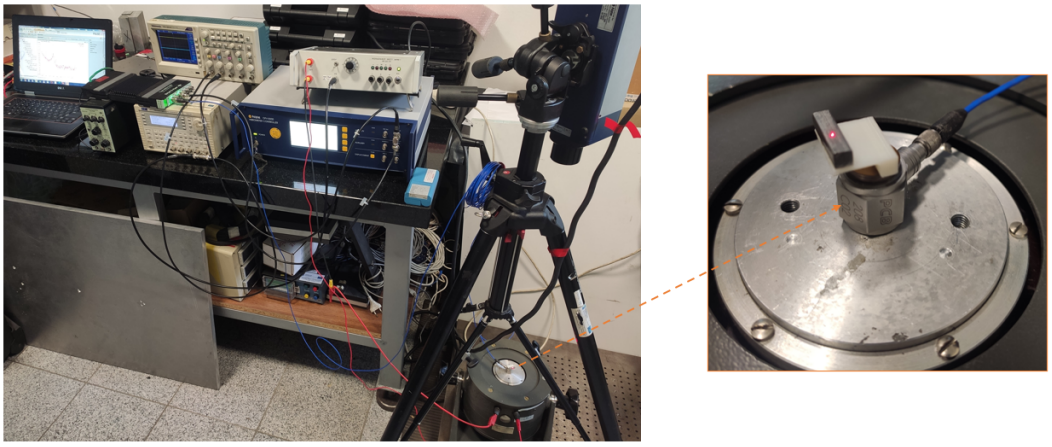

Figure 3.28: Experimental setup for verification of the micro-resonator tuning.

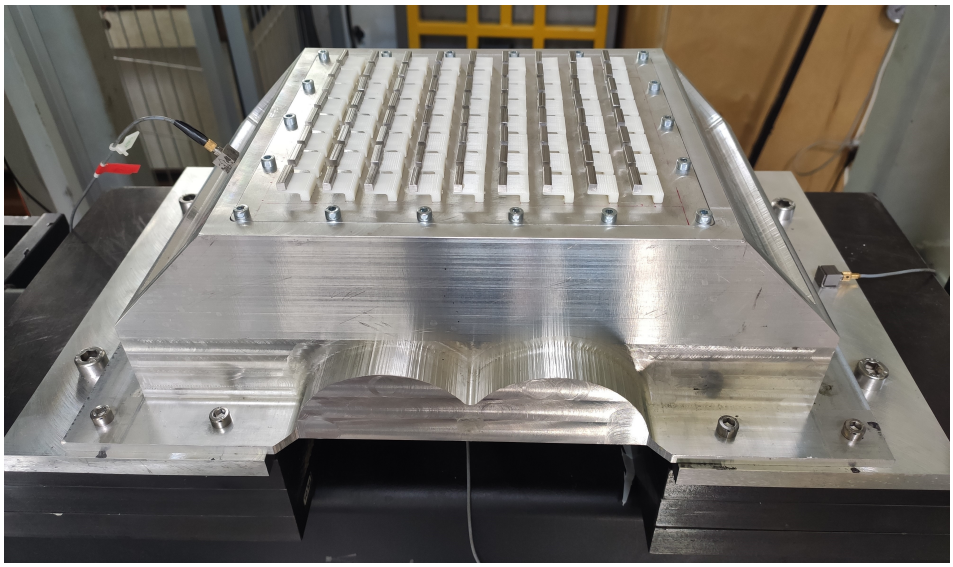

Figure 3.29: Aluminium GBH mock-up bolted to the experimental stand, with LRM solution applied on the top plate.

Figure 3.30: Accelerometers placement inside the housing.

3.5.2 Experimental Results and Discussion

Figure 3.31 presents the average normalized normal acceleration ($m/s^2/N$) measured by the accelerometer placed in the center of the top plate, for the baseline configuration and for the LRM solution configuration. It can be observed that the LRM solution achieves more than 30 dB vibration attenuation at the frequency where the micro-resonators are tuned. Additionally, the average vibration in the center of the top plate is reduced by 40% across the entire spectrum considered (50 to 5000 Hz) due to the presence of the LRM solution on the housing. Table 3.5 provides a summary of the relative attenuation of vibration for all the accelerometers placed on the housing structure. The locations of each accelerometer can be found in Figure 3.26. The frequency responses for all the sensors are included in the appendix A.

Considering an average across the entire spectrum, it can be observed that the LRM solution yields vibration attenuation in all acceleration sensors. The most substantial reduction in acceleration occurs in the top plate, where the micro-resonators are applied (P11, P1, P2, P3, and P5). Nevertheless, some degree of acceleration attenuation is also noticeable in other regions of the GBH, where the LRM solution was not applied. For instance, at positions P9 and P7, acceleration reduction of 11% and 3%, respectively, were observed. Moreover, the acceleration results in in-plane directions in the center of the top plate (P11), show attenuation in both directions (x and y). Even though the in-plane vibration is not responsible for the noise emission, this in-plane attenuation reduces the wave propagation for other parts of the structure where those waves can be normal to the surface, hence, further attenuating the noise emission.

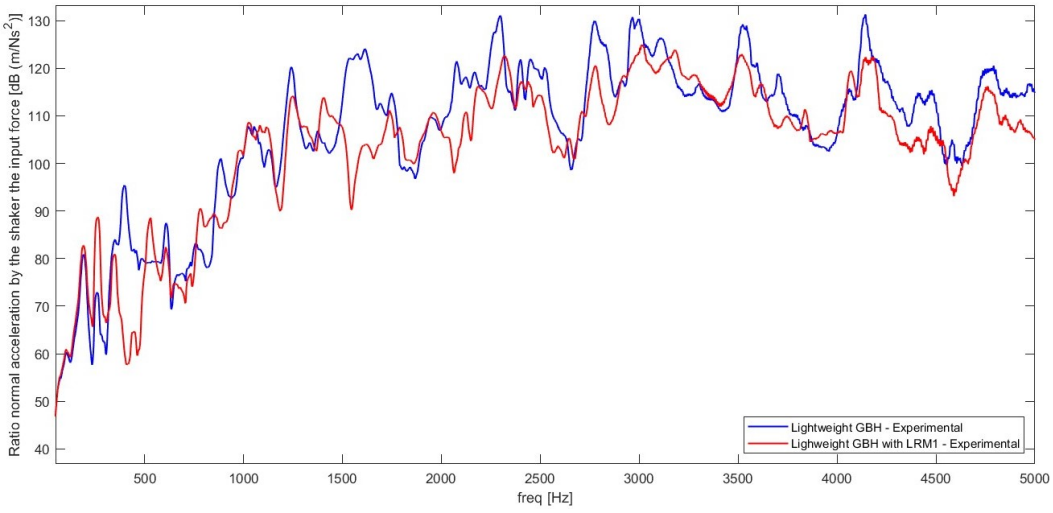

Figure 3.31: Normalized acceleration at the center of the top plate - Experimental.

In order to better align with the experimental data, a new numerical model was developed in COMSOL Multiphysics software. This model closely matches the

Accelerometer Position	Baseline	LRM Applied	Relative Variation
P11z (Center)	5.757	3.457	-40%
P1	5.309	3.467	-35%
P2	5.966	3.063	-49%
P3	3.652	2.748	-25%
P5	6.528	3.981	-39%
P11x	2.508	1.806	-28%
P11y	7.190	5.027	-11%
P9	3.988	3.543	-11%
P7	4.323	4.203	-3%

Table 3.5: Comparison between the normalized acceleration ($m/s^2/N$) of the baseline configuration and the configuration with the LRM applied for all the accelerometers placed on the housing structure and the respective relative variation.

experimental setup by adapting the geometry of the housing and setting the material to aluminium alloy. The aluminium alloy material properties are outlined in Table 3.3. Moreover, the numerical force input was placed in the same location as the force input generated by the electrodynamic shaker in the experimental setup. The first eigenmode of the housing in the numerical model occurs at 520 Hz, whereas in the experimental setup, it is at 393 Hz. Although it would have been possible to adjust the numerical eigenfrequency to match the experimental one by modeling the full bolted connection with non-linear contacts, this was not the objective of this study. Therefore, the micro-resonators in the numerical simulation were tuned for 520 Hz to replicate the same tuning conditions as those in the experimental setup.

Figure 3.32 displays the normalized normal acceleration measured at the center of the top plate in the numerical simulation. Comparing the numerical and experimental results, similar trends are evident. Specifically, the micro-resonators exhibit high attenuation at the frequency they were tuned for; there is average broadband attenuation across the spectrum, and the noise/acceleration peaks shift in frequency. The numerical model assumes a fixed condition that represents higher stiffness than the actual bolted connection to the experimental stand. The boundary conditions have a considerable impact on the lower frequency range. Consequently, the vibration levels at low frequencies are lower in the numerical simulation than in the experiments. In the numerical simulation, the structure is isolated from the external environment, resulting in a clearer frequency response. Compared with the numerical results, the frequency response peaks in the experimental results are less sharp since friction contacts introduce additional damping to the system.

Table 3.6 displays a comparison between the experimental and numerical average results of the normalized acceleration ($m/s^2/N$) at the center of the top plate of the baseline configuration and the configuration with the LRM applied. The absolute values of the normalized acceleration are identical for both the baseline configuration and the configuration with the LRM applied. On average, the numerical results are

	Baseline	LRM Solution	Relative Variation
Numerical Results	5,960	3,539	-40%
Experimental Results	5,757	3,457	-40%
Error (%)	3.5%	2.4%	

Table 3.6: Comparison between the experimental and numerical average results of the normalized acceleration ($m/s^2/N$) at the center of the top plate of the baseline configuration and the configuration with the LRM applied, and the respective relative variation.

overestimated by 3.5% for the baseline configuration and 2.4% for the configuration with LRM applied. However, regarding the relative variation with the presence of the LRM, the value is well estimated, being the relative reduction of 40% for both experimental and numerical results.

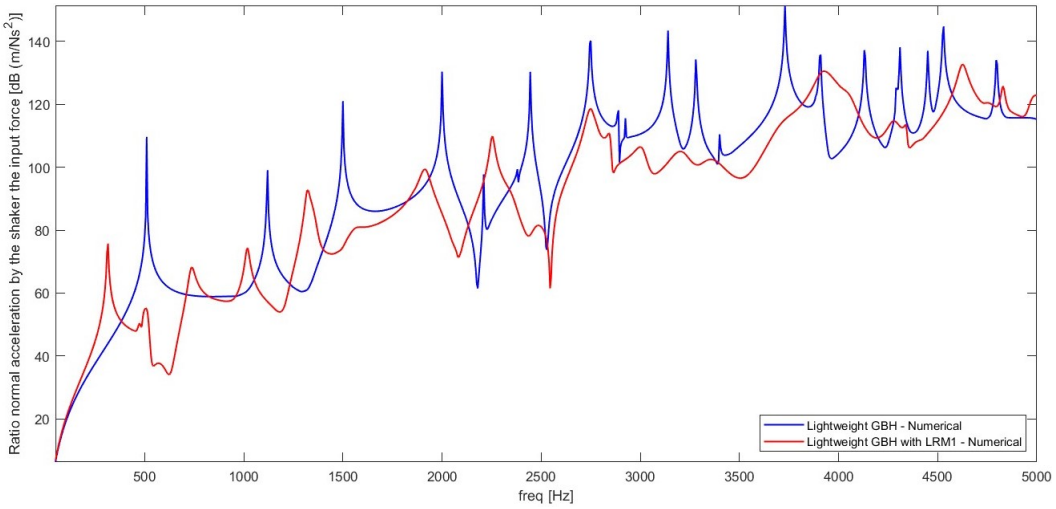

Figure 3.32: Normalized acceleration at the center of the top plate - Numerical.

For the purpose of discussing the impact of the acceleration attenuation on the noise emission, the sound power radiated by a vibrating structure is dependent of the square of the normal velocity of the outside surface of the structure [63]. In the frequency domain, a reduction in the acceleration amplitude implies a reduction in velocity amplitude for each frequency. Hence, disregarding the change in radiation efficiency, it is possible to estimate that a 40% reduction in acceleration represents a reduction of 64% in the sound power radiated by the GBH.

3.6 Conclusions and Remarks

As initially theoretically predicted, the mass reduction of a gearbox housing degraded its noise and vibration behavior, inducing more noise emission peaks in the low-frequency range. These lower frequency noise and vibration peaks are hard to

attenuate by conventional means. This work presented applications of locally resonant metamaterial solutions to attenuate the noise and vibration of a lightweight GBH.

The numerical simulation results indicate that the application of LRM solutions in GBHs can significantly reduce gearbox noise emissions. The analysis shows that the LRM solutions not only attenuate noise emission in the predicted BG but also provides a substantial average attenuation across the entire considered frequency spectrum (50-5000 Hz). In addition to the LRM solution consisting of one group of micro-resonators, a second LRM solution was analyzed, which comprised two groups of micro-resonators. This second LRM solution resulted in an even smoother response in the low-frequency range (50-1500 Hz). However, the average attenuation across the full spectrum was slightly lower compared to the LRM solution with only one group of micro-resonators.

The experimental results corroborated the LRM attenuation concept and trends observed in the numerical results, demonstrating the high attenuation on the predicted LRM BG and average broadband attenuation over the considered spectrum. The experimental results revealed that vibration was attenuated not only in the areas where the LRM solution was applied, but also in other parts of the GBH where no LRM was applied. The experiments also demonstrated that in the area of the application of the LRM, there was attenuation of in-plane vibration in both directions. Although in-plane vibration does not directly contribute to noise emissions, the observed attenuation in these directions can limit the propagation of waves to other parts of the GBH where they would radiate noise. This fact can further contribute to the reduction of gearbox noise emission.

The LRM solutions considered in this study results in a minimal increase in mass, typically ranging between 2% and 3% relative to the mass of the host structure, depending on the specific design and configuration. This increase is minor compared to the 20% mass reduction achieved by transitioning from the original GBH to the lightweight GBH. Therefore, the LRM solution enables the development of a lightweight version of the GBH with improved NVH characteristics.

The proposed LRM solutions are passive, lightweight and low-cost solutions that gearbox designers can implement in GBHs to enhance their NVH characteristics. These solutions do not require a control system, only an early design study identifying the area(s) to apply the LRMs and the main frequency region to attenuate. Additionally, the LRM solutions are expected to provide broadband attenuation, which will offer additional benefits beyond the targeted frequency range.

Gearbox and EV motor manufacturers face two significant issues when introducing new ideas or design approaches: one is the added cost, and another is the short development time available to bring products to market. The objective of this work was not to optimize the LRM solutions for a specific housing design, but rather to demonstrate that simple LRM solutions can effectively reduce noise emissions and vibration through the mechanisms described.

The micro-resonator spring parts were made of ABS and PMMA in this investigation. However, it is important to note that in industrial applications for

GBHs, high-temperature polyamides can be used for micro-resonator manufacturing to withstand the elevated temperatures experienced on the exterior of the GBH. To streamline the manufacturing process, coating layers with embedded micro-resonators can be manufactured and bonded to housing surfaces instead of bonding each resonator individually. This approach has the potential to significantly reduce production time and costs.

The findings of this study offer a step towards the industrial application of LRMs in GBHs and EV motor housings, offering a promising solution to the current conflicting design challenges.

Chapter 4

Lightweight Gearbox Housing with Novel Materials: Design and Assessment

This chapter delves into a comprehensive analysis aimed at identifying alternative materials to reduce the mass of GBHs. The study reveals that composite materials present a promising alternative to traditional metallic designs, thus focusing the research on composite GBH design. The conventional CLPT guided the initial design, while an innovative composite design process was subsequently formulated to exploit composite material advantages. The developed composite design process optimizes both lamina orientations and corresponding thicknesses across distinct regions. An illustrative application, substituting an aluminum GBH with a carbon-epoxy composite counterpart, showcases the superiority of the proposed composite design process. A thorough analysis of all GBH requirements is undertaken to ensure industrial applicability.

Contents

4.1 Novel Material Solutions for GBHs

Regardless of the material selected for gearbox housing manufacturing, it is crucial to ensure that the requirements outlined in the section 1.1.3 are respected. These requirements serve as guideline for designing a gearbox housing that meets the necessary criteria for mechanical support, load carriage, component protection, lubricant containment, heat dissipation, integration into the vehicle system, and NVH characteristics, among others. Thus, regardless of the specific material utilized, the gearbox housing must be designed and manufactured to fulfill these critical requirements to ensure optimal performance and functionality.

Materials are typically categorized into distinct families, encompassing ceramics, glasses, metals, and polymers. When it comes to constructing a gearbox housing, it's essential to consider the material's ability to absorb impacts. Therefore, brittle materials like glass or ceramics are unsuitable for this purpose.

Metallic materials, particularly steel and aluminium alloys, have been traditionally used in the manufacturing of gearbox housings for several reasons. Firstly, metallic materials provide the necessary strength and durability required to withstand the demanding loads and stresses experienced by GBHs during operation. They ensure the long-term reliability and performance of the gearbox components. In addition to strength, metallic materials exhibit good thermal conductivity, allowing for effective heat dissipation within the GBH. This property helps maintain optimal operating temperatures and prevents overheating of internal components, thereby extending their lifespan. The use of metallic materials is also driven by their cost-effectiveness. Metals are widely produced materials with well-established manufacturing processes, particularly for large-scale manufacturing.

The extensive experience and infrastructure developed for working with metallic materials contribute to their widespread usage in GBH manufacturing. Manufacturers have established expertise in shaping, machining, and joining metallic materials using conventional manufacturing processes like casting, machining, and welding. This compatibility with existing manufacturing technologies makes metallic materials an efficient and cost-effective choice for GBH production. Metallic materials also offer design flexibility, allowing for the creation of complex shapes and geometries required for GBHs. This design freedom enables the integration of various components and facilitates the efficient assembly of the gearbox system.

While metallic materials have served the industry well, advancements in materials science and manufacturing technologies have prompted the exploration of alternative materials, such as polymers and composites, for GBH manufacturing. These new materials offer potential benefits in terms of weight reduction, cost-effectiveness, and specific performance characteristics, addressing the evolving demands of modern vehicles. However, the selection of materials for GBH manufacturing involves a careful evaluation of factors such as mechanical support, heat dissipation, assembly requirements, cost considerations, and weight reduction goals. Each material option, including metallic materials, polymers, and composites, should be assessed based on their ability to meet the specific requirements of GBHs and contribute to

the overall performance and cost-effectiveness of the transmission system.

Polyamides are thermoplastic polymers that possess desirable characteristics such as strength, impact resistance, and dimensional stability. They are also known for their ease of processing, making them suitable for mass production. However, their Young's modulus is significantly lower compared to traditional metallic materials, ten to hundred times lower. Other thermoplastic polymers can be mentioned, like Polyetheretherketone (PEEK) or ABS, but none of them is able to provide Young's modulus close to the ones of metals. Consequently, adopting these polymers as a housing material would require impractical thicknesses to achieve stiffness levels comparable to those attained with metallic materials. The same holds true for thermoset polymers, such as phenolic and epoxy resins without reinforcement.

Despite the fact that polymers alone may not possess sufficient stiffness, it is important to highlight that the Young's modulus of polymers can be greatly enhanced by incorporating reinforcing materials such as fibers, resulting in the formation of FRP. These composites exhibit significantly increased stiffness and improved mechanical properties compared to unfilled polymers.

For composite manufacturing, thermoplastics are melted, whereas thermosets undergo a chemical process known as cross-linking, which establishes robust covalent bonds between polymer chains. Notably, thermosets tend to exhibit a lower initial viscosity in their liquid or uncured state compared to molten thermoplastics used in composite manufacturing. This lower viscosity characteristic of thermosets facilitates the production of larger or intricately designed composite components, simplifying the manufacturing process. Moreover, this fact enables the attainment of superior composite properties when utilizing thermoset matrices.

Epoxy resins are widely used in thermoset matrices in composite materials due to their excellent mechanical properties, adhesion, chemical resistance, thermal stability, low cure temperature, durability and dimensional stability [200]. Epoxy resins adhere well to a variety of reinforcement materials, including fibers like carbon and glass. This strong adhesion results in effective stress transfer between the matrix and the fibers, enhancing overall composite performance. Epoxy resins have good chemical resistance, making them suitable for applications where exposure to chemicals or harsh environments is a concern. Epoxy resins have good thermal stability associated with their high glass transition temperature (Tg), ranging from 120°C to 200°C depending on the specific epoxy resin.

Epoxy-based composites find widespread use in various industries, including automotive applications. Specifically, carbon-epoxy composites have the ability to achieve stiffness levels comparable to the traditional metallic materials commonly employed in gearbox housings. Consequently, due to their higher stiffness-to-mass ratio, carbon-epoxy composites offer a compelling alternative for the lightweight design of gearbox housings.

One consideration when evaluating the use of carbon-epoxy composites in gearbox housings is their relatively lower thermal conductivity compared to steel or aluminium alloys. Aluminium and its alloys typically exhibit thermal conductivities ranging from 80 to 250 W/m K, while carbon steel has a thermal conductivity of

about 45 W/m K, and stainless steel has a thermal conductivity of about 15 W/m K. In contrast, carbon-epoxy composites have thermal conductivities ranging from 0.5 to 6 W/m K, which are substantially lower [165, 177]. Techniques to address this issue will be presented afterward in this research. By employing innovative approaches, it is possible to enhance the thermal conductivity of carbon-epoxy composites and ensure that they meet the requirements for effective heat dissipation in gearbox housings.

While GFRP can be considered as an alternative material for GBHs, its lower stiffness compared to CFRP should be taken into account. For the UD reinforcements with the same volume fractions, GFRPs typically have stiffnesses more than three times lower than CFRPs. Consequently, using GFRP in the GBH design would necessitate an excessive thickness to achieve the desired stiffness. This increased thickness can pose challenges, especially in terms of heat dissipation, as it would impede the efficient dissipation of heat generated during gearbox operation. Moreover, the density of glass fibers is typically around 2500 kg/m^3 while the density of carbon fiber is normally between 1500 and 2100 kg/m^3 [1]. That implies that for the same volume fraction, the GFRPs will be heavier than CFRPs, which is a drawback for lightweight design.

On the other hand, GFRP offer a more cost-effective solution and can provide sufficient mechanical support for GBHs in less demanding applications. However, when it comes to optimizing stiffness-to-mass ratios, CFRPs are the preferred choice. Carbon-epoxy composites offer high stiffness and low weight, making them ideal for applications where minimizing weight is crucial.

Based on the considerations discussed in this qualitative and quantitative evaluation, carbon-epoxy composites emerge as the optimal alternative material for gearbox housing due to their ability to reduce mass while meeting the housing requirements. Therefore, the subsequent sections will present studies focusing on the design of composite housing solutions. These studies aim to explore the potential of carbon-epoxy composites in achieving lightweight yet robust gearbox housings that can effectively withstand operational demands and enhance overall performance.

4.2 Classical Composite Design according to the CLPT

4.2.1 Composite Laminate Design

In this section presents a classical composite design approach based in the CLPT and the ABD matrix. As mentioned in the section 4.3.3, the CLPT is based on the principle of virtual work and the theory of elasticity. The ABD matrix, discussed in the section 4.3.3, is a fundamental tool in the analysis of laminated composite structures.

The primary objective of the design was to identify a composite material that exhibits stiffness properties at least equivalent to the aluminium alloy employed in the housing. To meet this criterion according to the CLPT, the stiffness components within the composite ABD matrix must possess values equal to or greater than

those of the aluminium alloy. Afterward, an assessment of the static response of the housing must be conducted and compared against the original aluminium GBH. The composite housing design's safety should be evaluated based on the failure criteria specified in the section 1.2.3

An ABD matrix calculator script was implemented in MATLAB R2020b, enabling the investigation of various laminate configurations by evaluating the components of their respective stiffness matrices. The script calculates the ABD matrix using the CLPT. It iterates through the ply orientations, computes the ply stiffness matrices, performs coordinate transformations, and updates the stiffness matrix accordingly. Finally, the script displays the resulting ABD matrix. The results of the ABD matrix calculator script were validated with results obtained from laminate models in COMSOL Multiphysics (version 5.6).

The script requires the specification of material properties, including Young's modulus in the fiber direction, Young's modulus in the transverse direction, shear modulus in the plane and Poisson's ratio. Additionally, the ply thicknesses and orientations in degrees must be provided for each lamina. The output matrix follows the format defined in Table 4.1. Regarding the units, the components of the [A] matrix are stated in N/mm, the components of the [B] matrix are stated in N and the components of the [D] matrix are stated in $N \cdot mm$.

The composite design approach was based in the comparison of the ABD matrix of the designed composite with the ABD matrix of the aluminium alloy used in the original design. To initiate the design process, the values of the ABD matrix for an aluminium alloy layer were calculated with the script. The input material properties for the aluminium alloy are outlined in Table 3.3. The original housing maintains a constant thickness of 6 mm across its geometry, and this thickness was used to compute the ABD matrix of the aluminium alloy, as presented in Table 4.2.

	N_x	N_y	N_{xy}	M_x	M_y	M_{xy}
ε_x	A11	A12	A13	B11	B12	B13
ε_y	A21	A22	A23	B21	B22	B23
γ_{xy}	A31	A32	A33	B31	B32	B33
κ_x	B11	B12	B13	D11	D12	D13
κ_y	B21	B22	B23	D21	D22	D23
κ_{xy}	B31	B32	B33	D31	D32	D33

Table 4.1: Format of the output ABD Matrix from the script.

The design of the composite was accomplished through an iterative method based on the CLPT. The lamina properties of the considered UD carbon-epoxy prepreg are stated in the Table 4.3, where E_1 is the longitudinal Young's modulus, E_2 is the transversal Young's modulus, G_{12} is the shear modulus in the lamina plane, υ_{12} is the Poisson's ratio when loaded in the longitudinal direction, X_t is the longitudinal tensile strength, Y_t is the transverse tensile strength, X_c is the longitudinal compressive strength, Y_c is the transverse compressive strength and S is

	N_x	N_y	N_{xy}	M_x	M_y	M_{xy}
ε_x	4.71	1.56	0	0	0	0
ε_y	1.56	4.71	0	0	0	0
γ_{xy}	0	0	1.56	0	0	0
κ_x	0	0	0	14.1	4.67	0
κ_y	0	0	0	4.67	14.1	0
κ_{xy}	0	0	0	0	0	4.68

Table 4.2: Aluminium Alloy ABD Matrix (values divided by 10^5).

the shear strength. The laminate consisted of a 64-layer quasi-isotropic configuration with a stacking sequence of $[45°/-45°/0°/90°/90°/0°/-45°/45°]_{8s}$. In the first design approach, for the substitution of the aluminium (isotropic material), a quasi-isotropic configuration was chosen. This configuration was selected to achieve a near-uniform distribution of strength and stiffness across multiple directions, effectively creating mechanical properties that resemble isotropic behavior.

Property	Value	Unit
E_1	159	GPa
E_2	9.2	GPa
G_{12}	4.37	GPa
υ_{12}	0.253	
ρ	1700	kg/m^3
X_t	1500	MPa
Y_t	50	MPa
X_c	1200	MPa
Y_c	250	MPa
S	70	MPa

Table 4.3: Lamina Properties of the Carbon-Epoxy Prepreg (IM7/977-2) [130].

The iterative process commenced with a layer thickness of 0.1 mm, resulting in a total laminate thickness of 6.4 mm. Using the MATLAB script, the composite laminate's stiffness matrix was calculated, as depicted in Table 4.4. Subsequently, the stiffness values were compared to those of the aluminium alloy stiffness matrix. The relative stiffness comparisons are shown in Table 4.5. From the table, it is evident that several components of the composite ABD matrix are under-dimensioned. Specifically, the extensional stiffness matrix is statically under-dimensioned, along with various components of the bending stiffness matrix.

In order to ensure the composite possessed a stiffness at least equal to that of the metal, it was necessary for all values within the composite ABD matrix to be equal to or higher than their respective counterparts in the metal stiffness matrix. Therefore, the design process entailed iteratively increasing the lamina

	N_x	N_y	N_{xy}	M_x	M_y	M_{xy}
ε_x	4.23	1.32	0	0	0	0
ε_y	1.32	4.23	0	0	0	0
γ_{xy}	0	0	1.45	0	0	0
κ_x	0	0	0	14.4	4.56	0
κ_y	0	0	0	4.67	14.1	0
κ_{xy}	0	0	0	0	0	5.01

Table 4.4: First Iteration of the Carbon-Epoxy Composite ABD Matrix (values divided by 10^5).

thickness, thereby increasing the total thickness of the laminate, until all values in the composite ABD matrix matched or surpassed the corresponding values in the aluminium stiffness matrix. When this condition is verified, the composite design is obtained. In the application case, this condition was met when the lamina thickness reached 0.118 mm, resulting in a total composite laminate thickness of 7.552 mm. The final composite ABD matrix is provided in Table 4.6. The relative stiffness comparisons between the designed composite and the aluminium alloy are outlined in Table 4.7. It can be observed that in order to fulfill the required stiffness in the extensional stiffness matrix, the bending stiffness matrix is significantly over-dimensioned.

Final remarks can be made regarding the design process. Firstly, it is worth highlighting that this straightforward process enables the substitution of metallic materials with composite laminate materials. In this specific application case, it successfully facilitated the development of a carbon-epoxy laminate composite as a practical alternative to the original aluminium alloy design. Furthermore, it is important to note that the thicknesses in each direction can be adjusted to align with the discrete standard lamina thickness provided by the prepreg manufacturer. Lastly, it is worth considering that the significant over-dimensioning of the bending stiffness matrix reduces the potential benefits of employing sandwich configurations in the housing design. Since, the sandwich structures mainly help to increase the bending stiffness.

	N_x	N_y	N_{xy}	M_x	M_y	M_{xy}
ε_x	-10%	-15%				
ε_y	-15%	-10%				
γ_{xy}			-7%			
κ_x				+2%	-2%	
κ_y				-2%	+2%	
κ_{xy}						+7%

Table 4.5: ABD Matrices comparison between the first iteration composite against the aluminium alloy.

	N_x	N_y	N_{xy}	M_x	M_y	M_{xy}
ε_x	4.99	1.56	0	0	0	0
ε_y	1.56	4.99	0	0	0	0
γ_{xy}	0	0	1.71	0	0	0
κ_x	0	0	0	23.7	7.50	0
κ_y	0	0	0	7.50	23.6	0
κ_{xy}	0	0	0	0	0	8.23

Table 4.6: Designed Carbon-Epoxy Composite ABD Matrix (values divided by 10^5).

	N_x	N_y	N_{xy}	M_x	M_y	M_{xy}
ε_x	+6%	0%				
ε_y	0%	+6%				
γ_{xy}			+10%			
κ_x				+67%	+61%	
κ_y				+61%	+67%	
κ_{xy}						+76%

Table 4.7: ABD Matrices comparison between the designed composite against the aluminium alloy.

4.2.2 GBH Static Evaluation

In order to reach a capable global design, after designing the composite laminate, it is important to perform a global analysis of the composite component and compare it with the original component design. The new designed composite housing must ensure similar or even better static behavior, with displacements from applied forces equal to or lower than in the original GBH. Additionally, the bearing displacements should also be equal to or lower than those in the original GBH to ensure proper alignment of the gearbox shafts and gears. These two aspects must be verified during the analysis process by applying different loading directions and evaluating the global housing displacements and bearing displacements. This analysis is fundamental to ensure a successful transition from a metallic housing to a composite housing design.

For the static response comparison in the application case, the designed composite material was applied in the GBH geometry and compared with the aluminium version of the GBH. The Figure 4.1 displays the two models in comparison and the materials applied in each of them. Specifically, Figure 4.1 a) showcases the aluminium housing model, while Figure 4.1 b) depicts the composite housing model. The composite housing model was built considering the composite laminate designed in the section 4.2.1, a 64-layer quasi-isotropic laminate with a stacking sequence of $[45, -45, 0, 90, 90, 0, -45, 45]_{8s}$, with total composite laminate thickness of 7.552 mm. The lamina properties of the considered carbon-epoxy prepreg are stated in the Table 4.3.

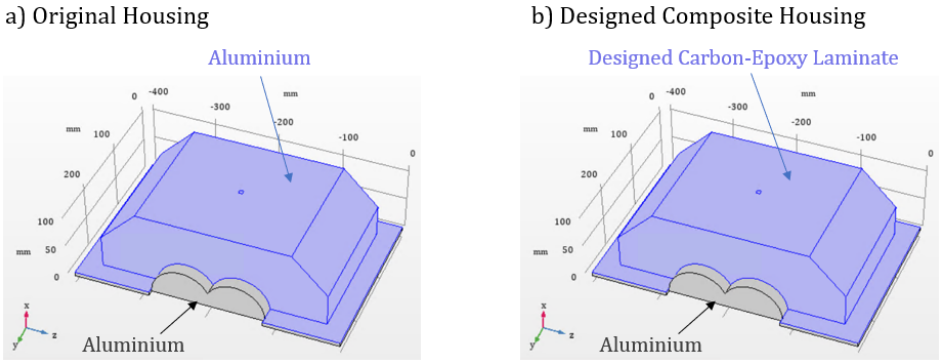

Figure 4.1: Housing models for static response comparison: a) Aluminium housing model; b) Composite housing model.

Different critical load cases were applied in the bearing area and the corresponding static response was evaluated. Three load cases were considered: a 50 kN radial upwards force, a 50 kN radial sidewards force and a 20 kN axial force. The housing and bearings displacements were compared for all the loading cases between the composite and aluminium design. The displacement comparisons are shown in the Figure 4.2 for the 50 kN radial upwards force load case, in the Figure 4.3 for the 50 kN radial sidewards force load case and in the Figure 4.2 for the 20 kN axial force load case.

The simulations were performed in the COMSOL Multiphysics (version 5.6). Table 4.8 presents a summary of the displacement comparisons between the designed composite housing and the baseline aluminium housing for the different load cases. Moreover, Table 4.9 provides a comparison of the stiffness results between the design composite housing and the baseline aluminium housing for the various load cases. Notably, the composite GBH exhibits higher stiffness values in all the load cases, indicating a superior static response.

In the next section, the safety of the composite design will be evaluated by examining failure criteria. This assessment is crucial to ensure that the composite structure meets the required safety standards. The subsequent section will provide a detailed analysis of the composite's performance under various loading conditions and assess its ability to withstand applied stresses without failure. By conducting this evaluation, necessary adjustments can be made to enhance the overall safety and reliability of the composite structure.

4.2.3 Failure Criterion Evaluation and Safety

As indicated in the section 1.2.3, there are several criteria for safety evaluation of the composite designs. According to the advantages highlighted in the section, the Tsai-Wu failure criterion was used in this evaluation. The Tsai-Wu failure criterion is a widely used criterion in composite material analysis to predict failure under

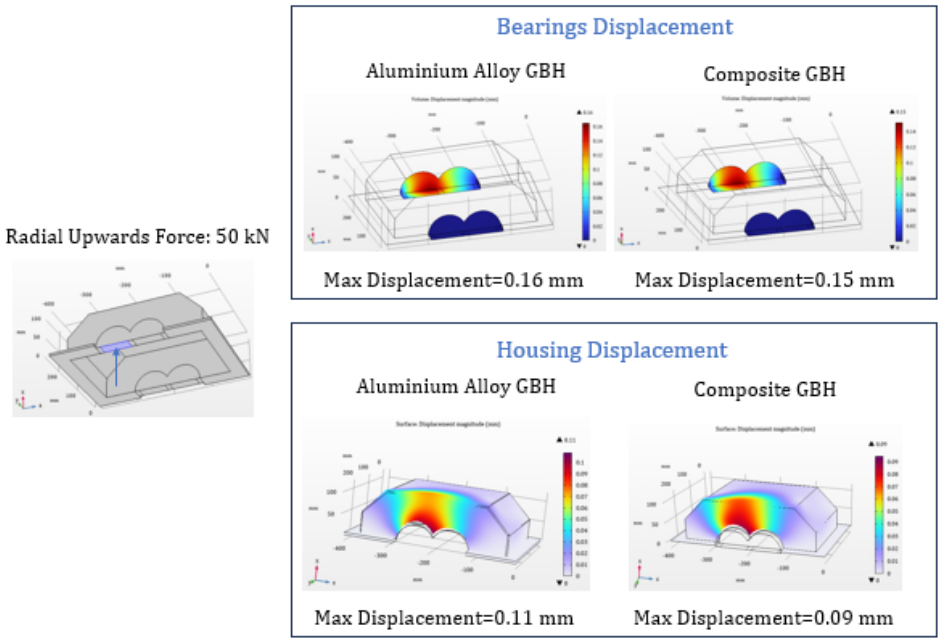

Figure 4.2: Comparison of housing and bearings displacements with a 50 kN radial upwards force applied in the bearing area.

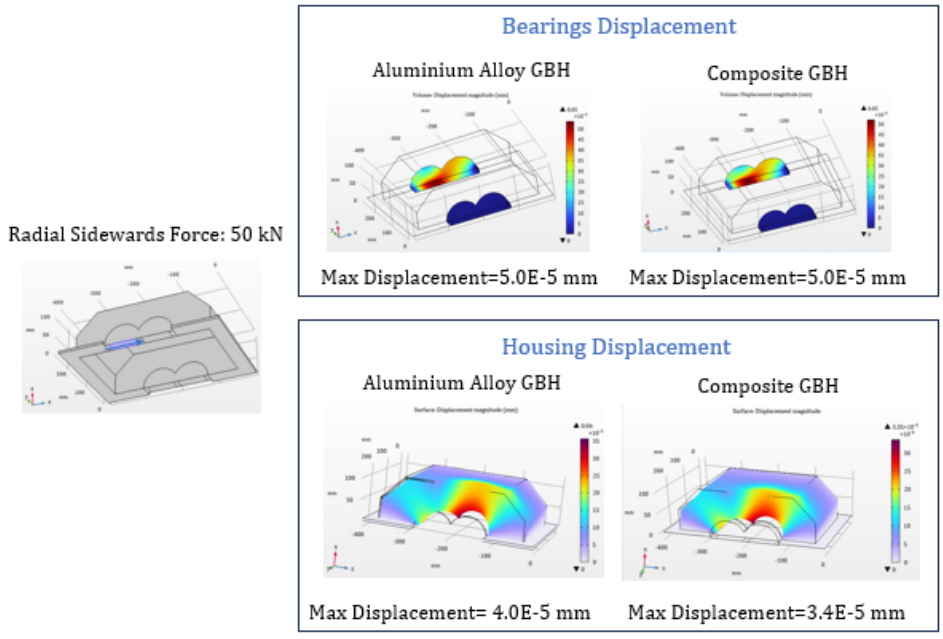

Figure 4.3: Comparison of housing and bearings displacements with a 50 kN radial sidewards force applied in the bearing area.

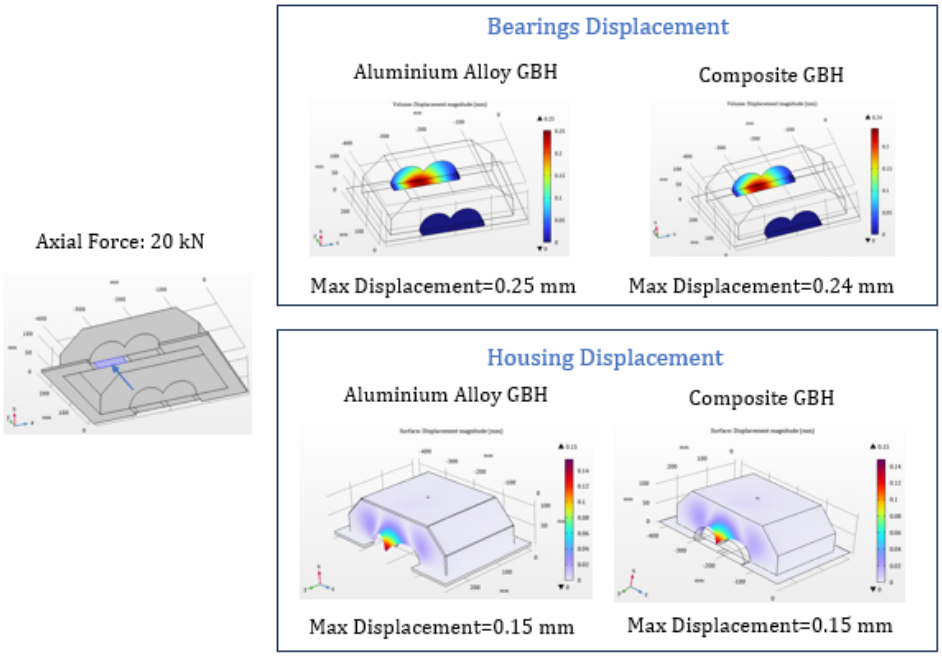

Figure 4.4: Comparison of housing and bearings displacements with a 20 kN axial force applied in the bearing area.

	Bearings Displ. (mm)		Housing Displ. (mm)	
	Al. Alloy	Composite	Al. Alloy	Composite
LC1: Radial Upwards	1.60E-01	1.50E-01	1.10E-01	9.00E-02
LC2: Radial Sidewards	5.00E-05	5.00E-05	4.00E-05	3.40E-05
LC3: Axial	2.50E-01	2.40E-01	1.50E-01	1.50E-01

Table 4.8: Comparison of housing and bearings displacements with different LCs.

	Bearings Stiffness (N/m)		Housing Stiffness (N/m)	
	Al. Alloy	Composite	Al. Alloy	Composite
LC1: Radial Upwards	3.13E+08	3.33E+08	4.55E+08	5.56E+08
LC2: Radial Sidewards	1.00E+12	1.00E+12	1.25E+12	1.47E+12
LC3: Axial	8.00E+07	8.33E+07	1.33E+08	1.33E+08

Table 4.9: Comparison of housing and bearings stiffnesses with different LCs.

complex multiaxial loading conditions. It takes into account both the tensile and compressive strengths of the material, as well as the interaction between different stress components.

For failure prediction, the Tsai-Wu failure criterion as outlined in Equation 1.10, along with the corresponding parameter calculation expressions presented in Equation 1.11 were employed. Safety factors are commonly used to evaluate the safety of a composite structures. These factors provide a margin of safety by comparing the applied loads to the failure limit. In the case of the Tsai-Wu criterion, the computation of safety factors involves scaling the stress tensor in such a way that the failure criterion is set to zero [167]. The stress components are determined based on the applied forces and moments, as well as the geometry and material properties of the structure.

A safety factor greater than 1 indicates that the applied stress is below the failure strength, implying a safe design. Conversely, a safety factor less than 1 suggests that the applied stress exceeds the failure strength, indicating a potential failure risk. By evaluating the Tsai-Wu failure criterion and considering the safety factors, it is possible to make informed decisions about the composite material's performance and ensure that the design meets the required safety standards.

For the designed composite housing, the computation of the safety factors based in the Tsai-Wu failure criterion was performed in the COMSOL Multiphysics (version 5.6). The lamina strength properties of the carbon-epoxy of the considered prepreg are stated in the Table 4.3.

The safety evaluation process involves the selection of critical load cases to thoroughly assess the structural integrity of the composite system. It is important to note that different critical load cases can occur concurrently, necessitating the evaluation of combined load cases to capture extreme loading conditions effectively. For the safety evaluation of the designed housing, different LCs were considered. First, a radial upwards force of 20 kN was applied to test the system's response to vertical forces. Next, a radial sidewards force of 20 kN was applied to examine the system's ability to withstand lateral forces. Lastly, an axial force of 5 kN was applied in the bearings to evaluate the housing resilience to axial loads. In addition to these individual load cases, a combined load case was also considered, where all the aforementioned load cases (LC1, LC2, and LC3) were simultaneously applied. This extreme load case, LC4, aimed to test the system's capacity to endure the combined effect of all the critical LCs acting on it simultaneously.

Figure 4.5 illustrates the safety factor distribution in the housing composite structure for LC1, with a minimum Tsai-Wu safety factor of 6.86. Similarly, Figure 4.6 displays the safety factor distribution for LC2, where the minimum Tsai-Wu safety factor is 13.2. Figure 4.7 shows the safety factor distribution for LC3, with a minimum Tsai-Wu safety factor of 10.0. Lastly, Figure 4.8 portrays the safety factor distribution for LC4, where the minimum Tsai-Wu safety factor is 5.96. For a comprehensive overview, Table 4.10 summarizes the minimum Tsai-Wu safety factor for each load case considered.

The results reveal that the Tsai-Wu safety factors in the majority of the com-

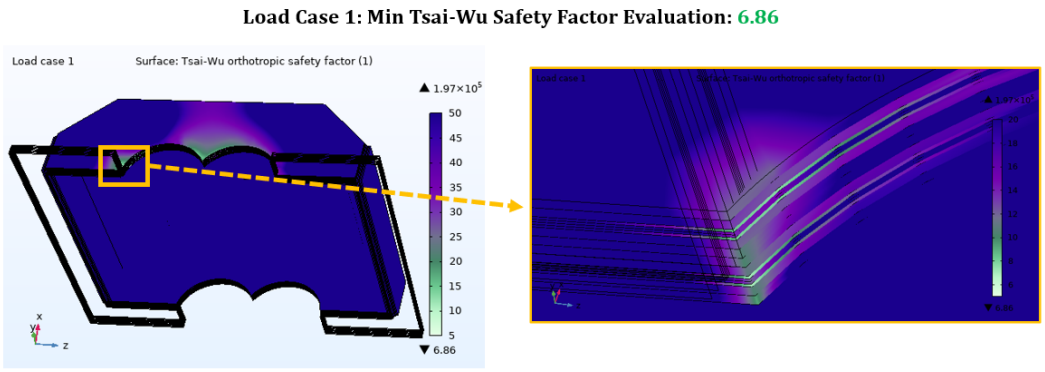

Figure 4.5: Safety factor distribution in the housing composite structure for the LC1, zoom in the area of the minimum safety factor for the LC1.

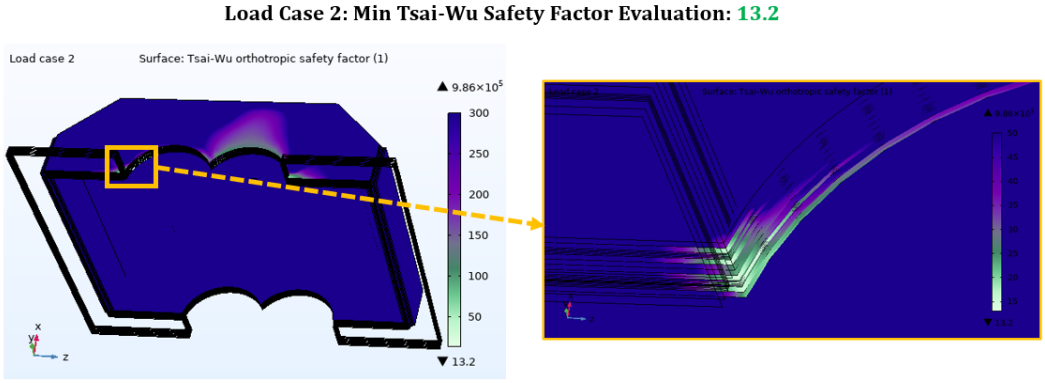

Figure 4.6: Safety factor distribution in the housing composite structure for the LC2, zoom in the area of the minimum safety factor for the LC2.

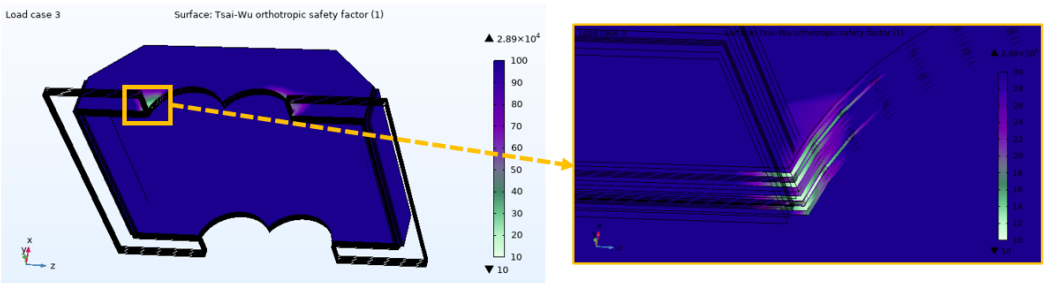

Figure 4.7: Safety factor distribution in the housing composite structure for the LC3, zoom in the area of the minimum safety factor for the LC3.

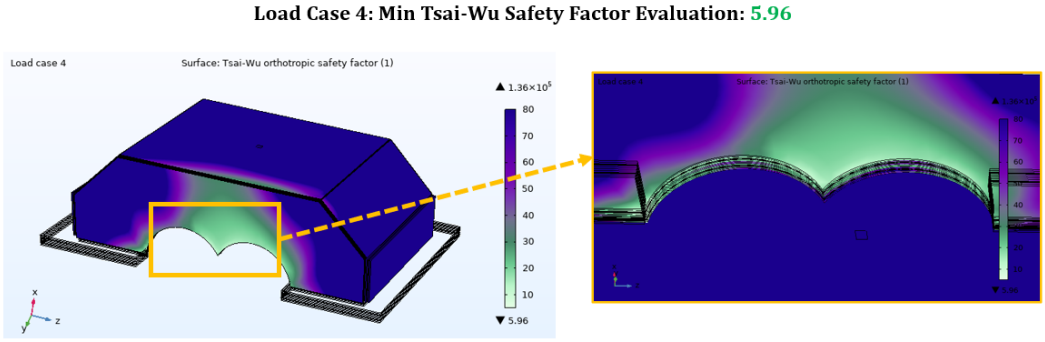

Figure 4.8: Safety factor distribution in the housing composite structure for the LC4, zoom in the area of the minimum safety factor for the LC4.

Load Case	Tsai-Wu Min SF
LC1	6.86
LC2	13.2
LC3	10.0
LC4	5.96

Table 4.10: Minimum Tsai-Wu Safety Factor in the designed composite housing for each considered Load Case.

posite design are significantly higher than 1. Although concentrated areas near the bearings exhibit lower safety factors, they still remain considerably above 1. Globally, the minimum Tsai-Wu safety factor of 5.96 was obtained for LC4 (combined loading case), which is still substantially above the critical threshold.

Based on the Tsai-Wu failure criterion, it can be concluded that the design is safe. However, it is important to consider that there are other composite failure modes, as mentioned in the section 1.2.3. For a more comprehensive safety evaluation, alternative approaches such as the Hashin, Puck, or LaRC03 criteria should be employed. These criteria offer a more detailed analysis of failure modes in composites, taking into account both fiber and matrix failure, as well as their interactions. It is worth noting that these approaches necessitate extensive material characterization, including experimental tests to induce and capture specific failure modes accurately.

4.2.4 Discussion

In the preceding sections, it has been demonstrated that a composite gearbox housing can be successfully designed using the classical approach based on the CLPT. The composite gearbox housing was designed to substitute a traditional aluminium housing. The composite housing offers superior static response with comparable or increased stiffness, allowing it to effectively withstand bearing loading.

Moreover, the design of the composite housing has been verified as structurally safe according to the Tsai-Wu failure criterion, ensuring its integrity under various loading conditions. This validation provides confidence in the reliability and durability of the composite housing.

Furthermore, one of the key advantages of this design approach is the significant reduction in mass. The composite housing weighs 2.00 kg, while the aluminium housing weighs 2.53 kg, resulting in a notable weight reduction of 21% compared to the aluminium alloy housing. This reduction in mass offers benefits such as improved efficiency and reduced inertia. The first design of the composite gearbox housing already demonstrates its potential to outperform traditional aluminium housings.

On the other hand, it's important to note that the current design approach does not fully exploit a specific characteristic of composite materials: their higher degree of design freedom compared to isotropic materials. Composite materials offer exceptional potential for optimization due to this increased design freedom. By carefully defining fiber orientations and layer thicknesses within the composite structure, further optimization of the housing design can be achieved. This enables the fine-tuning of the material's properties to better suit specific requirements and maximize performance.

By strategically selecting and arranging the fiber orientations of each layer, it is possible to tailor the material's mechanical properties to meet specific performance requirements. This process involves considering factors such as load distribution, stiffness, and strength in different directions. Additionally, the determination of the appropriate thicknesses for each layer allows for structural optimization aiming to mass efficiency of components, and in this specific case of the GBH. By carefully considering the distribution of forces and load paths within the composite housing, it is possible to allocate material where it is most needed and reduce unnecessary mass in areas of lower stress.

Through the manipulation of fiber orientations and layer thicknesses, composite housing designs can be fine-tuned to maximize performance and functionality. This flexibility offers an unprecedented level of control over the material's behavior and enables the creation of efficient and tailored housing designs for distinct setups. The section 4.3 introduces a composite design approach that specifically addresses these additional design variables, highlighting the importance of optimizing fiber orientations and layer thicknesses.

4.3 Variable Thickness Composite Gearbox Housing

The following section presents a composite design approach considering fiber orientations and the respective layer thicknesses. The objective is to demonstrate that this design method can yield improved composite housing architectures. The mentioned process unlocks the potential of composite materials and permits the creation of innovative lightweight solutions that meet the GBH requirements.

Following the definition of the optimization process, the obtained results are

subjected to post-processing and evaluation. Furthermore, a safety evaluation of the design is conducted, employing a similar process as described in the section 4.2.3. On the section 4.3.6, the focus will be on the NVH analysis of the composite solution developed in this section.

4.3.1 Optimization Method for Lamina Orientations and Thicknesses

In this section, a systematic approach to composite design optimization is presented. The process involves identifying and defining independent optimization areas within the design, allowing for different thicknesses and fiber orientations in each area. For the considered gearbox housing, four areas were identified for optimization. Figure 4.9 provides a visual representation of these four areas.

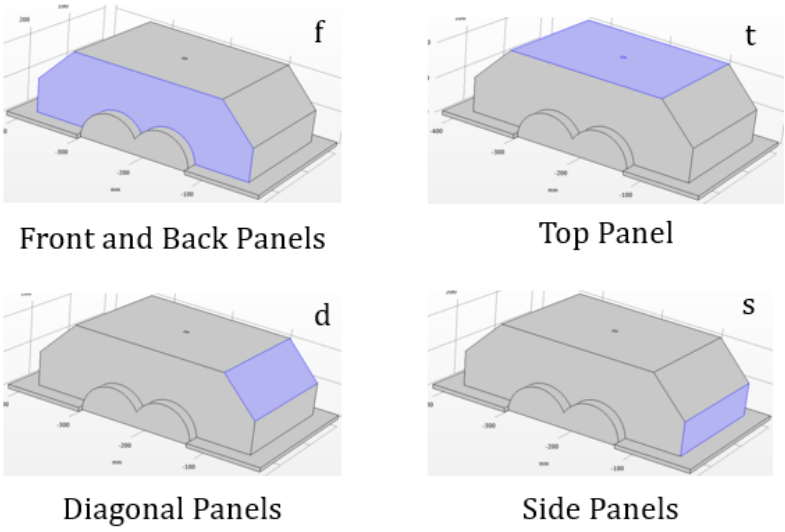

Figure 4.9: GBH optimization areas.

In each of the areas, a set of four different fiber orientations was considered, leading to a total of four prepreg orientations and four thicknesses for each orientation within the areas. The general composite laminate definition is stated in the Equation 4.1. The considered general laminate configuration is symmetric. As mentioned in the section 4.3.3, symmetric laminates are preferred for two main reasons. First, their structure balances the thermal residual stresses and deformations that can occur due to differential thermal expansion between the fibers and matrix during temperature changes. Second, symmetric laminates evenly distribute applied loads, minimizing the generation of shear stresses within the laminate. For these two reasons, risks of delamination and interlaminar shear failure are reduced. Hence, the use of symmetric laminates improves the overall load-carrying capacity and structural integrity of the composite.

$$[Ori1^\circ\ Ori2^\circ\ Ori3^\circ\ Ori4^\circ\ -Ori4^\circ\ -Ori3^\circ\ -Ori2^\circ\ -Ori1^\circ]_s \tag{4.1}$$

The Table 4.11 shows the association between the orientation variables and the corresponding thickness variables for each of the optimization areas. In this particular scenario, there are four areas, each with eight independent control parameters, resulting in a total of 32 control parameters for the optimization process. While it is possible to increase the number of fiber orientations, incorporating more than four different directions would yield only marginal efficiency improvements in the optimization while significantly escalating complexity. This heightened complexity impacts not only the optimization computations but also extends to the manufacturing phase, potentially leading to practical challenges during the fabrication of the composite housing. Hence, a balance is sought between optimizing the design and maintaining practical feasibility. An illustration of the laminate can be seen in the Figure 4.10.

Layer	Orientation (°)	Thickness (mm)
Layer 1	Ori1	Th_Ori1
Layer 2	Ori2	Th_Ori2
Layer 3	Ori3	Th_Ori3
Layer 4	Ori4	Th_Ori4
Layer 5	- Ori4	Th_Ori4
Layer 6	- Ori3	Th_Ori3
Layer 7	- Ori2	Th_Ori2
Layer 8	- Ori1	Th_Ori1

Table 4.11: Laminate design control parameters for each of the optimization areas

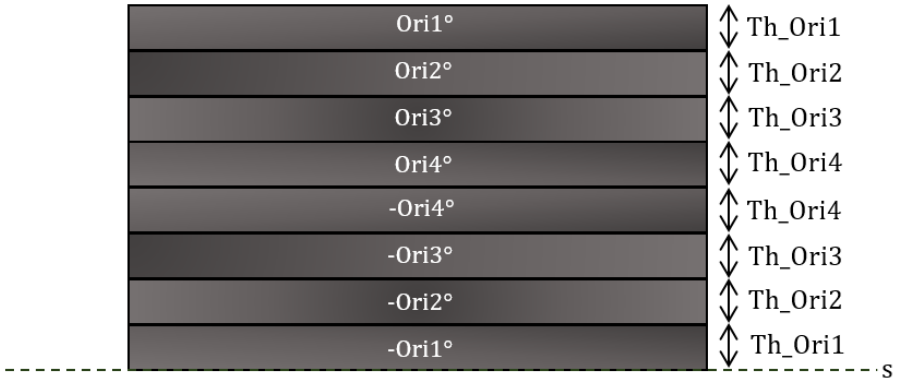

Figure 4.10: Illustration of the general composite laminate definition.

A fundamental aspect is the establishment of local coordinate systems for each optimization area. This step is vital to analyze and interpret the global outcomes of the optimization process. This ensures that the design variables, fiber orientations and layer thicknesses, are correctly aligned and oriented according to the results for each specific area. Figure 4.11 show the local coordinate systems considered for each GBH area.

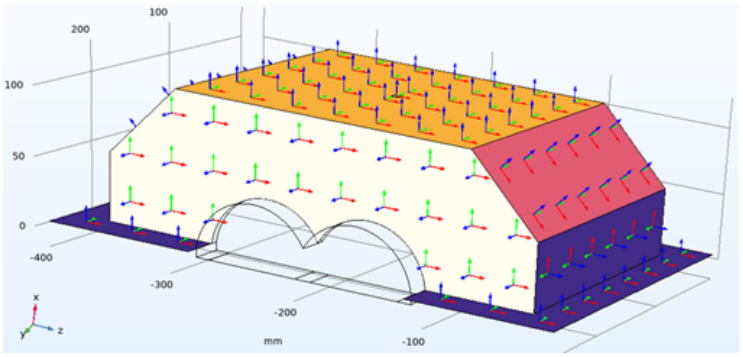

Figure 4.11: Laminate Local Coordinate Systems in the GBH

4.3.1.1 Bounds of the Control Parameters

To ensure that the lamina thicknesses remain within the same order of magnitude for each laminate area, it is possible to set variable lower and upper bounds for the optimization process. This approach also ensures that each ply angle makes up a minimum proportion of the plies in every composite patch.

The variable lower and upper bounds can be established by solving the equation system stated in the Equation 4.2, where min_ratio is the minimum ratio of the thickness of one orientation in relation with the total thickness, N_{layers} is the number of different orientation layers, and Th_Sum is an auxiliary variable that represents the sum of the four thicknesses.

By solving the equation system in terms of Th_Ori1, it is possible to define the variable lower and upper bounds for the parameter Th_Ori1. The lower bound can be formulated using Equation 4.3, and the upper bound can be formulated using Equation 4.4. A similar process should be carried out for the other thickness variables by adjusting the specific thickness variable to define its bounds. This method ensures that the optimization process maintains the desired balance of thicknesses across different fiber orientations.

To restrict the maximum global laminate thickness, each control parameter's upper bound should be defined as the maximum value between the calculated upper bound variable and the global maximum upper bound. Similarly, to restrict the minimum global laminate thickness, each control parameter's lower bound should be defined as the minimum value between the calculated lower bound variable and the global minimum upper bound. This approach ensures that the optimization process

maintains the desired range of thicknesses for the composite laminate, preventing excessively thick or thin laminates that may not meet the design requirements.

$$\begin{cases} Th\_Sum = Th\_Ori1 + Th\_Ori2 + Th\_Ori3 + Th\_Ori4 \\ Lower\ bound : Th\_Ori1 = min\_ratio \cdot Th\_Sum \\ Upper\ bound : Th\_Ori1 = (1 - min\_ratio \cdot (N_{layers} - 1)) \cdot Th\_Sum \end{cases} \tag{4.2}$$

$$Lower\ bound : Th\_Ori1 = \frac{Th\_Ori2 + Th\_Ori3 + Th\_Ori4}{1/min\_ratio - 1} \tag{4.3}$$

$$Upper\ bound : Th\_Ori1 = \frac{Th\_Ori2 + Th\_Ori3 + Th\_Ori4}{1/(1 - min\_ratio \cdot (N_{layers} - 1)) - 1} \tag{4.4}$$

For the application case, the min_ratio was set to 0.1, or in other words, the laminate will be constituted by at least 10% of each ply angle. Based on this criterion, the lower and upper bounds for all the thickness variables were defined accordingly.

4.3.1.2 Objective Function

The objective function in this optimization process is to minimize the total mass of the composite housing. The mass is calculated in each iteration by considering the total volume of the housing and the corresponding densities of the composite materials used. By minimizing the mass, the aim is to create a lightweight housing design that meets the required structural and performance criteria.

4.3.1.3 Critical Load Cases

The optimization process considered a bundle of critical load cases, similar to the ones used in the section 4.2.3, to determine the optimal design of the composite housing. The load cases consisted of radial forces of 20 kN and axial forces of 5 kN applied in the bearings region. In addition to these individual load cases, a combined load case was also considered, where both the radial and axial forces were simultaneously applied.

4.3.1.4 Optimization Constraints

The constraints in the optimization process are the maximum displacement in the bearing regions, since the housing has the requirement of supporting and ensuring the correct gear meshing by respecting the assembly tolerances of the rotating components, as discussed in the section 1.1.3. Within each iteration for each Load Case (LC), all the bearing displacements in all the direction are calculated and compared with the maximum allowable displacement tolerance. If any of the displacement values is higher than their respective tolerances, the associated composite

housing configuration is not acceptable. If the value of all the calculated displacements is lower than their respective tolerances, the design can be considered and the optimization proceeds.

In the application case, the bearings displacements were evaluated through probes in the bearings areas, as depicted in Figure 4.12. For the application example, the maximum allowable displacement tolerance was set to 80 μm in the three directions for all the bearings, leading to twelve constraint conditions in total. It is important to note that in industrial applications, the values for the maximum allowable displacement tolerances should be determined based on the specific design requirements and operational conditions. The defined constraints play a significant role in shaping the final design solution. Hence, it is important to set correct maximum allowable displacement tolerances.

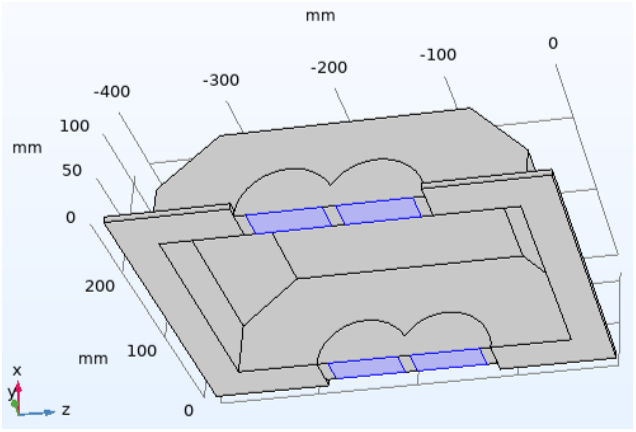

Figure 4.12: Composite housing design with the evaluation probes (blue) in the bearings regions

4.3.1.5 Optimization Method

The optimization of the fiber orientations and the respective lamina thicknesses, for the global design of the GBH, was performed using a Nelder-Mead method. This method, also known as the downhill simplex method, is an iterative numerical optimization technique used to find the minimum or maximum of an objective function in multidimensional space.

The optimization process starts by defining a starting design point, which in this case is an over-dimensioned composite housing design. Once the initial point is established, a simplex is initialized, comprising a set of points within the parameter space. The size of the simplex is influenced by the variable scales, which are determined by the specific characteristics of the problem being addressed. In the present case, the initial point encompassed fiber directions of $0°, 45°, 90°, and -45°$ with considerably over-dimensioned thicknesses.

Afterward, the objective function is evaluated at each vertex of the simplex and the vertices are sorted based on their objective function values, with the best (in this case, the lowest mass) at the first position and the worst at the last. After a reflection of the worst vertex is done through the centroid of the remaining vertices to obtain a new point. The objective function is evaluated at this new point and compared with the other simplex points. Depending on the comparison, one of the following actions is executed:

- If the reflected point is better than the best point, an expansion is done by reflecting the point even further.
- If the reflected point is worse than the second-worst point, a contraction is done by shrinking the simplex towards the best point.
- If the reflected point is worse than the worst point, an outside contraction is done by shrinking the simplex away from the worst point.
- If none of the above conditions are met, the reflected point is accepted as a new vertex.

The worst simplex vertex is replaced with the new point, allowing for the contraction of the simplex towards the best point. The process continues iteratively until termination conditions are met, reaching a maximum number of iterations or achieving the defined optimality tolerance. The composite housing optimization involves 32 control parameters, resulting in a 32-dimensional optimization space. Consequently, visually representing the operations becomes difficult. However, to aid comprehension, a simplified illustration of these operations is depicted in Figure 4.13 for the 2-dimensional case.

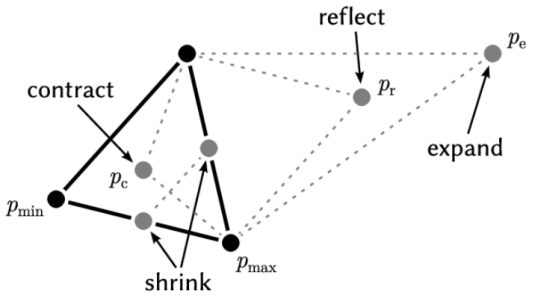

Figure 4.13: Optimization Operations with the Nelder-Mead Method [32]

For the effective operation of the optimization process, proper scaling and normalization of the control variables are essential. Scaling ensures that all the control parameters are within a similar order of magnitude, allowing for better convergence and avoiding potential numerical issues that may arise from wide differences in parameter magnitudes. Additionally, the definition of the optimality tolerance

significantly influences the effectiveness of the Nelder-Mead optimization method. Setting an excessively loose leads to fast convergence, but the solution will likely be far from the optimum. Conversely, a very tight tolerance can cause the optimization process to iterate for a prolonged period, even after convergence has been reached. Therefore, it is essential to attain the right balance in defining the optimality tolerance. It ensures that the optimization process efficiently reaches the best outcome. The optimal tolerance should be determined considering the trade-off between computational demand and the desired level of optimality, allowing for an efficient optimization process.

Once the aforementioned setup is established, the optimization algorithm iteratively adjusts the fiber orientations and layer thicknesses to find the combination that results in the lowest total mass while still satisfying the design constraints. By evaluating the performance of the composite housing under different loading scenarios, the optimization algorithm is able to identify the optimal fiber orientations and layer thicknesses that provide the desired structural integrity and strength while minimizing the total mass of the housing.

4.3.2 Optimization Results

In the application case, the optimization process involved 5973 iterations, ultimately leading to the attainment of the globally optimized results for composite housing. The fiber orientations were discretized in 15° increments. The optimized laminate stacking sequences obtained from the process are as follows:

- Front and back laminates: $[-60°/60°/0°/0°/-60°/60°]_s$
- Top laminate: $[45°/0°/75°/60°/-60°/-75°/0°/-45°]_s$
- Diagonal laminates: $[45°/0°/-30°/30°/0°/-45°]_s$
- Side laminates: $[90°/30°/-15°/15°/-30°/90°]_s$

The optimized fiber directions and their respective thicknesses for the front and back laminates are detailed in Table 4.12. Similarly, Table 4.13 provides the optimized fiber directions and corresponding thicknesses for the top laminate. For the diagonal laminates, the optimized fiber directions and their corresponding thicknesses can be found in Table 4.14. Lastly, the optimized fiber directions and their corresponding thicknesses for the side laminates are presented in Table 4.15.

These optimized results lead to a total thickness in the front and back laminates of 9.59 mm, a total thickness in the top laminate of 3.68 mm, a total thickness in the diagonal laminates of 3.77 mm and a total thickness in the side panels of 6.03 mm. The total mass of the composite housing coming directly from the optimization is 1.61 kg, which represent a 36.1% mass reduction in comparison with the original aluminium housing, which weights 2.52 kg. For reference, the composite optimization starting point mass was 4.17 kg, as mentioned before, a substantially over-dimensioned design.

Orientation	-60°	60°	0°	0°	-60°	60°
Thickness (mm)	1.46	0.74	0.20	0.20	0.74	1.46

Table 4.12: Optimization Results for the Front and Back Composite Laminates.

Orientation	45°	0°	75°	60°	-60°	-75°	0°	-45°
Thickness (mm)	0.22	0.23	0.23	0.23	0.23	0.23	0.23	0.22

Table 4.13: Optimization Results for the Top Composite Laminate.

Orientation	45°	0°	-30°	30°	0°	-45°
Thickness (mm)	0.24	0.24	0.47	0.47	0.24	0.24

Table 4.14: Optimization Results for the Diagonal Composite Laminates.

Orientation	90°	30°	-15°	15°	-30°	90°
Thickness (mm)	0.75	0.38	0.38	0.38	0.38	0.75

Table 4.15: Optimization Results for the Side Composite Laminates.

The optimization process involves exploring the continuous design space, allowing the optimization results to span the entire range of values within the defined lower and upper bounds. This flexibility enables the algorithm to freely select values that optimize the objective function within the given constraints, without being constrained to standard prepreg thicknesses or discretized values. However, it is important to consider the manufacturability of the composite design. In order to ensure the manufacturability after the optimization, it is necessary to discretize the thicknesses of each fiber direction according to the thickness of the prepreg lamina. This discretization allows for the use of readily available prepreg lamina. The following section presents the outcomes for a discretization of the optimization results.

4.3.3 Global Design Post-Processing

In order to have discrete layer thicknesses and maintain a conservative design, each thickness should be increased to the closest multiple of the prepreg lamina thickness. For the application, a 0.1 mm thickness was considered for the prepreg lamina. The discretized thicknesses for each fiber directions for the front and back laminates are detailed in Table 4.16. Similarly, Table 4.17 provides the discretized thicknesses for each fiber directions for the top laminate. For the diagonal laminates, the discretized thicknesses for each fiber directions can be found in Table 4.18. Lastly, the discretized thicknesses for each fiber directions for the side laminates are presented in Table 4.19.

During the discretization process, the thicknesses of the laminates were slightly increased, resulting in an increase in the overall mass of the composite housing. However, even with this increase, the final mass of the composite housing reached 1.78 kg, which is still significantly lower compared to the original aluminium housing

Orientation	-60°	60°	0°	0°	-60°	60°
Thickness (mm)	1.50	0.8	0.20	0.20	0.80	1.50

Table 4.16: Optimization Results for the Front and Back Composite Laminates.

Orientation	45°	0°	75°	60°	-60°	-75°	0°	-45°
Thickness (mm)	0.23	0.30	0.30	0.30	0.30	0.30	0.30	0.30

Table 4.17: Optimization Results for the Top Composite Laminate.

Orientation	45°	0°	-30°	30°	0°	-45°
Thickness (mm)	0.30	0.30	0.50	0.50	0.30	0.30

Table 4.18: Optimization Results for the Diagonal Composite Laminates.

Orientation	90°	30°	-15°	15°	-30°	90°
Thickness (mm)	0.80	0.40	0.40	0.40	0.40	0.80

Table 4.19: Optimization Results for the Side Composite Laminates.

that weighed 2.57 kg.

As discussed in the section, it is important to consider additional constraints when designing the laminates. One significant constraint is the avoidance of consecutively placing more than four plies with the same orientation. To address this, lamina shuffling is recommended, placing the prepregs with the same orientation intercalated with the prepregs aligned with others directions within the laminate structure. Commercial software solutions are available to facilitate this task, such as Altair OptiStruct, which features a ply stacking optimization module. The composite laminate layup should optimize strength, stiffness, and weight while also considering the manufacturability and cost.

In addition to the considerations mentioned earlier, stacking sequence rearrangement plays a vital role in optimizing the continuity of the laminate interfaces, ultimately leading to a more robust design for the global composite housing. This strategic reorganization of the stacking sequence enables the enhancement of overall structural integrity of the housing without increasing its mass.

Therefore, a rearrangement of the stacking sequence was performed in the specific application case to achieve these objectives. The resulting laminate stacking sequences, after the rearrangement, are outlined below:

- Front and back laminates: $[0°/-60°/60°/60°/-60°/0°]_s$
- Top laminate: $[0°/45°/75°/60°/-60°/-75°/-45°/0°]_s$
- Diagonal laminates: $[0°/45°/-30°/30°/-45°/0°]_s$
- Side laminates: $[90°/-15°/-30°/30°/15°/90°]_s$

To exemplify key advantages of this rearrangement: The connection between front laminate and top laminate will have the 0°, the -60° and the 60° orientations aligned in the stacking order. Figure 4.14 depicts the connection between the front and top laminates, illustrating the thickness change and the continuity of the layers with the same orientation. Similarly, the interface between the top laminate and the diagonal laminates showcases an alignment of the 0°, 45°, and -45° orientations in the same stacking sequence, further improving the integrity of their connection.

In the two previous examples, the coordinate systems of the affected laminates are aligned, however, there may be cases where the coordinate systems of the laminates are not aligned. This is evident, for instance, in the connection between the front laminate and the side laminate, as depicted in Figure 4.11. Consequently, specific considerations must be made during the rearrangement of lamina orientations. For example, the 0° orientation in the front laminate should be aligned in the same stacking sequence as the 90° orientation in the side laminate. Similarly, the 60° orientation in the front laminate should be aligned with the -30° orientation in the side laminate, and the -60° orientation in the front laminate should be aligned with the 30° orientation in the side laminate.

In this design step, it is also possible to slightly increase certain orientation thicknesses to allow a better match between laminates. To illustrate this in the application case, the thickness of the 0° orientation in the front and back laminates was increased from 0.2 mm to 0.3 mm. This thickness increase makes the total mass of the composite housing increase by 30 g to 1.82 kg. Hence, the final relative mass reduction from the aluminium alloy housing is 27.9%, which is a substantial weight reduction. The post-processing leads to a total thickness in the front and back laminates of 10.4 mm, a total thickness in the top laminate of 4.8 mm, a total thickness in the diagonal laminates of 4.4 mm and a total thickness in the side panels of 6.4 mm.

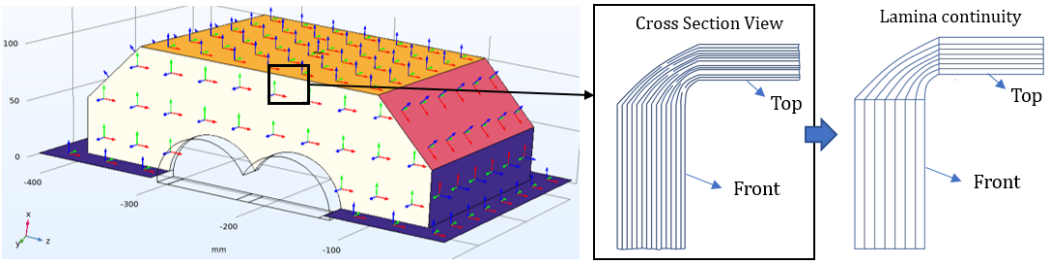

Figure 4.14: Connection between front and top laminates, illustrating the thickness change and the continuity of the layers with the same orientation.

4.3.4 Failure Criterion Evaluation and Safety

Following the optimization process and composite design post-processing, the subsequent step involved conducting a safety evaluation for the composite housing. This

evaluation aimed to ensure the structural integrity and reliability of the design. The same evaluation process outlined in the section 4.2.3 was utilized for this purpose. The computation of the safety factors based on the Tsai-Wu failure criterion was performed in the COMSOL Multiphysics (version 5.6). The lamina strength properties of the Carbon-Epoxy of the considered prepreg are stated in the Table 4.3.

As outlined before, to fully evaluate the structural integrity of the composite system, the safety evaluation procedure requires the selection of critical load scenarios. It is crucial to remember that various critical load cases may occur simultaneously, necessitating the evaluation of combined load cases in order to effectively capture extreme loading conditions.

In the safety evaluation of the designed housing, various LCs were taken into consideration. Firstly, a radial upwards force of 20 kN was applied to examine its response to vertical forces. Subsequently, a radial sidewards force of 20 kN was applied to assess its resistance to lateral forces. Finally, an axial force of 5 kN was applied to the bearings to evaluate the housing's resilience against axial loads. In addition to these individual load cases, a combined load case, referred to as LC4, was also examined. LC4 involved the simultaneous application of all the aforementioned load cases (LC1, LC2, and LC3). The purpose of LC4 was to test the system's ability to withstand the combined effect of all critical load cases acting on it simultaneously, representing an extreme load scenario.

The distribution of safety factors in the housing composite structure for different load cases can be observed in the following figures. Figure 4.15 illustrates the safety factor distribution for LC1, where the minimum Tsai-Wu safety factor is 7.14. Similarly, Figure 4.16 presents the safety factor distribution for LC2, with a minimum Tsai-Wu safety factor of 11.20. In Figure 4.17, the safety factor distribution for LC3 is depicted, and the minimum Tsai-Wu safety factor is 8.10. Lastly, Figure 4.18 showcases the safety factor distribution for LC4, where the minimum Tsai-Wu safety factor is 5.10. To provide a concise summary, Table 4.20 presents the minimum Tsai-Wu safety factor for each load case considered, ensuring a comprehensive overview of the results.

Load Case	Tsai-Wu Min SF
LC1	7.14
LC2	11.20
LC3	8.10
LC4	5.10

Table 4.20: Minimum Tsai-Wu Safety Factor in the optimized composite housing for each considered Load Case.

The majority of the composite design has Tsai-Wu safety factors significantly higher than 1, indicating a high level of safety. The lowest safety factors are near the bearings region; but they are still above 1. The minimum Tsai-Wu safety factor

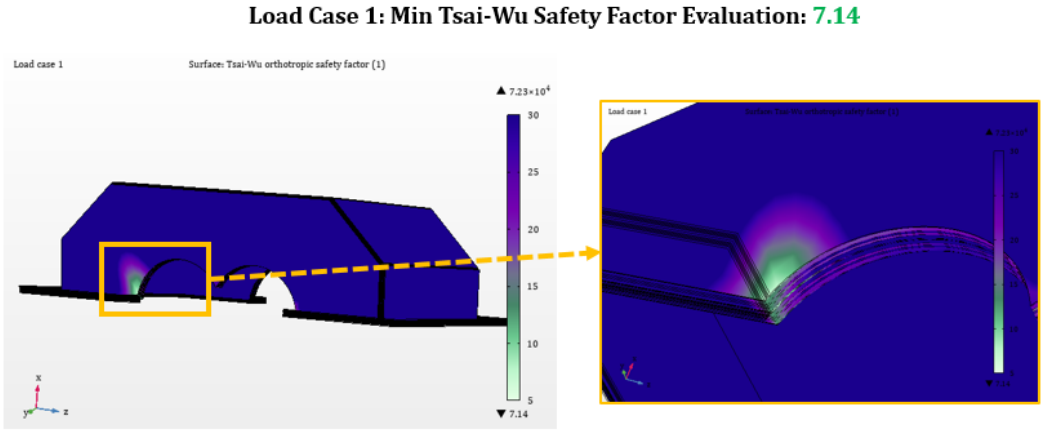

Figure 4.15: Safety factor distribution in the optimized housing composite structure for the LC1, zoom in the area of the minimum safety factor for the LC1.

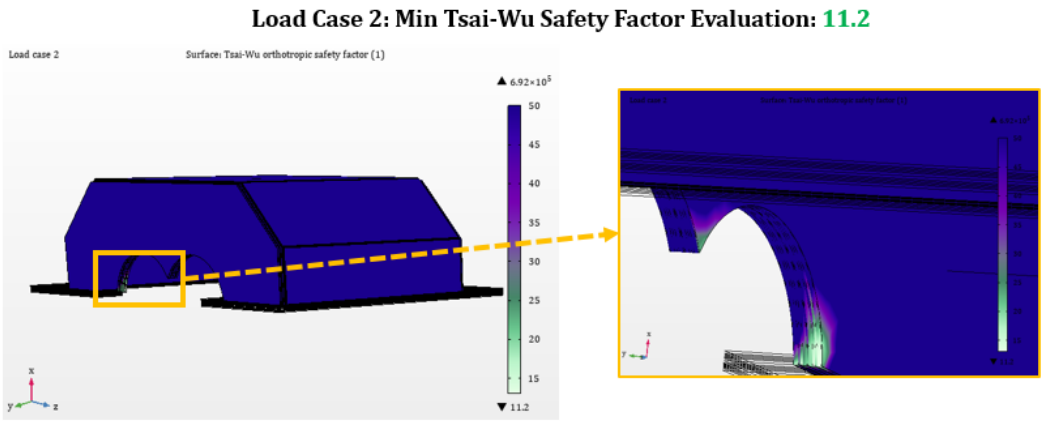

Figure 4.16: Safety factor distribution in the optimized housing composite structure for the LC2, zoom in the area of the minimum safety factor for the LC2.

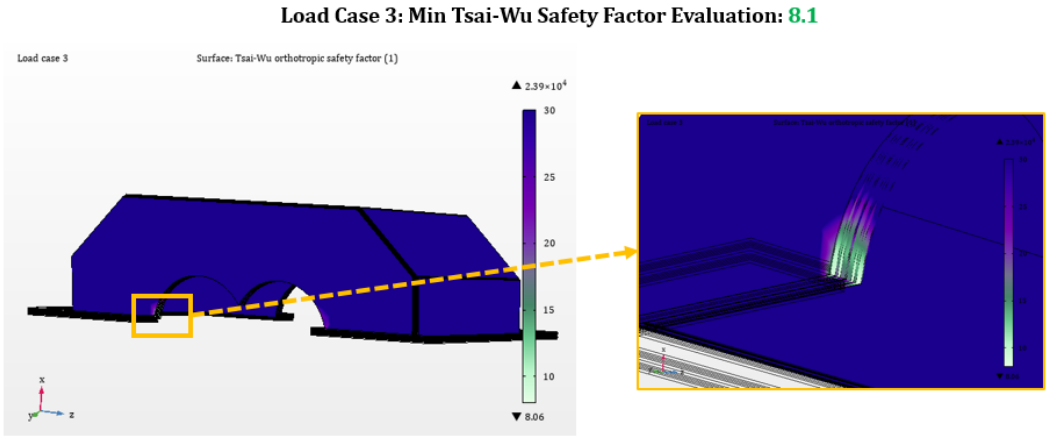

Figure 4.17: Safety factor distribution in the optimized housing composite structure for the LC3, zoom in the area of the minimum safety factor for the LC3.

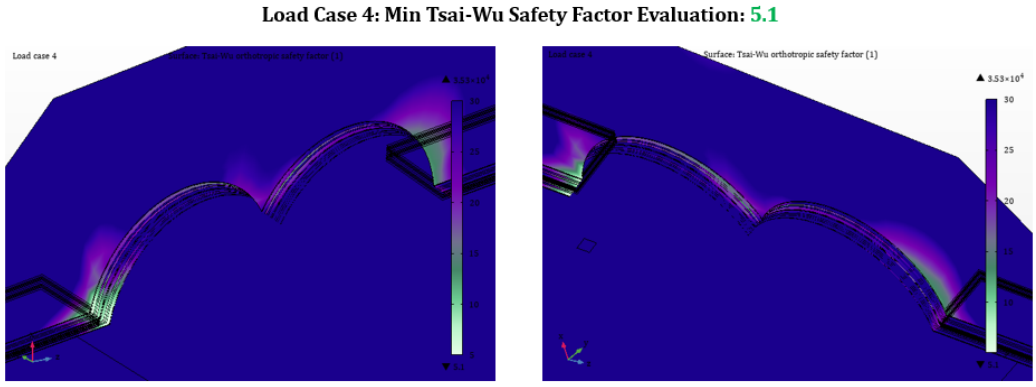

Figure 4.18: Safety factor distribution in the optimized housing composite structure for the LC4, zoom in the area of the minimum safety factor for the LC4.

obtained was 5.10 for a combined loading case, which is well above the critical threshold. Based on the Tsai-Wu failure criterion, the design is considered safe. As mentioned in the section 4.2.3, if there is a possibility for extensive material characterization, including failure mode testing, more complex approaches (such as Hashin, Puck, or LaRC03 criteria) can be further performed.

4.3.5 Composite Design Compliance with GBH Requirements

The composite design presented successfully fulfills the majority of the gearbox housing requirements outlined in the section 1.1.3. The design can provide mechanical support for the primary rotating gearbox components, coping with system loading generated by the transmitted torque. It ensures correct gear meshing by respecting the assembly tolerances of the rotating components.

The composite housing, devoid of any openings, offers mechanical protection for the inner components of the gearbox. In order to enable the assembly of the gearbox components, one requirement relates to the shape of the housing. The housing has a simple geometry that allows the assembly of the gearbox components, hence respecting this requirement. And finally, the composite housing design is considered safe based on the Tsai-Wu failure criterion.

However, there are three gearbox requirements that have not been addressed or evaluated thus far. These requirements include:

- Contain the lubricant inside the gearbox and guarantee the correct oil flow.
- Dissipate the inner generated heat.
- Provide good NVH characteristics.

The first mentioned requirement will be addressed in the section 4.3.5.1, while the second requirement will be discussed in the section 4.3.5.2. And the third, and last, requirement will be covered in the section 4.3.6 and in Chapter 5. The preliminary NVH assessment is presented in the section 4.3.6 and an in-depth NVH enhancement strategy with LRM solutions for composite GBHs is presented in Chapter 5.

4.3.5.1 Gearbox Lubricant Containment and Flow

There are two questions regarding the lubricant presence inside the gearbox housing. The first is regarding the housing geometry and the surface in the inner side of the housing, where the lubricant will be flowing. The housing inner geometry should allow the correct lubricant flow inside the GBH. And the second is related with the impact of the lubricant oil in the mechanical properties of the housing.

Concerning the geometric and inner surface issue, gearbox housing manufacturers currently conduct oil flow simulations and experimental oil flow evaluations in prototypes to validate the proper lubricant circulation within the gearbox. This process is also anticipated to be performed for composite housing prototypes, ensuring that potential issues are identified and addressed during the design process.

By conducting these studies, problems related to oil flow can be anticipated and addressed through subsequent redesign. This will ensure optimal contribution from the gearbox housing for the gear lubricant flow.

Conclusions about the effect of the lubricating oil on the mechanical characteristics of the composite housing can be drawn from recent research works. Kim et al. [85] conducted a study to examine the impact of lubricant on carbon-epoxy composites. The researchers evaluated UD lamina specimens and observed a minimal diffusion behavior ranging from 0.27% to 0.45%. Furthermore, they noted only a slight reduction in tensile strength, ranging from 0.72% to 2.21%. The study findings also indicated that a higher thermal curing conversion of the epoxy polymer, achieved through prolonged heating at high temperatures, resulted in the formation of a dense epoxy network on the surface. This, in turn, conferred an excellent oil barrier property to the CFRP material. This fact highlights the importance of fully curing the epoxy resin for preventing oil diffusion and degradation of the mechanical properties of carbon-epoxy composites. Additionally, the lamina with a higher epoxy resin content exhibited a thicker polymer layer on its surface. This layer functioned as a protective barrier, effectively preventing oil penetration into the composite material.

Instead of evaluating carbon-epoxy lamina specimens, Kazda et al. [84] conducted an investigation on larger specimens (310 mm long tubes with outer diameter 15 mm and inner diameter 9.9 mm, manufactured by filament winding). The study involved dividing the specimens into two groups: one group was tested immediately, while the other group was immersed in gearbox lubricant at an elevated temperature of 80 °C for a duration of 83 days. Static and dynamic tests were performed on the specimens using a 4-point bending setup. During the immersion period, the immersed specimens were regularly weighed to monitor mass changes and observe diffusion behavior. The results revealed no detrimental effects of the lubricant on the CFRP material and there was no evidence of oil diffusion. Furthermore, the flexural stiffness and maximal force of the specimens increased, while the degradation of stiffness during cyclical loading decreased following oil exposure.

Overall, the current research on the topic suggests that lubricating oil has a limited impact on the mechanical characteristics of CFRP with epoxy matrix, and in some cases, it can even improve certain properties such as stiffness and the maximal force the composite material can stand. Hence, the CFRPs with epoxy matrix are materials suited for building the GBH while respecting its requirement of containing the lubricant inside the gearbox and guaranteeing the correct lubricant flow.

4.3.5.2 Gearbox Heat Dissipation

Carbon-epoxy composites offer an excellent strength-to-weight ratio, high stiffness, and good resistance to corrosion. However, in terms of heat conductivity, they have relatively low values. The epoxy resin matrix, being a polymer, has poor thermal conductivity compared to metallic materials. The carbon fibers themselves have relatively high thermal conductivity, but the heat transfer within the composite

is hindered by the epoxy matrix. On the other hand, metallic materials, such as aluminium and steel, have much higher thermal conductivity compared to CFRPs. Metals have a highly ordered structure, with closely packed atoms, allowing for efficient heat transfer through the material. This property makes metallic materials excellent heat conductors. Therefore, the material modification from metallic materials to composite materials might have an adverse effect on the gearbox's ability to dissipate heat.

The heat transfer coefficients of aluminium and its alloys typically range from 80 to 250 W/m K, while CFRPs exhibit a lower heat transfer coefficient ranging from 0.5 to 6 W/m K [165, 177]. To enhance the heat conductivity of carbon epoxy composites, various techniques can be employed. One approach is incorporating highly conductive fillers into the composite matrix, such as carbon nanotubes or graphene. These additives can improve the overall thermal conductivity of the composite by facilitating heat transfer paths. Burger et al. [24] successfully increased the thermal conductivity of carbon composites by a factor of 10 using this technique. However, a major challenge lies in achieving a uniform dispersion of these fillers throughout the matrix while simultaneously maintaining the mechanical properties of the composite. Another method for augmenting thermal conductivity involves incorporating a copper mesh into the composites, as demonstrated by Wu et al. [184]. Wang et al. [177] introduced a novel approach to enhance the thermal conductivity of composites by utilizing three-dimensional high conductivity networks. Their study incorporated metal-coated carbon fibers to establish connection points between adjacent carbon fibers, thereby creating an efficient thermal conduction path and improving overall thermal conductivity.

Finally, a macro-level solution to dissipate the internally generated heat in the gearbox can be achieved by incorporating vapor chamber heat pipes into the composite housing. Vapor chamber heat pipes are hollow structures usually made of copper or aluminium. Inside them is a working fluid, often a low-boiling-point liquid such as water or an ammonia-based compound. When heat is applied to one section of the vapor chamber, the working fluid in that region evaporates due to the high temperature. The vaporized fluid moves to the cooler regions of the chamber, condenses back into liquid, and releases the absorbed heat. The liquid is then wicked back to the hot region using capillary action, completing the cycle. This passive heat dissipation technique offers notable advantages over relying solely on metallic inserts for improving heat dissipation. Firstly, vapor chamber heat pipes exhibit higher thermal conductivity, enabling more efficient transfer and dissipation of heat. Secondly, they mitigate the formation of localized hotspots by evenly distributing heat through vaporization and condensation across the entire chamber. Furthermore, due to their hollow structure, vapor chamber heat pipes are lighter compared to equivalent metallic inserts such as copper, providing an additional weight-saving advantage.

4.3.6 NVH Evaluation of the Composite Housing Solution

In order to evaluate the effects of the material change in the NVH signature of the housing, this section describes a vibroacoustic study on the housing noise emission. As a preliminary study, a modal evaluation of the design composite housing was performed to provide insights for interpreting the subsequent noise emission response results. Figure 4.19 displays the eigenmodes of the composite housing within the frequency range up to 5000 Hz.

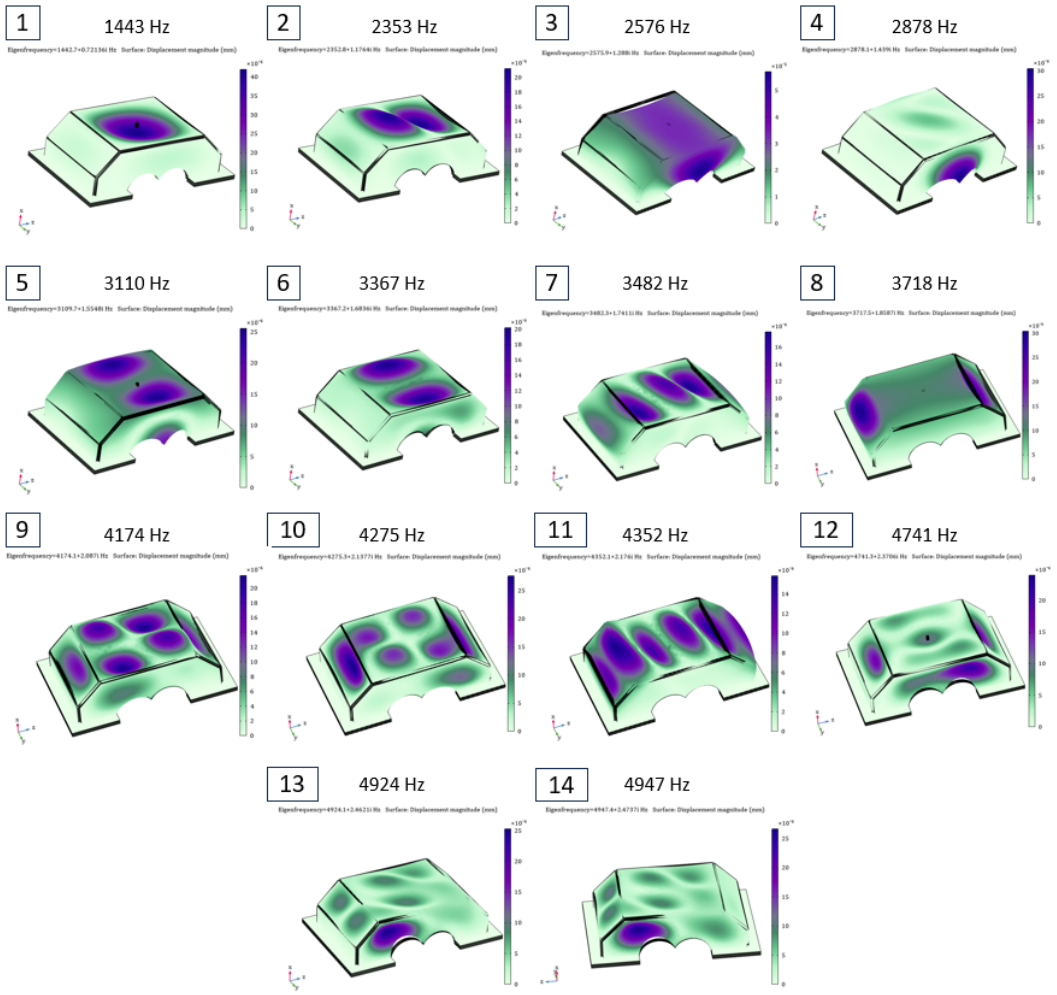

Figure 4.19: Designed composite housing eigenmodes up to 5000 Hz.

The structural-acoustic models were constructed similarly to the models presented in the section 2.3.1. To simulate the operating conditions, a characteristic loading pattern was applied to the bearing connections within the GBH, as depicted in Figure 2.14. The loading distribution for each of the four bearing connection regions is visualized in Figure 2.15. A fixed support was considered in the connecting interface to the other half of the GBH, as shown in Figure 2.14.

The numerical simulations were performed in the commercial software COMSOL Multiphysics (version 5.6). The model was solved in the frequency domain using the solid mechanics, pressure acoustics and composite materials modules, with an acoustic-structure boundary. The sound power radiated across the frequency spectrum was determined by integrating the far-field intensity over a hemispherical surface centered on the structure. This integration is represented by Equation 1.15. Sound Power Levels are expressed in decibels using the formula provided in Equation 1.16, where the reference power $P_0 = 10^{-12}$ W.

The structural-acoustic models closely resemble the one depicted in Figure 2.16, except for the housing geometries. Specifically, the housing designs employed in the models are those illustrated in Figure 4.1, where one model represents the aluminium housing and the other represents the designed carbon-epoxy composite housing. The material properties of the aluminium used in the analysis are presented in Table 3.3. Similarly, the material properties of the carbon-epoxy prepreg lamina are provided in Table 4.3. The complete composite housing design, comprising all lamina orientations and stacking definitions, is defined at the end of section 4.3.3. Due to the significant variation in damping characteristics of composite materials based on their specific configuration, and the absence of precise experimental data for the designed composite, two models were assessed for the composite case. One model incorporated an isotropic structural loss factor of 0.1%, while the other employed a factor of 1%. This allowed for the plotting of two composite responses, representing the maximum and minimum sound power radiated. It is expected that the actual manufactured composite housing will exhibit sound power radiated values within this range.

A hemispherical acoustic air domain of 0.4 m radius was set around the GBH. The considered air material properties depend on the ambient pressure p_A and temperature T. The speed of sound c and the density ρ are defined through the ideal gas law (assuming adiabatic behavior), according to Equation 2.22 where R stands for universal gas constant ($R = 8.3144621[J/(molK)]$), γ stands for the ratio of specific heats ($\gamma = 1.4$) and the M_n is the molar mass $M_n = 0.02897[kg/mol]$. The considered ambient pressure and temperature were 1 atm and 20°C (293.15 [K]), respectively. A PML was set between the radius of 0.35 m and 0.4 m to represent the open environment, details stated in the section 2.3.1. Regarding the FEM mesh, the global maximum element size was set as the speed of sound divided by five times the highest frequency to be modelled. The PML mesh has 4 elements through its thickness, similar to the Figure 2.17. The structural-acoustic models were constituted by 806758 elements, with an average and minimum quality of 67% and 20%, respectively.

The sound power radiated was integrated at a distance of 0.3 m, as specified in Equation 1.15. The computational analysis was performed on a high-performance server featuring two E5-2680 v2 processors running at 2.80GHz and equipped with 380 Gb of RAM memory. The comparison of the sound power radiated from the aluminium housing and the composite housing is shown in Figure 4.20. The figure clearly illustrates that the material change results in a noticeable shift in the

frequency location of the peaks in sound power radiation. Furthermore, the deformation patterns of the housing indicate a correlation between the peaks in sound power and the eigenmodes of the structure. Specifically, many of these peaks align with the local eigenmodes of the top plate, highlighting their influence on the radiated sound power.

The composite housing response is smoother in the lower frequencies in comparison with the response of the aluminium housing. The first eigenmode of the GBH is shifted from 845 Hz to 1440 Hz. For both composite configurations the sound emission peaks are placed in the same frequency location and the frequency response shape is the similar for both values of damping. However, as can be seen in the plot, the increase in damping reduces the amplitude of the sound emission peaks, by around 10 dB to 20 dB. The increase in the composite material damping provides a higher reduction in the NVH response, especially in the higher frequencies. The frequency response of the real composite response is expected to be between these boundary responses.

Predictably, it is evident that the initial peak in the emitted sound power, occurring at 1440 Hz, corresponds to the first eigenmode of the composite housing, as depicted in Figure 4.19. Similarly, the second peak aligns with the second eigenmode displayed in the aforementioned figure, and this pattern continues for subsequent peaks. A LRM metamaterial incorporation into the upper section of the housing, where the predominant movement contributes to the generation of most sound power peaks, can lead to a significant attenuation of the sound emission response. This investigation is going to be performed in Chapter 5.

Specifically, this approach is expected to reduce the peaks associated with eigenmodes 1, 2, 6, 7, and 9. Additionally, eigenmode 5, which encompasses the motion of not only the top part but also the front and back sections of the housing, is expected also to experience a partial attenuation.

In order to ensure an equitable comparison, the sound power radiated results were normalized by dividing them by the power injected into the structure. The total power injected is calculated by the summation of the power injected in each bearing, see Equation 2.23. The power injected for each bearing was determined through integration over the area of load application, as expressed in Equation 1.17. Figure 4.21 shows the ratio of the sound power radiated to the power injected in the structure, as given by Equation 1.18, for the aluminium housing and the composite housing.

The observed trends in the nominal results of the radiated sound power align with the findings observed in the normalized results. Although, the small fluctuations observed in the lower frequency range of the sound power results for both configurations are smoothed out when the results are normalized. This suggests that these fluctuations, which occur at low frequencies, are not associated with housing resonances. Instead, they are primarily linked to an increase in power injected into the bearings, which is dependent on the loading applied to the bearings or, in other words, the gear excitation. The normalization process successfully eliminates the influence of loading on the noise radiation response.

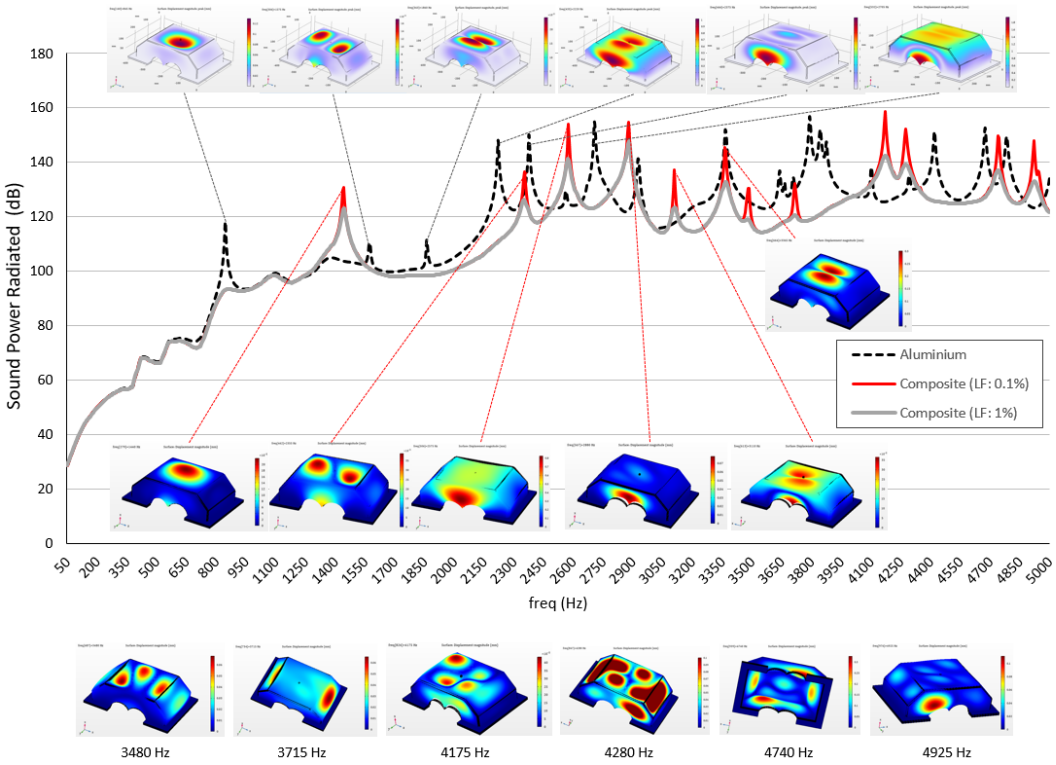

Figure 4.20: Sound power radiated comparison between the aluminium GBH (dashed black) and the composite housing configurations with 0.1% damping (red) and with 1% damping (grey), complemented with a number of housing deformation shapes.

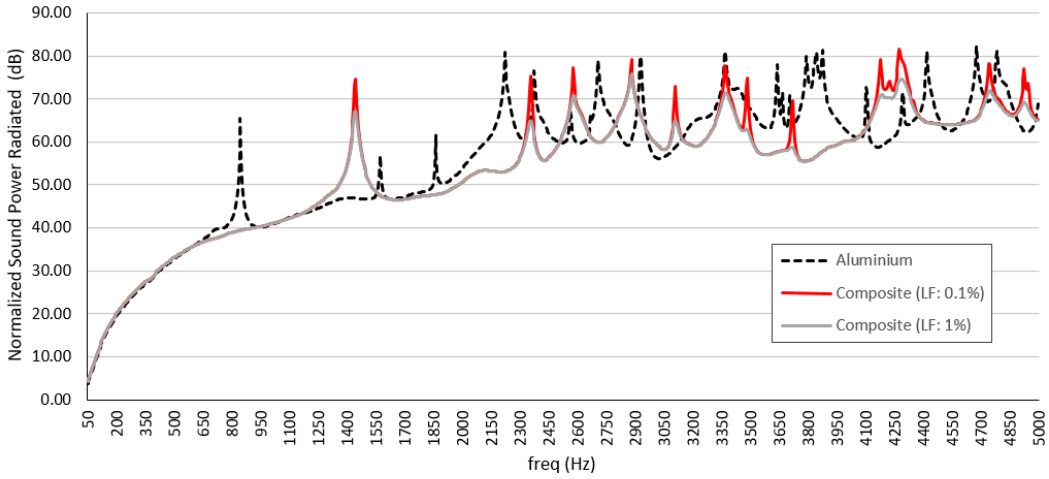

Figure 4.21: Ratio between the sound power radiated and the power injected in the structure of the aluminium GBH (dashed black) and the composite housing configurations with 0.1% damping (red) and with 1% damping (grey)

4.4 Final Remarks and Conclusion

Upon conducting a review and evaluation of potential alternative materials for GBHs, it was concluded that composite materials can offer benefits for its manufacturing in comparison with the traditional metallic design. This chapter presented two composite design approaches that can be applied for the development of GBHs.

The first approach utilized the classical composite design methodology based on the CLPT. The process began by identifying composite materials with equivalent or higher stiffness than the metallic materials currently employed in GBH manufacturing. This was followed by a static evaluation of the composite housing, comparing its performance to that of the original metallic design.

In addition to the aforementioned approach, another design method was introduced, capitalizing on the advantages of composite materials to achieve superior GBH designs. By optimizing lamina orientations and corresponding thicknesses across different areas, it becomes possible to create components that are capable and more lightweight. The design procedure was outlined, encompassing the definition of control parameters and their bounds, the objective function, the loading conditions definition, and the optimization method and constraints.

Significant considerations regarding manufacturability were addressed, particularly focusing on the utilization of standardized prepreg lamina thicknesses and ensuring fiber continuity in the various laminate interfaces. To ensure the safety of the designs, evaluations of failure criteria were conducted across all cases.

The proposed design process can be tailored to either simplify or enhance its complexity, recognizing the inherent trade-off between design and manufacturing complexity and the attainment of an optimal design solution. For instance, to simplify the process, the discrete orientation angles can be reduced, resulting in a more streamlined design approach. This is the case of some existing composite design methods found in the literature, which primarily focus on optimizing the thicknesses of pre-defined fiber orientations, such as 0°, 90°, 45°, and -45°.

The first composite housing design, employing a conventional laminate design technique, successfully replaced the metallic material with a carbon-epoxy composite. The material alteration resulted in 21% mass reduction (including the bearing parts) compared to the original aluminium design , while preserving the housing stiffness. The proposed global composite design process allowed to further reduce the mass of the housing, while respecting the housing requirements. In the application case, the mass of the final composite housing design was 1.82 kg, implying a remarkable 27.9% reduction in mass compared to the original aluminium alloy housing.

For the operation stage, two additional housing requirements were raised and discussed: ensure the appropriate lubricant flow within the housing and facilitate heat dissipation in the gearbox housing. It was concluded that the presence of lubricant oil is not anticipated to negatively impact the mechanical properties of the composite housing. Moreover, lubricant flow simulations and experimental prototype verifications can be carried out in a manner similar to traditional metallic

housings. In the case of heat dissipation, if issues arise, suitable techniques such as the implementation of vapor chamber heat pipes within the composite housing design can be employed to enhance heat extraction and dissipation.

It is important to highlight that the application of the proposed composite design method in industrial settings requires the establishment of maximum allowable displacement tolerances. These tolerances must be defined based on the specific design requirements and operational conditions of the application. This step is vital to ensure that the composite design meets the necessary performance criteria and operates within acceptable limits.

As stated in the literature review, automated composite manufacturing techniques are becoming more common in automotive industry. Hence, automated PCM procedures can be implemented in industrial production lines, to produce the designed composite housings cost-effectively. For the automated production of more intricate composite housing design, the FPP techniques, mentioned in the section 1.2.5, can be applied. To develop the inner mold design for the prepreg layering, its geometry should be the inverse of the housing model and specific manufacturing settings must be taken into account during the design process. For instance, the edges of the mold geometry should be rounded, and the design must facilitate the extraction of the composite housing once production is complete. In the manufacturing process of the composite housing, it is possible to incorporate an outer visual/cosmetic layer with a lower areal mass, serving primarily to enhance the aesthetics of the housing.

The proposed designs and techniques represent higher costs for the production of GBHs. Nevertheless, it is essential to recognize that costs are not static. They fluctuate based on various factors, including material availability, demand, the emergence of novel manufacturing techniques, and evolving technologies. In order to innovate, researchers and engineers should follow the motto of Isambard Kingdom Brunel (1806–1859), arguably the most eminent engineer of the Industrial Revolution. He took the view that "great things are not done by those who simply count the cost" [5].

It is crucial to be conscious of the environmental impacts of the GBHs production. This encompasses various aspects, such as the sourcing of raw materials, manufacturing processes, recycling and end-of-life. As time progresses, regulatory standards are becoming increasingly ambitious, setting higher minimum thresholds for the recycling percentages of vehicle parts and materials.

Regarding the sourcing of raw materials, they should be obtained from renewable sources. For composite manufacturing, resins of non-renewable origin must be avoided, and more eco-friendly solutions should be preferred. There are several examples of bio-based epoxy resins [121, 12, 133], that can be used for the manufacturing of composite GBHs.

The manufacture of GBHs should be done as close as possible to closed-loop production, hence it is of utmost importance to think about the recycling of the component and the recovery of its constitutive materials. A recent study from Zhao et al. [200], presented a process to recycle carbon-epoxy composite. The process

allowed near-complete recovery of the carbon fibers in the composite and the solvent used in the process, without producing any harmful waste. It was also possible to reuse the degraded epoxy resin in combination with the original epoxy resin system to prepare new resin material with good mechanical properties.

The NVH evaluation of the composite housing demonstrates a noticeable change in the frequency location of the sound power radiation peaks compared to the original aluminium housing. This change is directly linked to the modification of the housing's eigenmodes resulting from the implementation of the new composite design. And particularly, the majority of the noise emission peaks are associated with the local eigenmodes of the top plate. Furthermore, it was determined that the damping characteristics of the composite material significantly influence the noise levels of the response, particularly in the higher frequency range.

In conclusion, the proposed design approach harnesses the lightweight and high-strength properties of composites to achieve optimal results, ensuring that the housing's mass is decreased without compromising its structural integrity or safety considerations. The composite housing exhibits a significantly distinct NVH signature compared to the original metallic design. Particularly, there is a noticeable shift in the sound emission peak associated with the first eigenmode of the GBH, moving from 845 Hz to 1440 Hz. Since, the objective of this research is to develop innovative and lightweight designs for GBHs that possess desirable NVH characteristics, the forthcoming chapter will specifically concentrate on investigating LRM solutions for composite GBHs. As mentioned previously, recent advancements in the field of metamaterials can offer potential opportunities to leverage the NVH characteristics of GBHs. Hence, the focus will be on exploring simple and cost-effective LRM approaches that can be effectively applied in composite GBHs.

Chapter 5

Metamaterials for NVH Enhancement in Composite Gearbox Housing

This chapter examines the enhancement of NVH attributes in composite GBHs through the innovative application of metamaterial solutions. The central focus lies in the development and application of a membrane-based LRM solution in the designed composite housing structure. Sound power radiation analyses conducted in this study highlight that the integration of the LRM solution leads to a substantial reduction in sound emission, while incurring only a marginal increase in mass. The research findings also underline that a straightforward increase in the mass of the membrane-based LRM configuration does not necessarily yield significant improvements in the overall NVH profile of the GBH. The chapter extends its purview to practical implications for industrial applications of LRM solutions. It explores the feasibility of incorporating embedded LRM solutions within composite GBHs, emphasizing the potential benefits for real-world implementation. Furthermore, the chapter outlines strategies for the development of cost-effective LRM solutions utilizing a singular material composition.

Contents

5.1 LRM Solution for Composite GBH Application

5.1.1 LRM Design and Modelling

In Chapter 3, LRM solutions were developed for application in lightweight metallic gearbox housings. Similarly, in this chapter, LRM solutions will be explored in order to reach gearbox composite housings that are not only lightweight but also possess outstanding vibroacoustic behavior.

As mentioned in the section 3.4.1, a crucial step for the design of an LRM solution is the definition of its location in the GBH. As depicted in Figure 4.20, the elevated sound power radiated originates from the vibrations occurring in the upper part of the composite GBH. Accordingly, in this study, the top plate was targeted with an LRM solution to mitigate its vibration, and consequently the noise radiated. As shown in the composite housing sound power radiated plot over frequency, see Figure 4.20, there is a major sound emission peak at 1440 Hz. This frequency coincides with the first eigenmode of the composite housing, which corresponds to the loudspeaker movement of the top part of the housing. Furthermore, within this frequency range, there is an observable increase in the loading on the bearings, as illustrated in Figure 2.15.

Following the same design principles stated in Chapter 3, the LRM solution is going to be designed in a way that its resonating mechanisms are tuned for the lower frequency noise emission peak. This targeted approach aims to attenuate the more challenging lower frequency peak while also anticipating spectrum-wide attenuation, thereby reducing noise emission peaks at higher frequencies.

Considering the factors mentioned in the section 3.4.1, it was decided to utilize a uniform distribution of LRM UCs, even though it is acknowledged beforehand that the LRM solution may not be optimal. In order to achieve a compact design and enable better integration within the composite housing, a small UC was defined. For the LRM solution to be applied in the composite GBH, a UC size of 20 mm x 20 mm was considered, being possible to fit 110 (11x10) UCs in a rectangular pattern.

The extensive literature review highlights a wide range of UC shapes and resonant mechanisms. In Chapter 3, a flexible beam component with mass located at the tip (refer to Figure 3.14) was considered as a UC for the LRM solution. For the application in the composite housing, a different geometry of considered. In order to design an LRM solution tailored explicitly for the composite housing, allowing integration into the composite design and even potential embedding, a membrane-based LRM was considered. Despite the substantial differences in resonating geometries, both aim to address the issue of bending waves on the housing surface, which are the primary cause of GBH noise emission.

Despite the distinct design of the UC, it is crucial to uphold the primary UC design objectives outlined in the section 3.4.1. These objectives include ensuring that the LRM solution is lightweight, manufacturable and adaptable for mass production. The UC design should maximize the ratio of the modal mass of the relevant eigenmode by the total mass of the micro-resonator, minimizing any nonessential mass

addition. Hence, the dimensions of the functional/non-resonating parts should be minimized according to the manufacturing capabilities. Lastly, the designed LRM must be compatible with the composite structure and allow for easy integration within it.

The envisioned UC is constituted by a Polyamide (PA) membrane with a circular steel mass in the center, as seen in the Figure 5.1. Table 5.1 provides the mechanical properties of the considered PA. Steel was the selected material to act as concentrated mass due to its wide availability and low cost, allowing to obtain a cost-effective high mass concentration for the UCs. Steel material mechanical properties are stated in the Table 2.1. To keep the GBH housing lightweight, the global mass increase for the complete LRM solution, with 110 UCs, was limited to 150 g. Considering this limit and aiming for the previously stated design objectives, the UC dimensions were set. The supports for the membrane have a square section measuring 3 mm x 3 mm and a height of 2 mm. The membrane itself is 0.75 mm thick. The steel mass has a diameter of 7 mm and a height of 3 mm. As a result, the total height of the membrane LRM solution is 5.75 mm, making it a highly compact NVH solution.

Property	Symbol	Value
Young's Modulus	E	2 GPa
Poisson's Ratio	υ	0.4
Isotropic Loss Factor	η	5 %
Density	ρ	1150 kg/m^3
Glass Transition Temperature	T_g	85°C
Maximum Service Temperature	T_{max}	160°C

Table 5.1: Material Properties of the Polyamide (PA46 @25°C) [39]

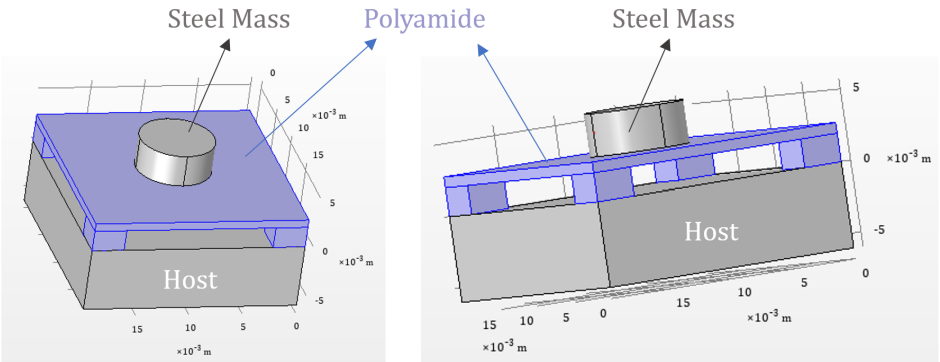

Figure 5.1: Membrane LRM UC to apply in the composite GBH

5.1.2 Membrane LRM Dispersion Curves

The dispersion curves were calculated using an inverse method for the reasons outlined in the section 3.2. The wave vector components, k_x and k_y, were spanned to obtain the corresponding eigenfrequencies. This allows the analysis of all propagation directions in the UC.

Employing the LRM analysis method stated in the section 3.2, an auxiliary variable k was introduced, which varied from 0 to 4. For k values ranging from 0 to 1, the wave vector $\mathbf{k} = (k_x, k_y)$ spanned from $(0, 0)$ to $(\pi/al, 0)$, where al represents the side length of the constitutive UC. Similarly, for k values ranging from 1 to 2, the wave vector $\mathbf{k} = (k_x, k_y)$ spanned from $(\pi/al, 0)$ to $(\pi/al, \pi/al)$. The ranges of $\mathbf{k}$ for k values from 2 to 3 and from 3 to 4 followed the patterns $(\pi/al, \pi/al)$ to $(0, \pi/al)$ and $(0, \pi/al)$ to $(0, 0)$ respectively.

The dispersion curves were determined by systematically varying the wave vector components, revealing the relationship between the eigenfrequencies and wave vectors for the considered LRM arrangement. Figure 5.2 displays the dispersion curves for the considered membrane LRM UC.

The membrane resonant mechanisms introduce discontinuities in the bending wave propagation dispersion curves. Notably, a complete BG is found between 1385 Hz and 1430 Hz, which is created by the up-and-down movement of steel mass in the membrane, which dampens the vibration of the structure and dissipates the vibrational energy. This behavior is crucial, as the BG acts as a vibration barrier for specific frequency ranges, preventing the transmission of unwanted vibrations through the structure.

5.1.3 Membrane LRM Solution Application in the Composite GBH

This section focuses on the implementation of the membrane LRM solution in the composite housing. Figure 5.3 provides a visual representation of the applied membrane LRM solution on the composite GBH, including a close-up view highlighting the specific area where the metamaterial integration took place.

The original aluminium GBH weighs 2.57 kg (excluding bearings), while the composite GBH weighs 1.82 kg (excluding bearings), resulting in a relative mass reduction of 27.9%. The membrane LRM solution increases the housing mass by 147 g, which corresponds to an 8% increase compared to the mass of the composite GBH. However, the introduction of the LRM in the composite configuration represents a substantially lower mass increase compared to the previously achieved mass reduction. Despite the increase in mass caused by implementing the LRM, the total mass of the composite GBH still demonstrates a substantial reduction of 23.5% when compared to the original aluminium GBH mass. The application of LRM technology offers a promising approach to maintaining a lightweight design.

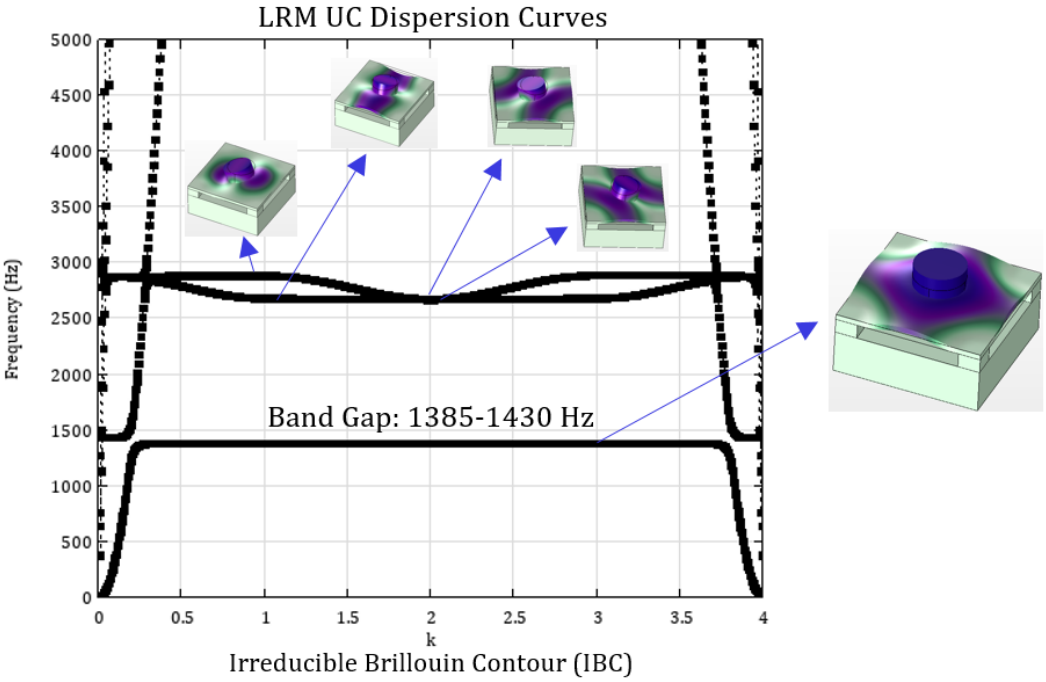

Figure 5.2: Dispersion curves of the membrane LRM UC including illustrations of the UC eigenmodes.

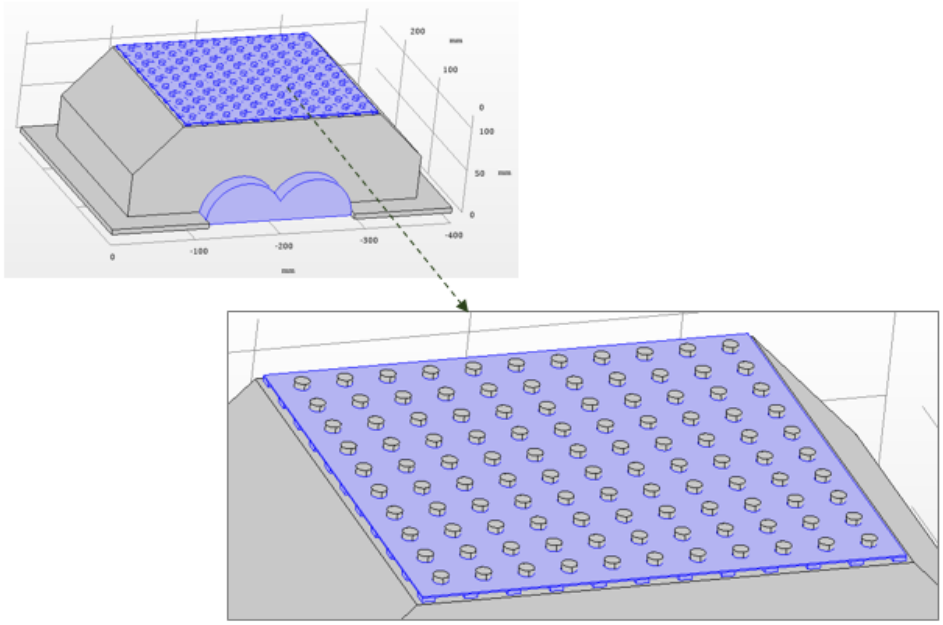

Figure 5.3: Membrane LRM solution applied in the composite GBH

5.1.4 NVH Improvements and Discussion

Numerical simulations were conducted to compute the sound power radiated by the composite gearbox housing with the membrane LRM solution applied under the same loading conditions described in Figure 2.15. The setup for these simulations remained consistent with the description provided in the sections 2.3 and 4.3.6.

The structural-acoustic model employed for the analysis of the composite GBH with the membrane LRM solution consisted of a total of 986209 elements. The elements exhibited an average quality of 65% and a minimum quality of 13%. The acoustic-structure boundary connection, considered in the model, was extended to encompass the composite GBH and the designed membrane LRM solution. This approach enables the consideration of noise emission resulting from the vibration of the LRM solution in itself during the simulation, leading to more realistic and accurate results.

The comparison of results among the original aluminium GBH, the composite GBH, and the composite GBH with the membrane LRM solution applied is presented in Figure 5.4. The results confirm the attenuation of the predicted BG between 1385 Hz and 1430 Hz for the membrane LRM solution. Moreover, there are additional changes in the response, which will be assessed and discussed in detail.

The incorporation of the LRM solution within the housing results in a 10 dB reduction in the first peak in sound power radiated. However, according to the plot, the designed membrane LRM solution offers a distinct form of attenuation than a traditional TMD. Rather than converting the main peak into two smaller peaks, it reduces its amplitude and causes a subtle shift of the mentioned peak. The reason for this is that the first peak noise emission is also associated with the movement of the front panel near the bearings' region. Therefore, it is not anticipated to achieve complete attenuation of this sound power radiated peak by solely applying the membrane metamaterial to the top part of the composite housing.

Nonetheless, in the targeted area, the LRM is expected to attenuate the vibration similarly to a TMD for the specific frequency it is tuned. Hence, it should be possible to observe this behavior in the meta-composite housing response. A further investigation allowed to observe the presence of mentioned two peaks, one at 1480 Hz and another at 1510 Hz, as shown in Figure 5.5. These peaks are located in the top part of the housing, where the membrane LRM is placed. However, the presence of the membrane LRM in the top part of the housing does not attenuate the movement of the front part of the GBH. Consequently, the introduction of the metamaterial does not completely attenuate the first peak.

Apart from the attenuation in the first sound emission peak, the LRM application induces a further attenuation across the considered spectrum, especially in the modes associated with the movement of the top part of the GBH, where the LRM was applied.

Starting with the most attenuated modes, significant noise emission reduction was observed in the second peak of sound emission at 2355 Hz, which is associated with eigenmode 2 of the composite housing (refer to Figure 4.19). Similar attenu-

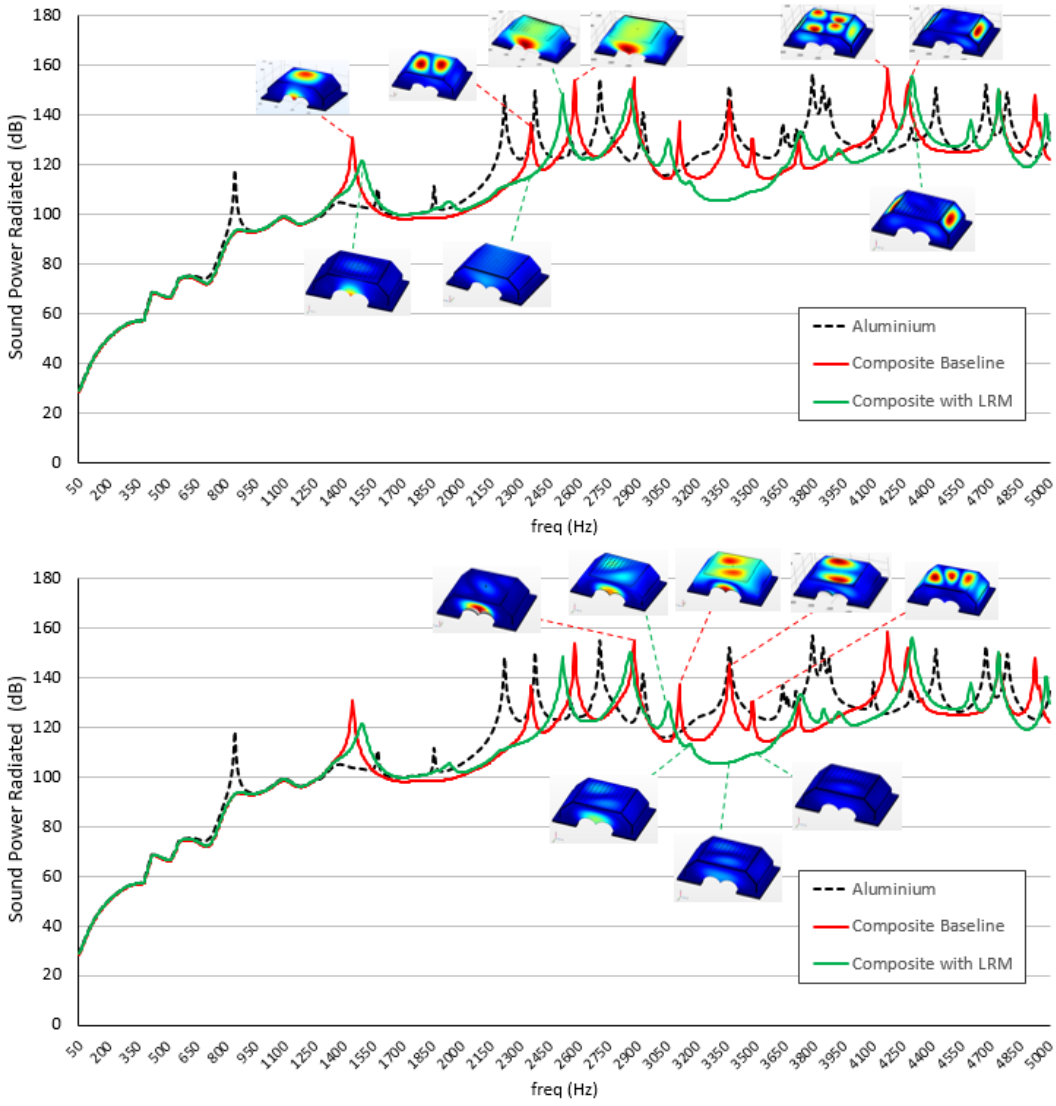

Figure 5.4: Sound power radiated comparison between the aluminium GBH (dashed black), the composite housing configuration (red) and the composite housing configuration with the membrane LRM solution applied (green), complemented with a number of housing deformation shapes.

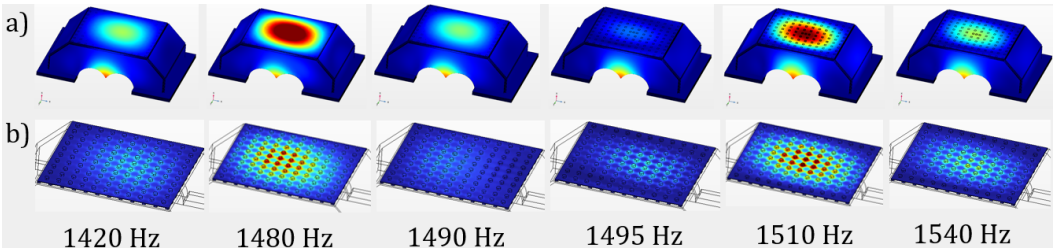

Figure 5.5: Displacements of the meta-composite housing for various frequencies in the vicinity of the first peak: a) composite housing displacements (scale 0 to 0.015 mm); b) membrane LRM displacements (scale 0 to 0.05 mm).

ation was observed in the peaks at 3370 Hz, 3485 Hz and 4175 Hz, corresponding to eigenmodes 6, 7, and 9, respectively. These modes are characterized by the movement of the top part of the composite housing, as depicted in Figure 4.19.

In terms of the peaks that remained mainly unaffected by the presence of the LRM, it is crucial to highlight that the peaks at 2575 Hz and 2880 Hz were not attenuated. These peaks primarily arise from the motion of the front and back GBH panels, corresponding to eigenmodes 3 and 4, as illustrated in Figure 4.19. Similarly, the peak at 3715 Hz and 4280 Hz remained unattenuated due to the piston-like movement of the diagonal panels, associated with eigenmodes 8 and 10, respectively, as shown in Figure 4.19. Lastly, the peak at 4740 Hz also exhibited no attenuation since it stems from the movement of both the front/back and diagonal panels, specifically eigenmode 12, as depicted in Figure 4.19.

In the case of the sound emission peak at 3110 Hz, which corresponds to a mixed-mode movement involving both the top panel and the front/back panels (eigenmode 5), it is important to note that the movement of the top panel was attenuated, while the movement of the front/back panels remained unaffected. This behavior is illustrated in the Figure 5.6. As a result, there is a partial attenuation in the radiated sound power at this frequency.

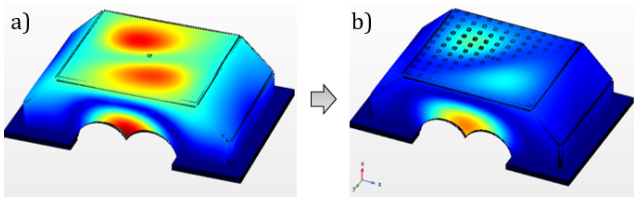

Figure 5.6: Housing displacements (linear scale from 0 to 0.035 mm) associated with the sound emission peak of the eigenmode 5: a) Baseline composite housing, b) Meta-composite housing.

It is imperative to emphasize that certain frequencies exhibit increased noise emission in the meta-composite compared to the baseline composite housing. This

occurs due to the introduction of new eigenmodes, for example at 4600 Hz, or the detuning of existing eigenmode peaks, which is the more frequent scenario. The Figure 5.7 highlights the introduction of the new eigenmode at 4600 Hz, inducing a new peak in the NVH response. The figure also highlights some displacement shapes responsible for increased noise emissions in particular frequencies around 3800 Hz. However, it is important to note that overall, the meta-composite response is significantly superior. The implementation of the LRM solution leads to an average sound power reduction of over 24%.

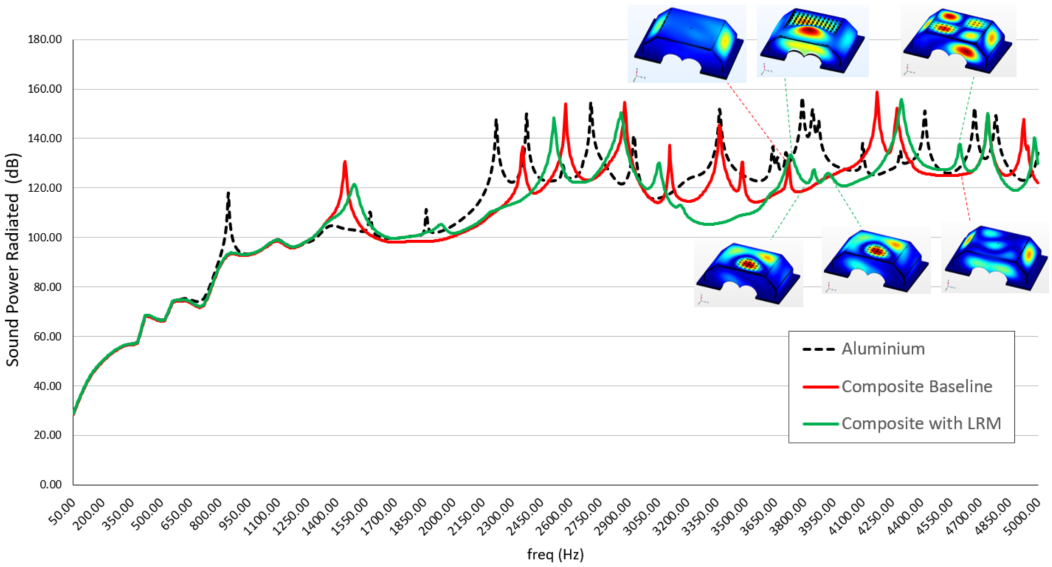

Figure 5.7: Meta-composite increased noise emission frequencies in the sound power radiated comparison between the aluminium GBH (dashed black), the composite housing configuration (red) and the composite housing configuration with the membrane LRM solution applied (green), complemented with a number of housing deformation shapes.

Regarding the final peaks at 4925 Hz and 4945 Hz, linked to the 13th and 14th eigenmodes of the composite housing, there is some attenuation in their amplitudes. However, drawing definitive conclusions based solely on this observation is challenging. This is due to the fact that the new eigenmodes frequencies fall at the end of the considered spectrum.

The sound power radiated results were normalized, dividing them by the power injected into the structures at each frequency. These normalized results allow a systematic and objective comparison. The ratio of the sound power radiated to the power injected in the structure was calculated using Equation 1.18 for the three configurations. The total power injected was calculated by the summation of the power injected in each bearing, according to the Equation 2.23. The power injected for each bearing was determined through integration over the area of load application, as expressed in Equation 1.17.

The comparison of the ratio of the sound power radiated to the power injected in the structure, including the original aluminium GBH, the composite GBH, and the composite GBH with the membrane LRM solution applied, is depicted in Figure 5.8. The normalized results demonstrate consistent trends with the nominal results in terms of sound power radiated, indicating that the membrane LRM solution effectively reduces the normalized sound power radiated as well. The conveyed observations and comments for the nominal results are valid for the normalized results of the sound emission. The implementation of the LRM solution leads to an average normalized sound power reduction of 22.5%.

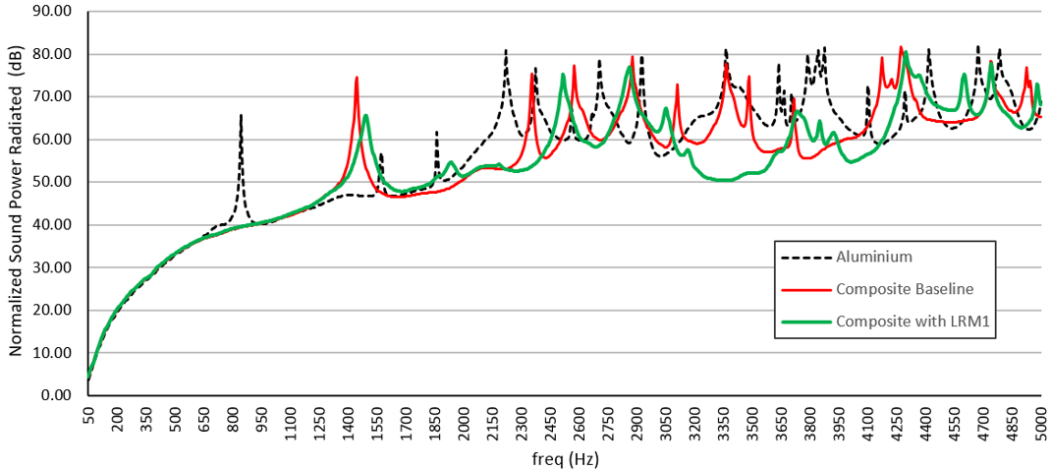

Figure 5.8: Normalized sound power radiated comparison between the aluminium GBH (dashed black), the composite housing configuration (red) and the composite housing configuration with the membrane LRM solution applied (green).

Ultimately, the membrane LRM solution effectively attenuates the sound radiation from the modes of the area where it is applied. The meta-composite housing exhibits improved acoustic performance, reducing specific peaks and providing overall noise improvement across a broad frequency range. These findings underscore the potential of lightweight membrane LRM solutions in achieving noise reduction in composite GBH applications.

In order to maintain the lightweight construction, the mass increase for the membrane LRM solution was kept to a maximum of 150g. Nonetheless, it is important to examine how the composite housing response could be further enhanced when not constrained by this mass limit. The following section investigates the potential noise reduction improvements with the increase of the membrane LRM solution mass.

5.1.5 Effects of Mass Increase in the Membrane LRM Solutions

For the development of membrane LRM solutions tuned for the same frequency but with greater mass increments, the geometric parameters were changed while keeping

the same global geometry and resonating mechanisms.

The previously studied membrane LRM solution was denominated membrane LRM1 and two new UCs were designed. These two new membrane LRM solutions were denominated membrane LRM2 and membrane LRM3. For the membrane LRM2, the UC steel mass diameter was increased to 8 mm and its height was increased to 4.8 mm. The UC membrane thickness was increased to 0.9 mm. For the membrane LRM3, the UC steel mass diameter was increased to 10 mm and its height was increased to 6.5 mm. The UC membrane thickness was increased to 1 mm. The supports for the membrane were kept the same for all the configurations. The UCs for the three considered configurations are shown in the Figure 5.9.

The resulting mass of the membrane LRM2 solution with 110 UCs is 263 g and for the membrane LRM3 the total mass is 500 g. The two new membrane LRM solutions are not only heavier but also less compact. The total height of the membrane LRM2 solution is 7.70 mm and the total height of the membrane LRM3 solution is 9.50 mm, in contrast with the 5.75 mm of the first membrane LRM solution. As a consequence, the integration in the composite will substantially increase its thickness.

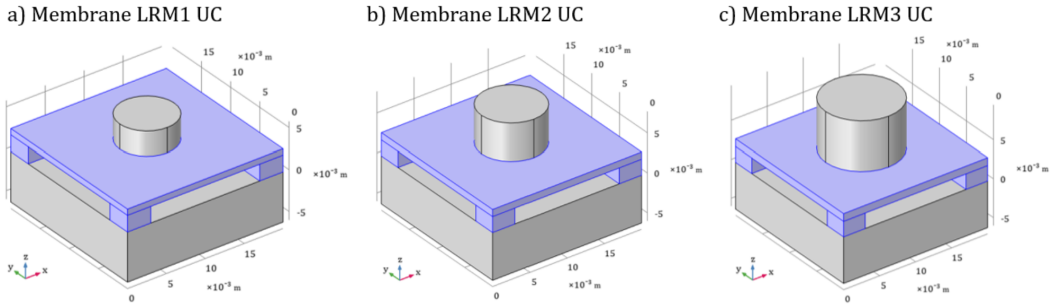

Figure 5.9: LRM UCs: a) Membrane LRM1, b) Membrane LRM2, c) Membrane LRM3.

The dispersion curves of all considered membrane LRM UCs are plotted in the Figure 5.10. The Figure 5.10 b) exhibits the dispersion curves for the membrane LRM2 UC and the Figure 5.10 for the membrane LRM3 UC. While the BG for the membrane LRM1 extends from 1385 Hz to 1430 Hz, for the membrane LRM2 it spans from 1384 Hz to 1447 Hz and for the membrane LRM3 it covers the range from 1385 Hz to 1442 Hz. The impact of geometry changes on the frequency location of the eigenmodes can be observed in Figure 5.10, where it is evident that the geometry changes shifted the other higher-order eigenmodes to lower frequencies.

Figure 5.11 illustrates the two new meta-composite configurations. One of these configurations incorporates the Membrane LRM2 solution applied in the baseline composite, while the other integrates the Membrane LRM3 solution into the baseline composite. These new configurations showcase the changes introduced by these two different membrane LRM solutions within the overall composite structure.

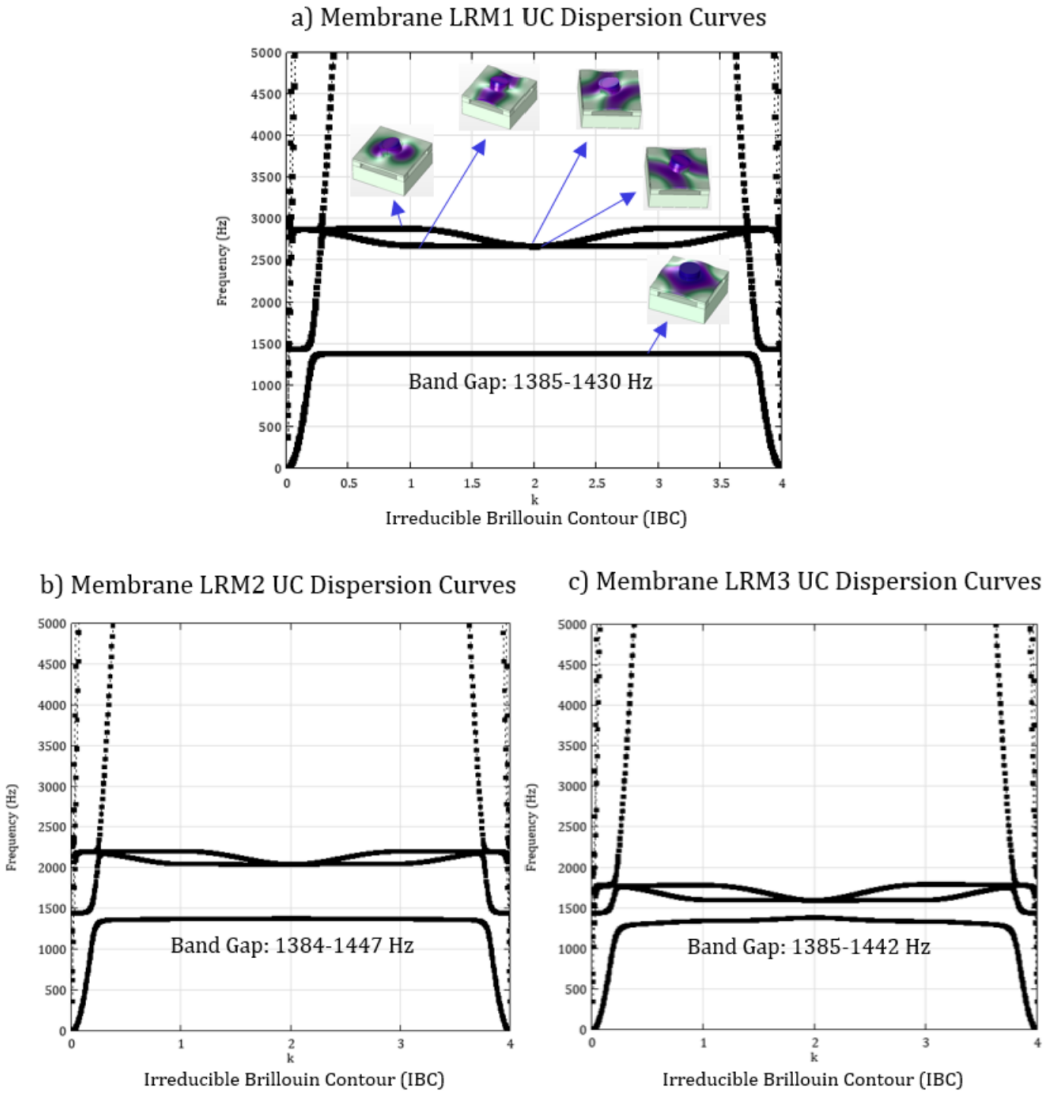

Figure 5.10: Dispersion curves of the membrane LRM UCs: a) Membrane LRM1, b) Membrane LRM2, c) Membrane LRM3.

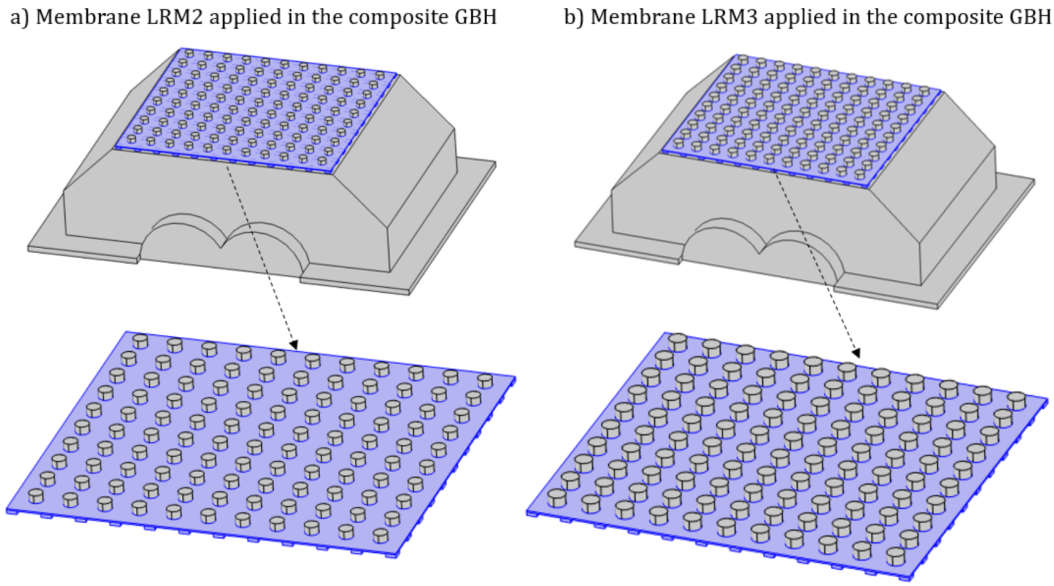

Figure 5.11: Membrane LRM solutions applied in the composite GBH a) Membrane LRM2, b) Membrane LRM3.

Figure 5.12 shows the plots of the sound power radiated by the three meta-composite configurations of over the considered frequency spectrum. Additionally, the plots are accompanied by relevant housing deformation shapes. To facilitate a more detailed analysis and discussion, certain deformations are grouped and highlighted separately. This visualization enables a comprehensive comparison of the sound power radiation behavior of each configuration across various frequencies.

As discussed in the previous section, the non-attenuated peaks in the response of the composite housing with the membrane LRM are mainly related with the movement of the other parts of the housing where the membrane LRM is not applied. Since the attenuation behavior was widely discussed in the previous section, in this section the analysis will focus on the differences in the response of the metamaterial solutions with different masses.

In the first noise emission peak, see highlight 1 in the Figure 5.12, all the metamaterial configurations attenuated the normal movement of the top part of the housing, where the metamaterial was applied. Besides, the global mass increase of the meta-composite configurations reduces slightly the movement of the front and back parts of the composite housing, attenuating further the sound power radiation in this peak. Moreover, the increase in the global mass of the new configurations shifts the peak to lower frequencies.

The second peak, see highlight 2 in the Figure 5.12, is associated with the back and forward movement of the top part of the housing in the axial direction. The steel masses integrated into the LRMs function as inertial masses during this movement, with the tendency to remain stationary, essentially opposing the motion induced by

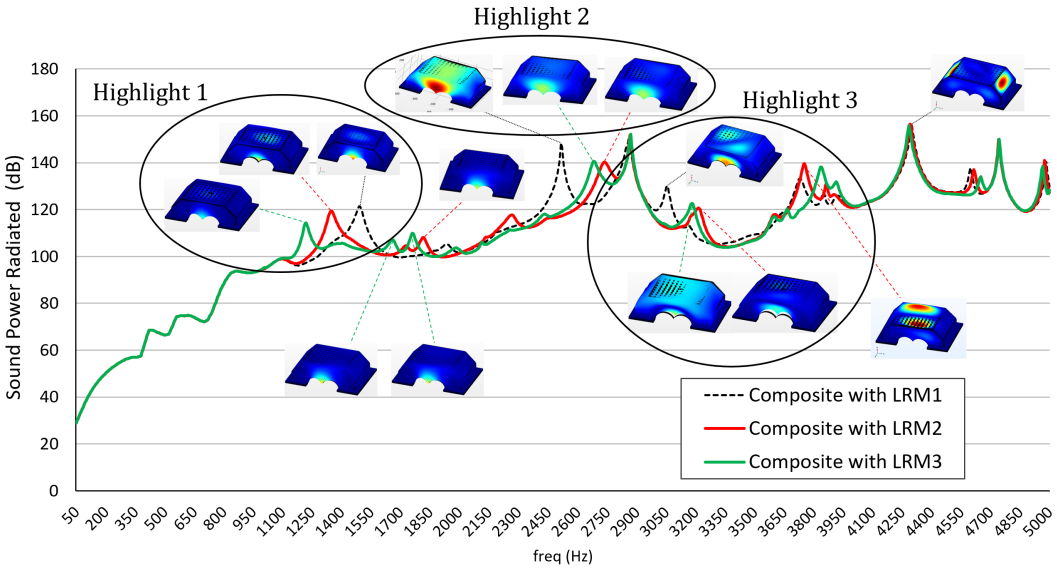

Figure 5.12: Sound power radiated comparison between the composite housing configuration with the membrane LRM1 solution applied (dashed black), the composite housing configuration with the membrane LRM2 solution applied (red) and the composite housing configuration with the membrane LRM3 solution applied (green), complemented with a number of housing deformation shapes.

the composite housing eigenmode. The Figure 5.13 depicts the discussed behavior. As a result, increasing the mass of the steel pieces will effectively reduce the motion associated with the second noise emission peak, attenuating the sound power radiated.

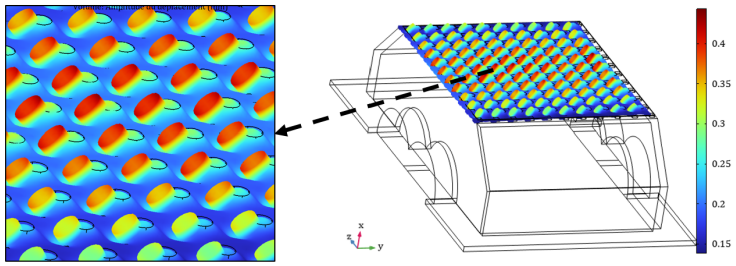

Figure 5.13: Metamaterial displacements for the membrane LRM3 solution at the second noise emission peak.

The highlight 3 in the Figure 5.12 underlines the further attenuation of the fourth sound emission peak, associated with the eigenmode 5 present in the Figure 4.19. For the membrane LRM1, this attenuation is described in the Figure 5.6. For the heavier membrane LRM configurations, this attenuation is even more pronounced

as seen in the highlight 3, further reducing the sound radiated amplitude.

The heavier membrane LRM solutions demonstrate a more pronounced fifth noise emission peak, which falls within the frequency range of 3700 Hz to 3800 Hz. This increased prominence in the peak indicates that these solutions exhibit more degraded NVH signatures in this frequency region. The remaining response is similar for all the analyzed configurations. Notably, the noise emission peaks at 2860 Hz, 4300 Hz, and 4750 Hz exhibit the same amplitude in each configuration.

The results display that the additional mass does not provide a substantial further improvement of the NVH response. Hence, increasing the membrane LRM mass is not an efficient way of enhancing the global GBH NVH characteristics. Since, the LRM mass is not the preponderant factor in its NVH attenuation, even with lightweight membrane LRM solutions, as is the case of the membrane LRM1, it is possible to achieve better NVH characteristics in the composite GBHs.

5.2 Industrial Application and LRM Manufacturing

5.2.1 Embedded Solutions in Industrial Production

The investigated membrane LRM solutions were applied in the outside part of the composite GBHs. However, it is possible to develop a similar metamaterial solution for embedding within the composite laminate. Figure 5.14 illustrates this embedded metamaterial composite concept.

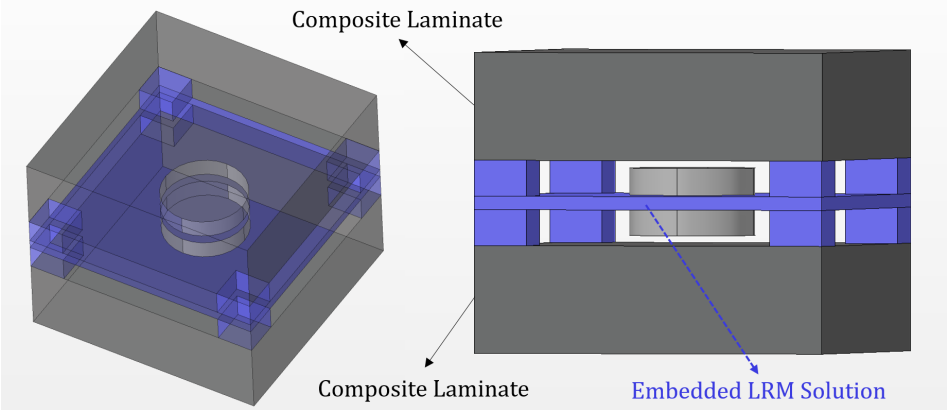

Figure 5.14: Envisioned UC example of composite embedded LRM solutions for GBHs.

The integration of a metamaterial solution within the composite laminate of a GBH offers potential advantages, including enhanced protection for the LRM solution and improved vibration isolation. Nevertheless, this approach comes with certain drawbacks: increased complexity in both the manufacturing and assembly processes and a reduction in the laminate stiffness. Careful consideration and trade-offs are necessary to determine the feasibility and suitability of implementing this

embedded metamaterial composite approach in practical applications.

Viscoelastic layers to intercalate with prepregs are an example of an already available vibroacoustic solution for embedding inside composite laminates. A commercial example from the company SMAC is shown in the Figure 5.15. They can be introduced before or after the composite laminate cure, since they are available in cured and uncured versions. Compared to existing commercial solutions, the proposed LRM concept offers distinct benefits.

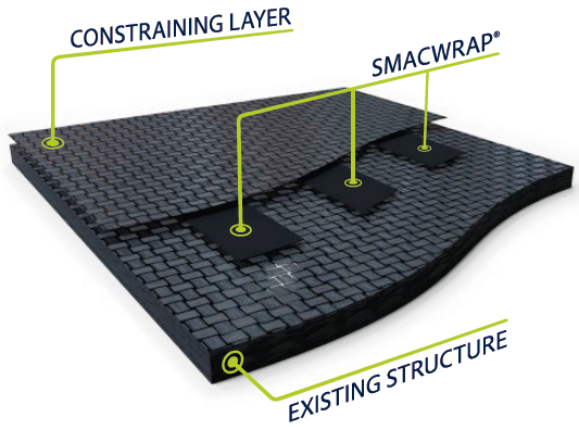

Figure 5.15: Viscoelastic layer SMACWRAP® to embed in composite structures, sourced from SMAC 2021 Catalog.

The commercial viscoelastic dampers demonstrate good attenuation performance at higher frequencies. However, they often face challenges in effectively attenuating low-frequencies. The LRM concept provides a promising enhancement to their attenuation behavior, offering the potential to address low-frequency vibrations more effectively and thereby significantly improving the overall vibroacoustic performance of composite structures.

An alternative compromise option for protecting the moving parts of the LRM solutions in the GBH is to apply an additional polyamide cover on the external surface instead of embedding the LRM solution within the laminate. This approach offers an effective mean of safeguarding the LRM components while avoiding the complexity associated with internal embedding. The polyamide cover provides a protective layer and ensures the durability and reliability of the LRM system while simplifying the manufacturing and assembly processes of the composite GBH.

5.2.2 Industrial Manufacturing: Strategies for Production Streamlining and Cost-effectiveness

It is acknowledged that within the automotive industry, the gearbox housing is typically considered a relatively inexpensive component. As a result, even a slight cost increase could lead to a significant relative cost escalation, rendering the proposed

solution potentially impractical for widespread industrial adoption. Therefore, any new GBH solutions designed for the automotive industry should carefully consider cost-effectiveness to ensure their viability and successful implementation.

The LRM solutions discussed in this manuscript have been composed of two materials thus far. However, for more efficient production, a significant streamlining can be achieved by using only one material. A LRM solution was developed for demonstration of this concept.

The concept involved designing a polyamide layer with embedded polyamide resonators tuned to 1440 Hz, aiming to create a BG within the frequency region of the sound emission peak observed in the section 4.3.6. For the UC, two resonators were positioned in opposing directions, dividing and balancing the moving masses.

The UC is depicted in the Figure 5.16. Even though this is just an illustration example, the dimensions of the considered resonators are as follows: the global width is 7 mm, the base has a height of 2 mm and a length of 5.5 mm, the beam part has a thickness of 1.5 mm and a length of 16 mm, and the tip of the resonator has a length of 6 mm and a height of 3 mm. The UC size was maintained at 20 mm x 20 mm.

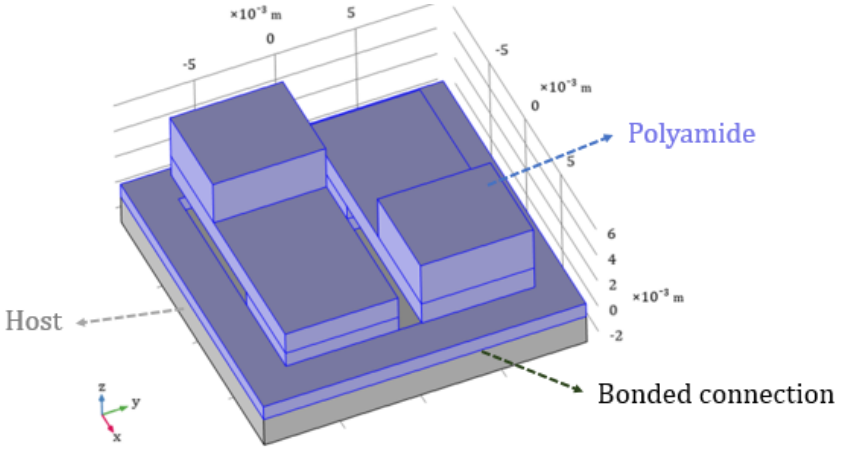

Figure 5.16: UC of an LRM solution with a single material (polyamide).

The dispersion curves were calculated for the proposed UC using an inverse method employing the LRM analysis method stated in the section 3.2. Figure 5.17 displays the dispersion curves for the full polyamide LRM UC. The dispersion curves plot denotes the creation of a complete BG from 1442 Hz to 1510 Hz. Vibration attenuation is anticipated in this frequency range for the areas where the LRM solution is applied.

The polyamide layers can be manufactured through compression injection molding, enabling cost-effective mass production. Subsequently, these layers can be bonded to various parts of the gearbox housing with adhesives. This streamlined manufacturing process significantly reduces the production and assembly costs associated with the LRM solution. Figure 5.18 shows the full polyamide LRM solution

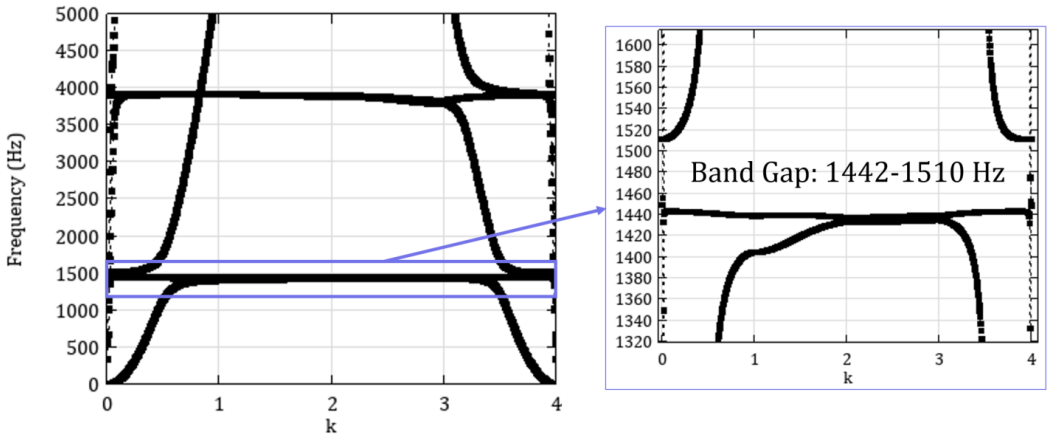

Figure 5.17: Dispersion Curves of the designed polyamide UC.

applied in the GBH.

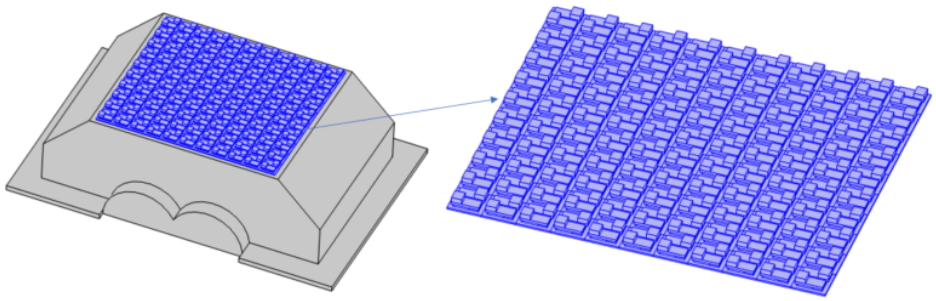

Figure 5.18: Single material (polyamide) LRM solution applied in the GBH.

It is important to note that this approach may result in a less compact UC design, necessitating a higher volume of moving mass due to the lower density of polyamide compared to metallic material such as steel. This trade-off must be considered when designing the LRM solution for technical applications.

5.3 Conclusion

This chapter focused on the design and application of metamaterial solutions to enhance the NVH characteristics of composite GBHs. A membrane LRM solution was developed and applied in the variable thickness composite housing designed accordingly to the composite design approach outlined in the section 4.3. NVH studies were performed and the results of the application of the membrane LRM solution were analyzed in detail. Overall, the implementation of the LRM solution led to an average normalized sound power reduction of 22.5% with a 150g mass increase.

Other membrane LRM solutions with higher masses were considered to evaluate if the increase in the moving mass of the LRM can further improve the global response of the composite GBH. The results displayed a slightly more attenuated response, but the additional mass does not provide a substantial further improvement of the NVH response. Hence, it was concluded that increasing the membrane LRM mass was not an efficient way of enhancing the global GBH NVH characteristics.

In the latter part of this chapter, the focus shifted to outlining industrial application considerations, specifically exploring the implementation of embedded LRM solutions within the composite GBHs, and the development of cost-effective LRM solutions utilizing a single material.

Conclusion and Perspectives

The primary aim of the research project was to enhance the design of gearbox housings, achieving a reduction in mass while attaining all the specific requirements. The research involved conducting an extensive examination of state of the art, with a focus on addressing unexplored challenges and potential innovative solutions to develop capable lightweight gearbox housings. By pushing the boundaries of conventional designs, this work aimed to establish new paradigms that can redefine the industry's perspective of gearbox housing possibilities.

A review of gearbox functions and their fundamental principles opened the manuscript. It subsequently focused on the housing specific requirements and trends in automotive gearboxes. Notably, investigations were conducted on gearbox housing traditional designs, materials, and manufacturing.

Afterward, the manuscript shifted to the topic of composite materials, concentrating in several aspects, namely composite matrices, reinforcing materials, and manufacturing processes. Particular emphasis was given to the reinforcement arrangements, specially on composite laminates, for which design and analysis methods were presented. Composite failure criteria and safety were discussed to ensure the reliability and durability of composite GBHs. In addition to this literature review, two other crucial aspects were examined. The first focused on the state-of-the-art manufacturing processes, essential to ensure the feasibility of mass production of composite GBHs. Furthermore, acknowledging the significance of environmentally friendly transportation and mobility solutions, an updated review of recycling methods for composite materials was conducted.

Subsequently, the manuscript delved into a review of the initial attempts to incorporate composite materials into GBH design, followed by an analysis of the latest documented applications of composites in this domain. However, it was evident from the analysis that the conducted studies were limited in scope, as they focused only on specific GBH requirements, overlooking the complete set of demands placed on GBHs. Furthermore, it was noted that the carried-out studies lacked composite design optimization, which is a crucial aspect to fully harness the potential benefits of these materials. Hence, this research encompassed a more holistic approach, considering all GBH requirements and incorporating advanced optimization techniques to develop superior composite-based solutions for GBHs. The composite materials literature review was concluded with an overview of the general current techniques employed for composite design optimization.

The literature review provided insights into NVH assessments and their corresponding metrics. It presented an overview of structure vibroacoustic interaction concepts and examined the existing noise-related challenges and regulations. Furthermore, the review described conventional vibroacoustic control methods and supplemented the discussion with illustrative examples of design processes geared towards vibroacoustic enhancement.

A comprehensive metamaterial study was performed, anticipating that LRM solutions could be designed for application in the GBH to enhance its NVH signature. The sub-wavelength nature of LRMs offers the advantage of enabling lighter and thinner vibroacoustic solutions, making them particularly suitable for addressing challenges in the low-frequency range, which are often difficult to tackle using conventional methods. The manuscript presented an overview of recent experiments involving LRM solutions in engineering applications. It also explored the LRM modeling aspects and the potential for optimization. The reviewed literature indicated that the process of optimizing metamaterial designs is particularly difficult in real-world applications. Hence, due to the industry tight development timelines, it was concluded the research should focus on evaluating if simple and fast design LRM solutions can yield substantial benefits when applied in GBHs.

The second chapter was centered around the design of lightweight metallic GBHs. Initial investigations led to the deduction of analytical expressions to define optimal dimensions of ribs to reinforce plate structures, in order to design lightweight ribbed panels. The study progressed with an exploration of a broader methodology involving topology optimization methods to enhance component geometry. The impacts of defined material and design constraints were evaluated on the results of the geometry optimization. Additionally, the research delved into modal optimization and conventional noise control techniques. Subsequently, noise radiation assessments were conducted, and a comparative analysis was carried out to examine the results obtained before and after applying topology optimization. The mass reduction of a gearbox housing degraded its noise and vibration behavior, inducing more noise emission peaks in the low-frequency range.

The third chapter explored the application of metamaterials for NVH control in metallic GBHs for improving their NVH signature. Preliminary studies were conducted to explore the influence of damping in the resonators and the LRM modelling options. The findings demonstrated that resonators with high damping exhibit a broader attenuation response and the solid modeling facilitates a more detailed representation of the LRM physical structure, leading to a more precise modelling of its behavior. According to the numerical simulations, implementing LRM solutions in GBHs reduce considerably the gearbox noise emissions. The analysis reveals that these LRM solutions not only attenuate noise emissions in the predicted BG, but they also provide a substantial average attenuation across the entire frequency spectrum.

The experimental results corroborated the efficacy of the LRM attenuation concept and the trends observed in the numerical simulations. They demonstrated significant attenuation in the predicted LRM BG and substantial broadband attenuation across the entire spectrum. The experiments revealed that vibration was not only attenuated in the areas where the LRM solution was applied but also in other parts of the GBH where no LRM was used. Furthermore, the experiments indicated that in the regions where the LRM was implemented, there was attenuation of in-plane vibration. Even though in-plane vibration might not directly contribute to noise emissions, this attenuation is important for limiting the propagation of

waves to other parts of the GBH. Consequently, this finding further underscores the positive impact of the LRM solution on reducing gearbox noise emissions. The LRM solutions represent a minimal increase in mass enabling the development of a lightweight GBHs with improved NVH characteristics.

In the fourth chapter, an analysis was conducted to identify prospective substitute materials for the GBH to decrease its mass. It was determined that composite materials could be an advantageous alternative to the conventional metallic design. Therefore, the research focused on the design of the composite GBHs. The first design followed a classical composite design approach according to the CLPT. In order to capitalize on the advantages of composite materials a new composite design process was developed.

The composite design process optimized both the lamina orientations and corresponding thicknesses across different areas. In the application example, where an aluminium GBH design was substituted by a carbon-epoxy composite GBH design, the conventional composite design method allowed a 21% mass reduction, while the proposed global composite design process allowed a 27.9% reduction in mass. Considering the inherent trade-off between optimal design and manufacturing complexity, the proposed design process might have its complexity adjusted. An analysis of all GBH requirements was carried out in order to reach a feasible and industrially applicable composite design. The rising adoption of automated composite manufacturing in the automotive industry, can enable the cost-effective production of composite housings using PCM procedures, while FPP techniques can be employed for more complex housing designs.

The proposed design approach harnesses the lightweight and high-strength properties of composites to achieve optimal results, ensuring that the housing's mass is decreased without compromising its structural integrity or safety considerations. The composite housing exhibits a significantly distinct NVH signature compared to the original metallic design.

The fifth chapter was dedicated to improving the NVH characteristics of composite GBHs through the application of metamaterial solutions. A membrane LRM solution was developed and applied to the designed composite housing. Detailed analysis of NVH studies revealed that the implementation of the LRM solution resulted in a considerable reduction of the sound power with a low mass increase. Moreover, it was concluded that increasing the membrane LRM mass was not an efficient way of enhancing the overall NVH characteristics of the GBH. Considerations were outlined regarding industrial application of LRM solutions, exploring the potential implementation of embedded LRM solutions within the composite GBHs and the development of cost-effective LRM solutions using a single material.

Holistically, this work was dedicated to developing practical GBH solutions with recent advancements in diverse scientific domains, creating a liaison between the research world and a relevant engineering application. Chapters 2 and 4 provided techniques to reduce the mass of GBHs by optimizing their designs and by incorporating new materials. As mentioned in the concluding remarks of Chapter 4, presently, the composite housing design entails high manufacturing costs. Hence,

they might just be economically viable for high-end vehicles. For lower-cost vehicles, where cost is the decisive factor, the adoption of the design principles outlined in Chapter 2 facilitates the creation of lighter and more cost-effective alternatives, maintaining the conventional metallic materials.

In parallel, chapters 3 and 5 proposed lightweight passive LRM solutions specifically designed to improve the NVH characteristics of GBHs. These solutions are cost-effective, as they can be conceived through a simple design process and do not require a control system. They provide noise and vibration attenuation to a targeted hard-to-address low-frequency range and, additionally, provide broadband attenuation. The findings of this study offer a step towards the industrial application of LRMs in GBHs and EV motor housings, offering a promising solution to the current conflicting design challenges without compromising efficiency or incurring substantial additional costs.

Appendices

Appendix A

Experimental Results - GBH with LRM solution

A.1 Comparison between the normalized acceleration $(m/s^2/N)$ of the baseline configuration and the configuration with the LRM applied for all the accelerometers placed on the housing structure

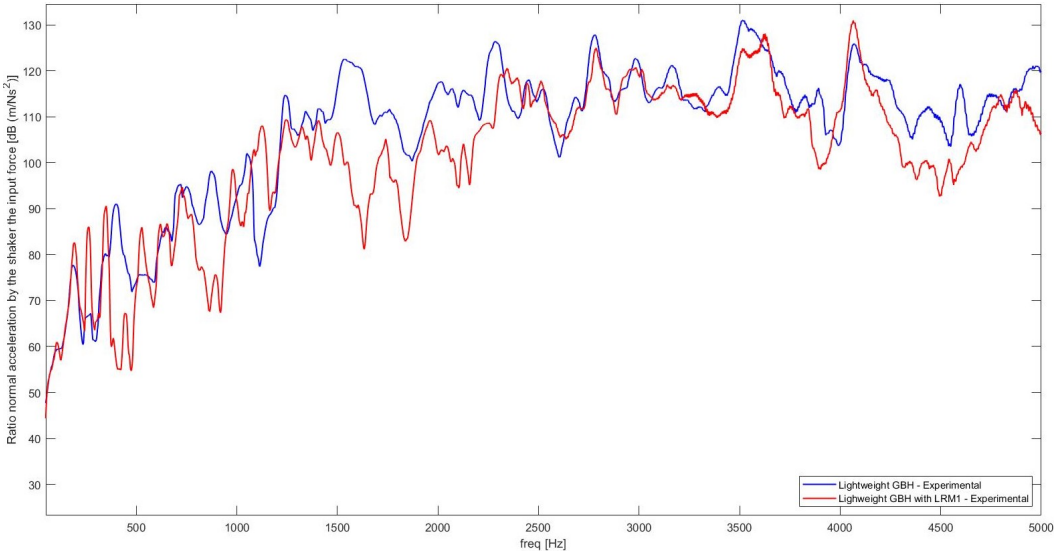

Figure A.1: Normalized acceleration at the position P1.

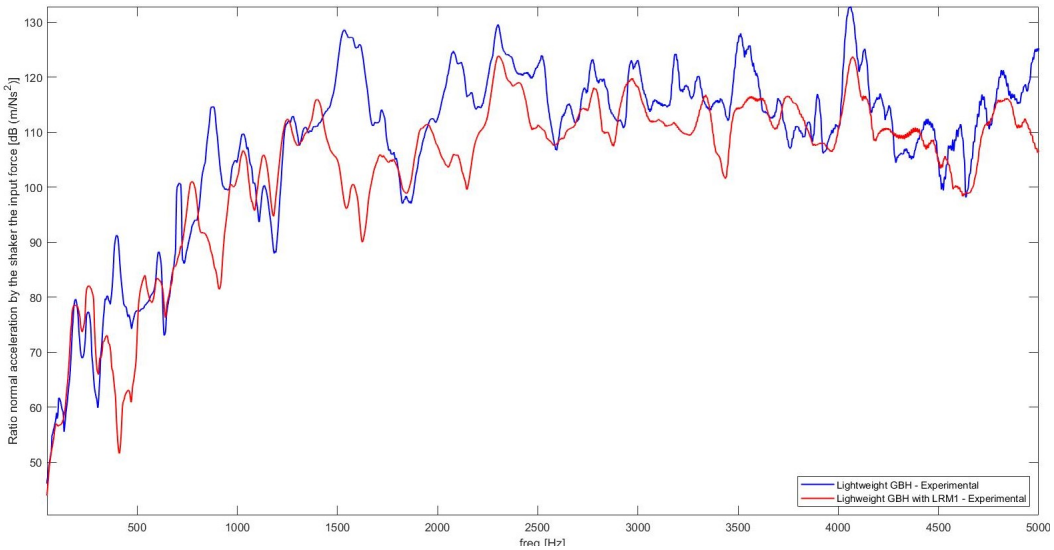

Figure A.2: Normalized acceleration at the position P2.

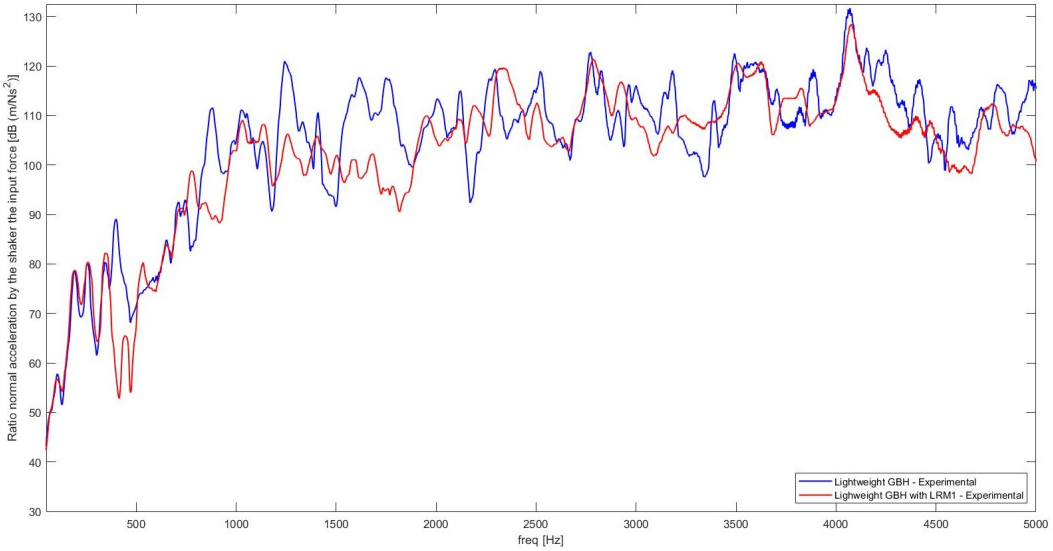

Figure A.3: Normalized acceleration at the position P3.

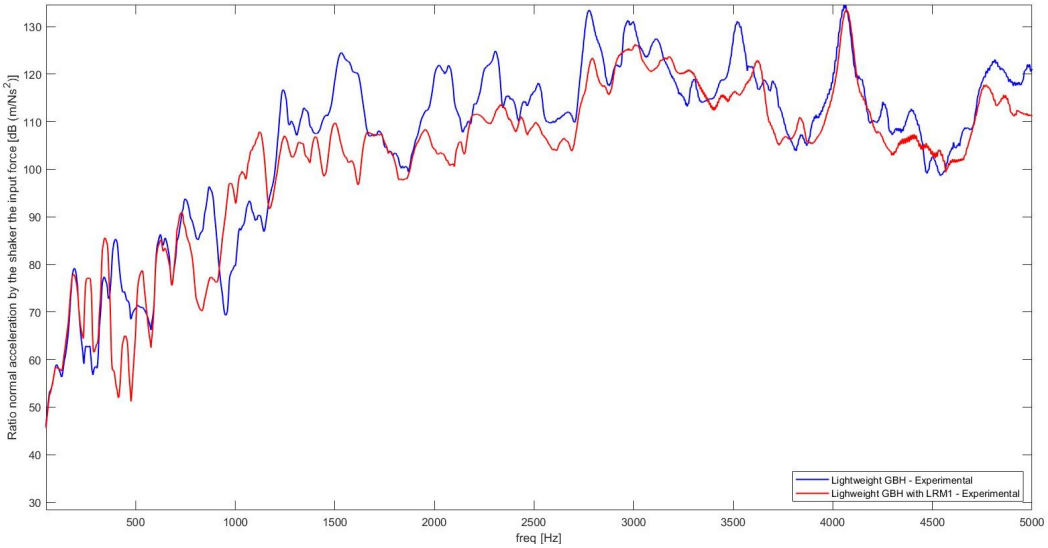

Figure A.4: Normalized acceleration at the position P5.

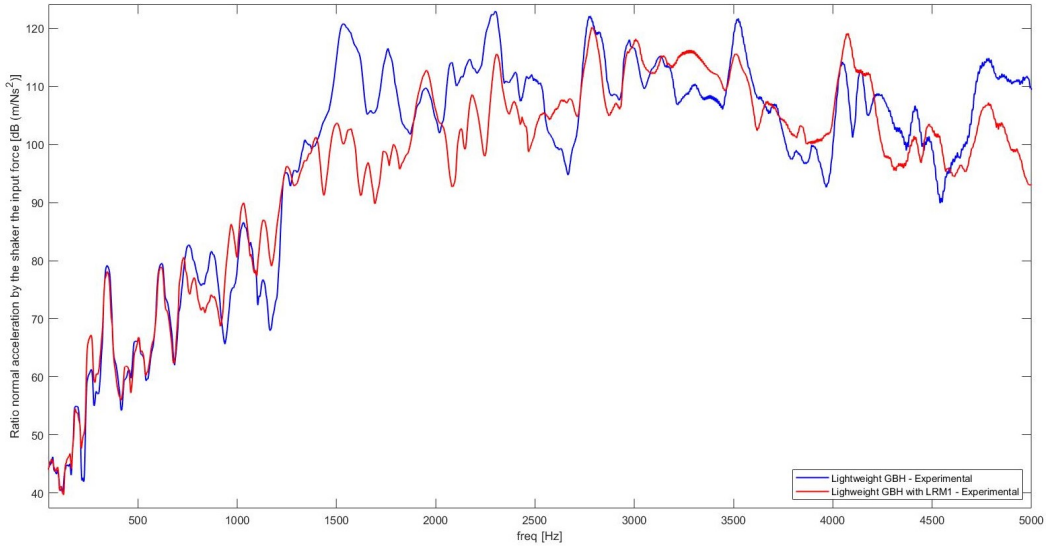

Figure A.5: Normalized acceleration at the position P11 in x direction.

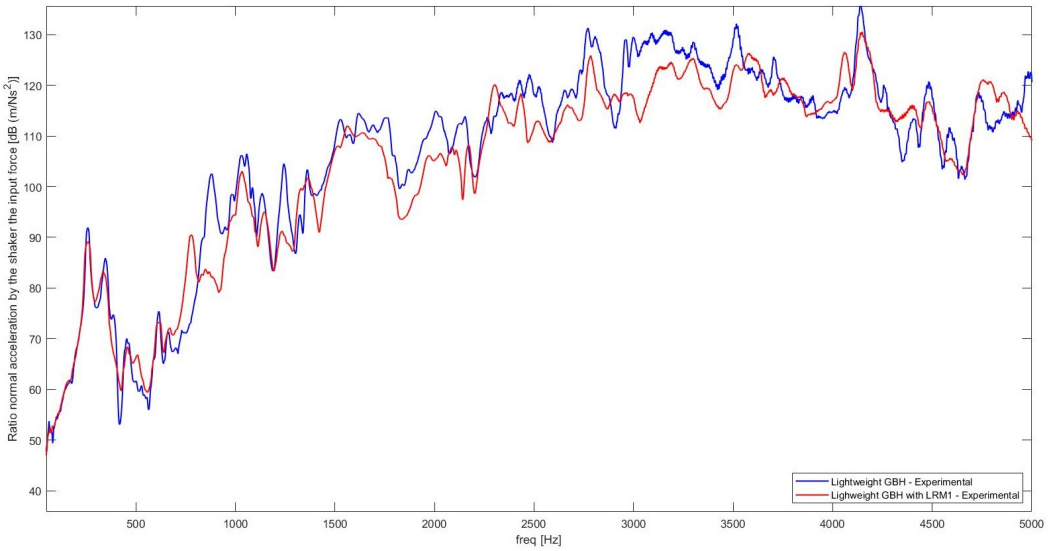

Figure A.6: Normalized acceleration at the position P11 in y direction.

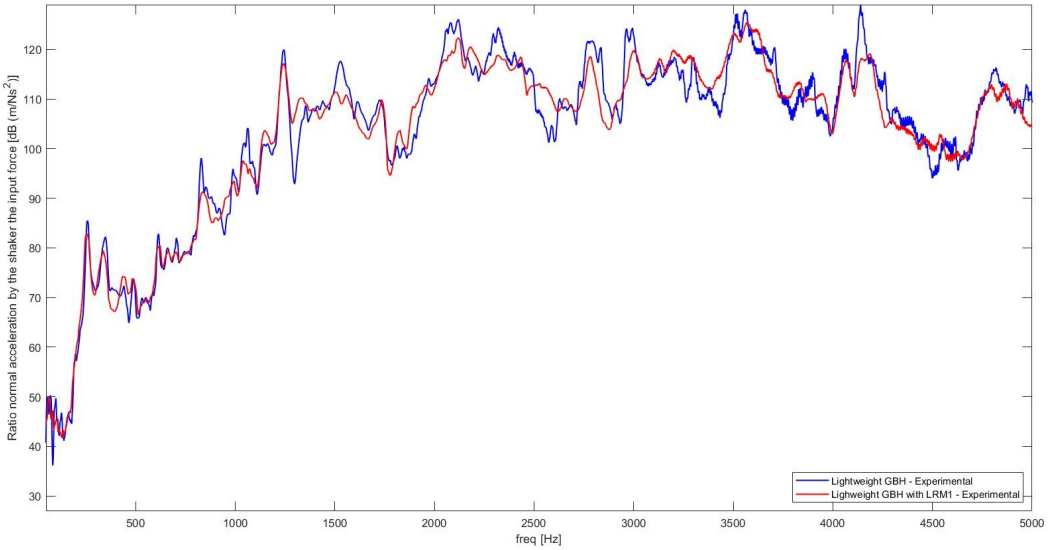

Figure A.7: Normalized acceleration at the position P9.

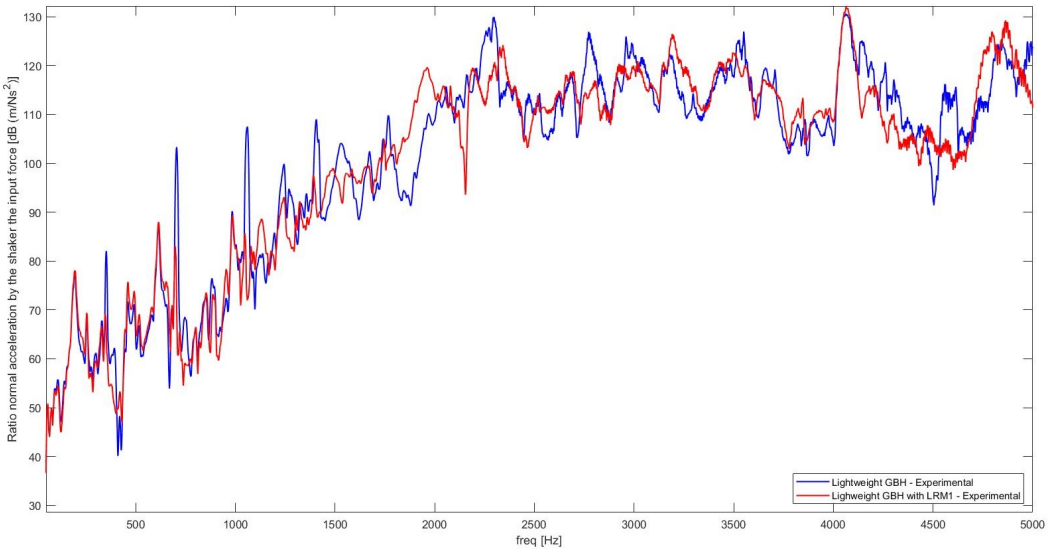

Figure A.8: Normalized acceleration at the position P7.

Appendix B

Technical drawing of the manufactured aluminium housing

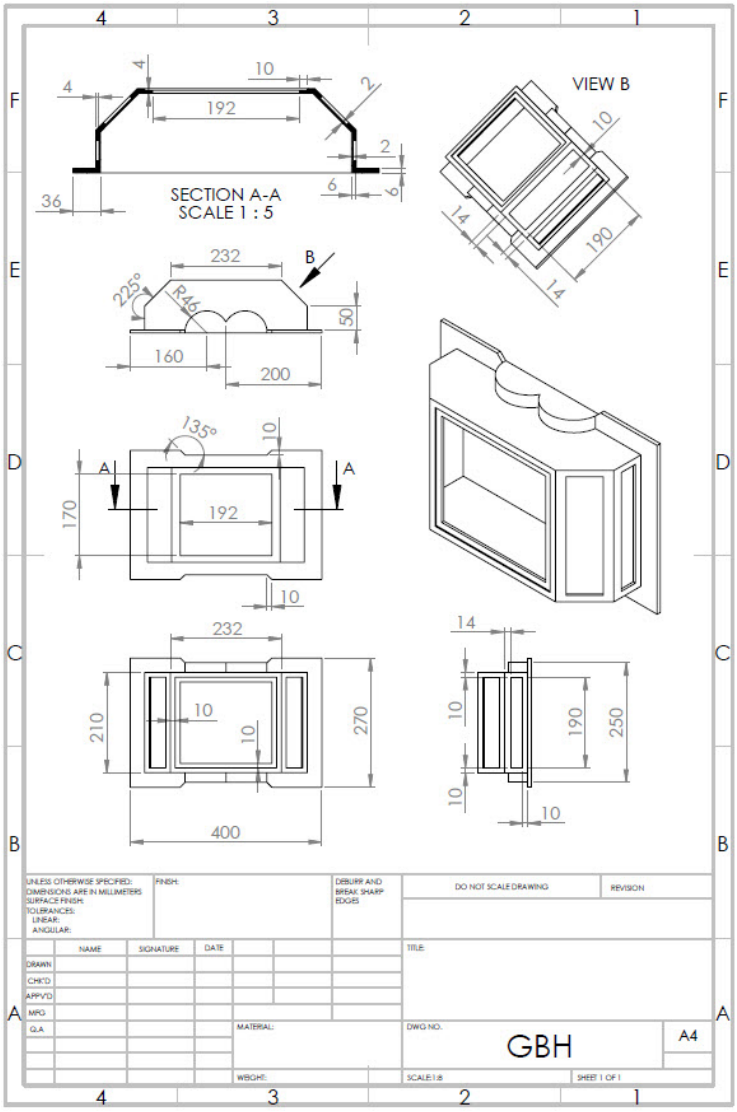

Figure B.1: Technical drawing of the manufactured aluminium housing.

Bibliography

[1] Abbood, I. S., Odaa, S. A., Hasan, K. F., and Jasim, M. A. Properties evaluation of fiber reinforced polymers and their constituent materials used in structures - A review. *Materials Today: Proceedings 43* (2021), 1003–1008. (Cited on page 118.)

[2] Acar, G., and Yilmaz, C. Experimental and numerical evidence for the existence of wide and deep phononic gaps induced by inertial amplification in two-dimensional solid structures. *Journal of Sound and Vibration 332*, 24 (2013), 6389–6404. (Cited on page 42.)

[3] Amaral, D. R., Ichchou, M. N., Kołakowski, P., Fossat, P., and Salvia, M. Lightweight gearbox housing with enhanced vibro-acoustic behavior through the use of locally resonant metamaterials. *Applied Acoustics 210* (2023), 109435. (Cited on page 81.)

[4] Americano da Costa, M. M., Castello, D. A., Magluta, C., and Roitman, N. On the optimal design and robustness of spatially distributed tuned mass dampers. *Mechanical Systems and Signal Processing 150* (2021), 107289. (Cited on page 54.)

[5] Ashby, M. F., Shercliff, H., and Cebon, D. *Materials: Engineering, Science, Processing and Design*. Materials 3e Edition. Elsevier Science, 2007. (Cited on pages 10, 13, 14, 16, 68 and 151.)

[6] Atalla, N., Sgard, F., and Hargreaves, J. *Finite element and boundary methods in structural acoustics and vibration*, vol. 41. 2016. (Cited on pages 37 and 38.)

[7] Attard, D., and Grima, J. N. A three-dimensional rotating rigid units network exhibiting negative Poisson's ratios. *Physica Status Solidi (B) Basic Research 249*, 7 (2012), 1330–1338. (Cited on page 42.)

[8] Bachy, E., Jaboviste, K., Sadoulet-Reboul, E., Peyret, N., Chevallier, G., Arnould, C., and Collard, E. Investigations on the performance and the robustness of a metabsorber designed for structural vibration mitigation. *Mechanical Systems and Signal Processing 170*, May (2022), 108830. (Cited on pages 47 and 54.)

[9] Badreddine Assouar, M., Senesi, M., Oudich, M., Ruzzene, M., and Hou, Z. Broadband plate-type acoustic metamaterial for low-frequency sound attenuation. *Applied Physics Letters 101*, 17 (2012), 1–5. (Cited on page 46.)

[10] Banerjee, A., Das, R., and Calius, E. P. Waves in Structured Mediums or Metamaterials: A Review. *Archives of Computational Methods in Engineering 26*, 4 (2019), 1029–1058. (Cited on page 41.)

[11] Barchiesi, E., Spagnuolo, M., and Placidi, L. Mechanical metamaterials: a state of the art. *Mathematics and Mechanics of Solids 24*, 1 (2019), 212–234. (Cited on page 42.)

[12] Baroncini, E. A., Yadav, S. K., Palmese, G. R., and Joseph F Stanzione III. Sustainable polymers and polymer science: Dedicated to the life and work of Richard P. Wool. *Journal of Applied Polymer Science 133*, 45 (2016). (Cited on page 151.)

[13] Beli, D., Fabro, A. T., Ruzzene, M., and Arruda, J. R. F. Wave attenuation and trapping in 3D printed cantilever-in-mass metamaterials with spatially correlated variability. *Scientific Reports 9*, 1 (2019), 1–11. (Cited on page 54.)

[14] Bendsøe, M. P., and Sigmund, O. *Topology Optimization: Theory, Methods, and Applications*, 2 ed. Springer-Verlag Berlin Heidelberg, 2004. (Cited on page 64.)

[15] Berenger, J.-P. A perfectly matched layer for the absorption of electromagnetic waves. *Journal of Computational Physics 114*, 2 (1994), 185–200. (Cited on page 76.)

[16] Berry, A., and Nicolas, J. Structural acoustics and vibration behavior of complex panels. *Applied Acoustics 43*, 3 (1994), 185–215. (Cited on pages 38 and 39.)

[17] Bertoldi, K., Vitelli, V., Christensen, J., and Van Hecke, M. Flexible mechanical metamaterials. *Nature Reviews Materials 2* (2017). (Cited on page 42.)

[18] Bhandari, V. B. *Design of machine elements*. Tata McGraw-Hill Education, 2010. (Cited on page 9.)

[19] Boutin, C., Fossat, P., Droz, C., and Ichchou, M. Dynamics of ribbed plates with inner resonance: Analytical homogenized models and experimental validation. *European Journal of Mechanics, A/Solids 79*, February 2019 (2020), 103838. (Cited on page 57.)

[20] Bria, D., and Djafari-Rouhani, B. Omnidirectional elastic band gap in finite lamellar structures. *Physical review E, Statistical, nonlinear, and soft matter physics 66* (2002). (Cited on page 43.)

[21] Bria, D., Djafari-Rouhani, B., Bousfia, A., El Houssaine, E. B., and Nougaoui, A. Absolute acoustic band gap in coupled multilayer structures. *EPL (Europhysics Letters) 55* (jan 2007), 841. (Cited on page 43.)

[22] Brillouin, L. Wave Propagation in Periodic Structures, 1946. (Cited on pages 83 and 84.)

[23] Brun, M., Guenneau, S., and Movchan, A. B. Achieving control of in-plane elastic waves. *Applied Physics Letters 94*, 6 (2009). (Cited on page 42.)

[24] Burger, N., Laachachi, A., Ferriol, M., Lutz, M., Toniazzo, V., and Ruch, D. Review of thermal conductivity in composites: Mechanisms, parameters and theory. *Progress in Polymer Science 61* (2016), 1–28. (Cited on page 145.)

[25] Caballero, D., Sánchez-Dehesa, J., Rubio, C., Mártinez-Sala, R., Sánchez-Pérez, J. V., Meseguer, F., and Llinares, J. Large two-dimensional sonic band gaps. *Physical Review E - Statistical Physics, Plasmas, Fluids, and Related Interdisciplinary Topics 60*, 6 (1999). (Cited on page 43.)

[26] Calius, E. P., Bremaud, X., Smith, B., and Hall, A. Negative mass sound shielding structures: Early results. *Physica Status Solidi (B) Basic Research 246*, 9 (2009), 2089–2097. (Cited on page 45.)

[27] Cebrecos, A., Krattiger, D., Sánchez-Morcillo, V. J., Romero-García, V., and Hussein, M. I. The finite-element time-domain method for elastic band-structure calculations. *Computer Physics Communications 238* (2019), 77–87. (Cited on page 84.)

[28] Cevolini, F., Davis, S., and Rinland, S. New Rapid Casting Techniques for Competitive Motor Sports. *Proceedings of the SFF Symposium* (2008), 558–569. (Cited on page 10.)

[29] Chalmers, L., Elford, D. P., Kusmartsev, F. V., and Swallowe, G. M. Acoustic band gap formation in two-dimensional locally resonant sonic crystals comprised of helmholtz resonators. *International Journal of Modern Physics B 23*, 20-21 (2009), 4234–4243. (Cited on page 44.)

[30] Chang, K. J., Rocha de Melo Filho, N. G., Van Belle, L., Claeys, C., and Desmet, W. A study on the application of locally resonant acoustic metamaterial for reducing a vehicle's engine noise. *INTER-NOISE 2019 MADRID - 48th International Congress and Exhibition on Noise Control Engineering* (2019). (Cited on pages 52 and 95.)

[31] Chen, Y., Hu, G., and Huang, G. A hybrid elastic metamaterial with negative mass density and tunable bending stiffness. *Journal of the Mechanics and Physics of Solids 105* (2017), 179–198. (Cited on page 53.)

[32] Cheng, J. Y., and Mailund, T. Ancestral population genomics using coalescence hidden Markov models and heuristic optimisation algorithms. *Computational Biology and Chemistry 57* (2015), 80–92. (Cited on page 135.)

[33] Christensen, J., Kadic, M., Kraft, O., and Wegener, M. Vibrant times for mechanical metamaterials. *MRS Communications 5*, 3 (2015), 453–462. (Cited on page 42.)

[34] Claeys, C., Deckers, E., Pluymers, B., and Desmet, W. A lightweight vibro-acoustic metamaterial demonstrator: Numerical and experimental investigation. *Mechanical Systems and Signal Processing 70-71* (2016), 853–880. (Cited on pages 49 and 96.)

[35] Claeys, C., Rocha de Melo Filho, N. G., Van Belle, L., Deckers, E., and Desmet, W. Design and validation of metamaterials for multiple structural stop bands in waveguides. *Extreme Mechanics Letters 12* (2017), 7–22. (Cited on pages 41, 49, 50 and 95.)

[36] Claeys, C. C., Sas, P., and Desmet, W. On the acoustic radiation efficiency of local resonance based stop band materials. *Journal of Sound and Vibration 333*, 14 (2014), 3203–3213. (Cited on pages 38, 46 and 51.)

[37] Claeys, C. C., Vergote, K., Sas, P., and Desmet, W. On the potential of tuned resonators to obtain low-frequency vibrational stop bands in periodic panels. *Journal of Sound and Vibration 332*, 6 (2013), 1418–1436. (Cited on pages 46, 53, 83, 84 and 95.)

[38] Comi, C., and Driemeier, L. Wave propagation in cellular locally resonant metamaterials. *Latin American Journal of Solids and Structures 15*, 4 (2018). (Cited on page 45.)

[39] COMSOL AB. *COMSOL Multiphysics® version 5.6, www.comsol.com, Stockholm, Sweden.* (Cited on pages 61, 68, 105 and 155.)

[40] Cremer, L., Heckl, M., and Petersson, B. A. *Structure-borne sound: Structural vibrations and sound radiation at audio frequencies.* 2005. (Cited on page 36.)

[41] Dai, Y., and Ramnath, D. M. A topographically structural optimization methodology for improving noise radiation in transaxles. *SAE Technical Papers*, 724 (2007). (Cited on pages 9 and 39.)

[42] Davis, M., Mohammed, Y. S., Elmustafa, A. A., Martin, P. F., and Ritinski, C. Designing for Static and Dynamic Loading of a Gear Reducer. *Power Transmission Engineering* (2010). (Cited on page 10.)

[43] Del Vescovo, D., and Giorgio, I. Dynamic problems for metamaterials: Review of existing models and ideas for further research. *International Journal of Engineering Science 80* (2014), 153–172. (Cited on pages 41 and 42.)

[44] Delpero, T., Hannema, G., Van Damme, B., Schoenwald, S., Zemp, A., and Bergamini, A. Inertia amplification in phononic crystals for low frequency bandgaps. In *8th Conference on Smart Structures and Materials, SMART 2017 and 6th International Conference on Smart Materials and Nanotechnology in Engineering, SMN 2017* (2017), pp. 1657–1668. (Cited on page 43.)

[45] Delpero, T., Schoenwald, S., Zemp, A., and Bergamini, A. Structural engineering of three-dimensional phononic crystals. *Journal of Sound and Vibration 363* (2016), 156–165. (Cited on page 43.)

[46] Deymier, P. *Acoustic Metamaterials and Phononic Crystals (Springer Series in Solid-State Sciences)*. Springer-Verlag Berlin Heidelberg, 2013. (Cited on pages 42 and 44.)

[47] Di Boon, Y., Joshi, S. C., Bhudolia, S. K., and Gohel, G. Recent advances on the design automation for performance-optimized fiber reinforced polymer composite components. *Journal of Composites Science 4*, 2 (2020). (Cited on page 31.)

[48] Domingues, D. *Composite Optimization of Gearbox Casing used in LMP1 race car under service and FIA regulation load cases*. PhD thesis, IST, 2015. (Cited on page 24.)

[49] Droz, C., Robin, O., Ichchou, M., and Atalla, N. Improving sound transmission loss at ring frequency of a curved panel using tunable 3D-printed small-scale resonators. *The Journal of the Acoustical Society of America 145*, 1 (2019), EL72–EL78. (Cited on pages 52 and 95.)

[50] Durrant, J. D., and Lovrinic, J. H. *Bases of Hearing Science*. Williams & Wilkins, 1977. (Cited on page 34.)

[51] Elford, D. P., Chalmers, L., Kusmartsev, F. V., and Swallowe, G. M. Matryoshka locally resonant sonic crystal. *The Journal of the Acoustical Society of America 130*, 5 (2011), 2746–2755. (Cited on page 44.)

[52] Elias, S., and Matsagar, V. Research developments in vibration control of structures using passive tuned mass dampers. *Annual Reviews in Control 44* (2017), 129–156. (Cited on page 53.)

[53] European Commission. *Handbook on the Implementation of EC Environmental Legislation - Noise Legislation - The Environmental Noise Directive*. 2008. (Cited on pages 32 and 33.)

[54] European Commission. Air Quality and Noise Legislation, 2016. (Cited on pages 32 and 33.)

[55] Ever J. Barbero. *Introduction to Composite Materials Design 2nd Edition*. 2011. (Cited on pages 13, 14, 16 and 21.)

[56] Fabro, A. T., Meng, H., and Chronopoulos, D. Uncertainties in the attenuation performance of a multi-frequency metastructure from additive manufacturing. *Mechanical Systems and Signal Processing 138* (2020), 106557. (Cited on page 54.)

[57] Fahy, F. J., and Gardonio, P. *Sound and Structural Vibration: Radiation, Transmission and Response*. EngineeringPro collection. Elsevier Science, 2007. (Cited on pages 33, 34, 35, 36, 37, 39, 62 and 74.)

[58] Figlus, T., Kozioł, M., and Kuczyński, Ł. Impact of application of selected composite materials on the weight and vibroactivity of the upper gearbox housing. *Materials 12*, 16 (2019), 40–44. (Cited on pages 3, 27, 28, 29, 65 and 68.)

[59] Figlus, T., Kozioł, M., and Kuczyński, Ł. The effect of selected operational factors on the vibroactivity of upper gearbox housings made of composite materials. *Sensors (Switzerland)* (2019). (Cited on pages 3, 27, 29, 65 and 68.)

[60] Fischer, B., Horn, B., Bartelt, C., and Blössl, Y. Method for an Automated Optimization of Fiber Patch Placement Layup Designs. *International Journal of Composite Materials 5*, 2 (2015), 37–46. (Cited on page 25.)

[61] Franz, M., Schleich, B., and Wartzack, S. Variation analysis of design parameters of fibre-reinforced plastic parts. *Proceedings of the International Conference on Engineering Design, ICED*, August (2019), 2725–2734. (Cited on page 16.)

[62] Fredianelli, L., Del Pizzo, A., and Licitra, G. Recent developments in sonic crystals as barriers for road traffic noise mitigation. *Environments - MDPI 6*, 2 (2019), 1–19. (Cited on page 44.)

[63] Fritze, D., Marburg, S., and Hardtke, H. J. Estimation of radiated sound power: A case study on common approximation methods. *Acta Acustica united with Acustica 95*, 5 (2009), 833–842. (Cited on pages 34 and 112.)

[64] Fuchs, A., Steffan, H., Bernasch, J., and Watzenig, D. *Automotive NVH Technology*. 2016. (Cited on page 35.)

[65] Fuller, C. R., and Harne, R. L. Advanced passive treatment of low frequency sound and vibration. *Annual Conference of the Australian Acoustical Society - Acoustics: Research to Consulting* (2009), 161–167. (Cited on page 95.)

[66] Gay, D., Hoa, S. V., Tsai, S. W., Chung, D. D. L., Gay, D., Hoa, S. V., and Tsai, S. W. *Composite Materials: Design and Applications*. CRC Press, 2003. (Cited on pages 11, 12, 13, 14, 15, 16, 19, 21 and 24.)

[67] Georgano, G. N. *The Complete Encyclopedia of Motorcars, 1885 to the Present*. Dutton, 1973. (Cited on pages 6 and 7.)

[68] Girvin, S. M., and Yang, K. *Modern condensed matter physics*. Cambridge University Press, 2019. (Cited on page 42.)

[69] Goffaux, C., Maseri, F., Vasseur, J. O., Djafari-Rouhani, B., and Lambin, P. Measurements and calculations of the sound attenuation by a phononic band gap structure suitable for an insulating partition application. *Applied Physics Letters 83*, 2 (2003), 281–283. (Cited on page 43.)

[70] Goffaux, C., Sánchez-Dehesa, J., Yeyati, A. L., Lambin, P., Khelif, A., Vasseur, J. O., and Djafari-Rouhani, B. Evidence of Fano-like interference phenomena in locally resonant materials. *Physical Review Letters 88*, 22 (2002). (Cited on pages 44 and 45.)

[71] Graf, B. J., Hubmann, C., Resch, M., and Mehrgou, M. A Hybrid Development Process for NVH Optimization and Sound Engineering Considering the Future Pass-by Homologation Demands. *SAE International Journal of Vehicle Dynamics, Stability, and NVH 1*, 1 (2016), 23–29. (Cited on pages 38, 39 and 40.)

[72] Hall, A., Calius, E. P., Dodd, G., and Chan, K. L. Development of locally resonant structures for sonic barriers. *Health Monitoring of Structural and Biological Systems 2013 8695* (2013). (Cited on pages 32, 33 and 47.)

[73] Han, X. K., and Zhang, Z. Topological Optimization of Phononic Crystal Thin Plate by a Genetic Algorithm. *Scientific Reports 9*, 1 (2019), 1–14. (Cited on page 53.)

[74] Hillier, V., and Thornes, N. *Hillier's Fundamentals of Motor Vehicle Technology*, 6th editio ed. Nelson Thornes Ltd, London, 2012. (Cited on page 7.)

[75] Ho, K. M., Chan, C. T., and Soukoulis, C. M. Existence of a photonic gap in periodic dielectric structures. *Physical Review Letters 65*, 25 (1990), 3152. (Cited on page 42.)

[76] Hu, X., Chan, C. T., and Zi, J. Two-dimensional sonic crystals with Helmholtz resonators. *Physical Review E - Statistical, Nonlinear, and Soft Matter Physics 71*, 5 (2005), 1–4. (Cited on page 46.)

[77] Hussein, M. I., Leamy, M. J., and Ruzzene, M. Dynamics of phononic materials and structures: Historical origins, recent progress, and future outlook. *Applied Mechanics Reviews 66*, 4 (2014), 1–38. (Cited on pages 82 and 84.)

[78] Ivanov, D. *Gearbox Housing Design – Topology Optimization through Generative Design*. PhD thesis, 2018. (Cited on pages 3, 9 and 63.)

[79] Jazar, R. N. *Vehicle Dynamics: Theory and Application*. SpringerLink : Bücher. Springer New York, 2013. (Cited on page 9.)

[80] Jucha, B., and Kozioł, M. Manufacturing gearbox housing case made of carbon fiber reinforced polymer composite by autoclave method. *Composites Theory and Practice 19*, 4 (2019), 135–142. (Cited on page 27.)

[81] Jung, J., Kim, H. G., Goo, S., Chang, K. J., and Wang, S. Realisation of a locally resonant metamaterial on the automobile panel structure to reduce noise radiation. *Mechanical Systems and Signal Processing 122* (2019), 206–231. (Cited on pages 38, 51, 84 and 96.)

[82] Karuppannan Gopalraj, S., and Kärki, T. A review on the recycling of waste carbon fibre/glass fibre-reinforced composites: fibre recovery, properties and life-cycle analysis. *SN Applied Sciences 2*, 3 (2020), 1–21. (Cited on pages 22 and 23.)

[83] Kazakis, G., Kanellopoulos, I., Sotiropoulos, S., and Lagaros, N. D. Topology optimization aided structural design: Interpretation, computational aspects and 3D printing. *Heliyon 3*, 10 (2017), e00431. (Cited on page 63.)

[84] Kazda, L., Růžička, M., Padovec, Z., Achtenová, G., and Poul, R. Influence of Oil on Filament Wound Composite Material Used in Automotive Gearbox. *Engineering Mechanics 2020 26*, January 2021 (2020), 270–273. (Cited on page 144.)

[85] Kim, C., Cho, C. H., Son, I., Lee, H., Han, J. W., Kim, J. G., and Lee, J. H. Effect of microscale oil penetration on mechanical and chemical properties of carbon fiber-reinforced epoxy composites. *Journal of Industrial and Engineering Chemistry 61* (2018), 112–118. (Cited on page 144.)

[86] Kim, J. G., Gang, G. A., Cho, S. J., Lee, G. H., and Park, Y. J. Dynamic stiffness effect of mechanical components on gear mesh misalignment. *Applied Sciences (Switzerland) 8*, 6 (2018). (Cited on page 53.)

[87] Kirchhof, J. N., Weinel, K., Heeg, S., Deinhart, V., Kovalchuk, S., Höflich, K., and Bolotin, K. I. Tunable Graphene Phononic Crystal. *Nano Letters* (2021). (Cited on page 44.)

[88] Kish, J. G. Sikorsky Aircraft Advanced Rotorcraft Transmission (ART) Program - Report. Tech. rep., 1993. (Cited on page 23.)

[89] Kittel, C. *Introduction to Solid State Physics*, 8th ed. John Wiley & Sons, New York, 2004. (Cited on page 84.)

[90] Kook, J., and Jensen, J. S. Topology optimization of periodic microstructures for enhanced loss factor using acoustic–structure interaction. *International Journal of Solids and Structures 122-123* (2017), 59–68. (Cited on page 53.)

[91] Krishna, M. M. Finite element topography and shape optimization of a jounce bumper bracket. *SAE Technical Papers*, 724 (2002). (Cited on page 9.)

[92] Krödel, S., Thomé, N., and Daraio, C. Wide band-gap seismic metastructures. *Extreme Mechanics Letters 4* (2015), 111–117. (Cited on page 42.)

[93] Krushynska, A. O., Kouznetsova, V. G., and Geers, M. G. D. Towards optimal design of locally resonant acoustic metamaterials. *Journal of the Mechanics and Physics of Solids 71*, 1 (2014), 179–196. (Cited on pages 45 and 82.)

[94] Krushynska, A. O., Miniaci, M., Kouznetsova, V. G., and Geers, M. G. Multilayered inclusions in locally resonant metamaterials: Two-dimensional versus three-dimensional modeling. *Journal of Vibration and Acoustics, Transactions of the ASME 139*, 2 (2017), 3–6. (Cited on page 49.)

[95] Kulekci, M. K. Magnesium and its alloys applications in automotive industry. *International Journal of Advanced Manufacturing Technology 39*, 9-10 (2008), 851–865. (Cited on page 10.)

[96] Kumar, D. S., Sasanka, C. T., Ravindra, K., and Suman, K. Magnesium and Its Alloys in Automotive Applications – A Review. *American Journal of Materials Science and Technology*, January (2015). (Cited on page 10.)

[97] Kumar, S., Bhushan, P., Prakash, O., and Bhattacharya, S. Double negative acoustic metastructure for attenuation of acoustic emissions. *Applied Physics Letters 112*, 10 (2018). (Cited on page 48.)

[98] Kushwaha, M. S. Stop-bands for periodic metallic rods : Sculptures that can filter the noise. *Applied Physics Letters* (1997). (Cited on page 43.)

[99] Kushwaha, M. S., Halevi, P., Dobrzynski, L., and Djafari-Rouhani, B. Acoustic band structure of periodic elastic composites. *Physical Review Letters 71*, 13 (1993), 2022–2025. (Cited on page 42.)

[100] Langfeldt, F., and Gleine, W. Membrane- and plate-type acoustic metamaterials with elastic unit cell edges. *Journal of Sound and Vibration 453* (2019), 65–86. (Cited on page 44.)

[101] Langfeldt, F., Gleine, W., and Von Estorff, O. Analytical model for low-frequency transmission loss calculation of membranes loaded with arbitrarily shaped masses. *Journal of Sound and Vibration 349* (2015), 315–329. (Cited on page 48.)

[102] Langfeldt, F., Gleine, W., and von Estorff, O. An efficient analytical model for baffled, multi-celled membrane-type acoustic metamaterial panels. *Journal of Sound and Vibration 417* (2018), 359–375. (Cited on page 48.)

[103] Langlet, P., Hladky-Hennion, A.-C., and Decarpigny, J.-N. Analysis of the propagation of plane acoustic waves in passive periodic materials using the finite element method. *Journal of The Acoustical Society of America 98*, 4 (1995), 2792–2800. (Cited on page 43.)

[104] Lazarov, B., and Sigmund, O. Filters in topology optimization based on Helmholtz-type differential equations. *International Journal for Numerical Methods in Engineering 86* (may 2011), 765–781. (Cited on pages 63 and 64.)

[105] Le Moyne, S., and Tébec, J. L. Ribs effects in acoustic radiation of a gearbox - Their modelling in a boundary element method. *Applied Acoustics 63*, 2 (2002), 223–233. (Cited on page 9.)

[106] Li, C. Optimum multiple tuned mass dampers for structures under the ground acceleration based on DDMF and ADMF. *Earthquake Engineering and Structural Dynamics 31*, 4 (2002), 897–919. (Cited on page 47.)

[107] Li, J., and Chan, C. T. Double-negative acoustic metamaterial. *Physical Review E - Statistical Physics, Plasmas, Fluids, and Related Interdisciplinary Topics 70*, 5 (2004), 4. (Cited on page 45.)

[108] Li, J., and Li, S. Sound transmission through metamaterial-based double-panel structures with poroelastic cores. *Acta Acustica united with Acustica 103*, 5 (2017), 869–884. (Cited on page 47.)

[109] Li, P., Yao, S., Zhou, X., Huang, G., and Hu, G. Effective medium theory of thin-plate acoustic metamaterials. *The Journal of the Acoustical Society of America 135*, 4 (2014), 1844–1852. (Cited on page 47.)

[110] Li, Y., Chen, T., Wang, X., Xi, Y., and Liang, Q. Enlargement of locally resonant sonic band gap by using composite plate-type acoustic metamaterial. *Physics Letters, Section A: General, Atomic and Solid State Physics 379*, 5 (2015), 412–416. (Cited on page 96.)

[111] Li, Y., Zhang, Y., and Xie, S. A lightweight multilayer honeycomb membrane-type acoustic metamaterial. *Applied Acoustics 168* (2020), 107427. (Cited on page 48.)

[112] Ling, L., and Huang, Y. Topology optimization design of gearbox housing in electric bus. *Applied Mechanics and Materials 574* (2014), 173–178. (Cited on pages 3, 9 and 63.)

[113] Lis, A. Current trends in composite thinking. *Racecar engineering* (2012). (Cited on page 24.)

[114] Liu, L., and Hussein, M. I. Wave motion in periodic flexural beams and characterization of the transition between bragg scattering and local resonance. *Journal of Applied Mechanics, Transactions ASME 79*, 1 (2012), 1–17. (Cited on page 46.)

[115] Liu, Q. H. Perfectly matched layers for elastic waves in cylindrical and spherical coordinates. *The Journal of the Acoustical Society of America 105*, 4 (1999), 2075–2084. (Cited on page 76.)

[116] Liu, Z., Chan, C. T., and Sheng, P. Analytic model of phononic crystals with local resonances. *Physical Review B - Condensed Matter and Materials Physics 71*, 1 (2005), 1–8. (Cited on page 45.)

[117] Liu, Z., Zhang, X., Mao, Y., Zhu, Y. Y., Yang, Z., Chan, C. T., and Sheng, P. Locally resonant sonic materials. *Science 289*, 5485 (2000), 1734–1736. (Cited on pages 44 and 82.)

[118] Lu, M. H., Feng, L., and Chen, Y. F. Phononic crystals and acoustic metamaterials. *Materials Today 12* (2009), 34–42. (Cited on page 42.)

[119] Luk, J. M., Kim, H. C., De Kleine, R. D., Wallington, T. J., and MacLean, H. L. Greenhouse gas emission benefits of vehicle lightweighting: Monte Carlo probabalistic analysis of the multi material lightweight vehicle glider. *Transportation Research Part D: Transport and Environment 62*, February (2018), 1–10. (Cited on page 1.)

[120] Ma, G., and Sheng, P. Acoustic metamaterials: From local resonances to broad horizons. *Science Advances 2*, 2 (2016). (Cited on pages 41 and 45.)

[121] Ma, S., Liu, X., Fan, L., Jiang, Y., Cao, L., Tang, Z., and Zhu, J. Synthesis and properties of a bio-based epoxy resin with high epoxy value and low viscosity. *ChemSusChem 7*, 2 (2014), 555–562. (Cited on page 151.)

[122] Maciejczyk, A., and Zdziennicki, Z. Design basic of industrial gearboxes: Calculation and Design Case Example. Tech. rep., Technical University of Lodz, 2011. (Cited on page 9.)

[123] Maidanik, G. Response of ribbed panels to reverberant acoustic fields. *The journal of the Acoustical Society of America 34* (1962), 809–826. (Cited on page 38.)

[124] Maldovan, M., and Thomas, E. L. *Periodic Materials and Interference Lithography for Photonics, Phononics and Mechanics*. 2009. (Cited on page 43.)

[125] Manzanares-Martínez, B., Sánchez-Dehesa, J., Håkansson, A., Cervera, F., and Ramos-Mendieta, F. Experimental evidence of omnidirectional elastic bandgap in finite one-dimensional phononic systems. *Applied Physics Letters 85*, 1 (2004), 154–156. (Cited on page 43.)

[126] Martínez-Sala, R., Sancho, J., Sánchez, J. V., Gómez, V., Llinares, J., and Meseguer, F. Sound attenuation by sculpture. *Nature 378*, 6554 (1995), 241. (Cited on page 43.)

[127] Matsimbi, M., Nziu, P. K., Masu, L. M., and Maringa, M. Topology Optimization of Automotive Body Structures: A review. *International Journal of Engineering Research and Technology 13*, 12 (2020), 4282–4296. (Cited on page 9.)

[128] Melo, N. F., Claeys, C., Deckers, E., Pluymers, B., and Desmet, W. Dynamic Metamaterials for Structural Stopband Creation. *SAE International Journal of Passenger Cars - Mechanical Systems 9*, 3 (2016). (Cited on pages 41, 49 and 50.)

[129] Miklos, I. Z., Miklos, C. C., Alic, C. I., and Raţiu, S. Analysis of gear reducer housing using the finite element method. *IOP Conference Series: Materials Science and Engineering 294*, 1 (2018). (Cited on page 10.)

[130] Mohammadi, B., Rohanifar, M., Salimi-Majd, D., and Farrokhabadi, A. Micromechanical prediction of damage due to transverse ply cracking under fatigue loading in composite laminates. *Journal of Reinforced Plastics and Composites 36*, 5 (2017), 377–395. (Cited on page 120.)

[131] Munro, A. H. Power-Transmission Gear, 1997. (Cited on page 7.)

[132] Nettles, A. T. Basic Mechanics of Laminated Composite Plates. *NASA reference pulication*, October (1994), 107. (Cited on pages 16 and 17.)

[133] Nikafshar, S., Zabihi, O., Hamidi, S., Moradi, Y., Barzegar, S., Ahmadi, M., and Naebe, M. A renewable bio-based epoxy resin with improved mechanical performance that can compete with DGEBA. *RSC Advances 7*, 14 (2017), 8694–8701. (Cited on page 151.)

[134] Oh, J. H., Min Seung, H., and Young Kim, Y. A truly hyperbolic elastic metamaterial lens. *Applied Physics Letters 104*, 7 (2014). (Cited on page 44.)

[135] Orrenius, U., and Finnvede, F. Calculation of Wave Propagation in Rib-Stiffened Plate Structures. *Journal of Sound and Vibration 198* (1996), 203–224. (Cited on page 62.)

[136] Oudich, M., Li, Y., Assouar, B. M., and Hou, Z. A sonic band gap based on the locally resonant phononic plates with stubs. *New Journal of Physics 12* (2010). (Cited on pages 95 and 96.)

[137] Oudich, M., Senesi, M., Assouar, M. B., Ruzenne, M., Sun, J. H., Vincent, B., Hou, Z., and Wu, T. T. Experimental evidence of locally resonant sonic band gap in two-dimensional phononic stubbed plates. *Physical Review B - Condensed Matter and Materials Physics 84*, 16 (2011), 3–8. (Cited on pages 44 and 46.)

[138] Palanisamy, C., Raman, R., and kumar Dhanraj, P. *Additive manufacturing: a review on mechanical properties of polyjet and FDM printed parts*, vol. 79. Springer Berlin Heidelberg, 2022. (Cited on page 25.)

[139] Park, J., Lee, D., and Rho, J. Recent advances in non-traditional elastic wave manipulation by macroscopic artificial structures. *Applied Sciences (Switzerland) 10*, 2 (2020). (Cited on page 44.)

[140] Pendry, J. B., Holden, A. J., Robbins, D. J., and Stewart, W. J. Magnetism from conductors and enhanced nonlinear phenomena. *IEEE Transactions on Microwave Theory and Techniques 47*, 11 (1999), 2075–2084. (Cited on page 44.)

[141] Pietroluongo, M., Padovano, E., Frache, A., and Badini, C. Mechanical recycling of an end-of-life automotive composite component. *Sustainable Materials and Technologies 23* (2020). (Cited on pages 22 and 23.)

[142] Pires, F. A., Claeys, C., Deckers, E., and Desmet, W. The impact of resonant additions' footprint on the stop band behavior of 1D locally resonant metamaterial realizations. *Journal of Sound and Vibration 491* (2021), 115705. (Cited on page 53.)

[143] Psarobas, I. E., Modinos, A., Sainidou, R., and Stefanou, N. Acoustic properties of colloidal crystals. *Physical Review B - Condensed Matter and Materials Physics 65*, 6 (2002), 643071–643076. (Cited on page 43.)

[144] Qin, Q., Sheng, M., and Guo, Z. Low-frequency vibration and radiation performance of a locally resonant plate attached with periodic multiple resonators. *Applied Sciences (Switzerland) 10*, 8 (2020). (Cited on pages 85 and 86.)

[145] Rackov, M., Knežević, I., Kuzmanović, S., Čavić, M., and Penčić, M. Analysis of housing models of modern single-stage universal gear reducers. *IOP Conference Series: Materials Science and Engineering 393*, 1 (2018). (Cited on page 10.)

[146] Sánchez-Pérez, J. V., Caballero, D., Mártinez-Sala, R., Rubio, C., Sánchez-Dehesa, J., Meseguer, F., Llinares, J., and Gálvez, F. Sound attenuation by a two-dimensional array of rigid cylinders. *Physical Review Letters 80*, 24 (1998), 5325–5328. (Cited on page 43.)

[147] Sangiuliano, L., Claeys, C., Deckers, E., De Smet, J., Pluymers, B., and Desmet, W. Reducing Vehicle Interior NVH by Means of Locally Resonant Metamaterial Patches on Rear Shock Towers. *SAE Technical Papers* (2019). (Cited on pages 52, 53 and 95.)

[148] Sangiuliano, L., Claeys, C., Deckers, E., Pluymers, B., and Desmet, W. Force Isolation by Locally Resonant Metamaterials to Reduce NVH. *SAE Technical Papers* (2018), 1–7. (Cited on pages 50, 51 and 95.)

[149] Sarfraz, M. S., Hong, H., and Kim, S. S. Recent developments in the manufacturing technologies of composite components and their cost-effectiveness in the automotive industry: A review study. *Composite Structures 266*, February (2021), 113864. (Cited on pages 21, 22 and 29.)

[150] Savage, G. Composite materials technology in formula 1 motor racing. *SPE Automotive and Composites Division - 8th Annual Automotive Composites Conference and Exhibition, ACCE 2008 - The Road to Lightweight Performance 1* (2008), 109–139. (Cited on pages 3, 24 and 25.)

[151] Schneider, T. Lightweight construction: First composite gearbox housing with layer-optimized organo sheeting weighs 30% less than a comparable aluminum component. *Reinforced Plastics 63*, 1 (2017), 40–45. (Cited on pages 3, 26 and 27.)

[152] Schurig, D., Mock, J., Justice, B. J., Cummer, S., Pendry, J., Starr, A., and Smith, D. Metamaterial Electromagnetic Cloak at Microwave Frequencies. *Science 314* (2006), 977–980. (Cited on page 42.)

[153] Šedivý, O., Padovec, Z., Kulíšek, V., and Růžička, M. Design and Analysis of Hybrid (Metal/Composite) Upper Case of the Gearbox. *Applied Mechanics* (2018), 87–91. (Cited on pages 26 and 27.)

[154] Shalaev, V. M. Physics: Transforming light. *Science 322*, 5900 (2008), 384–386. (Cited on page 42.)

[155] Sheng, P., Mei, J., Liu, Z., and Wen, W. Dynamic mass density and acoustic metamaterials. *Physica B: Condensed Matter 394*, 2 (2007), 256–261. (Cited on page 45.)

[156] Sheng, P., Zhang, X. X., Liu, Z., and Chan, C. T. Locally resonant sonic materials. *Physica B: Condensed Matter 338*, 1-4 (2003), 201–205. (Cited on pages 44 and 45.)

[157] Sigalas, M. M., and Economou, E. N. Elastic and Acoustic Wave Band Structure. *Physics 158* (1992), 377–382. (Cited on pages 42 and 43.)

[158] Slavov, S., and Konsulova-Bakalova, M. Optimizing weight of housing elements of two-stage reducer by using the topology management optimization capabilities integrated in SOLIDWORKS: A case study. *Machines 7* (2019). (Cited on pages 3, 9, 10, 63, 67 and 71.)

[159] Smoleń, J., Cyganek, A., and Kozioł, M. Manufacture of transmission housing by contact layer technique using vacuum bag. *Composites Theory and Practice 19*, 1 (2019), 18–22. (Cited on page 27.)

[160] Solymar, L., Walsh, D., and Syms, R. R. A. The band theory of solids. In *Electrical Properties of Materials*. Oxford University Press, 2018. (Cited on page 42.)

[161] Son, G. H., Cho, S. J., and Park, Y. J. Rib design for improving the local stiffness of gearbox housing for agricultural electric vehicles. *Applied Sciences (Switzerland) 9*, 21 (2019). (Cited on pages 38, 39 and 41.)

[162] Stratasys. *ABS-M30 Properties FDM Thermoplastic Filament*. (Cited on page 107.)

[163] Surjadi, J. U., Gao, L., Du, H., Li, X., Xiong, X., Fang, N. X., and Lu, Y. Mechanical Metamaterials and Their Engineering Applications. *Advanced Engineering Materials 21*, 3 (2019). (Cited on pages 41 and 42.)

[164] Thompson, E. A. Automatic gear-shifting mechanism for sliding gear transmission, 1922. (Cited on page 6.)

[165] Tian, T., and Cole, K. D. Anisotropic thermal conductivity measurement of carbon-fiber/epoxy composite materials. *International Journal of Heat and Mass Transfer 55*, 23-24 (2012), 6530–6537. (Cited on pages 118 and 145.)

[166] Toropov, V. V., Jones, R., Willment, T., and Funnell, M. Weight and Manufacturability Optimization of Composite Aircraft Components Based on a Genetic Algorithm. *6th World Congresses of Structural and Multidisciplinary Optimization*, June (2005). (Cited on pages 29 and 30.)

[167] Tsai, S. W., and Wu, E. M. A General Theory of Strength for Anisotropic Materials. *Journal of Composite Materials 5*, 1 (1971), 58–80. (Cited on page 126.)

[168] Van Belle, L., Claeys, C., Deckers, E., and Desmet, W. On the impact of damping on the dispersion curves of a locally resonant metamaterial: Modelling and experimental validation. *Journal of Sound and Vibration 409* (2017), 1–23. (Cited on page 95.)

[169] Van Belle, L., Claeys, C., Deckers, E., and Desmet, W. The acoustic insulation performance of infinite and finite locally resonant metamaterial and phononic crystal plates. *MATEC Web of Conferences 283*, June (2019), 9003. (Cited on page 49.)

[170] van Belle, L., de Melo Filho, N. G., Villanueva, M. C., Claeys, C., Deckers, E., Naets, F., and Desmet, W. Fast metamaterial design optimization using reduced order unit cell modeling. In *Proceedings of ISMA 2020 - International Conference on Noise and Vibration Engineering* (2020), pp. 2487–2501. (Cited on page 53.)

[171] Van Damme, B., Hannema, G., and Zemp, A. Sound transmission through checkerboard sandwich panels. In *ISMA conference on Noise and Vibration Engineering* (2018). (Cited on page 44.)

[172] Vasseur, J. O., Deymier, P. A., Frantziskonis, G., Hong, G., Djafari-Rouhani, B., and Dobrzynski, L. Experimental evidence for the existence of absolute acoustic band gaps in two-dimensional periodic composite media. *Journal of Physics Condensed Matter 10*, 27 (1998), 6051–6064. (Cited on page 43.)

[173] Vellar, L. S., Ontiveros-Pérez, S. P., Miguel, L. F. F., and Fadel Miguel, L. F. Robust Optimum Design of Multiple Tuned Mass Dampers for Vibration Control in Buildings Subjected to Seismic Excitation. *Shock and Vibration* (2019). (Cited on page 54.)

[174] Veselago, V. G. The Electrodynamic of Substances with Simultaneous Negative Values of E and μ. *Soviet Physics Uspekhi 10*, 4 (1968), 509–514. (Cited on page 44.)

[175] Wang, F., Lazarov, B. S., and Sigmund, O. On projection methods, convergence and robust formulations in topology optimization. *Structural and Multidisciplinary Optimization 43*, 6 (2011), 767–784. (Cited on page 64.)

[176] Wang, G., Wen, X., Wen, J., and Liu, Y. Quasi-one-dimensional periodic structure with locally resonant band gap. *Journal of Applied Mechanics, Transactions ASME 73*, 1 (2006), 167–170. (Cited on page 46.)

[177] Wang, Y., Tang, B., Gao, Y., Wu, X., Chen, J., Shan, L., Sun, K., Zhao, Y., Yang, K., Yu, J., and Li, W. Epoxy Composites with High Thermal Conductivity by Constructing Three-Dimensional Carbon Fiber/Carbon/Nickel Networks Using an Electroplating Method. *ACS Omega 6*, 29 (2021), 19238–19251. (Cited on pages 118 and 145.)

[178] Weisser, T., Foltête, E., Bouhaddi, N., and Gonidou, L. O. A power flow mode approach dedicated to structural interface dynamic characterization. *Journal of Sound and Vibration 334* (2015), 202–218. (Cited on page 35.)

[179] Wester, E. C., Brémaud, X., and Smith, B. Meta-Material Sound Insulation. 21–30. (Cited on page 45.)

[180] Wilson, A. H. The theory of electronic semi-conductors. *Proceedings of the Royal Society of London. Series A, Containing Papers of a Mathematical and Physical Character 133*, 822 (1931), 458–491. (Cited on page 42.)

[181] World Health Organization (WHO). *Night noise guidelines for Europe*. 2009. (Cited on page 33.)

[182] Wormser, M., Wein, F., Stingl, M., and Körner, C. Design and additive manufacturing of 3D phononic band gap structures based on gradient based optimization. *Materials 10*, 10 (2017), 1–15. (Cited on page 53.)

[183] Wu, T. T., Huang, Z. G., Tsai, T. C., and Wu, T. C. Evidence of complete band gap and resonances in a plate with periodic stubbed surface. *Applied Physics Letters 93*, 11 (2008), 4–7. (Cited on page 46.)

[184] Wu, W., Yang, X., Zhang, G., Ke, X., Wang, Z., Situ, W., Li, X., and Zhang, J. An experimental study of thermal management system using copper mesh-enhanced composite phase change materials for power battery pack. *Energy* (2016), 909–916. (Cited on page 145.)

[185] Xiao, W., Zeng, G. W., and Cheng, Y. S. Flexural vibration band gaps in a thin plate containing a periodic array of hemmed discs. *Applied Acoustics 69*, 3 (2008), 255–261. (Cited on page 45.)

[186] Xiao, Y., Wen, J., Huang, L., and Wen, X. Analysis and experimental realization of locally resonant phononic plates carrying a periodic array of beam-like resonators. *Journal of Physics D: Applied Physics 47*, 4 (2014). (Cited on page 47.)

[187] Xiao, Y., Wen, J., Wang, G., and Wen, X. Theoretical and experimental study of locally resonant and bragg band gaps in flexural beams carrying periodic arrays of beam-like resonators. *Journal of Vibration and Acoustics, Transactions of the ASME 135*, 4 (2013). (Cited on pages 46 and 95.)

[188] Xiao, Y., Wen, J., and Wen, X. Flexural wave band gaps in locally resonant thin plates with periodically attached springmass resonators. *Journal of Physics D: Applied Physics 45*, 19 (2012). (Cited on page 46.)

[189] Xiao, Y., Wen, J., Yu, D., and Wen, X. Flexural wave propagation in beams with periodically attached vibration absorbers: Band-gap behavior and band formation mechanisms. *Journal of Sound and Vibration 332*, 4 (2013), 867–893. (Cited on page 46.)

[190] Yablonovitch, E. Inhibited spontaneous emission in solid-state physics and electronics. *Physical review letters 58*, 20 (1987), 2059. (Cited on page 42.)

[191] Yablonovitch, E., Gmitter, T. J., and Leung, K.-M. Photonic band structure: The face-centered-cubic case employing nonspherical atoms. *Physical review letters 67*, 17 (1991), 2295. (Cited on page 42.)

[192] Yang, X. W., Lee, J. S., and Kim, Y. Y. Effective mass density based topology optimization of locally resonant acoustic metamaterials for bandgap maximization. *Journal of Sound and Vibration 383* (2016), 89–107. (Cited on page 53.)

[193] Yang, Z., Dai, H. M., Chan, N. H., Ma, G. C., and Sheng, P. Acoustic metamaterial panels for sound attenuation in the 50-1000 Hz regime. *Applied Physics Letters 96*, 4 (2010). (Cited on page 48.)

[194] Yang, Z., Mei, J., Yang, M., Chan, N. H., and Sheng, P. Membrane-type acoustic metamaterial with negative dynamic mass. *Physical Review Letters 101*, 20 (2008), 1–4. (Cited on page 48.)

[195] Yu, J., Nerse, C., Lee, G., Wang, S., and Kyoung-Jin, C. Mass production applicable locally resonant metamaterials for NVH applications. In *Proceedings of the 26th International Congress on Sound and Vibration, ICSV26* (Montreal, 2019). (Cited on pages 50, 95 and 96.)

[196] Zadpoor, A. A. Mechanical meta-materials. *Materials Horizons 3*, 5 (2016), 371–381. (Cited on page 42.)

[197] Zhang, J., Chevali, V. S., Wang, H., and Wang, C. H. Current status of carbon fibre and carbon fibre composites recycling. *Composites Part B: Engineering 193*, April (2020), 108053. (Cited on pages 22 and 23.)

[198] Zhang, X., Chi, X., and Ji, C. Discrete path planning of carbon fiber patch placement with complex surface. *Textile Research Journal* (2023). (Cited on page 25.)

[199] Zhang, Y., Wen, J., Xiao, Y., Wen, X., and Wang, J. Theoretical investigation of the sound attenuation of membrane-type acoustic metamaterials. *Physics Letters, Section A: General, Atomic and Solid State Physics 376*, 17 (2012), 1489–1494. (Cited on page 48.)

[200] Zhao, X., Lu, S., Li, W., Zhang, S., Li, K., Nawaz, K., Wang, P., Yang, G., Ragauskas, A., Ozcan, S., and Webb, E. Epoxy as Filler or Matrix for Polymer Composites. (Cited on pages 117 and 151.)

[201] Zhou, M., Fleury, R., and Kemp, M. Optimization of composite - Recent advances and application. *13th AIAA/ISSMO Multidisciplinary Analysis and Optimization Conference*, September (2010), 1–9. (Cited on page 30.)

[202] Zhou, Y., Nomura, T., and Saitou, K. Multi-component topology and material orientation design of composite structures (MTO-C). *Computer Methods in Applied Mechanics and Engineering 342* (2018), 438–457. (Cited on page 31.)

[203] Zouari, S., Brocail, J., and Génevaux, J. M. Flexural wave band gaps in metamaterial plates: A numerical and experimental study from infinite to finite models. *Journal of Sound and Vibration 435* (2018), 246–263. (Cited on pages 54, 95 and 96.)

DEMANDE D'AUTORISATION DE SOUTENANCE

Arrêté du 25 mai 2016 modifié par l'arrêté du 26 août 2022 fixant le cadre national de la formation et les modalités conduisant à la délivrance du diplôme national de doctorat

Nom : **AMARAL** *nom marital :* *prénom :* **Daniel**

Directeur de thèse : Mohamed ICHCHOU et Michelle SALVIA (co-directrice)

Laboratoire : Laboratoire de Tribologie et Dynamique des Systèmes (LTDS)

Spécialité : MECANIQUE

*Rapporteurs proposés (**nom, prénom, titre, adresse professionnelle et e-mail**) :*

- habilités à diriger des recherches
- extérieurs à l'Ecole Doctorale et à l'Etablissement du doctorant

Professeur El Mostafa DAYA, Université de Lorraine, Laboratoire d'Etude des Microstructures et de Mécanique des Matériaux,7 rue Félix Savart, 57070 METZ
Professeur Stephan RINDERKNECHT, Institut for Mechatronic Systems, TU DARMSTADT, L1|01 210, Otto-Berndt-Straße 2, 64287 DARMSTADT

*Jury proposé, y compris les rapporteurs s'ils en font partie (**nom, prénom, titre, adresse professionnelle et e-mail**) :*
Entre 4 et 8 membres

- dont la moitié au moins extérieurs à l'ED et à l'établissement du doctorant
- dont la moitié au moins professeurs ou assimilés ou d'enseignants de rang équivalent ne dépendant pas du Ministère de l'Enseignement Supérieur
- le directeur de thèse fait partie du jury (mais ne prend pas part à ses décisions)

NB : la composition du jury doit permettre une représentation équilibrée des femmes et des hommes
(art. 18 de l'arrêté du 25 mai 2016 modifié par l'arrêté du 26 août 2022)
« un jury comprenant moins de 7 membres devra au moins comporter 1 femme (et au moins 1 homme). Pour un jury comportant 7 ou 8 membres, il faudra prévoir au moins 2 femmes (et au moins 2 hommes) »
(CS de l'ECL du 13/09/2016)

El Mostafa DAYA, Professeur, Université de Lorraine, Laboratoire d'Etude des Microstructures et de Mécanique des Matériaux,7 rue Félix Savart, 57070 METZ (el-mostafa.daya@univ-lorraine.fr)

Pascal FOSSAT, Ingénieur de Recherche et co-encadrant, ECL/LTDS (pascal.fossat@ec-lyon.fr)

Mohamed ICHCHOU, Professeur et Directeur de thèse, ECL/LTDS (mohamed.ichchou@ec-lyon.fr)

Przemysław KOŁAKOWSKI, Docteur et Directeur, ADAPTRONICA sp. z o.o. ul. Szpitalna 32, 05-092 Łomianki, Poland (pkolak@adaptronica.pl)

Cécile LANGLADE, Professeure, Université de Technologie Belfort Montbéliard, Dépt PMDM, Site de Belfort-Sevenans, rue de Leupe, 90010 BELFORT (cecile.langlade@utbm.fr)

Stephan RINDERKNECHT, Professeur, Institut for Mechatronic Systems, TU DARMSTADT, 64277 DARMSTADT (rinderknecht@ims.tu-darmstadt.de)

Michelle SALVIA, Maître de Conférences HDR et co-Directrice de thèse, ECL/LTDS (michelle.salvia@ec-lyon.fr)

Date de soutenance prévue : fin novembre 2023/début décembre 2023 (en cours)

Titre de la thèse :

Lightweight gearbox using novel housing architecture and materials

Avis du directeur de thèse, date et signature : 12/09/2023

Avis Favorable

M. ICHCHOU

Avis favorable

M. SALVIA

Avis du directeur de laboratoire, date et signature :

Jean-Luc LOUBET

Signature numérique de Jean-Luc LOUBET
DN : cn=Jean-Luc LOUBET, o=CNRS ECL ENTPE, ou=LTDS UMR5513, email=jean-luc.loubet@ec-lyon.fr, c=FR
Date : 2023.09.13 10:57:12 +02'00'

Avis du directeur de l'école doctorale, date et signature :

Signature numérique de Pr. Jocelyn BONJOUR
Date : 2023.09.14 10:41:54 +02'00'

Liste de travaux publiés durant la thèse

Conférences:

Amaral, D. R., Ichchou, M. N., Kołakowski, P., Fossat, P., & Salvia, M. (2022). Enhanced vibro-acoustic behavior of lightweight gearbox housing through the use of locally resonant metamaterials. In 7th European Conference on Structural Control (EACS2022), Warsaw, Poland, July 10-13, 2022.

Amaral, D. R., Ichchou, M. N., Fossat, P., Kołakowski, P., & Salvia, M. (2023). Composite Gearbox Housing Design and its NVH Assessment. In 9th International Conference on Computational Methods in Structural Dynamics and Earthquake Engineering (COMPDYN2023), Athens, Greece, June 12-14, 2023.

Journal Publications :

Amaral, D. R., Ichchou, M. N., Kołakowski, P., Fossat, P., & Salvia, M. (2023). Lightweight gearbox housing with enhanced vibro-acoustic behavior through the use of locally resonant metamaterials. Applied Acoustics, 210, 109435.

(To be submitted) Amaral, D. R., Ichchou, M. N., Salvia, M., Fossat, P., & Kołakowski, P. (2023). Design Optimization and NVH Enhancement of a Composite Gearbox Housing.

Validation du directeur de l'école doctorale de rattachement de la formation complémentaire :

Avis du directeur de la recherche, date et signature :